

ABSTRACT

JACOBS, NEIL. The role of marine thermal gradient structure on Gulf Stream-related extratropical cyclogenesis. (Under the direction of Sethu Raman and Gary Lackmann)

Mid-latitude cyclones, or Nor'easters, have a long history of producing severe, and sometimes catastrophic, blizzard conditions along the eastern seaboard. These winter weather events have been perplexing meteorologists and forecasters for as long as records have been kept. The coastal region east of the Carolinas, in association with the warm Gulf Stream current, is considered by most to be an epicenter of extratropical cyclogenesis. This is a three part study combining a 20 year climatology, a numerical model simulation, and a sensitivity study which links both of the above.

The climatological part of this study extends the previously published Atlantic surface cyclone intensification index (ASCII) database to include dates from October 1991 to April 2002. This added another 115 extratropical cyclogenetic cases to double the total number of storms to 231. As in the first study, linear regression fits were done on the comparison of surface-level thermal gradient with the deepening rate of the coastal low. The statistical relation for the 1991-2002 data are within 2% of the 1982-1990 data, thus verifying the results of the original study. Although the climatological comparison was in full agreement, 69% of the variance in storm deepening rate remains unexplained by this method. To address this issue of scatter, storms were separated into 3 bins based on their 500-mb absolute vorticity. Separate fits were done for the individual bins which were found to explain as much 74% of the variance.

For the second part of this study, a numerical mesoscale weather model (MM5) was employed to test the cyclogenetic response to high resolution sea surface temperature (SST) initialization data using the 24-25 January 2000 winter storm case. While leaving all other model parameters and initialization the same, two different SST distributions were used for the two simulations. The control simulation was initialized with the standard NCEP Eta-212 gridded analysis, while the experimental simulation was initialized with a very high resolution (1.1 km) SST file. The experimental's results show a noticeable response with a more defined coastal front, increased deepening rate, and more accurate track.

A final 2-part study was conducted on the sensitivity of lower-tropospheric cyclogenesis to the sea surface thermal gradient induced by the Gulf Stream. The first part was carried out by systematically reducing the magnitude of the SST gradient for three consecutive mesoscale model simulations. Results show significant decrease in deepening rate with each successive run. The combined results are also in agreement with the regression fits from the ASCII climatology. In the second part, the Gulf Stream was shifted to the east while leaving the unique features such as curvature and SST values unchanged. Results reveal an ASCII limitation within the Gulf Stream Front position parameter, and show that by altering the track of the surface low, the feedback link to the upper-level trough is weakened thus reducing the surface-level cyclogenesis.

**THE ROLE OF MARINE THERMAL GRADIENT STRUCTURE ON GULF
STREAM-RELATED EXTRATROPICAL CYCLOGENESIS**

by

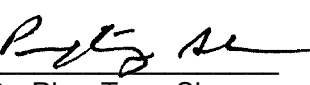
Neil A. Jacobs Jr.

A dissertation submitted to the Graduate Faculty of
North Carolina State University
In partial fulfillment of the
requirements for the Degree of
Doctor of Philosophy

MARINE, EARTH AND ATMOSPHERIC SCIENCES

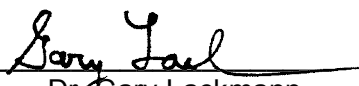
Raleigh
2005

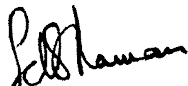
Approved by:


Dr. Ping-Tung Shaw


Dr. Kiran Alapaty


Kermit Keeter


Dr. Gary Lackmann
Co-Chair of the Advisory Committee


Dr. Sethu Raman
Co-Chair of the Advisory Committee

BIOGRAPHY

Neil Andrew Jacobs Jr. was born in Colorado Springs, CO on 12 December 1973. He graduated from Summerville High School, in Summerville, SC, in 1992. From 1992 to 1997, he attended the University of South Carolina, choosing a plan of study in physics with emphasis in condensed matter. In May 1996, after defending an undergraduate thesis on the quantum Hall effect in semiconductors, he obtained a Bachelor of Science degree in physics and a Bachelor of Science degree in mathematics with minors in marine and computer science. During 1994, Neil conducted a research project on the physical limnology of Winyah Bay, SC. From 1996 to 1997, he was a member of the Baikal Research Group where he studied isotope composition in sediment mixing and transport of Lake Baikal, Siberia. In the fall of 1997, Neil enrolled in the Graduate School of North Carolina State University to study physical oceanographic processes and air-sea interactions associated with extratropical cyclogenesis during the Ocean Margins Program under the direction of Dr. Leonard J. Pietrafesa. He obtained a Master of Science degree in 2000, and decided to continue Ph.D. studies at North Carolina State University. Neil was interested in the Gulf Streams influence on extratropical cyclogenesis, and was working on expanding a comprehensive climatology of storms when his topic literally fell out of the sky. On 24 January 2000, Raleigh, NC experienced what is now referred to as the "surprise snowstorm". Neil wondered if the Gulf Stream's warm temperatures and chaotic flow pattern, in some way, contributed to this major weather event, and he spent the next four years trying to unravel this mystery.

ACKNOWLEDGMENTS

I would like to take this opportunity to express my deepest appreciation to my committee members Drs. Sethu Raman, Gary Lackmann, Ping-Tung Shaw, Kiran Alapaty, and Kermit Keeter for their valuable time and patience with me. I would also like to thank them for taking time out of their busy schedules to accommodate me when it came down to the final months before the deadline.

More specifically, I would like to thank Dr. Sethu Raman, my co-chair, for being an outstanding advisor with priceless advice, and patience beyond belief. His motivating positive reinforcement is the only reason why I got far enough to write this section.

I am so lucky to have had the chance to work with Dr. Gary Lackmann, my other co-chair, in the final two years of my program. His commitment to accurate science and relentless questioning is just as remarkable as his contagious enthusiasm. What he has taught me, as a mentor and advisor, go well beyond the classroom.

I am also very grateful for the many classes and discussion I have had with Dr. Ping-Tung Shaw. If it were not for him, my two line MATLAB programs would still be two hundred line FORTRAN scripts. I would also like to thank Dr. Kiran Alapaty for his computer modeling expertise, and Kermit Keeter for his valuable advice on North Carolina weather and real world applications of my research.

There are so many people who have contributed so much to this entire research effort. Let me begin by thanking Dr. Fuqing Zhang (TAMU) for providing me with several data sets, and answering countless MM5 questions, Robert Gilliam (EPA) for

MATLAB advice, Peter Childs for being the Linux super-expert, and Ryan Boyles (SCO of NC), who provided the best IT support I have ever witnessed. I would also like to thank Dr. Dev Niyogi for his helpful advice over espresso at Cup-A-Joe. I am also very grateful for the conversations and comments from Dr. Joseph Cione (NOAA HRD), and Richard Neuherz (NWS ILM) regarding ASCII and the Gulf Stream. I owe a great deal of thanks to Connie Hockaday (MEAS) and Bic Fort (SCO of NC) for taking care of all the graduate school related paperwork and scheduling. Finally, thank you to all the State Climate Office of North Carolina staff who contributed to this research, as well as adding fun and humor to the lab.

Funding for this research was provided by the State Climate Office of North Carolina, and by the Atmospheric Sciences Division, National Science Foundation under grant ATM-0342691. The PSU/NCAR MM5 model was made available through NCAR. The meteorological data for model initialization was provided by NCEP via Dr. Fuqing Zhang. The high resolution sea surface temperature data was made available through NOAA's Coastwatch program. I would also like to acknowledge the State Climate Office of North Carolina for providing the computing resources to operate the models in the lab, and from remote connections.

I am forever indebted to Dr. Robert Morrison for always showing me the bright side of life, for reminding to keep my head up, and for always being there for me. His advice with a smile transcends what I can put into words. My '98 Le Montrachet – Grand Cru will always be half full!

I would like to acknowledge my wonderful parents who have encouraged and supported me throughout my entire life. Without their steadfast love and selfless financial

assistance, none of this work could have been completed. I owe them everything, but once again, they will have to settle for this book.

Finally, I would like to express my deepest appreciation and love to my wife Jen. Supporting me throughout, even when things got tough. In retrospect, juggling two ironman triathlons and two part-time jobs in the last year of a Ph.D. program probably wasn't the smartest move. Regardless, Jen was on the roadside cheering at my races, at the SCO at 3am doing research because I locked my keys in the car, and taking care of me when the stress got to be too much. I am looking forward to returning the favor over the next three years while she balances racing with graduate school.

CONTENTS

	Page
List of Tables	x
List of Figures.	xi
List of Symbols	xxv
Chapter 1: Introduction	1
1.1 Background	1
1.2 Scientific Objectives of this Study.	2
<i>1.2.1 Some outstanding questions</i>	2
<i>1.2.2 On the scientific objectives</i>	3
1.3 Layout of this Dissertation	5
Chapter 2: Gulf Stream Overview	7
2.1 Introduction	7
2.2 The Gulf Stream Front and the "Charleston Bump"	7
2.3 The Gulf Stream Mixed Layer	10
2.4 Wind-Induced Surface Currents and the Coriolis Force	10
2.5 Upwelling and Downwelling Along the Carolina Coast	11
2.6 Thermal Properties of Water	12
2.7 Gulf Stream Heat Budget.	13
2.8 Westward Boundary Current Intensification	14
Chapter 3: Marine Boundary Layer Overview	19
3.1 Introduction	19
3.2 Processes Within the MBL	19

3.3 Mixing Within the MBL	21
3.3.1 <i>Fluxes in the MBL</i>	22
3.3.2 <i>Bulk aerodynamic closure scheme</i>	23
3.3.3 <i>Turbulent kinetic energy and flux</i>	23
3.3.4 <i>Sensible and latent heat flux</i>	24
3.4 Thermally-Induced Coastal Winds.	25
3.5 The Interaction of Storms on the East Coast	26
 Chapter 4: Extratropical Cyclogenesis Overview	27
4.1 Introduction	27
4.2 Vorticity	27
4.3 Quasigeostrophic Theory.	28
4.3.1 <i>QG momentum equation</i>	30
4.3.2 <i>QG vorticity equation</i>	30
4.3.3 <i>QG thermodynamic equation</i>	31
4.3.4 <i>QG omega equation</i>	32
4.3.5 <i>QG height tendency equation</i>	33
4.4 Summary and Application to Extratropical Cyclogenesis	34
 Chapter 5: The Atlantic Surface Cyclone Intensification Index.	38
5.1 Introduction	38
5.2 Background	39
5.2.1 <i>ASCII Thermodynamics</i>	40
5.2.2 <i>Preconditioning Period.</i>	41
5.2.3 <i>ASCII and PSBI</i>	42
5.2.4 <i>Upper-tropospheric Forcing</i>	47
5.3 Data	48
5.4 Results.	56
5.5 Summary	72

Chapter 6: Mesoscale Numerical Model	73
6.1 Model System Overview	73
6.2 Initialization and Boundary Conditions	76
6.3 Model Equations	78
6.4 MM5 Surface Flux Calculations	79
6.4.1 <i>Stability Cases</i>	81
6.4.2 <i>PBL Regimes</i>	82
6.5 Model Physics Schemes	85
 Chapter 7: 24-25 January 2000 Case Study	87
7.1 Introduction	87
7.2 Background	88
7.3 Baroclinicity and ASCII	90
7.4 24-25 January 2000 Case Background	92
7.5 Experiment Design.	102
7.5.1 <i>Model background and simulation history</i>	102
7.5.2 <i>Model description</i>	104
7.5.3 <i>SST data pre-processing methods</i>	108
7.5.4 <i>SST ingestion for the 24-25 January 2000 case</i>	110
7.6 Results.	113
7.7 Summary	165
 Chapter 8: Sensitivity to Boundary Layer Baroclinicity	168
8.1 Introduction and Motivation.	168
8.2 Model Configuration and Methods	169
8.3 Results.	173
8.3.1 <i>Sea-level pressure comparison</i>	173
8.3.2 <i>500-mb absolute vorticity comparison</i>	181
8.3.3 <i>PSBI comparison.</i>	186
8.3.4 <i>ASCII comparison</i>	186

8.4 Summary	191	
Chapter 9: Sensitivity to Gulf Stream Position		192
9.1 Introduction and Motivation.	192	
9.2 Model Configuration and Methods	193	
9.2.1 <i>SST data pre-processing methods</i>	197	
9.2.2 <i>SST ingestion for the sensitivity to GSF position experiment.</i> . .	198	
9.3 Results.	202	
9.3.1 <i>Sea-level pressure comparison</i>	202	
9.3.2 <i>Frontogenesis and surface to upper-level feedback.</i>	214	
9.3.3 <i>PSBI and ASCII comparison</i>	239	
9.4 Summary	242	
Chapter 10: Conclusions		244
10.1 The Atlantic Surface Cyclone Intensification Index.	244	
10.2 24-25 January 2000 Case Study	245	
10.3 Sensitivity to Boundary Layer Baroclinicity	247	
10.4 Sensitivity to Gulf Stream Position	248	
References	252	
Appendix A: Porting MM5 to OS X	269	

List of Tables

List of Figures

Page

Figure 2.1	High resolution AVHRR SST imagery showing the turbulent eddy formation caused by the deflection off the "Charleston bump" (arrow).	8
Figure 5.1.	Map of the eastern United States. The domain used to study East Coast cyclogenesis or cyclone redevelopment using climatological data is shaded in gray.	44
Figure 5.2.	The updated ASCII dataset (1980-2002) of ETC's $\Delta P/12h$ vs. PSBI. The linear regression fit combines both set of storms (1980-1990 and 1991-2002).	46
Figure 5.3.	The ASCII dataset (1991-2002) of ETC's ($\Delta P/12h$ vs. PSBI) broken down into bins of 500mb vorticity ($10^{-5}s^{-1}$).	58
Figure 5.4.	The maximum absolute vorticities (s^{-1} , averaged for each bin) plotted against the corresponding slope of the linear regressions seen in Figure 5.3.	60
Figure 5.5.	The ASCII dataset (1991-2002) of ETC's ($\Delta P/12h$ vs. PSBI) broken down into bins of 500mb vorticity ($10^{-5}s^{-1}$).	62
Figure 5.6a.	The full distribution's observed deepening rate (mb/12h) of cases from the 1991-2002 data set plotted against the predicted deepening rate (mb/12h) from the updated ASCII regression equation seen in Figure 2. The center line shows a perfect	

correlation bound on both sides by a 95% confidence interval calculated for the entire data set. The horizontal line marks the mean deepening rate for the entire data set. 64

Figure 5.6b. The *strong* bin's observed deepening rate (mb/12h) of cases from the 1991-2002 data set plotted against the predicted deepening rate (mb/12h) from the updated ASCII regression equation seen in Figure 2. The center line shows a perfect correlation bound on both sides by a 95% confidence interval calculated for the entire data set. The horizontal line marks the mean deepening rate for the entire data set. 65

Figure 5.6c. The *moderate* bin's observed deepening rate (mb/12h) of cases from the 1991-2002 data set plotted against the predicted deepening rate (mb/12h) from the updated ASCII regression equation seen in Figure 2. The center line shows a perfect correlation bound on both sides by a 95% confidence interval calculated for the entire data set. The horizontal line marks the mean deepening rate for the entire data set. 66

Figure 5.6d. The *weak* bin's observed deepening rate (mb/12h) of cases from the 1991-2002 data set plotted against the predicted deepening rate (mb/12h) from the updated ASCII regression equation seen in Figure 2. The center line shows a perfect correlation bound on both sides by a 95% confidence interval calculated for the entire data set. The horizontal line marks the mean deepening rate for the entire data set. 67

Figure 5.7. The ASCII dataset (1991-2002) of ETC's ($\Delta P/12h$ vs. PSBI) broken down into bins of 500-mb positive vorticity

advection(s ⁻²)	68
Figure 5.8. The maximum absolute vorticity advection (s-2, averaged for each bin) plotted against the corresponding slope of the linear regressions seen in Figure 5.7.	69
Figure 5.9. The observed deepening rate (mb/12h) of cases from the 1991-2002 data set plotted against the predicted deepening rate (mb/12h) from the separate regression equations of the respective bins. The center line shows a perfect correlation bound on both sides by a 95% confidence interval calculated for the entire data set. The horizontal line marks the mean deepening rate for the entire (a), and the binned (b), (c), and (d) data sets. The full distribution (a), as well as the weakly forced (b), moderately forced (c), and strongly forced (d) bins are shown.	71
Figure 6.1. Flow chart of the MM5 routines within the modeling system . . .	74
Figure 6.2. Vertical sigma levels within the model domain used in all the experiments in this study.	75
Figure 7.1a Metar obs and Ship/buoy obs (SST is the top value) valid 06Z 23 Jan 2000 overlaid the most recent corresponding GOES8 imagery.	94
Figure 7.1b Metar obs and Ship/buoy obs (SST is the top value) valid 00Z 25 Jan 2000 overlaid the most recent corresponding GOES8 imagery.	95

Figure 7.1c	Metar obs and Ship/buoy obs (SST is the top value) valid 12Z 25 Jan 2000 overlaid the most recent corresponding GOES8 imagery.	96
Figure 7.1d	Metar obs and Ship/buoy obs (SST is the top value) valid 18Z 25 Jan 2000 overlaid the most recent corresponding GOES8 imagery.	97
Figure 7.2	Observations of sea-level pressure (mb, solid lines) and 500- mb geopotential height (dashed lines) valid 12Z 24 Jan (a), 00Z 25 Jan (b), and 12Z 25 Jan (c).	100
Figure 7.3	NOWRAD 2 km base reflectivity valid 12Z 24 Jan (a), 00Z 25 Jan (b), and 12Z 25 Jan (c).	101
Figure 7.4	North Carolina snowfall totals for the 24-25 January 2000 winter storm.	102
Figure 7.5a	The full domain plots of the SST input data files for (a) the control simulation's NCEP's 2.5 resolution data.	106
Figure 7.5b	The full domain plots of the SST input data files for (b) the experimental simulation's 1.1 km grid spacing data.	107
Figure 7.5c	Ship and buoy observations of SST valid 06Z Jan 23 2000 overlaid a section of the digitized SST file used for initialization.	112
Figure 7.6	Tracks of the observed (red), experimental simulation (green), and control simulation (blue).	115

Figure 7.14	Plots of surface-level sensible heat flux (W/m^2) and pressure (mb) for (a) the control simulation and (b) the experimental simulation valid 12Z 25 Jan (36h after initialization).	131
Figure 7.15	Plots of surface-level sensible heat flux (W/m^2) and pressure (mb) for (a) the control simulation and (b) the experimental simulation valid 18Z (2pm EDT) 25 Jan (42h after initialization).	133
Figure 7.16	Surface-level wind field plots (m/s) for (a) the control simulation and (b) the experimental simulation valid 12Z 24 Jan (12h after initialization).	136
Figure 7.17	Surface-level wind field plots (m/s) for (a) the control simulation and (b) the experimental simulation valid 21Z 24 Jan (21h after initialization).	137
Figure 7.18	Surface-level wind field plots (m/s) for (a) the control simulation and (b) the experimental simulation valid 12Z 25 Jan (36h after initialization).	138
Figure 7.19	Plots of 950-hPa stretching (s^{-2}) valid 21Z Jan 24 (21 h after initialization) for the control simulation (a), the experimental simulation (b), and the experimental simulation minus the control simulation difference field (c).	141
Figure 7.20	Plots of 950-hPa stretching (s^{-2}) valid 12Z Jan 25 (36 h after initialization) for the control simulation (a), the experimental simulation (b), and the experimental simulation minus the control simulation difference field (c).	143

Figure 7.21	Time series of sea-level pressure (mb) for experimental simulation (red) and control simulation (blue). Initialization 00Z 24 Jan 2000 (0 h into simulation) through 00Z 26 Jan 2000 (48 h into simulation).	146
Figure 7.22	Cumulative precipitation (mm) valid 01Z 24 Jan 2000 (1h into simulation) for control simulation (a) and experimental simulation (b) initialized 00Z 24 Jan 2000.	149
Figure 7.23	Cumulative precipitation (mm) valid 06Z 24 Jan 2000 (6h into simulation) for control simulation (a) and experimental simulation (b) initialized 00Z 24 Jan 2000.	150
Figure 7.24	Cumulative precipitation (mm) valid 12Z 24 Jan 2000 (12h into simulation) for control simulation (a) and experimental simulation (b) initialized 00Z 24 Jan 2000.	151
Figure 7.25	Cumulative precipitation (mm) valid 00Z 25 Jan 2000 (24h into simulation) for control simulation (a) and experimental simulation (b) initialized 00Z 24 Jan 2000.	152
Figure 7.26	Cumulative precipitation (mm) valid 12Z 25 Jan 2000 (36h into simulation) for control simulation (a) and experimental simulation (b) initialized 00Z 24 Jan 2000.	153
Figure 7.27	Cumulative precipitation (mm) valid 00Z 26 Jan 2000 (48h into simulation) for control simulation (a) and experimental simulation (b) initialized 00Z 24 Jan 2000.	154

Figure 7.28	Simulated dBZ for the control / experimental valid 12Z 24 Jan 2000 (a/b, 12 h), 00Z 25 Jan 2000 (c/d, 24 h), and 12Z 25 Jan 2000 (e/f, 36 h).	156
Figure 7.29	Cross sections of vorticity (10-5, s-1) at latitude 34.5N, and covering longitudes 78W to 72W for control / experimental valid 18Z 24 Jan 2000 (a/b), 00Z 25 Jan 2000 (c/d), and 06Z 25 Jan 2000 (e/f).	158
Figure 7.30	Cross sections of potential vorticity (pvu) at latitude 34.5N, and covering longitudes 78W to 72W for control / experimental simulations valid 00Z 25 Jan 2000 (a/b), and 06Z 25 Jan 2000 (c/d).	161
Figure 7.31	Cloud moisture colored to temperature (height) valid 12Z 24 January 2000. The control is on the top, and the experimental is on the bottom.	162
Figure 7.32	Cloud moisture colored to temperature (height) valid 00Z 25 January 2000. The control is on the top, and the experimental is on the bottom.	163
Figure 7.33	Cloud moisture colored to temperature (height) valid 12Z 25 January 2000. The control is on the top, and the experimental is on the bottom.	164
Figure 8.1	The SST sensitivity simulation's single outer domain of 10 km grid spacing. This domain was chosen based on the balance between having a domain large enough to minimizes forcing from boundary conditions, and the CPU memory limitations of	

a high resolution grid file with 38 sigma levels.	170
Figure 8.2 The three SST input files used in the simulations where (a) is the SST file with the largest gradient (with almost unrealistic values for January), (b) is the product of the first smoothing run, and (c), the weakest gradient, a product of the second smoothing run. The PSBI values are 2.8°C/10km, 1.8°C/10km, 1.2°C/10km for (a), (b), and (c) respectively.	172
Figure 8.3 Plots of sea-level pressure for simulations (a), (b), and (c) valid 12Z 24 Jan (12 h into simulation). The low pressure seen is a small area of low pressure forming along the coastal front.	176
Figure 8.4 Plots of sea-level pressure for simulations (a), (b), and (c) valid 18Z 24 Jan (18 h into simulation). The initial stages of the main coastal storm can be seen.	177
Figure 8.5 Plots of sea-level pressure for simulations (a), (b), and (c) valid 00Z 25 Jan (24 h into simulation).	178
Figure 8.6 Plots of sea-level pressure for simulations (a), (b), and (c) valid 06Z 25 Jan (30 h into simulation).	179
Figure 8.7 Plots of sea-level pressure for simulations (a), (b), and (c) valid 12Z 25 Jan (36 h into simulation).	180
Figure 8.8 Plots of 500-mb vorticity (10 ⁻¹ s ⁻¹) for simulations (a), (b), and (c) valid 00Z 25 Jan 2000 (24 h into simulation).	183
Figure 8.9 Plots of 500-mb vorticity (10 ⁻¹ s ⁻¹) for simulations (a), (b),	

and (c) valid 06Z 25 Jan 2000 (30 h into simulation).	184
Figure 8.10 Plots of 500-mb vorticity (10^{-1} s^{-1}) for simulations (a), (b), and (c) valid 12Z 25 Jan 2000 (36 h into simulation).	185
Figure 8.11 The ASCII dataset (1991-2002) of ETC's ($\Delta P/12\text{h}$ vs. PSBI) broken down into bins of 500mb vorticity (10^{-5} s^{-1}) plotted with the (a), (b), and (c) sensitivity simulations.	189
Figure 8.12 The updated ASCII dataset (1980-2002) of ETC's $\Delta P/12\text{h}$ vs. PSBI. The "Storms" (blue) linear regression fit combines both sets of storms (1980-1990 and 1991-2002), and the sensitivity simulations (a), (b), and (c) with regression fit (red).	190
Figure 9.1 The model's domain used for all simulations showing the terrain features colored to 100 m contours over the high resolution United States map.	194
Figure 9.2a The SST initialization file for the <i>Cntl</i> simulation. Post regridded to 10 km with no shift to the high resolution data. The high resolution data is from 22 Jan 2000.	196
Figure 9.2b The SST initialization file for the <i>Exp-1</i> simulation. Post regridded to 10 km with a 1 degree of longitude shift to the high resolution data. The high resolution data is valid 22 Jan 2000.	200
Figure 9.2c The SST initialization file for the <i>Exp-2</i> simulation. Post regridded to 10 km with a 2.5 degree of longitude shift to the high resolution data. The high resolution data is valid 22 Jan	

	2000.	201
Figure 9.3	Sea-level pressure (mb) and model derived 950-hPa reflectivity (dBZ) valid 18Z Jan 24 (18 h into the simulation) for the <i>Cntl</i> (a), <i>Exp-1</i> (b), and <i>Exp-2</i> (c). A sea-level pressure difference field (mb) of <i>Cntl - Exp-2</i> (a-c) is shown in (d).	204
Figure 9.4	Sea-level pressure (mb) and model derived 950-hPa reflectivity (dBZ) valid 00Z Jan 25 (24 h into the simulations) for the <i>Cntl</i> (a), <i>Exp-1</i> (b), and <i>Exp-2</i> (c). A sea-level pressure difference field (mb) of <i>Cntl - Exp-2</i> (a-c) is shown in (d).	205
Figure 9.5	Sea-level pressure (mb) and model derived 950-hPa reflectivity (dBZ) valid 06Z Jan 25 (30 h into the simulations) for the <i>Cntl</i> (a), <i>Exp-1</i> (b), and <i>Exp-2</i> (c). A sea-level pressure difference field (mb) of <i>Cntl - Exp-2</i> (a-c) is shown in (d).	206
Figure 9.6	Sea-level pressure (mb) and model derived 950-hPa reflectivity (dBZ) valid 09Z Jan 25 (33 h into the simulations) for the <i>Cntl</i> (a), <i>Exp-1</i> (b), and <i>Exp-2</i> (c). A sea-level pressure difference field (mb) of <i>Cntl - Exp-2</i> (a-c) is shown in (d).	207
Figure 9.7	Sea-level pressure (mb) and model derived 950-hPa reflectivity (dBZ) valid 12Z Jan 25 (36 h into the simulations) for the <i>Cntl</i> (a), <i>Exp-1</i> (b), and <i>Exp-2</i> (c). A sea-level pressure difference field (mb) of <i>Cntl - Exp-2</i> (a-c) is shown in (d).	208
Figure 9.8	Sea-level pressure (mb) and 500-hPa heights and divergence (s^{-1}) valid 09Z Jan 25 (33 h into the simulations) for the <i>Cntl</i> (a), <i>Exp-1</i> (b), and <i>Exp-2</i> (c).	209

Figure 9.9	Sea-level pressure (mb) and 500-hPa heights and divergence (s^{-1}) valid 12Z Jan 25 (36 h into the simulations) for the <i>Cntl</i> (a), <i>Exp-1</i> (b), and <i>Exp-2</i> (c).	210
Figure 9.10	Plots of 2-m temperatures (K) and 10-m wind vectors for valid 00Z Jan 25 (24 h into the simulations) for the <i>Cntl</i> (a), <i>Exp-1</i> (b), and <i>Exp-2</i> (c).	216
Figure 9.11a	Plot of 10-m wind streamlines colored to velocity (ms^{-1}) for the <i>Cntl</i> simulation valid 00Z Jan 25 (24 h into the simulation).	217
Figure 9.11b	Plot of 10-m wind streamlines colored to velocity (ms^{-1}) for the <i>Exp-1</i> simulation valid 00Z Jan 25 (24 h into the simulation).	218
Figure 9.11c	Plot of 10-m wind streamlines colored to velocity (ms^{-1}) for the <i>Exp-2</i> simulation valid 00Z Jan 25 (24 h into the simulation).	219
Figure 9.12	Plots of 2-m temperatures (K) and 10-m wind vectors for valid 06Z Jan 25 (30 h into the simulations) for the <i>Cntl</i> (a), <i>Exp-1</i> (b), and <i>Exp-2</i> (c).	222
Figure 9.13a	Plot of 10-m wind streamlines colored to velocity (ms^{-1}) for the <i>Cntl</i> simulation valid 06Z Jan 25 (30 h into the simulation).	223
Figure 9.13b	Plot of 10-m wind streamlines colored to velocity (ms^{-1}) for the <i>Exp-1</i> simulation valid 06Z Jan 25 (30 h into the simulation).	224

List of Symbols

C_d	Surface drag coefficient
C_h	Exchange coefficient of heat
C_e	Exchange coefficient of moisture
c_p	Specific heat of air, $1005 \text{ J kg}^{-1} \text{ K}^{-1}$
c_{pm}	Specific heat of moist air, $1850 \text{ J kg}^{-1} \text{ K}^{-1}$
d	Depth in z direction
E_T	Net turbulent kinetic energy
E_s	Surface moisture flux
F	Flux of moisture, heat, or momentum
f	Coriolis parameter
g	Gravity, at sea level = 9.81 m s^{-2}
H_s	Surface heat flux
H	Vertical sensible heat flux
h	Fluid of depth d
J	Diabatic heating rate
K_a	Molecular diffusivity, $2.4 \times 10^{-5} \text{ m}^2 \text{s}^{-1}$
K	von Karman constant, 0.4
k	Wave number
L	Monin-Obukhov length
L_v	Latent heat of vaporization, $2.5 \times 10^{-4} \text{ J kg}^{-1}$
m	Mass flux
\bar{m}	Mixing coefficient
M	Surface moisture availability
P, p	Pressure
Q_a	Net heat
Q_e	Latent heat
Q_h	Sensible heat
Q_{sw}	Short wave radiation

Q_{lw}	Long wave radiation
q_c	Cloud water mixing ratio
q_v	Water vapor mixing ratio
R, R_d	Gas constant for dry air, $287 \text{ J kg}^{-1} \text{ K}^{-1}$
R_v	Gas constant for saturated air, $461.5 \text{ J kg}^{-1} \text{ K}^{-1}$
R_{iB}	Bulk Richardson number
T	Temperature
T_a	Air temp at surface
T_w	Sea surface temperature (SST)
T_{GSF}	SST at Gulf Stream Front
T_l	Surface air temp over land (ASCII)
t	Time
U	Velocity vector in x, y, z
u	x component of velocity
u_*	Friction velocity
V	Horizontal velocity vector
V_a	Wind speed at the lowest sigma level
V_{ag}	Ageostrophic wind
V_c	Convective velocity
V_g	Geostrophic wind
v	y component of velocity
w	z component of velocity
x	Eastward axis
y	Northward axis
z, s	Vertical (upward) axis
z_0	Lowest sigma level
z^*	Vertical coordinate in log pressure system
α	Specific volume
β	Variation of Coriolis parameter as a function of latitude
χ	Geopotential tendency

ε	Rate of energy dissipation, entrainment coefficient
Φ	Geopotential
ϕ	Latitude
γ	Ratio of specific heats, ~ 1.4
η	Surface elevation of fluid from depth d
φ	Non-dimensional stability parameter
θ	Potential temperature
ρ	Density
σ	Vertical coordinate
τ, τ_s	Surface stress
τ_a	Wind stress
Ω	Angular velocity of earth
ω	Vertical velocity
ψ	Stream function
ζ	Vorticity
ζ_g	Geostrophic vorticity

CHAPTER 1: INTRODUCTION

1.1 Background

The coastal region offshore of the Carolinas and Virginia is known to be a favorable setting for the development of extratropical cyclones (e.g., Zishka and Smith 1980; Sanders and Gyakum 1980). Cyclones that track northward along the East Coast of the U.S. can produce gale-force winds, heavy wintry precipitation, and coastal storm surges that result in severe beach erosion and major property damage. This region is favorable for cyclogenesis because of i) its position adjacent to the warm waters of the Gulf Stream, and ii) the frequent passage of mobile upper-tropospheric disturbances embedded within the upper jet stream. Extensive research has been conducted on the pre-storm marine boundary layer and air-sea interactions associated with extratropical cyclones forming in this region (e.g., Bosart et al. 1972; Sanders and Gyakum 1980; Bosart 1981; Rogers and Bosart 1986; Grossman 1988; Kuo and Reed 1988; Holt and Raman 1990; Kuo and Low-Nam 1990; Reed et al. 1992; Reddy and Raman 1994).

Several factors are important in the development of an extratropical winter cyclone. Different degrees of storm intensity depend on which factors are present at specific times. The factors associated with falling pressure and rising motion above the surface are vorticity advection becoming more cyclonic with an increase in height, a local maximum in temperature advection, the vertical component of the curl of the frictional force becoming more cyclonic with height, pre-existing vorticity, and a local maximum in diabatic heating.

The effects of differential geostrophic vorticity advection arise from wavetrains above the 500 mb level. In a series of baroclinic ridges and troughs, the vorticity maximum is

generally located along the trough axes, and the vorticity minimum is located along the ridge axes. Downstream from the maxima in absolute vorticity is the zone of cyclonic vorticity advection (e.g., Sutcliffe 1939, Bjerknes and Holmboe 1944). Upward vertical motion in the cyclonic vorticity advection region is generated by an upper-level vorticity maximum. Stretching of the column from the vertical motion can enhance the surface circulation which is aided by the low-level warm-air advection. The enhanced warm advection and vertical motion produces greater drops in surface pressure. This falling pressure contributes to the formation of surface troughs or cyclones.

The influence of upper-level disturbances is directly linked to the lower-level thermal advection. However, in the Gulf Stream region, it is important to know to what degree these factors promote cyclogenesis. The interaction of upper-level cyclonic vorticity with the contributions of lower-tropospheric thermal gradients must be studied to better understand individual forcing mechanisms driving their mutual interactions.

1.2 Scientific Objectives of this Study

1.2.1 Some outstanding questions

Why does extratropical cyclogenesis tend to occur more frequently off the coast of North Carolina? How much influence in rapid storm development is Gulf-Stream related, and how much is due to upper-level forcing? Can Gulf-Stream-Front-induced atmospheric baroclinicity be simulated with a numerical mesoscale weather model? If so, will a more realistic representation of the SST translate into a more accurate simulation of a winter cyclone? What boundaries are the current pre-storm baroclinic index subject to? How does the pre-conditioning period interact with the Gulf Stream? What climatological patterns may

the Gulf Stream have as far as position and the relationship to extratropical cyclogenesis?

In order to address these questions, the following objectives have been identified: *to understand the role of the Gulf Stream in extratropical cyclogenesis.* This will be accomplished through the following sub-objectives:

(1) *Investigate the contribution of factors such as Gulf Stream position and temperature (warm-core eddy formation, and filaments) in the development of wintertime coastal storms.*

(2) *Study the sensitivity of model simulations to high resolution SSTs.*

(3) *Resolve the degree of influence upper-level processes have on extratropical cyclogenesis versus surface- level processes in the Gulf Stream region.*

(4) *Verify and improve upon the original ASCII climatology by incorporating upper-level forcing and more observations.*

1.2.2 On the scientific objectives

A) The influence of the Gulf Stream as a function of temperature and position

The Gulf Stream influence can be broken down into thermal magnitude and position. The position of the Gulf Stream can vary significantly due to the motion of filaments and eddies. The SST of the features is dictated by the upwelling and downwelling of the current flow and how it interacts with the coastline. The warm-core eddies and the warm-core filaments are of the most interest because of their ability to generate surface-level cyclonic

rotation from thermally induced pressure gradients. The surface-level winds will be subjected to increased convergence with a greater amount of vertical motion. Likewise, the more defined the front is in terms of the temperature gradient, the stronger the influence. The position of the Gulf Stream with respect to land also has an effect on the extratropical cyclogenesis since the closer it is to the cooler land mass, the tighter the temperature gradient.

B) Simulate the air-sea interaction processes that cause cyclogenesis

Numerous observational case studies have been conducted on how low-level thermal gradients can enhance cyclogenesis. There have also been several "box-model" and simplified numerical simulations of mesocyclogenesis over thermal gradients (Cione and Raman 1995; Raman and Reddy 1996), but there have been no attempts, to the author's knowledge, to incorporate very high resolution Gulf Stream data into an actual case of extratropical cyclogenesis to understand and verify the chain of events predicted by the quasigeostrophic omega and height tendency equations. There have been numerical simulations verifying the theory of self-development over the Midwest, but the thermal contrast of the GSF is far greater, and warrants being studied in greater detail.

C) The contribution of upper- level forcing compared to surface processes

The influence of upper-level vorticity anomalies is directly linked to the lower-level thermal advection. However, in the area of the Gulf Stream, it is important to know to what degree these factors promote cyclogenesis. There exists a phase shift between the upper and lower-level anomalies that allows mutual interactions between the levels, in which the circulations associated with the upper-level anomalies enhance the surface circulation. The relative importance of various perturbations and their mutual interactions associated with

extratropical cyclogenesis need to be separated from the contributions of thermally induced baroclinicity to better understand individual forcing mechanisms. This can be done using the 20-years of climatological storm data separated according to various features in an attempt to isolate the degree of contribution.

D) Improve the explained variance of ASCII by incorporating upper-level forcing

There are two schools of thought on cyclogenesis. Those who are convinced surface cyclogenesis is induced by upper-level vorticity advection, and those who believe surface-level cyclogenesis can be induced by surface fluxes. In reality, both are likely true, with the later weighing in with a slightly smaller contribution. However, it is an objective of this study to quantify the amount of contribution, particularly in the Gulf Stream region, by a climatological study of East Coast winter storms.

1.3 Layout of the Dissertation

In the next chapter, the features and characteristics of the Gulf Stream are reviewed. This includes the bottom features responsible for the turbulent eddies, upwelling, downwelling, and the sea surface temperatures associated with these motions. The chapter concludes with a basic heat budget description. In Chapter 3, the marine boundary layer processes that are related to the coastal Carolina region are discussed, as well as surface fluxes and how they pertain to the Gulf Stream. Chapter 4 contains a mathematical overview of vorticity and quasigeostrophic theory. This chapter concludes with a Gulf Stream specific "self-development" explanation of how cyclogenesis occurs based on the equations presented. Chapter 5 contains the ASCII experiment. This section begins with an extension

of the original ASCII climatology, and concludes with a new version which incorporates upper-level forcing to further explain the variance in the deepening rate distribution. Chapter 6 is a review of the MM5 architecture and various options that were tested during the study which is presented in Chapter 7. In this chapter (7), a case study of the 24-25 January 2000 winter storm is conducted where dependence on SST grid resolution is tested. The results are used to explain the effects that the GSF has on surface-level cyclogenesis. Chapter 8 is a baroclinicity sensitivity study where systematically altered SST grid files were fed into an MM5 simulation to quantify the contribution SST thermal gradient has on cyclogenesis. The final study, presented in Chapter 9, is a second sensitivity study where the Gulf Stream is shifted to the east without altering the SSTs. The conclusions appear in Chapter 10.

CHAPTER 2: GULF STREAM OVERVIEW

2.1 Introduction

The Gulf Stream is an extensive western boundary current that begins in the Caribbean and ends in the north Atlantic. It plays an important role in the poleward transfer of heat and salt. The Gulf Stream system is powerful enough to be readily seen from space. Strong thermal gradients make it visible to infrared measurements, like VHRR (Very High Resolution Radiometer) readings using the early NOAA satellites, THIR (Temperature and Humidity Infrared Radiometer) readings from Nimbus satellites, and Advanced VHRR (AVHRR) readings from more recent NOAA satellites. The Gulf Stream begins well south of Cape Hatteras at the straits of Florida.

2.2 The Gulf Stream Front and the "Charleston Bump"

Within a hundred kilometers off the Carolina coast lies the Gulf Stream Front (GSF), which in the fall, winter, and spring months, has a sea surface temperature warmer than those of the near-coastal waters. Large horizontal temperature gradients occur during winters off the mid-Atlantic coast because of the presence of the Gulf Stream with a sea surface temperature of 24 to 28°C. Coastal waters have surface temperatures typically in the range of 6 to 9°C (Wayland and Raman 1989) during the winter months, and up to 20°C in the late spring and early fall. During the occurrence of coastal fronts and cold-air outbreaks, air temperatures generally range from -5 to 5°C. The net effect is a large cross-shelf air temperature differential. This temperature gradient is a highly baroclinic region in the MBL especially when the Gulf Stream is closer to the coast. The degree of MBL baroclinicity is

dependent on the ratio of the offshore-onshore air temperature difference to the distance of the Gulf Stream Front to the coast. These horizontal thermal gradients can result in the rapid and intense destabilization of the MBL within the Gulf Stream region through moist convection (Cione et al. 1998).

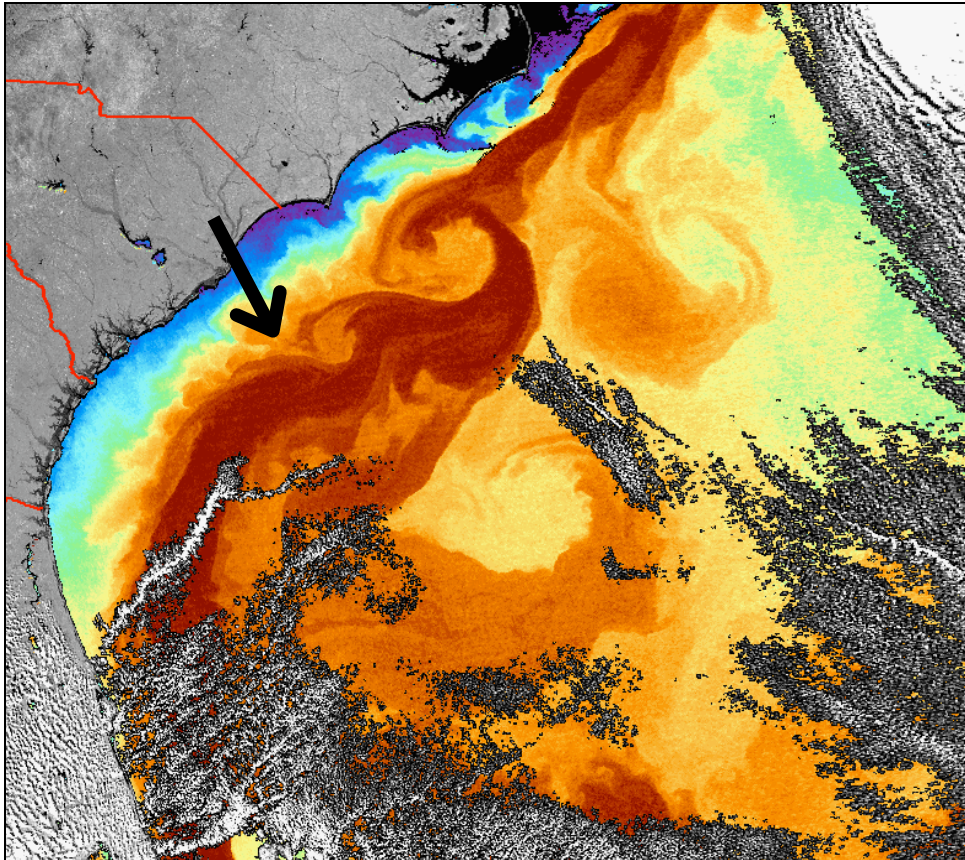


Figure 2.1 High resolution AVHRR SST imagery showing the turbulent eddy formation caused by the deflection off the "Charleston bump" (arrow).

The distance of the GSF from the coast can fluctuate significantly. Lateral meandering of the GSF makes these distances vary, such that at Cape Hatteras, offshore distance to the GSF can vary from 15 to 120 km from the coast, while offshore of

Wilmington, the front can vary between 100 and 300 km (Cione et al. 1993). These variations are caused by the lateral or cross shelf meandering of the Gulf Stream Front which is essentially a manifestation of the down stream propagation of topographic Rossby waves created at the site of a topographic bump or hill-like bottom feature offshore Charleston, South Carolina (Figure 2.1) located at 32°N and 79°W; also known as the "Charleston bump" (Brooks and Bane 1978; Pietrafesa et al. 1978; Rooney et al. 1978; Pietrafesa et al. 1985).

The position of the Gulf Stream as it leaves the coast changes throughout the year. Compared with the width of the current (100-200 km), the range of this variation near the southern East Coast (30-40 km) is relatively small (Hogg and Johns 1995). However, recent studies by Mariano et al. (2002) suggest that the meridional range of the annual variation in stream path may be closer to 100-200 km which are in agreement with the findings of Cione et al. (1993). Other characteristics of the current are more variable. Significant changes in its transport, meandering, and structure can be observed through many time scales as it travels northeast. The transport of the Gulf Stream nearly doubles downstream of Cape Hatteras (Hall and Fofonoff 1993) at a rate of 8 Sv every 100 km (Johns et al. 1995). It appears that the downstream increase in transport between Cape Hatteras and 55°W is mostly due to increased velocities in the deep waters of the Gulf Stream (Johns et al. 1995). This increase in velocity is thought to be associated with deep recirculation cells found north and south of the current (Hall and Fofonoff 1993). The meandering of the Gulf Stream intensifies downstream of Cape Hatteras, reaching a maximum near 65°W. Meanders often pinch off from the current to form Gulf Stream rings. On average, the Stream sheds 22 warm-core rings and 35 cold-core rings per year (Hogg and Johns 1995). The region of the Gulf Stream's branch point is highly dynamic and subject to rapid change. The high degree of

mesoscale activity, along with rapid changes in the major surface currents, make this a very difficult region to study. Part of this variability arises from the high amount of eddy activity. Eddy kinetic energy along both the Gulf Stream and the North Atlantic Current is at peak values here (Richardson 1983).

2.3 The Gulf Stream Mixed Layer

The surface layers of the ocean form a part of the air-sea boundary layer system, and are dominated by turbulent mixing processes and interface fluxes. These layers are referred to as the mixed layer because there is almost always at least one homogeneous layer near the surface in which the temperature and salinity profiles are constant with depth. The situation is normally more complicated because the mixed layer is actually composed of several stratified homogeneous layers. The principal requirement for the understanding of these processes is the correct parameterization of the fluxes of momentum and heat across the air-sea interface (discussed in the next chapter), as well as turbulent mixing due to surface wave breaking and shear of the wind driven currents.

2.4 Wind-Induced Surface Currents and the Coriolis Force

Friction between wind and the ocean surface helps produce the large scale horizontal water movements of the ocean's surface. These currents tend to resemble the patterns of the prevailing surface winds. If the Earth did not rotate, friction between the wind and the ocean surface would drive the surface currents in the same direction as the wind. As the depth of the water column increases, the speed of the current would become slower; however, it would remain in the same direction. Since the Earth does rotate, the shallow layer of surface

water set in motion by the wind is deflected to the right of the wind direction in the Northern Hemisphere, and to the left of the wind direction in the Southern Hemisphere. This deflection is called the Coriolis effect. The Coriolis effect is latitude-dependent and becomes more noticeable further from the equator. Earth's rotation causes a change in direction of each layer of water that is put into motion by the layer above. Viewed from above, changes in the direction of horizontal water motion (and decreased speed) with increasing depth form a spiral known as the Ekman spiral. Although the motion of the surface-water layer can be up to 45 degrees to the right (Northern Hemisphere) of the wind direction, the Ekman spiral causes the net transport of water in the mixed layer to be approximately 90 degrees to the right of the wind direction.

2.5 Upwelling and Downwelling along the Carolina Coast

Ocean winds can induce advection of surface water away from a land boundary. Colder water is then replaced from below. This process is called upwelling. Upwelling occurs in a horizontal region on the order of the Rossby radius of deformation when the prevailing winds blow in a direction parallel to the shoreline. This offshore Ekman transport is compensated by an onshore flow deeper in the water column. The net transport of surface water in the Northern Hemisphere is to the right of the surface wind. Along the Carolina coast, upwelling occurs when the wind blows from the south, or southwest, because the net transport of surface water is away from land. Upwelling takes place wherever favorable wind occurs. However, it does take more than a day of sustained winds for the current to “spin-up”. The intensity and duration of the wind-driven current is a function of the duration of the wind (Dalu and Pielke 1990). If the wind stress is periodic, upwelling will only occur when

the duration of forcing is longer in time than the sum of the inertial period and the friction e-folding time. Likewise, upwelling will continue for a day or more after the winds cease. There are regions in the ocean where surface water is transported towards the coast by onshore and sideshore winds. These winds cause the water to pile up against the shoreline. As a result, the surface water sinks. This downward movement is called downwelling. Along the Carolina coast, downwelling occurs when the wind blows from the northeast, or east because the net transport of surface water is toward land. Sea surface temperatures are relatively high in regions of downwelling because the colder temperatures are held below. Blanton et al. (1981) show that additional continuous upwelling along the western boundary of the Gulf Stream is linked to topographic bottom features on the edge of the continental shelf.

Upwelling and downwelling are very important in generating large changes in the SST that can persist for several days. Along the Carolina coast, these changes can be as large as 10°C and can develop within a day and last for several days.

2.6 Thermal Properties of Water

Compared to other naturally occurring substances, the specific heat of water is exceptionally high. The heat required to raise the temperature of one kilogram of water 1°C is 4 times greater than air. Thus, for equal volumes of air and water, about 3000 times more heat energy is required to bring about the same temperature change in water as in air. A change in phase of water is brought about by either an input of heat or a release of heat to the environment. Heat involved in phase changes of any substance is known as latent heat. Compared to other naturally occurring substances, water has very high latent heat values.

Solar radiation energy that enters the ocean is largely absorbed in the near-surface water layer. The wind driven ocean circulation distributes that heat through several hundred meters of ocean depth. As a result, the ocean is a vast reservoir of stored heat. Evaporation of ocean water followed by condensation within the atmosphere is the major heat transfer mechanism operating between the ocean and atmosphere. Heat required to evaporate water is released to the atmosphere when water vapor condenses forming clouds.

2.7 Gulf Stream Heat Budget

The momentum exchange through Ekman transport carries though to the base of the mixed layer or Ekman depth. It is at this boundary where shear is generated, and results in a deepening of the mixed layer. Without the Ekman forcing, convection is the main driving force behind vertical mixing within the water column. The stratification is a result of density changes caused by variation in temperature and salinity. The temperature changes result from the net heat exchange through the surface and advection of nearby currents. The surface heat budget can be expressed as:

$$Q_a = Q_e + Q_h + Q_{lw\uparrow} + Q_{lw\downarrow} + Q_{sw\uparrow} + Q_{sw\downarrow} \quad (2.1)$$

where Q_a is the net heat, Q_e is the net latent heat, Q_h is the net sensible heat, and the longwave and shortwave radiation are denoted by the subscripts lw and sw. This increase in temperature, approaching the surface, enhances the stratification because the warmer water is nearer the surface and is less dense. However, during latent heat driven convection, the surface is cooled. During this shift, the density increases as a result of the evaporative processes increasing salinity. Therefore, convective conditions tend to lead to enhanced mixing in the surface layer. This is shown, sometimes, by a layer of rain water on the surface

of the ocean water. Even if the rain is cooler, the warmer saltwater will remain at a higher density. However, the heat budget is still altered because the evaporative cooling and the change in SST through the layer of rain. This cooler layer greatly reduces the sensible heat flux. When the surface layer is becoming less dense either through solar heating or by rainfall, the resulting mixed layer depth will increase. When there is no shear stress from wind induced Ekman pumping, the circulation is driven by the thermal inequalities.

2.8 Westward Boundary Current Intensification

In the Northern Hemisphere between 0°N and 30°N , the Trade Winds blow out of the northeast, while the Westerlies, between 30°N and 60°N , are out of the southwest. The forcing from the wind, combined with the Coriolis force, causes the ocean's surface layer to move in a direction approximately 45 degrees to the right of the wind. As the water column depth increases, the direction of transport continues to shift to the right forming a downward spiral which decreases in magnitude with increasing depth. The net Ekman transport, discussed earlier, is 90 degrees to the right of the wind. Since the Ekman transport from the Trade Winds forces water towards the north, and transport from the Westerlies forces water towards the south, higher sea levels result in the middle of the ocean between these zones. As a result of the elevated sea-level in the center, a geostrophic flow forms when the pressure gradient force balances the Coriolis force. In the Northern Hemisphere, this geostrophic flow forms an anticyclonic gyre.

There are three types of currents which make up the gyre: eastern boundary, western boundary, and transverse. In the Northern Hemisphere, the eastern boundary current flows north to south, and the western boundary flows south to north. In the North Atlantic, the

western boundary current is known as the Gulf Stream. As typical of western boundary currents, the Gulf Stream is a very tight and fast flowing current as compared to the eastern boundary current (i.e., Canary Current).

The first attempt at explaining this motion was outlined by Sverdrup (1947) where it was shown that the curl of the wind stress is directly related to the Ekman layer circulation. Sverdrup assumed a uniform depth with geostrophic flow. The calculations resulted in values which agreed with observations with the exception of the western boundary. Stommel (1948) expanded this idea by adding a linear frictional relationship and finite depth, thus, showing that the gyre was asymmetric because the Coriolis force varies with latitude.

This asymmetry, or westward intensification, is a result of the conservation of absolute vorticity. Along both east and west boundaries, the wind stress causes a decrease in relative vorticity. This is balanced, to some degree, on the eastern boundary by the increase in planetary vorticity since the Coriolis force increases with latitude. However, along the western boundary, an increase in the Coriolis force causes planetary vorticity to decrease (not balancing the relative vorticity). To achieve balance, positive vorticity is generated through current shear against the land mass of the western boundary. A fast flowing current, which extends deeper in the water column, can obtain more positive vorticity resulting in net absolute vorticity conservation.

The simplified asymmetric gyre, and resulting western boundary current intensification, can be derived with a few simple assumptions (Stommel 1948). Beginning with the equations of motion for a barotropic fluid of depth d with a bottom stress proportional to current velocity:

$$\frac{Du}{Dt} = -g \frac{\partial \eta}{\partial x} - \gamma u + \frac{\tau_x}{\rho d} + fv \quad (2.2)$$

$$\frac{Dv}{Dt} = -g \frac{\partial \eta}{\partial y} - \gamma v + \frac{\tau_y}{\rho d} - fu \quad (2.3)$$

and defining the mid-latitude beta-plane Coriolis parameter, $f = f_0 + \beta y$:

$$\frac{Du}{Dt} = -g \frac{\partial \eta}{\partial x} - \gamma u + \frac{\tau_x}{\rho d} + (f_0 + \beta y)v \quad (2.4)$$

$$\frac{Dv}{Dt} = -g \frac{\partial \eta}{\partial y} - \gamma v + \frac{\tau_y}{\rho d} - (f_0 + \beta y)u \quad (2.5)$$

Defining the rate change of vorticity,

$$\frac{D\xi}{Dt} = \frac{\partial}{\partial x} \frac{Dv}{Dt} - \frac{\partial}{\partial y} \frac{Du}{Dt} \quad (2.6)$$

and substituting Equations 2.4 and 2.5 yields:

$$\begin{aligned} \frac{D\xi}{Dt} = & -g \frac{\partial^2 \eta}{\partial x \partial y} - \frac{\partial}{\partial x} \gamma v + \frac{\partial}{\partial x} \frac{\tau_y}{\rho d} - \frac{\partial}{\partial x} (f_0 + \beta y)u \\ & + g \frac{\partial^2 \eta}{\partial x \partial y} + \frac{\partial}{\partial y} \gamma u - \frac{\partial}{\partial y} \frac{\tau_x}{\rho d} - \frac{\partial}{\partial y} (f_0 + \beta y)v \end{aligned} \quad (2.7)$$

After canceling terms, and assuming the Coriolis parameter only varies with y , Equation 2.7 reduces to:

$$\frac{D\xi}{Dt} = -\frac{\partial}{\partial y} (f_0 + \beta y)v - \frac{\partial}{\partial x} \gamma v + \frac{\partial}{\partial y} \gamma u - \frac{\partial}{\partial y} \frac{\tau_x}{\rho d} + \frac{\partial}{\partial x} \frac{\tau_y}{\rho d} \quad (2.8)$$

The derivative of the first term reduces to $-\beta v$. By grouping and factoring the remaining terms, the following relation is obtained:

$$\frac{D\xi}{Dt} = -\beta v - \left(\frac{\partial v}{\partial x} - \frac{\partial u}{\partial y} \right) \gamma + \frac{1}{\rho d} \left(\frac{\partial \tau_y}{\partial x} - \frac{\partial \tau_x}{\partial y} \right) \quad (2.9)$$

The final form can be written in terms of vorticity, $\zeta = \frac{\partial v}{\partial x} - \frac{\partial u}{\partial y}$, and the curl of the wind

stress:

$$\frac{D\zeta}{Dt} = -\beta v - \zeta\gamma + \frac{1}{\rho d} \nabla \times \bar{\tau} \quad (2.10)$$

According to Equation 2.10, the relative vorticity is a function of latitude via the beta effect, friction, and wind stress. The first term on the right hand side reduces relative vorticity by increasing planetary vorticity as latitude increases. The second term reduces relative vorticity through friction. The third, and final, term on the right is the curl of the wind stress. This term increases vorticity if the curl is positive, or decreases vorticity if the curl is negative. Using Equation 2.10, and assuming a non-divergent flow, the vorticity

equation can be expressed in terms of a stream function where, $u = -\frac{\partial \psi}{\partial y}$, $v = \frac{\partial \psi}{\partial x}$, $\zeta = \nabla^2 \psi$:

$$\frac{D}{Dt} \nabla^2 \psi = -\beta \frac{\partial \psi}{\partial x} - \gamma \nabla^2 \psi + \frac{1}{\rho d} \nabla \times \bar{\tau} \quad (2.11)$$

Stommel (1948) made the assumption that the advection term was negligible when calculating the steady state solution to Equation 2.11:

$$\nabla^2 \psi + \frac{\beta}{\gamma} \frac{\partial \psi}{\partial x} = \frac{1}{\gamma \rho d} \nabla \times \bar{\tau} \quad (2.12)$$

Using the wind stress in the x-direction, $\tau_x = -\tau_0 \cos\left(\frac{\pi y}{y_n}\right)$, and assuming the wind stress in

the y-direction is zero, the curl can be expressed as:

$$\nabla \times \bar{\tau} = -\frac{\pi \tau_0}{y_n} \sin\left(\frac{\pi y}{y_n}\right) \quad (2.13)$$

Substituting this, as well as β , back into Equation 2.12 yields the final form of the stream function:

$$\nabla^2\psi + \frac{(f - f_0)}{\gamma y} \frac{\partial\psi}{\partial x} = -\frac{\tau_0\pi}{\gamma\rho dy_n} \sin\left(\frac{\pi y}{y_n}\right) \quad (2.14)$$

Stommel (1948) plotted the solution to this stream function for two cases. In the first case, assuming a constant Coriolis parameter (i.e., $\beta=0$), the second term on the left hand side goes to zero, thus eliminating the $\partial\psi/\partial x$ dependence. This resulted in a symmetrical gyre within the box model. However, in the second case, which varied the Coriolis parameter with latitude, the term remains in the equation, thereby inducing a westward biased asymmetry. Stommel (1948) concluded that changing the Coriolis parameter with latitude was the cause of westward boundary current intensification within gyres in the Northern Hemisphere.

Munk (1950) expanded Stommel's simplified equations, by adding lateral eddy viscosity in place of Stommel's bottom stress term, thereby eliminating the need for a uniform depth. This set of solutions, although much more complex, was more realistic since the current is known to approach zero before reaching the ocean floor. Munk's results were very similar to Stommel's in that both solutions showed westward intensification.

CHAPTER 3: MARINE BOUNDARY LAYER OVERVIEW

3.1 Introduction

The marine boundary layer (MBL) is an inherently mixed layer, and is primarily driven by large temperature gradients. Processes at the air-sea interface are directly affected by the surface layer of the ocean. These processes are functions of momentum, heat, and moisture fluxes. The development of marine and atmospheric flow patterns, such as pressure gradients in the atmosphere and eddies in the ocean, enhance these fluxes at the air-sea interface (e.g. Smith 1992; Friehe et al. 1991; Flament et al. 1994).

Within the marine boundary layer, the winds increase with height in the atmosphere. At the top of the boundary layer, wind speed and direction are determined by the dominant pressure patterns. The friction induced by the surface can influence the wind speeds in the boundary layer. Over the ocean, in neutral conditions, the increase in winds with height in the surface layer follows a logarithmic profile. The rate of change depends upon atmospheric stability. The more unstable conditions, the more uniformly in the vertical the winds are mixed, so there is less change from one level to the next. In stable conditions, there is less transport of momentum from one level to another, so the wind decreases more rapidly approaching the surface.

3.2 Processes Within the MBL

Within the surface layer, buoyancy flux is more notable; however, at the top of the boundary layer, clouds formation may be associated with wave interactions and mechanisms that couple processes within the inversion layer (Kraus and Businger 1994). The forcing

mechanisms can enhance the exchange from both directions. An ocean eddy may have a distinct boundary that produces a large SST gradient. Air flowing across this boundary is rapidly modified, changing the stability of the surface layer (Wayland and Raman 1992).

Large current formation in the ocean and resulting atmospheric response have been observed in the Gulf Stream as discussed in the previous chapter. Studies of eddy formation in the Gulf Stream have observed surface eddies and fronts embedded within the surface flow parallel to the southeast facing coastline (Cione et al. 1993, Raman and Riordan 1988). Accurate coastal wind prediction requires knowledge of the local responses to a given synoptic forcing scenario that is unique to the Gulf Stream region.

The unique SST features that are observed off the coast of the Carolinas present a complex structure to the atmosphere. These are regions of particularly intense air-sea interactions because of the large thermal contrast. The structure of the atmospheric boundary layer becomes increasingly complex in the vicinity of the Gulf Stream front. Changes in stability allow the development of internal boundary layers that affect the exchange processes of the surface with the overall boundary layer. The wind circulation patterns develop in response to these surface temperature fronts, and in response to the enhanced thermal gradients by the land-sea boundary. Research within the Gulf Stream region shows that frontogenesis is a common occurrence as a result of the Southeast facing coastline and the sea surface temperature gradient field (e.g., Bunker 1976; Kocin and Uccellini 1985a,b; Chou et al. 1986; Reed and Albright 1986; Dirks et al. 1988; Raman and Riordan 1988; Holt and Raman 1990; Kuo et al. 1990; Warner et al. 1990; Vukovich et al. 1991; Cione et al. 1993; Cione et al. 1998; Xie et al. 1999).

The wind-induced current formation is important because it drives upwelling and

downwelling. These flow patterns are partly responsible for the contrast of SSTs along the coastline. The effects of topography on the current, and local thermally-driven atmospheric circulation on the wind flow, are important in determining the wind induced marine circulation. Childs et al. (2003) used a numerical model and observations to determine the boundary layer structure in the vicinity of a developing coastal front. Even though a sea-breeze developed and propagated landward, baroclinic instability associated with the cloud formations resulted in a redevelopment of circulation that caused the cloud edge to remain offshore above the Gulf Stream Front.

3.3 Mixing Within the MBL

The process of shear instability transfers kinetic energy down from large scale circulations to smaller scale circulations. Due to the frictional drag, the shear is normally found in or near the boundary layer. The smaller motions are referred to as turbulent eddies. These eddies can range in size from mesoscale to microscale. Ultimately the kinetic energy is dissipated through viscous effects. These eddies form the boundary layer depth to a height defined by continuous turbulence (Stull 1988). When considering horizontally homogeneous conditions, the equations of motion can be written as:

$$fv - \frac{1}{\rho_a} \frac{\partial P}{\partial x} = f(v - v_g) = -\frac{\partial}{\partial z} \left(\frac{\tau_{ax}}{\rho_a} \right) \quad (3.1)$$

$$-fu - \frac{1}{\rho_a} \frac{\partial P}{\partial y} = f(u_g - u) = -\frac{\partial}{\partial z} \left(\frac{\tau_{ay}}{\rho_a} \right) \quad (3.2)$$

These equations show the balance of force between the pressure gradient, friction, and the Coriolis force. u and v are the mean wind components, u_g and v_g is the geostrophic wind

components, τ is the vertical momentum transport. The turbulent mixing causes the transport of momentum in the vertical plane. The influence of this flux is of great importance when dealing with the air-sea interface. The vertical momentum flux is also known as the shear stress. Using the shear stress relationship, a solution for the equations of motion can be obtained. More complex closure schemes can be used for solving the equations; however, the simplest solution can be derived by assuming $K=0$.

3.3.1 Fluxes in the MBL

The irreversible processes of turbulent momentum, heat and mass transfer follow the same general theory that *flux = force / resistance*. When irreversible processes occur, they change the entropy of a system. According to the second law of thermodynamics, the rate of entropy change is always positive. That is to say, that most systems generate more entropy over time. This production rate of entropy is proportional to the product of the flux and force. The transfer laws of the air sea interface are prime examples of the flux and force relationship. A general flux-force expression can be applied using a summation of the unique properties, X_i , that effect the transfer laws through the relationship:

$$f\left(\text{flux, force, } \sum_{i=1}^n X_i\right) = 0 \quad (3.3)$$

The flux-force relationship between heat flux, temperature gradient, and other irreversible processes is discussed in greater detail by De Groot and Mazur (1984).

3.3.2 Bulk aerodynamic closure scheme

Considering the amount of chaotic turbulence occurring in the ocean on many levels from many mechanisms, it is accepted that certain assumptions must be made to arrive at certain answers. The degree of complexity within a set of solutions depends on the accepted parameterizations and the order of the closure schemes. The bulk aerodynamic method is the simplest, most general, and therefore the most widely used method of estimating the momentum and heat fluxes. In its most basic form, Taylor (1916), states that the momentum flux or surface stress tau is proportional to the square of the wind speed:

$$\tau_a = \rho_a C_D U^2 \quad (3.4)$$

where C_D is the drag coefficient or simply the measure of the roughness of a surface, and is a function of wind speed over water. This method is most commonly used over the open ocean where changing boundary conditions are kept to a minimum. The bulk aerodynamic closure scheme is applied in the verification of the ASCII and is discussed later in the text.

3.3.3 Turbulent kinetic energy and flux

Assuming a constant stress layer over the ocean, Charnock's law states that the properties of turbulent flow are only dependent on the friction velocity and length scales u^* and z . The air-sea momentum transfer is controlled by the processes resulting from hydrodynamic instability and turbulence. The density of the air can be altered by changing temperature and evaporation rates. As a result, the sensible heat flux changes the stability of the air by changing the density within the layers. Downward flux increases the stability by increasing the density in the lower layers, and upward flux decreases the stability by reducing the density via temperature changes. For the purposes of this research, upward sensible heat

flux over the Gulf Stream was of most concern. Upward sensible heat flux intensifies vertical motion by decreasing the stability. This vertical motion can also transport heat and moisture as expressed through the Reynolds fluxes for temperature and humidity $\overline{w'\theta'}$ and $\overline{w'q'}$. Turbulence and buoyancy can be related to kinetic energy through the TKE equation:

$$\frac{\partial \overline{E}_T}{\partial t} = \overline{w'b'} - \overline{u'w'} \frac{dU}{dz} - \frac{\partial (\overline{w'p'}/\rho + \overline{w'E'_T})}{\partial z} - \varepsilon \quad (3.5)$$

where \overline{E}_T is the mean TKE, ρ is the density of air, and ε is the rate of dissipation. The kinetic energy is increased when there is an upward or positive buoyancy flux and decreased when the buoyancy flux is negative.

3.3.4 Sensible and latent heat flux

The application of sensible and latent heat fluxes will be discussed in greater detail in the following chapters. For the purpose of including them in this section, the bulk aerodynamic closure scheme is used to estimate the fluxes. In terms of potential temperature flux $(\overline{w'\theta'})_0$, and the absolute humidity flux $(\overline{w'q'})_0$, the values are define as:

$$Q_s = \rho C_p (\overline{w'\theta'})_0 \quad (3.6)$$

$$Q_l = L_v (\overline{w'q'})_0 \quad (3.7)$$

where ρ is density, C_p is specific heat of air, and L_v is the latent heat of vaporization.

3.4 Thermally-Induced Coastal Winds

Coastal wind flow can affect the weather along most coastal zones as the air above the land rises and air flows in from the ocean to replace it. The temperature contrast is enhanced when the land cools faster than the ocean. This land-to-sea breeze will be referred to as an "offshore" flow throughout the duration of this text. In the case of the Carolinas, that predominant direction ranges from westerly to northerly. There is generally a large thermal contrast between the ocean and the land that drives this circulation, which results in a thermally established pressure gradient (Raman and Riordan 1988). This coastal front is characteristic of the Carolina coast (Riordan 1990).

Along the Carolinas, coastal fronts are typically several hundred kilometers long, with temperature contrasts as large as 20°C, and may persist for several days. The mechanisms for the initiation of these features include differential friction, differential diabatic heating, and land-sea circulations (Raman and Riordan 1988). These fronts can also form in response to SST gradients produced by differential heating across the GSF (Holt and Raman 1992). These fronts are particularly important because they are often associated with cyclogenesis and heavy precipitation (Doyle and Warner 1993b). Huang and Raman (1992) used a numerical model to show that differential boundary layer modification may be the main mechanism for the formation of coastal fronts along the North Carolina coast. Dodge and Burpee (1993) studied the variation in convective bands over the Gulf Stream. Boybeyi and Raman (1992) found that the spatial and temporal variation of sea breeze convergence and the associated convective activity depend on the direction and magnitude of the prevailing wind.

3.5 The Interaction of Storms on the East Coast

Severe extratropical storms affect the majority of the East Coast during the winter months. The processes that are associated with East Coast cyclogenesis are partly a consequence of the formation of coastally-trapped Kelvin waves from the Gulf Stream (Pietrafesa et al. 1985), and low-level frontogenesis caused by large gradients in surface temperature (Riordan and Lin 1992; Holt and Raman 1992). These extratropical cyclones, or nor'easters, are low pressure systems that rarely deepen as much as tropical systems, but can cause significant damage along stretches of the East Coast due to their large coverage. Their formation will be discussed in greater detail in the next chapter.

CHAPTER 4: EXTRATROPICAL CYCLOGENESIS OVERVIEW

4.1 Introduction

Cyclogenesis, or the "spin-up" of cyclonic vorticity, in a mathematical sense, occurs when the rate change in time of vorticity about a vertical axis (ζ) increases (e.g. $\partial\zeta/\partial t > 0$). Below is a fundamental overview of the mathematics behind vorticity and quasigeostrophic (QG) theory (Holton 1992), and how it applies to extratropical cyclogenesis unique to the Gulf Stream region. Thus, the inherent "Northern Hemisphere" assumption is in effect for the use of positive vorticity advection (PVA).

4.2 Vorticity

Beginning with the total derivative expansion in isobaric coordinates,

$$\frac{D}{Dt} = \frac{\partial}{\partial t} + u \frac{\partial}{\partial x} + v \frac{\partial}{\partial y} + \omega \frac{\partial}{\partial p}, \quad 4.1$$

and the conservation of mass for a fluid evaluated at constant pressure, which can be expressed through the isobaric continuity equation,

$$\nabla \cdot \bar{V} + \frac{\partial \omega}{\partial p} = \frac{\partial u}{\partial x} + \frac{\partial v}{\partial y} + \frac{\partial \omega}{\partial p} = 0 \quad 4.2$$

The hydrostatic equation will also be used, and is expressed in terms of the geopotential (Φ) height:

$$\frac{\partial \Phi}{\partial p} = -\alpha = -\frac{RT}{p}. \quad 4.3$$

The isobaric momentum equations for zonal (4.4) and meridional (4.5) flow are expressed as

$$\frac{Du}{Dt} = \frac{\partial u}{\partial t} + u \frac{\partial u}{\partial x} + v \frac{\partial u}{\partial y} + \omega \frac{\partial u}{\partial p} = -g \frac{\partial z}{\partial x} + fv + F_x, \quad 4.4$$

$$\frac{Dv}{Dt} = \frac{\partial v}{\partial t} + u \frac{\partial v}{\partial x} + v \frac{\partial v}{\partial y} + \omega \frac{\partial v}{\partial p} = -g \frac{\partial z}{\partial y} - fu + F_y. \quad 4.5$$

The vorticity equation is formed by taking $\partial/\partial x$ of Equation 4.5, and subtracting $\partial/\partial y$ of Equation 4.4, to obtain

$$\begin{aligned} \frac{\partial(\zeta + f)}{\partial t} &= -\bar{V} \cdot \nabla(\zeta + f) - \omega \frac{\partial(\zeta + f)}{\partial p} \\ &\quad - (\zeta + f) \left(\frac{\partial u}{\partial x} + \frac{\partial v}{\partial y} \right) - \left(\frac{\partial \omega}{\partial x} \frac{\partial v}{\partial p} - \frac{\partial u}{\partial p} \frac{\partial \omega}{\partial y} \right) + \left(\frac{\partial F_y}{\partial x} - \frac{\partial F_x}{\partial y} \right) \end{aligned} \quad 4.6$$

Substitution of the continuity equation (4.2) for term four in Equation 4.6 yields another expression for the "full" vorticity equation:

$$\begin{aligned} \frac{\partial(\zeta + f)}{\partial t} &= -\bar{V} \cdot \nabla(\zeta + f) - \omega \frac{\partial(\zeta + f)}{\partial p} \\ &\quad + (\zeta + f) \left(\frac{\partial \omega}{\partial p} \right) - \left(\frac{\partial \omega}{\partial x} \frac{\partial v}{\partial p} - \frac{\partial u}{\partial p} \frac{\partial \omega}{\partial y} \right) + \left(\frac{\partial F_y}{\partial x} - \frac{\partial F_x}{\partial y} \right) \end{aligned} \quad 4.7$$

According to this equation, the rate of vorticity change with respect to time is a function of horizontal and vertical advection of the absolute vorticity, horizontal divergence (stretching), tilting, and friction. If the rate of change of absolute vorticity is greater than zero, cyclogenesis can be induced. Absolute vorticity greater than zero at the cyclone center can also be interpreted as a strengthening of circulation about the storm.

4.3 Quasigeostrophic Theory

The main assumption behind the quasigeostrophic approximation is that the geostrophic wind is much greater than the ageostrophic wind, $|\bar{V}_g| \gg |\bar{V}_{ag}|$. This is justified

through the assumption that the difference between the geostrophic and total wind, known as the ageostrophic wind, is small. Thus, the ratio $|\vec{V}_{\text{ag}}| / |\vec{V}_{\text{g}}|$ is on the same order of magnitude as the Rossby number (~ 0.1). This leads to the primary quasigeostrophic assumption that the advected and advecting velocities are geostrophic. The remaining approximations are that the flow is adiabatic and frictionless, and static stability is only a function of height; however, these assumptions can be relaxed in the QG equations. The hydrostatic approximation from Equation 4.3 is also assumed, as well as the beta-plane assumption, defined below.

Starting with the frictionless version of the horizontal momentum equation,

$$\frac{D\vec{V}}{Dt} = f \hat{k} \times \vec{V} = -\nabla \Phi, \quad 4.8$$

where the velocity vector, $\vec{V} = \vec{V}_{\text{g}} + \vec{V}_{\text{ag}}$, is broken into the geostrophic and ageostrophic components. If the ageostrophic component is assumed to be negligible, the quasigeostrophic form of Equation 4.8 can be expressed as

$$\frac{D\vec{V}_g}{Dt_g} = (f_0 + \beta y) \hat{k} \times \vec{V}_g = -\nabla \Phi, \quad 4.9$$

where the midlatitude beta-plane approximation of $f = f_0 + \beta y$ is used for the Coriolis parameter. Thus, the geostrophic wind relationship is defined as:

$$\vec{V}_g = \frac{1}{f_0} \hat{k} \times \nabla \Phi. \quad 4.10$$

4.3.1 QG Momentum Equation

Equation 4.8 can be rewritten in terms of \bar{V}_g and \bar{V}_{ag} , where Equation 4.10 is substituted to obtain:

$$\frac{D\bar{V}_g}{Dt_g} = -f_0 \hat{k} \times \bar{V}_{ag} - \beta y \hat{k} \times \bar{V}_g, \quad 4.11$$

and when broken into zonal (x) and meridional (y) components, the horizontal momentum equation can be expressed as:

$$\frac{Du_g}{Dt_g} = f_0 v_{ag} + \beta y v_g, \quad 4.12a$$

$$\frac{Dv_g}{Dt_g} = -f_0 u_{ag} - \beta y u_g. \quad 4.12b$$

4.3.2 QG Vorticity Equation

Expanding Equations 4.12a and 4.12b according to Equation 4.1 yields another expression for the horizontal momentum equations in component form:

$$\frac{\partial u_g}{\partial t} + u_g \frac{\partial u_g}{\partial x} + v_g \frac{\partial u_g}{\partial y} - f_0 v_{ag} - \beta y v_g = 0, \quad 4.13a$$

$$\frac{\partial v_g}{\partial t} + u_g \frac{\partial v_g}{\partial x} + v_g \frac{\partial v_g}{\partial y} + f_0 u_{ag} + \beta y u_g = 0. \quad 4.13b$$

As in the full vorticity equation derivation above (Equation 4.6), take $\partial/\partial x$ of (4.13b) and subtract $\partial/\partial y$ of (4.13a), cancel terms, and substitute Equation 4.9 to obtain the quasigeostrophic vorticity equation:

$$\frac{\partial \zeta_g}{\partial t} = -\bar{V}_g \cdot \nabla(\zeta_g + f) + f_0 \frac{\partial \omega}{\partial p}, \quad 4.14$$

where the geostrophic vorticity is related to the horizontal Laplacian of the geopotential through:

$$\zeta_g = \frac{\partial v_g}{\partial x} - \frac{\partial u_g}{\partial y} = \frac{1}{f_0} \nabla^2 \Phi. \quad 4.15$$

The rate of change in the geostrophic vorticity is a function of the advection of geostrophic relative vorticity and planetary vorticity by the geostrophic wind, and horizontal divergence. In the region upstream of an existing trough, the relative vorticity is reduced by the relative vorticity advection. The opposite is true of the planetary vorticity advection. These terms act against each other to progress (or retrogress) the trough to ridge pattern.

4.3.3 QG Thermodynamic Equation

The first law of thermodynamics is expressed as

$$c_p \frac{DT}{Dt} - \alpha \frac{Dp}{Dt} = J, \quad 4.16$$

where c_p is the specific heat, T is temperature, J is the diabatic heating rate, and the specific volume, α , is the inverse of density from the equation of state, $p = \rho RT = \alpha^{-1}RT$. Using Equations 4.1 and 4.2, the first law of thermodynamics can be expressed as

$$\frac{DT}{Dt_g} - \left(\frac{\sigma p}{R} \right) \omega = \frac{J}{c_p}, \quad 4.17$$

where

$$\sigma = -\frac{RT}{p} \frac{d \ln \theta}{dp}.$$

By ignoring the diabatic heating term in Equation 4.17, and using the hydrostatic relationship (Equation 4.3), the thermodynamic energy equation can be written in terms of χ :

$$\frac{\partial \chi}{\partial p} = -\vec{V}_g \cdot \nabla \left(\frac{\partial \Phi}{\partial p} \right) - \sigma \omega \quad 4.18$$

where, $\chi = \partial \Phi / \partial t$. According to Equation 4.18, the vertical derivative of the geopotential tendency equals the sum of the thickness advection and adiabatic thickness change from vertical motion.

Substituting the horizontal Laplacian of the geopotential from Equation 4.15 into Equation 4.14, the quasigeostrophic vorticity equation can also be rewritten in terms of χ :

$$\nabla^2 \chi = -f_0 \vec{V}_g \cdot \nabla \left(\frac{1}{f_0} \nabla^2 \Phi + f \right) + f_0^2 \frac{\partial \omega}{\partial p}. \quad 4.19$$

According to Equation 4.19, the horizontal Laplacian of the geopotential tendency is equal to the sum of the vorticity advection and vorticity generation through stretching. The two equations above (4.18) and (4.19) form the quasigeostrophic system, and can be solved for either the height tendency, χ , or the vertical velocity, ω .

4.3.4 QG Omega Equation

The quasigeostrophic omega equation is considered by most to be the basis for synoptic meteorology. Since the equation does not include any time derivatives, it is a useful diagnostic tool for calculating vertical motion as a function of geopotential. To solve the quasigeostrophic system of equations for the vertical velocity, ω , take the horizontal Laplacian of Equation 4.18:

$$\nabla^2 \frac{\partial \chi}{\partial p} = -\nabla^2 \left[\vec{V}_g \cdot \nabla \left(\frac{\partial \Phi}{\partial p} \right) \right] - \sigma \nabla^2 \omega, \quad 4.20$$

and take $\partial/\partial p$ of Equation 4.19:

$$\frac{\partial}{\partial p}(\nabla^2 \chi) = -f_0 \frac{\partial}{\partial p} \left[\vec{V}_g \cdot \nabla \left(\frac{1}{f_0} \nabla^2 \Phi + f \right) \right] + f_0^2 \frac{\partial^2 \omega}{\partial p^2}. \quad 4.21$$

Eliminate χ , by subtracting Equation 4.20 from 4.21. To obtain the quasigeostrophic omega equation, group like terms, and factor out ω to yield:

$$\left(\sigma \nabla^2 + f_0^2 \frac{\partial^2}{\partial p^2} \right) \omega = f_0 \frac{\partial}{\partial p} \left[\vec{V}_g \cdot \nabla \left(\frac{1}{f_0} \nabla^2 \Phi + f \right) \right] + \nabla^2 \left[\vec{V}_g \cdot \nabla \left(-\frac{\partial \Phi}{\partial p} \right) \right]. \quad 4.22$$

The term on the left hand side of Equation 4.22 is the Laplacian of the vertical motion (ω) which describes the rising and sinking motion with appropriate scaling for the vertical anisotropy. The first term on the right hand side is the differential absolute geostrophic vorticity advection by the geostrophic wind. The differential vorticity advection term is responsible for positive and negative vorticity advection. Positive vorticity advection (PVA) that increases with height provides forcing for rising motion. Likewise, negative vorticity advection (NVA) increasing with height forces sinking motion. The last term on the right hand side is the Laplacian of the temperature advection by the geostrophic wind. The local maxima of warm air advection (WAA) also forces rising motion, just as cold air advection (CAA) forces sinking motion.

4.3.5 QG Height Tendency Equation

The quasigeostrophic system of equations can also be solved for height tendency, χ , by multiplying Equation 4.18 by $f_0^2 \partial / \partial p$ and rearranging terms to obtain

$$\sigma f_0^2 \frac{\partial \omega}{\partial p} = -f_0^2 \frac{\partial}{\partial p} \left(\vec{V}_g \cdot \nabla \left(\frac{\partial \Phi}{\partial p} \right) \right) - f_0^2 \frac{\partial}{\partial p} \left(\frac{\partial \chi}{\partial p} \right), \quad 4.23$$

and multiplying a rearranged version of Equation 4.19 by σ ,

$$\sigma f_0^2 \frac{\partial \omega}{\partial p} = \sigma \nabla^2 \chi + \sigma f_0 \vec{V}_g \cdot \nabla \left(\frac{1}{f_0} \nabla^2 \Phi + f \right). \quad 4.24$$

Since the left hand sides are equal, the right hand sides of Equations 4.23 and 4.24 can be set equal to one another:

$$\sigma \nabla^2 \chi + \sigma f_0 \vec{V}_g \cdot \nabla \left(\frac{1}{f_0} \nabla^2 \Phi + f \right) = -f_0^2 \frac{\partial}{\partial p} \left[\vec{V}_g \cdot \nabla \left(\frac{\partial \Phi}{\partial p} \right) \right] - f_0^2 \frac{\partial}{\partial p} \left(\frac{\partial \chi}{\partial p} \right). \quad 4.25$$

The quasigeostrophic height tendency equation is obtained by grouping like terms, and solving for χ :

$$\left[\nabla^2 + \frac{\partial}{\partial p} \left(\frac{f_0^2}{\sigma} \frac{\partial}{\partial p} \right) \right] \chi = -f_0 \vec{V}_g \cdot \nabla \left(\frac{1}{f_0} \nabla^2 \Phi + f \right) - \frac{\partial}{\partial p} \left[-\frac{f_0^2}{\sigma} \vec{V}_g \cdot \nabla \left(\frac{\partial \Phi}{\partial p} \right) \right] \quad 4.26$$

The term on the left hand side is the Laplacian of the height tendency, where $\chi = \partial \Phi / \partial t$, and represents the rate at which geopotential height decreases with time. The first term on the right hand side is the vorticity advection, and the last term is the differential temperature advection. According to Equation 4.26, positive vorticity advection, and cold air advection decreasing with height, or warm-air advection increasing with height, correspond to geopotential height falls. This is because advecting cold air below an upper-level trough decreases the thickness, thus deepening the upper-level trough. The opposite is true for advecting warm air, thereby building the downstream upper-level ridge.

4.4 Summary and Application to Extratropical Cyclogenesis

In the case of rapid cyclogenesis off the Carolina coast, there are two key ingredients that must come together. A region of low-level baroclinicity is generally in place offshore while an upper-level trough approaches from the west. Troughs embedded in the westerlies

are not that uncommon, and due to the warm Gulf Stream SST, neither is inherent baroclinicity. However, the later feature is enhanced by CAOs, discussed earlier, and will be referred to throughout the text as the "pre-conditioning period". Pre-existing cyclonic vorticity is typically present along the coastal baroclinic zone east of NC and VA during this pre-conditioning period. The horizontal convergence along the coastal front, which often forms over the GSF, contributes to the cyclonic vorticity generation, thus establishing a favored region for cyclonic development. Once established, the surface cyclone will tend to track along this zone of pre-existing vorticity. In addition to the pre-existing vorticity enhancing surface cyclogenesis, the very low static stability over the warm coastal waters, and inherent thermal advection pattern within this baroclinic zone, also contribute to rapid deepening as the cyclone tracks along the coastal front.

According to Equation 4.22, positive vorticity advection ahead of the upper-level trough that is increasing with height is associated with rising motion. This rising motion, according to the stretching term in the vorticity equation (4.7 or 4.14), would increase the cyclonic vorticity at the surface ahead of the trough. It should be noted that the contribution from pre-existing vorticity, seen in conjunction with the coastal front, is only accounted for in the "full" vorticity equation (4.7).

The deepening surface low is also associated with surface-level warm air advection ahead of its track, and cold air advection in its wake. According to the omega equation (4.22), this warm air advection ahead of the surface low is also associated with rising motion. Likewise, the cold air advection behind the surface low results in sinking motion. The height tendency equation (4.26) states that cold air advection decreasing with height is associated with geopotential height falls, and warm air advection decreasing with height is associated

with geopotential height rises. Thus, the upper-level trough deepens and the upper-level ridge builds causing the wave pattern to amplify (Sutcliffe and Forsdyke 1950).

The differential diabatic heating term, which was neglected earlier, can be added to the right hand side of the quasigeostrophic height tendency equation (4.26):

$$\begin{aligned} \left[\nabla^2 + \frac{\partial}{\partial p} \left(\frac{f_0^2}{\sigma} \frac{\partial}{\partial p} \right) \right] \chi = & -f_0 \vec{V}_g \cdot \nabla \left(\frac{1}{f_0} \nabla^2 \Phi + f \right) \\ & - \frac{\partial}{\partial p} \left[-\frac{f_0^2}{\sigma} \vec{V}_g \cdot \nabla \left(-\frac{\partial \Phi}{\partial p} \right) \right] - \frac{f_0^2}{\sigma} \frac{\partial}{\partial p} \left(\frac{R}{c_p p} \frac{dQ}{dt} \right) \end{aligned} \quad 4.27$$

This term also contributes to the layer's increase in thickness through latent heating which helps build the downstream ridge. Thus, through thermal advection and latent heat release, the trough-ridge amplitudes are increased, and the wavelength is shortened. This results in greater differential positive vorticity advection aloft, thereby enhancing the rising motion and height falls at the surface. The deepening surface low pressure, in turn, has increasing winds which enhance the warm (cold) air advection ahead of (behind) the surface low pressure. This amplification through mutual feedback between the upper-level trough and the surface low is the basis of the Sutcliffe-Petterssen "self-development" concept (Sutcliffe and Forsdyke 1950).

The region ahead of the surface cyclone is warmed and moistened by turbulent fluxes. These heat and moisture fluxes enhance the thermal gradient, and as a result, strengthen the warm air advection. The increase in warm air advection strengthens the surface-low (as discussed above), which results in increased surface winds. Since the strength of the surface fluxes is proportional to the wind speed, because the exchange coefficients are a function of wind speed over water, the stronger winds increase the fluxes, thereby further enhancing the thermal gradient. This is a "non-linear" cycle, and while the individual components

contribute to deepening a surface-low pressure, their mutual feedback is greater than their individual contributions.

The pressure falls ahead of the surface cyclone due to ascent caused by warm advection, as well as the pre-existing vorticity along the coastal front, cause the surface low pressure to follow a northeasterly track parallel to the GSF. According to Sutcliffe (1947), this gives the appearance that the surface low is being steered by the 500-mb winds, but the motion is more a function surface-level height falls ahead of, and surface-level height rises behind, the cyclone. As the mutual amplification continues, the thermal advection, through altering the dynamics, is acting to steer the surface cyclone on a more northerly track. This thermal advection, as well as latent heating, will also cause the upper-level trough to develop a more negative tilt. This negative, or westward with increasing latitude, tilt of the system is oriented such that the upper-level and surface disturbances act to intensify each other. This mutual amplification pattern also affects the horizontal translation of both disturbances, and is referred to as phase locking because the horizontal displacement of the systems with respect to each other remains constant. However, during rapid deepening, the surface cyclone remains downstream, or east, of the upper-level disturbance, thus forming a negatively tilted trough axis in the vertical (+z) direction. Eventually, the upper-level trough will overtake the surface cyclone, thereby reducing the vertical tilt of the trough axis. At this point, the storm becomes occluded, the positive feedback weakens (or stops), and the cyclone weakens.

CHAPTER 5: THE ATLANTIC SURFACE CYCLONE INTENSIFICATION INDEX

5.1 Introduction

The Atlantic Surface Cyclone Intensification Index (ASCII) is a forecast index that quantifies the amount of low-level baroclinicity off the coast of the Carolinas during a cold-air outbreak (CAO). ASCII is based on the gradient between the coldest 24 hour average air temperature during a CAO and the temperature of the GSF. The resulting pre-storm baroclinic index (PSBI) is used to forecast the probability that a cyclone in the domain will exhibit rapid cyclogenesis. The initial ASCII data covered years 1980-1990. This dataset was recently expanded to cover the years 1991-2002 which doubled the number of storms. This additional data provides similar position and slope of the linear regression fits verifying the previous threshold values defined in the PSBI, and explaining as much as 30% of the variance in deepening rate.

Despite operational value, the neglect of upper-tropospheric forcing as a predictor in the original ASCII formulation precludes explanation of a large fraction of the deepening rate variance. Here, a modified index is derived in which an approximate measure of upper-level forcing is included. The 1991-2002 cyclone events were separated into bins of “strongly forced”, “moderately forced”, and “weakly forced” based on the strength of the nearest upstream maximum of 500-mb absolute vorticity associated with the surface low. This separation method reduced the scatter and further isolated the contributions of surface forcing versus upper-level forcing on extratropical cyclogenesis. Results of the combined upper-level index and surface PSBI demonstrate that as much as 74% of the deepening rate variance can be explained for cases with stronger upper-level forcing.

A climatological study investigating the relationship between thermal gradient of the Gulf Stream off the mid-Atlantic coast and subsequent cyclogenesis was conducted by Cione et al. in 1993. Findings from this study suggest that as much as 30% of the variance in deepening rate can be explained by quantifying this surface thermal structure. However, a major limitation of this study is neglect of upper forcing, which has been shown by Sanders (1986) to explain as much as 75% of the variance in deepening rate. This research extends the Cione et al. (1993) climatology using the same methods, but including upper-level forcing as an additional parameter to test the hypothesis that part of the unexplained variance is a function of 500hPa vorticity.

5.2 Background

The coastal region of the Carolinas has proven to be a major epicenter for the spawning of extratropical cyclones. The protrusion of the Outer Banks into the Gulf Stream's warm water can magnify the thermal gradient. The contrasting temperatures near the surface along this coastal region can cause shearing that distorts the polar front. In addition to this, the southeasterly facing coastline yields a perfect angle for the perpendicular offshore air flow typical of the winds from a cold-air outbreak (Wayland and Raman 1989). These winds further enhance the already large thermal contrast resulting in extreme marine boundary layer baroclinicity. Fantini (1991) has shown that this pre-storm destabilization may act to significantly increase the likelihood for subsequent rapid cyclogenesis. This rapid growth, due to the extensive kinetic energy derived from the baroclinic conversion of warm air over the Gulf Stream, can result in a large winter cyclone (Raman and Riordan 1988; Wayland and Raman 1989; Holt and Raman 1990; Huang and Raman 1990; Kuo et al. 1990;

Vukovich et al. 1991; Cione et al. 1993; Cione et al. 1998; Xie et al. 1999).

5.2.1 ASCII Thermodynamics

When considering the Outer Banks, the cold air to the northwest and the warm air to the southeast form a strong, vertically oriented thermal wind pattern off the coast. This can be expressed by the thermal wind (V_T) equation:

$$V_T = \frac{-R_d}{f} \int_{P_0}^{P_1} (\hat{k} \times \nabla T) d(\ln p) \quad (5.1)$$

where ∇T is the horizontal temperature gradient, p is the atmospheric pressure, f is the Coriolis parameter, and R_d is the dry air gas constant (Cione et al. 1993). Since the geostrophic wind varies with height in the presence of a thermal gradient, the components of the thermal wind can be calculated using air temperature (T). Letting T equal the mean temperature in a layer of thickness h between pressures $p(sfc)$ and $p(h)$, the x and y components of the thermal wind can be written as:

$$U_T = -\frac{hg}{fT} \frac{\partial T}{\partial y}; V_T = \frac{hg}{fT} \frac{\partial T}{\partial x} \quad (5.2)$$

As the colder air flowing off the land moves over the warm water, it forms the MBL. The convection in this region is increased by the moistening and warming of the cooler surface air. This atmospheric preconditioning period occurs during the CAO, and is accompanied by large sensible and latent heat fluxes over the Gulf Stream (Raman and Riordan 1988; Wayland and Raman 1989). The bulk aerodynamic relations of sensible and latent heat fluxes from Equations 3.6 and 3.7, can be approximated by:

$$Q_s = -C_1 C_h V \frac{(T_a - T_w)}{T_a}; Q_l = -C_2 C_e V \frac{(q_a - q_w)}{T_a} \quad (5.3)$$

where V is the surface wind speed, C_h and C_e are exchange coefficients for heat and moisture, T_a is the surface air temperature, T_w is the sea surface temperature, q_a is the surface specific humidity of air, q_s is the saturation specific humidity at the sea surface, and:

$$C_1 = \frac{c_p p}{R}; \quad C_2 = \frac{L_v p}{R} \quad (5.4)$$

where c_p is the specific heat at constant pressure, and L_v is the latent heat of vaporization. Vukovich et al. (1991) show that the maximum heat flux over the north Atlantic was found over the Gulf Stream and north of 35°N northeast of Cape Hatteras during cases of strong CAOs. These values were in agreement with the previous findings of Bunker (1976), Bunker and Worthington (1976), Hasse et al. (1978), Gorshkov (1978), and Liu et al. (1979). Although it is assumed that baroclinic processes are the single most important factor in the development of cyclones (e.g. Rogers and Bosart 1986; Sanders 1986a), more evidence shows that surface heat fluxes and their horizontal gradient, as discussed above, work to enhance baroclinicity for the explosive growth of a marine cyclone (Kuo and Reed 1988; Holt and Raman 1990; Huang and Raman 1990; Kuo and Low-Nam 1990; Cione et al. 1993; Cione et al. 1998; Xie et al. 1999).

5.2.2 Pre-conditioning Period

Explosive development can also be influenced by stronger wind velocities. A cold air outbreak occurs when strong northerly quadrant winds force cold air further south. About 15 to 20 of these events occur annually from November through April, and last for 1 to 3 days (Grossman, 1988). Vukovich et al. (1991) observed that the minimum air temperature coincides with the maximum wind speed during this type of event, and that the largest values

and strongest gradients of total heat flux exist offshore to the north and east of Cape Hatteras. This is because the region allows for very little time and distance for the colder continental air mass to modify before encountering the much warmer waters offshore.

For this preconditioning to occur off the coast of the Carolinas, the winds are favored from the north to north-westerly direction. These winds are usually a result of the presence of a strong anticyclone over the continent. This high, known as the “parent” high, usually moves southeast out of Canada into the northeastern United States sending a dome of cold air with its strong northerly to northeasterly winds. This phenomenon is known as cold-air damming (Forbes et al., 1987). As the northeasterly winds around this high encounter the Appalachian mountains, the cold air mass becomes blocked. A low pressure system is often present or can sometimes form off the coast due to this increased thermal gradient. Extensive research has gone into studying these events and how they relate to the MBL (Nowlin and Parker, 1974; Lenschow and Agee, 1976; Lenschow et al., 1980; Chou and Atlas, 1982; Huh et al., 1984; Chou et al., 1986; Raman et al., 1986; Wayland and Raman, 1989; Vukovich et al., 1991; Cione et al., 1993; Reddy and Raman, 1994; Xie et al., 1996; Li et al., 1997; and Cione et al., 1998).

5.2.3 ASCII and PSBI

The Atlantic Surface Cyclone Intensification Index (ASCII) is a forecast index that quantifies the amount of low-level baroclinicity off the coast of the Carolinas during a CAO. ASCII is based on the gradient between the coldest 24-h average air temperature at the coast (T_c) during a CAO and the temperature at the GSF (T_{GSF}). The resulting pre-storm baroclinic

index (PSBI):

$$PSBI = \frac{T_{GSF} - T_l}{d}, \quad (5.5)$$

where d is the distance of the GSF from the coast, is used to forecast the probability that a cyclone in the domain will exhibit rapid cyclogenesis. PSBI values less than $1.0^{\circ}\text{C}/10\text{km}$ indicate that a storm in the domain would be unlikely to undergo explosive development while values greater than $1.7^{\circ}\text{C}/10\text{km}$ indicate that there is a strong chance for rapid cyclogenesis.

The initial ASCII climatological study conducted by Cione et al. (1993) investigated winter coastal cyclonic events from 1982 to 1990 during the months November through April. The objective of this research was to investigate the potential effects Gulf Stream induced low-level baroclinicity on cyclonic intensification within the US mid-Atlantic coastal zone. To determine the effects of marine boundary layer baroclinicity directly associated with the presence of the Gulf Stream off the Carolinas and Virginia, Cione et al. (1993) chose the region between 38° N and 32° N and 79° W and 72° W as the study domain (Figure 5.1).

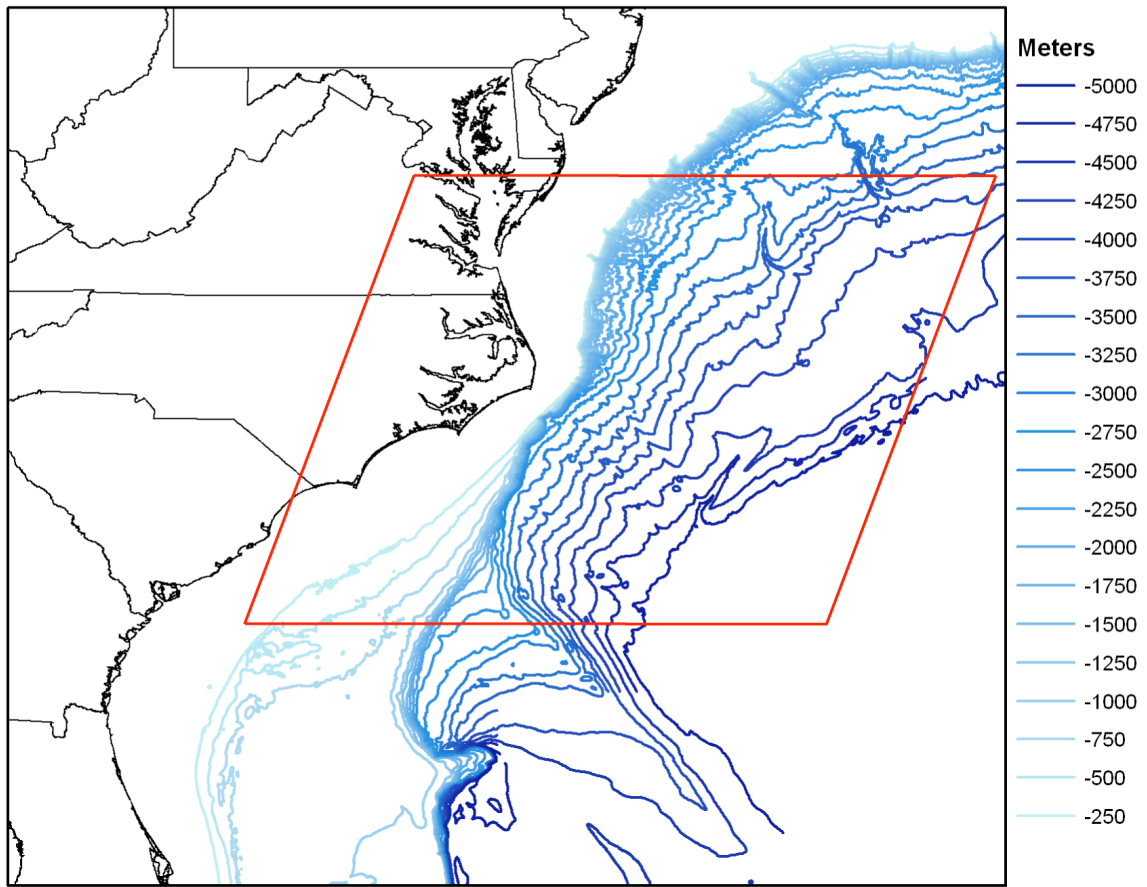


Figure 5.1. Map of the eastern United States and bathymetry. The domain used to study East Coast cyclogenesis or cyclone redevelopment using climatological data is shaded in gray.

Cione et al. (1993) catalogued all cyclonically oriented, surface low pressure systems with a closed isobar contained within the study domain for more than 6 h. The 1982 to 1990 storm track information was retrieved from the National Center for Environmental Prediction's (NCEP) North American surface weather maps. A 13 year (1978-1990), digitized twice weekly composite was used to ascertain Gulf Stream SST values.

A measure of the low-level pre-storm baroclinicity was obtained using the surface air temperatures at Wilmington and Cape Hatteras, NC and the corresponding GSF SST east of these locations. Cione et al. (1993) obtained hourly air temperatures at the above locations. The air temperatures were then averaged for the pre-storm period. After the air temperatures were averaged, they were combined with the SST of the GSF to calculate an average air-sea temperature contrast. A low-level pre-storm thermal gradient was also calculated using the distance of the GSF from the coastal locations. It should be noted that Cione et al. (1993) assumed the surface air temperature over the Gulf Stream to be the same as the SST, and the SST was assumed to be constant over the 12 h observed deepening period for each storm.

Results from the 1982-1990 winter storm climatology show that the pre-storm baroclinicity off the coastal mid-Atlantic region was strongly linked to the subsequent development of regional coastal cyclones (Cione et al. 1993). The data from this study, as well as the additional 11 year climatology, presented later, is shown in Figure 5.2. The linear regression of the total pressure change of the surface cyclone dependent on the low-level pre-storm thermal gradient, or pre-storm baroclinic index (PSBI), also seen in Figure 5.2, is for the entire 20 year span. Cione et al. (1993) concluded that this 116 storm study illustrates a statistically significant geometric mean of the regression coefficient (r) of 0.562 between the

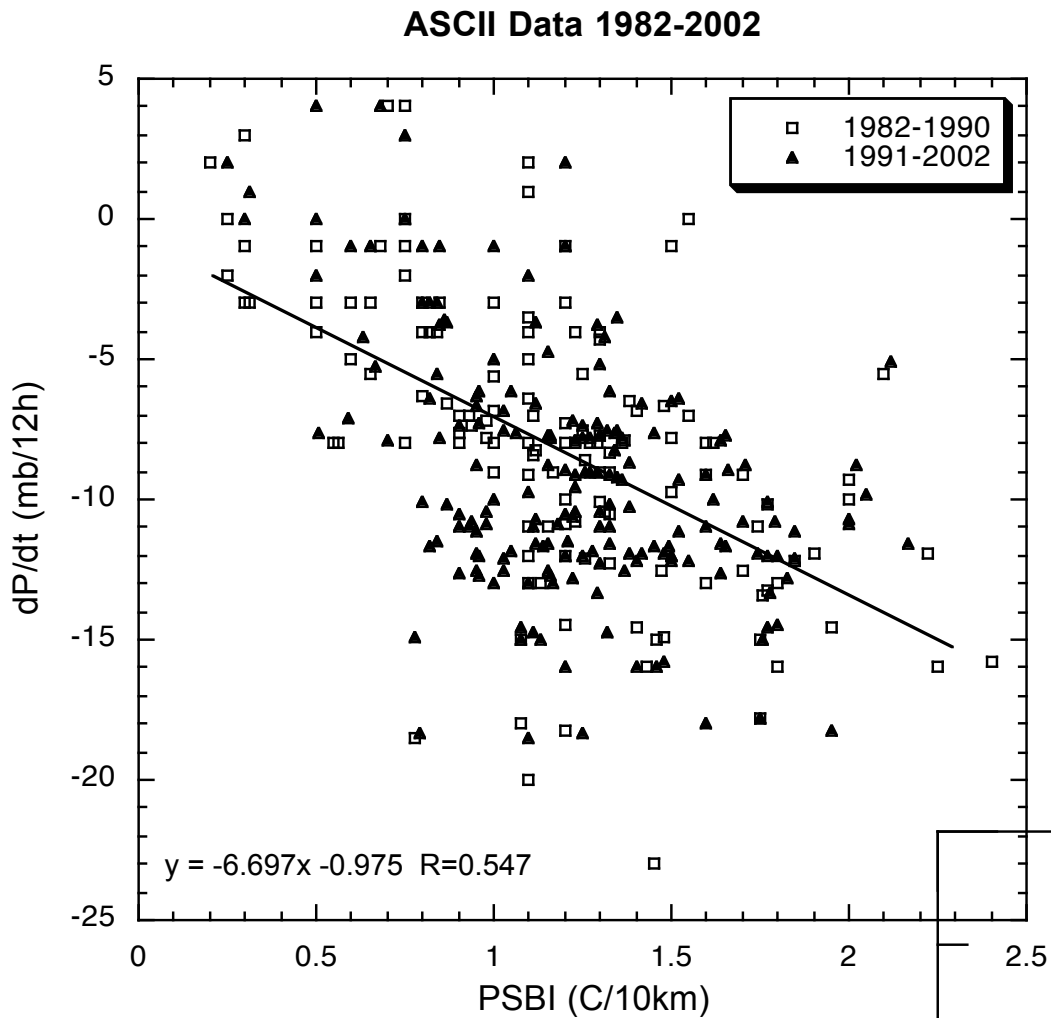


Figure 5.2. The updated ASCII dataset (1980-2002) of ETC's $\Delta P/12h$ vs. PSBI. The linear regression fit combines both set of storms (1980-1990 and 1991-2002).

pre-storm baroclinicity and storm development that explains 31.6% of the total variance. This assumes that a pre-existing cyclonic disturbance enters the destabilized region at upper levels, and also that other contributing factors such as upper level forcing conditions remain favorable for cyclonic development.

According to Cione et al. (1998), the successful utilization of ASCII at the NWS Wilmington, NC (ILM) forecast office has offered additional guidance during winter events. Findings from the February 1994 through February 1996 test period suggest that the ASCII forecast guidance may be most significant in cases where weak to moderate cyclonic intensification is anticipated (Cione et al. 1998). For storms that intensified at a rate equal to or less than -11mb/12h, the RMS forecast error and forecast bias were considerably lower for ASCII forecasts of surface cyclonic intensification when compared to similar NGM forecasts (Cione et al. 1998). When numeric values of the PSBI are less than $1.0^{\circ}\text{C}/10\text{km}$, the likelihood that a storm would undergo explosive (-12mb/12h) development decreases, while values greater than $1.7^{\circ}\text{C}/10\text{km}$ dramatically increase the probability of explosive development.

5.2.4 Upper-tropospheric Forcing

It has long been known that upper-level divergence is required for surface cyclogenesis (e.g., Sutcliffe 1939, Bjerknes and Holmboe 1944), and that this divergence is associated with regions of cyclonic vorticity advection aloft. Although differential vorticity advection is the factor linked to cyclogenesis, if the low-level vorticity advection is assumed to be weak in the majority of cases, then the forcing is primarily a function of the strength of

the upper-level vorticity advection.¹ Sutcliffe (1947) shows that there is a strong correlation between the absolute vorticity advection at the 500 mb level and surface cyclogenesis. Climatological studies of rapid extratropical cyclogenesis verify that the magnitude of cyclonic vorticity advection downstream of a trough at the 500 mb level is highly correlated to the deepening rate of the surface cyclone (e.g., Sanders and Gyakum 1980; Sanders 1986; Sanders 1987; Kocin and Uccellini 1990; Uccellini 1990). Climatology of explosive cyclogenesis from 1981 to 1984 studied by Sanders' (1986) included 48 storms stratified into three bins based on the surface cyclone's deepening rate. Results from the study by Sanders (1986) show that the mean 500-mb absolute vorticity advection associated with the surface cyclone averaged over 12 h versus the surface cyclone's 12-h deepening rate can explain as much as 75% of the deepening rate variance in sea-level deepening rate for "strong bombs"², or cyclones with pressure falls greater than 1.9 mb/h. Sanders (1986) also concluded that the largest mean deepening rate of 24 mb in 12 h occurred while cyclones crossed a region of strong SST gradient associated with the GSF.

5.3 Data

For the continuation of the original study, the same region between the latitudes 38° and 32°N and longitudes 77° and 71°W was chosen as the storm domain (Figure 5.1). This

¹ This assumption is considered to be valid for most, but not all cases, and is a foreseen limitation of cyclogenetic events with strong low-level vorticity advection.

² The 12 "strong bomb" cases, as defined by Sanders (1986), had a mean deepening rate of 24 mb in 12 h.

region was selected by Cione et al. so that storms entering this area would be in a highly variable baroclinic zone caused by the lateral meanders of the Gulf Stream (1993). As in the first ASCII dataset, cyclonically oriented, closed circulations at the surface were considered storm events. The area coverage for this study is 650x550 km, or roughly 350,000 km². All east coast winter storms during the months of October to April between 1991 and 2002 that remained within this region for a period exceeding 6 h were analyzed. Past storm data were obtained from NCEP's 2.5 x 2.5 degree 6-h analysis maps viewed using GEMPAK. The SST data and maps were obtained from NOAA's Coastwatch program. The digital images of 1.1 km resolution were acquired by the Advanced Very High Resolution Radiometer (AVHRR) carried onboard the NOAA-12 and NOAA-14 polar orbiting satellites. Since these are single pass images, if the SST was less than 50% visible because of cloud cover, the first acceptable preceding pass was chosen.³ The imagery was then processed through an interpolation routine to filter out the remaining cloud cover. The air temperature data at the coastal stations were obtained at 3h intervals through the State Climate Office of North Carolina.

The same method for determining a low-level baroclinic indicator was used in this study as in the original ASCII study. This indicator was devised by Cione et al. (1993) to calculate the average horizontal low-level thermal contrasts present between the GSF and the North Carolina coastline during pre-storm conditions. The measure of pre-storm baroclinicity

³ In most cases an acceptable image was obtained within the preceding 48 h. A limit of 7 days was imposed, but never needed, as the longest duration required for a particular case was 4 days.

is obtained using the near-surface air temperatures at the coastal locations of Cape Hatteras and Wilmington, NC and the corresponding SST of the Gulf Stream front. Near-surface air temperatures were obtained at 3 h intervals (over 24 h) at both locations. The air temperatures were averaged during the coldest 24 h of the pre-storm period. This isolates the time with maximum low-level baroclinicity. After combining the averaged surface temperatures with the SST of the Gulf Stream front, the average horizontal air-sea temperature contrast was calculated. As in the original study, the SSTs were assumed to be constant throughout the 24 h period over which surface air temperature was averaged. The surface air temperature over the Gulf Stream was assumed to be the same as the observed Gulf Stream SST. An average air-temperature gradient was computed using the location of the western edge of the GSF that was obtained via the high resolution AVHRR imagery. Storm intensification was taken to be the 12 h surface central-pressure decrease of any extratropical cyclone within the study area. Extratropical storms that began as tropical systems were not included in this study.

The 500-mb maximum absolute vorticity values were obtained from the same NCEP reanalysis as those used for the surface data. The method for determining the maximum absolute vorticity value was based on the 12-h time window defined by the maximum deepening rate of the surface low. During this 12-h period, three (0 h, 6 h, 12 h) 500-mb vorticity fields, superimposed on sea-level pressure, were analyzed for each storm event. During this period, the maximum value of absolute vorticity at the 500 mb level upstream of the surface disturbance was recorded. An upper limit of horizontal distance separation between the 500-mb absolute vorticity maximum and surface low center of 1000 km was imposed. However, in the majority of the cases, the associated absolute vorticity maximum

was within 750 km. In rare cases where two maxima were located at the same distance (+/- 100 km), the stronger of the two was chosen⁴. Tables 5.1, 5.2, and 5.3 show the data separated in the *strong, moderate, and weak* bins discussed below.

⁴ The authors chose this method based on its simplicity within a future operational setting, but acknowledge that other measures of forcing, such as Q-vector convergence, or vorticity advection by thermal wind directly over the surface cyclone, would yield more accurate results.

Table 5.1 The 1991-2002 ASCII climatology *strong* bin showing dates, pressure drops (mb) for the 12 h window, 500-mb maximum absolute vorticity (10^{-5} s^{-1}) during the 12 h window, and PSBI ($^{\circ}\text{C}/10\text{km}$).

<i>Strong</i>				
Date		Delta P (mb)	500-mb Vorticity (10^{-5} s^{-1})	PSBI ($^{\circ}\text{C}/10\text{km}$)
14 Mar	1993	16	24	1.20
7 Jan	1996	12	24	0.90
21 Mar	2001	6	23	0.70
8 Feb	1995	14	22	1.10
30 Dec	2000	14	22	0.80
4 Feb	2001	13	22	0.90
16 Feb	1996	12	22	1.00
17 Oct	1991	8	22	0.50
3 Nov	1996	8	22	0.55
28 Jan	1998	11	21	0.80
21 Mar	1992	17	20	1.10
24 Jan	2000	17	20	2.00
11 Dec	1992	15	20	1.00
25 Feb	1999	12	20	0.95
10 Apr	1996	11	20	1.00
3 Jan	2002	11	20	0.92
21 Dec	1993	9	20	0.90
17 Jan	1998	7	20	0.70
24 Jan	2001	7	20	0.60
5 Apr	1992	6	20	0.70
9 Nov	1997	6	20	0.70
14 Nov	1995	12	19	1.10
15 Dec	1993	10	19	1.00
4 Feb	1998	5	19	0.72
4 Dec	2000	4	19	0.45

Table 5.2 The 1991-2002 ASCII climatology *Moderate* bin showing dates, pressure drops (mb) for the 12 h window, 500-mb maximum absolute vorticity (10^{-5} s^{-1}) during the 12 h window, and PSBI ($^{\circ}\text{C}/10\text{km}$).

<i>Moderate</i>				
Date		Delta P (mb)	500-mb Vorticity (10^{-5} s^{-1})	PSBI ($^{\circ}\text{C}/10\text{km}$)
20 Jan	2000	25	18	2.00
30 Dec	1997	16	18	1.39
31 Jan	1995	14	18	1.16
21 Feb	1998	12	18	1.20
8 Dec	1996	11	18	1.04
18 Jan	2000	11	18	1.19
12 Jan	1996	9	18	0.88
7 Feb	1998	9	18	1.17
9 Feb	1997	8	18	0.62
5 Apr	1998	8	18	1.01
16 Dec	1998	8	18	0.98
8 Apr	1996	7	18	0.78
25 Dec	1994	6	18	0.59
1 Dec	1997	6	18	0.59
27 Apr	2001	6	18	0.81
10 Feb	2000	4	18	0.62
25 Feb	2002	2	18	0.64
25 Dec	1993	12	17	1.50
19 Oct	1997	11	17	1.23
24 Feb	1998	11	17	1.34
20 Jan	1998	8	17	1.18
9 Oct	1996	5	17	1.02
3 Mar	1998	5	17	1.03
14 Mar	2002	3	17	0.72
28 Apr	1992	17	16	1.78
13 Feb	1993	14	16	1.73
27 Feb	1993	13	16	1.55
24 Jan	1995	11	16	1.51
28 Dec	1997	11	16	1.36
19 Dec	1994	10	16	1.28
2 Mar	1996	10	16	1.25
26 Mar	1992	9	16	1.25
23 Dec	1993	9	16	1.26
14 Nov	1997	9	16	1.24
23 Apr	1998	9	16	1.21
10 Mar	1999	8	16	1.16
3 Jan	1992	6	16	1.00
2 Apr	1996	6	16	0.92
11 Feb	1997	6	16	0.68
8 Feb	1991	5	16	0.67
24 Apr	1997	4	16	0.34
19 Apr	2000	3	16	0.32
29 Apr	2000	2	16	0.78
26 Apr	2000	1	16	0.59

Table 5.3 The 1991-2002 ASCII climatology *weak* bin showing dates, pressure drops (mb) for the 12 h window, 500-mb maximum absolute vorticity (10^{-5} s^{-1}) during the 12 h window, and PSBI ($^{\circ}\text{C}/10\text{km}$).

Date		Delta P (mb)	500-mb Vorticity (10^{-5} s^{-1})	PSBI ($^{\circ}\text{C}/10\text{km}$)
21 Feb	1995	16	15	1.47
3 Mar	1994	10	15	1.22
26 Dec	2001	10	15	1.26
6 Feb	1992	7	15	1.32
20 Feb	1999	6	15	0.82
29 Dec	2000	6	15	1.17
21 Nov	1996	5	15	0.93
17 Jan	1995	4	15	0.86
8 Feb	1993	2	15	1.03
20 Jan	1991	14	14	1.23
15 Mar	1994	12	14	1.72
25 Feb	2001	12	14	1.61
20 Apr	1991	10	14	1.33
14 Dec	1998	10	14	1.55
17 Mar	1994	8	14	0.93
16 Jan	1993	7	14	1.38
29 Mar	1996	7	14	1.53
14 Mar	1991	5	14	1.14
24 Apr	1995	5	14	0.67
6 Nov	1998	4	14	1.13
5 Mar	2000	4	14	1.28
2 Oct	2000	4	14	1.30
16 Mar	2001	2	14	0.62
31 Jan	1997	11	13	2.00
8 Dec	1995	7	13	1.50
9 Oct	1993	4	13	1.10
17 Nov	1994	2	13	0.78
14 Jan	1994	14	12	1.79
23 Dec	1994	9	12	1.61
12 Oct	1993	8	12	1.25
1 Mar	1994	8	12	1.22
16 Oct	1994	7	12	0.90
30 Dec	1993	6	12	1.17
30 Mar	1994	6	12	1.27
7 Apr	1993	4	12	1.03
5 Oct	1992	2	12	0.85
27 Jan	1993	2	12	1.15
27 Oct	1993	11	11	1.97
7 Apr	1995	6	11	1.13
16 Dec	1995	8	10	1.41
25 Feb	1991	7	10	1.26
22 Mar	2002	7	10	1.48
3 Feb	1996	6	10	1.51
4 Oct	1994	2	8	1.27
17 Oct	1993	6	4	2.10

For this study, it is assumed, for operational simplicity, that the value of maximum vorticity at the 500 mb level is directly related to the 500-mb vorticity advection. However, the same criteria were applied to the selection of maximum positive vorticity advection (PVA) at the 500 mb level. The results obtained when maximum PVA was used in place of vorticity were similar to those obtained from the simpler vorticity classification, except that the former produced a much noisier signal, as well as inconsistencies in localized maxima. The complications related to coarse grid resolution yielded a wide range of numerical values, thus making the binning procedure less accurate. In addition to these obstacles, multiple regions of equal PVA sharing the same horizontal displacement were linked to the surface low pressure during the 12-h selection window. This made for a more subjective process in identifying the most appropriate upper-level forcing. Therefore, the results presented below will be based on the vorticity classification.

5.4 Results

The extension of the ASCII data set covered an additional 11 years and 4 months (1991-2002) beyond the original Cione et al. (1993) study. This 20-year climatology almost doubled the number of storms to 231. A linear regression of the (dependent) observed surface cyclone central pressure decrease for the 231 cyclonic events that occurred from 1982-2002 on the (independent) PSBI is shown in Figure 5.2. These additional data provide similar position and slope of the linear regression fit verifying the previous threshold values defined in the PSBI. The combined results from this study and the previous one by Cione et al. (1993) yield a regression coefficient (r) of 0.55 between the pre-storm baroclinicity and storm development that explains 30% of the total deepening rate variance. The remaining 70% of the variance is assumed to be due to other contributing factors such as upper-level forcing.

One of the objectives of this study is to test the hypothesis that the unexplained variance (i.e., $1 - r^2$) observed in Figure 5.2, is a result of other important contributing cyclogenetic processes such as variability in the strength of the upper-tropospheric forcing. Using the values of maximum absolute vorticity at the 500 mb level recorded for 111 out of the 115 cyclonic events (1991-2002), the storms were separated into three bins. The remaining four storms were not included due to missing data. The bins are defined by storms with 500-mb maximum absolute vorticity values equal to or greater than $19 \times 10^{-5} \text{ s}^{-1}$ or “strongly forced” (24 storms), values between $15 \times 10^{-5} \text{ s}^{-1}$ and $19 \times 10^{-5} \text{ s}^{-1}$ or “moderately forced” (44 storms), and values equal to or less than $15 \times 10^{-5} \text{ s}^{-1}$ or “weakly forced” (43 storms).

In order to objectively distribute the number of storms per bin, the span of absolute

vorticity values covered by each bin are greater at both extremes. This was done by dividing the absolute vorticity of the data set in half at the mean ($17 \times 10^{-5} \text{ s}^{-1}$), and setting the "moderately forced" bin limits to the mean of the upper half ($19 \times 10^{-5} \text{ s}^{-1}$), and the mean of the lower half ($15 \times 10^{-5} \text{ s}^{-1}$). Thus, several storms with a maximum absolute vorticity greater than $15 \times 10^{-5} \text{ s}^{-1}$ and less than $19 \times 10^{-5} \text{ s}^{-1}$ fell in the "moderately forced" bin. Likewise, bins "strongly forced" and "weakly forced" were grouped by default because of the lack of storms with maximum absolute vorticity above $20 \times 10^{-5} \text{ s}^{-1}$, and below $14 \times 10^{-5} \text{ s}^{-1}$. By using the mean instead of the median, the "strongly forced" bin, albeit fewer cases, isolated the extreme rapid cyclogenetic events from the more typical coastal storms⁵.

⁵ Experiments with different binning strategies demonstrated that the results are not strongly sensitive to these choices.

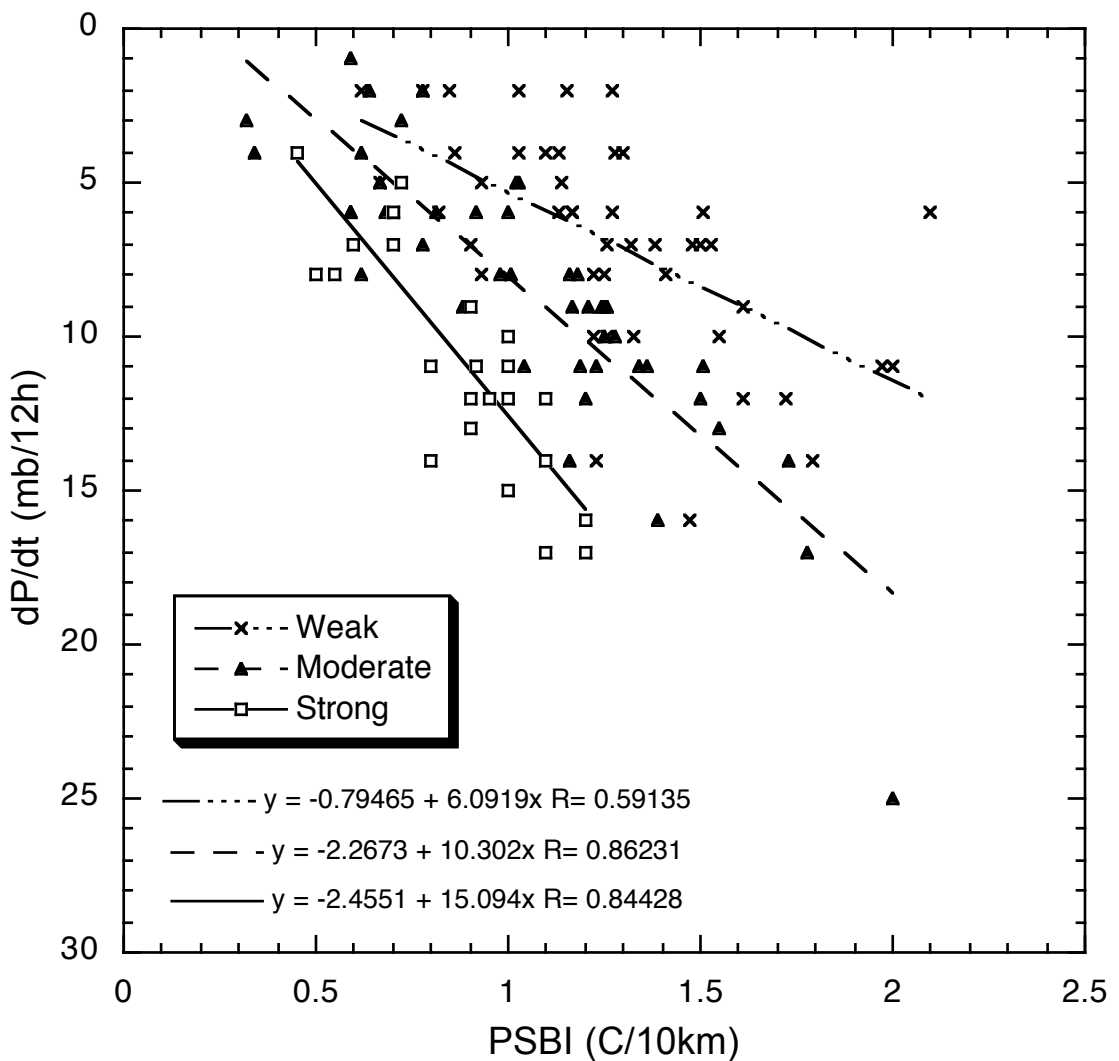


Figure 5.3. The ASCII dataset (1991-2002) of ETC's ($\Delta P/12h$ vs. PSBI) broken down into bins of 500mb vorticity ($10^{-5}s^{-1}$).

Linear regression fits were computed for each bin of the observed surface cyclone central pressure decrease for the 111 cyclonic events that occurred from 1991-2002 on the Pre-Storm Baroclinic Index (Figure 5.3). The slopes for the “strongly forced”, “moderately forced”, and “weakly forced” bins are -15.1, -10.3, and -6.1 respectively. Not only do the slopes of the regression fits decrease at a nearly linear rate as seen in Fig. 4, but the bins are found to be naturally stratified in the order of increasing vorticity. The correlation coefficients for the “strongly forced”, “moderately forced”, and “weakly forced” bins are 0.84, 0.86, and 0.59 respectively. For the “moderately forced” bin , the average deepening rate was -9 mb/12h, accounting for 74% of the variance. The correlation coefficient for the “strongly forced” bin, which had an average deepening rate of -11 mb/12h, was 0.84 explaining 71% of the variance. This was slightly lower than the correlation coefficient for the “moderately forced” storm bin, but considering there were half the number of storms, and of those storms many were extreme events, it is comparatively high. This suggests that for stronger cases, the deepening rate is more sensitive to changes in PSBI thus increasing the slope of the regression fit. For the “weakly forced” bin, where the average deepening rate was -7 mb/12h, the correlation coefficient of 0.59 explaining 35% of the variance. This is likely related to the fact that weaker disturbances are more easily influenced by various other forcing mechanisms not accounted for in this study such as trough axis tilt, moist diabatic processes such as convection, and Gulf Stream front curvature, thus increasing the scatter. However, the correlation coefficients for all three bins are substantially higher than the non-binned correlation coefficient of 0.55.

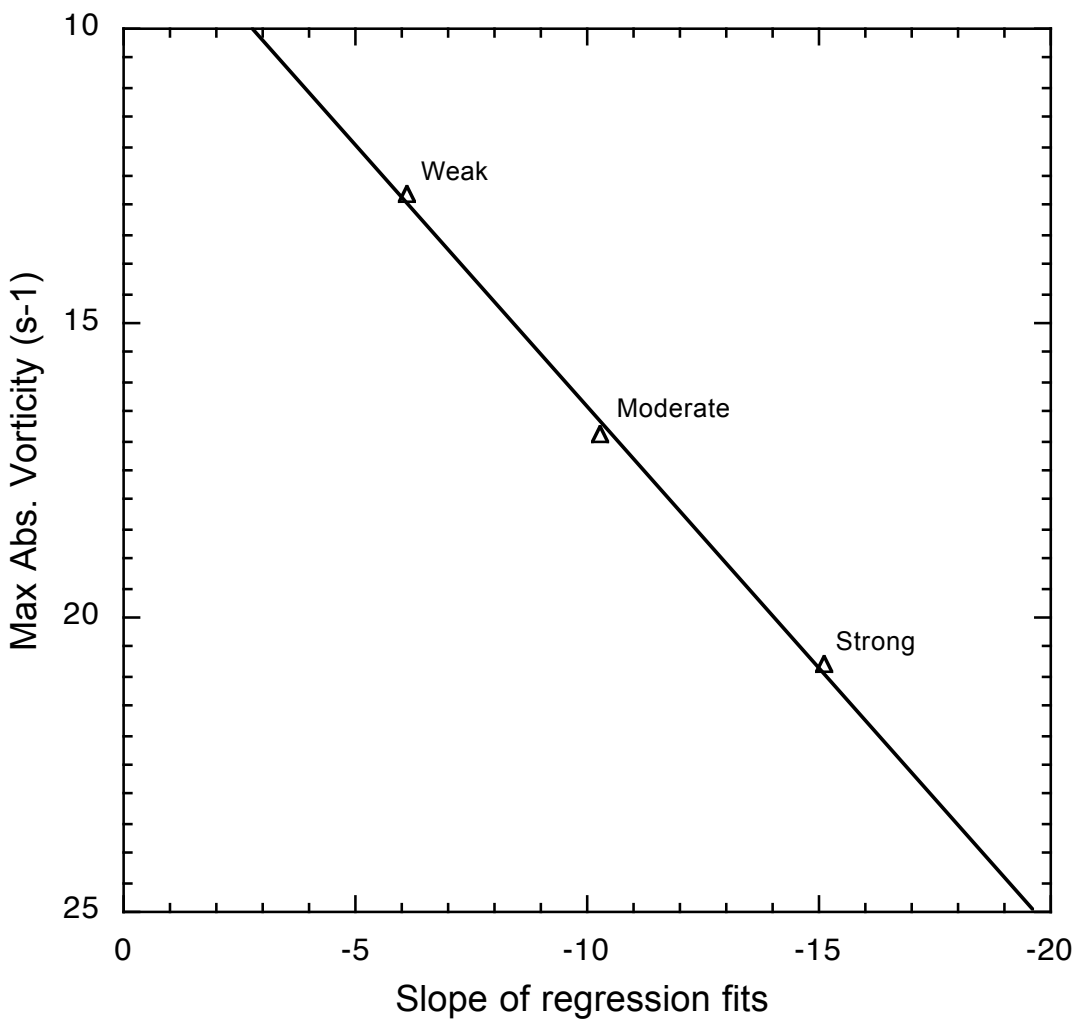


Figure 5.4. The maximum absolute vorticities (s^{-1} , averaged for each bin) plotted against the corresponding slope of the linear regressions seen in Figure 5.3.

The above 3-bin procedure was done for the purpose of future operational usage. However, an additional 6-bin procedure was conducted based on the strength of the nearest maximum of 500mb absolute vorticity associated with the surface low (Fig. 5.5). The maximum absolute vorticity value for each storm was selected during the same 12h period used for ΔP in the ASCII dataset. In order to achieve similar quantity in terms of the amount of storms per bin, the absolute vorticity values covered by each bin are greater at both extremes. For example, bin "16" is by itself because there were several storms with a maximum absolute vorticity greater than $15 \times 10^{-5} \text{ s}^{-1}$ and less than $17 \times 10^{-5} \text{ s}^{-1}$. Likewise, bins "21+" and "13-" were grouped because of the lack of storms with maximum absolute vorticities above $20 \times 10^{-5} \text{ s}^{-1}$, and below $14 \times 10^{-5} \text{ s}^{-1}$. Tropical to extratropical transition storms were not included. Linear regression fits were done for each bin in Figure 5.4. Even more noticeable in this distribution, is the decrease in slope with lower 500mb vorticity. Once again, the stratified bin positions, suggest that there is a shifting degree of mutual dependency on surface versus upper level forcing. The correlation coefficients range from 0.63 to 0.93 suggesting that there is a stronger dependence with weaker upper forcing for bins in the middle. For storms in the "21+" bin, the increasing cyclonic vorticity advection with height outweighs the PSBI to the point where it does not follow the other bin's slope trends as closely.

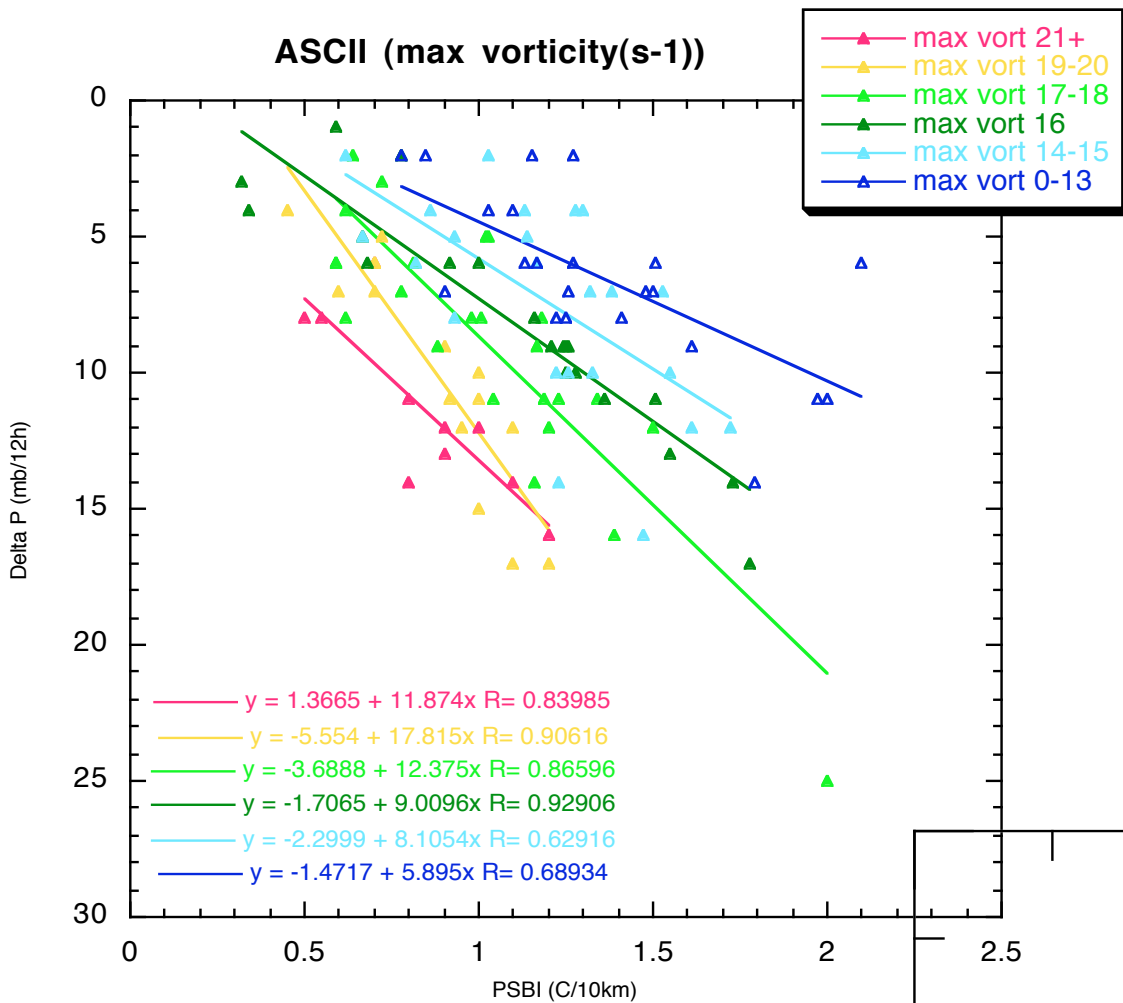


Figure 5.5. The ASCII dataset (1991-2002) of ETC's ($\Delta P/12h$ vs. PSBI) broken down into bins of 500mb vorticity ($10^{-5}s^{-1}$).

Predicted deepening rates for the events in the 1991-2002 data set were calculated using the updated regression equation shown in Figure 5.2. These predicted deepening rates are compared to the observed deepening rates for the 1991-2002 data set in Figure 5.6a. Figures 5.6b, 5.6c, and 5.6d show the same comparison stratified by bin. It is evident from Figure 5.6d, that ASCII, based on PSBI alone, breaks down in cases where upper-level forcing is the primary influence. However, it is the forecasting of "moderately forced" cases, seen in Figure 5.6c, where the ASCII provides the best fit to the observations. These findings verify the outcome of the binned regressions discussed above. Figures 5.6b (5.6d) also reveal a trend for ASCII to "over-predict" ("under-predict") the deepening rate of storms involving weak (strong) upper-level forcing. In other words, storms with greater cyclonic vorticity are able to extract more energy from the Gulf Stream, while the opposite is true for storms with weak upper-forcing.

As mentioned above, the same criteria were applied to the data set to bin the cases based on vorticity advection. There were numerous obstacles when undertaking this task, however, the results were quite similar as far as stratification. Linear regressions can be seen for the PVA binning method in Figure 5.7. A fit of the sloped of the regressions are seen in Figure 5.8. The variance in the positions are likely a result of the complications related to grid resolution, as verified by the reduced correlation from the absoulte vorticity method.

ASCII Verification (1991 - 2002)

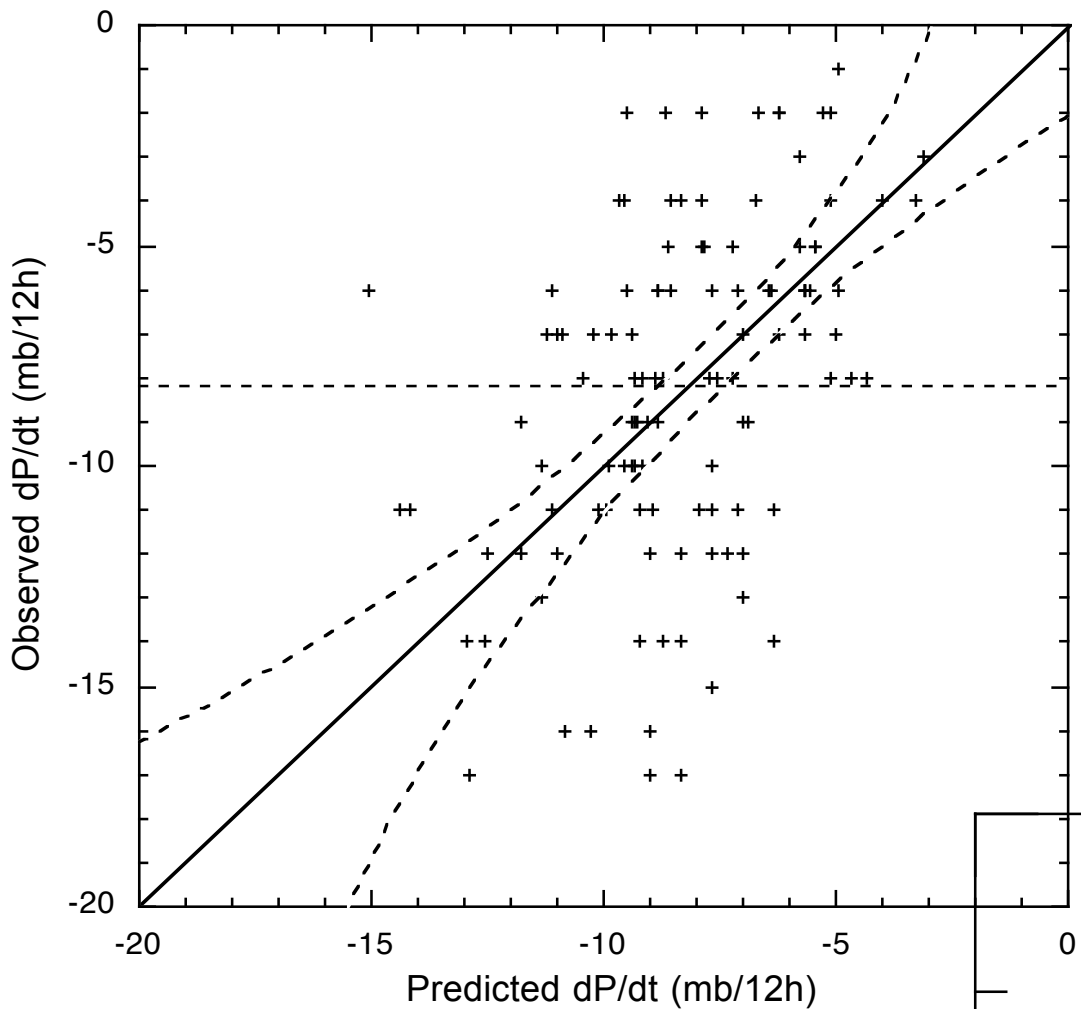


Figure 5.6a. The full distribution's observed deepening rate (mb/12h) of cases from the 1991-2002 data set plotted against the predicted deepening rate (mb/12h) from the updated ASCII regression equation seen in Figure 2. The center line shows a perfect correlation bound on both sides by a 95% confidence interval calculated for the entire data set. The horizontal line marks the mean deepening rate for the entire data set.

ASCII Verification (1991 - 2002)

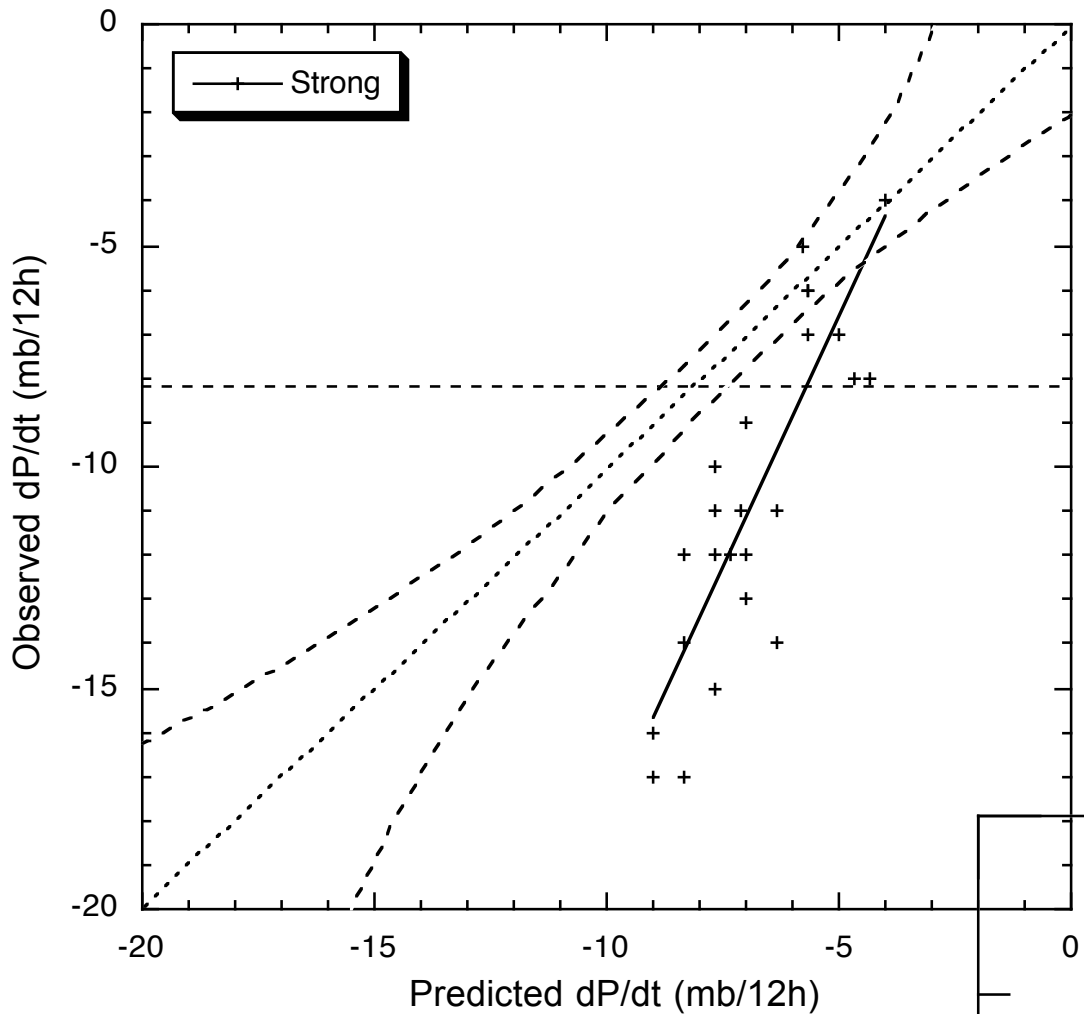


Figure 5.6b. The *strong* bin's observed deepening rate (mb/12h) of cases from the 1991-2002 data set plotted against the predicted deepening rate (mb/12h) from the updated ASCII regression equation seen in Figure 2. The center line shows a perfect correlation bound on both sides by a 95% confidence interval calculated for the entire data set. The horizontal line marks the mean deepening rate for the entire data set.

ASCII Verification (1991 - 2002)

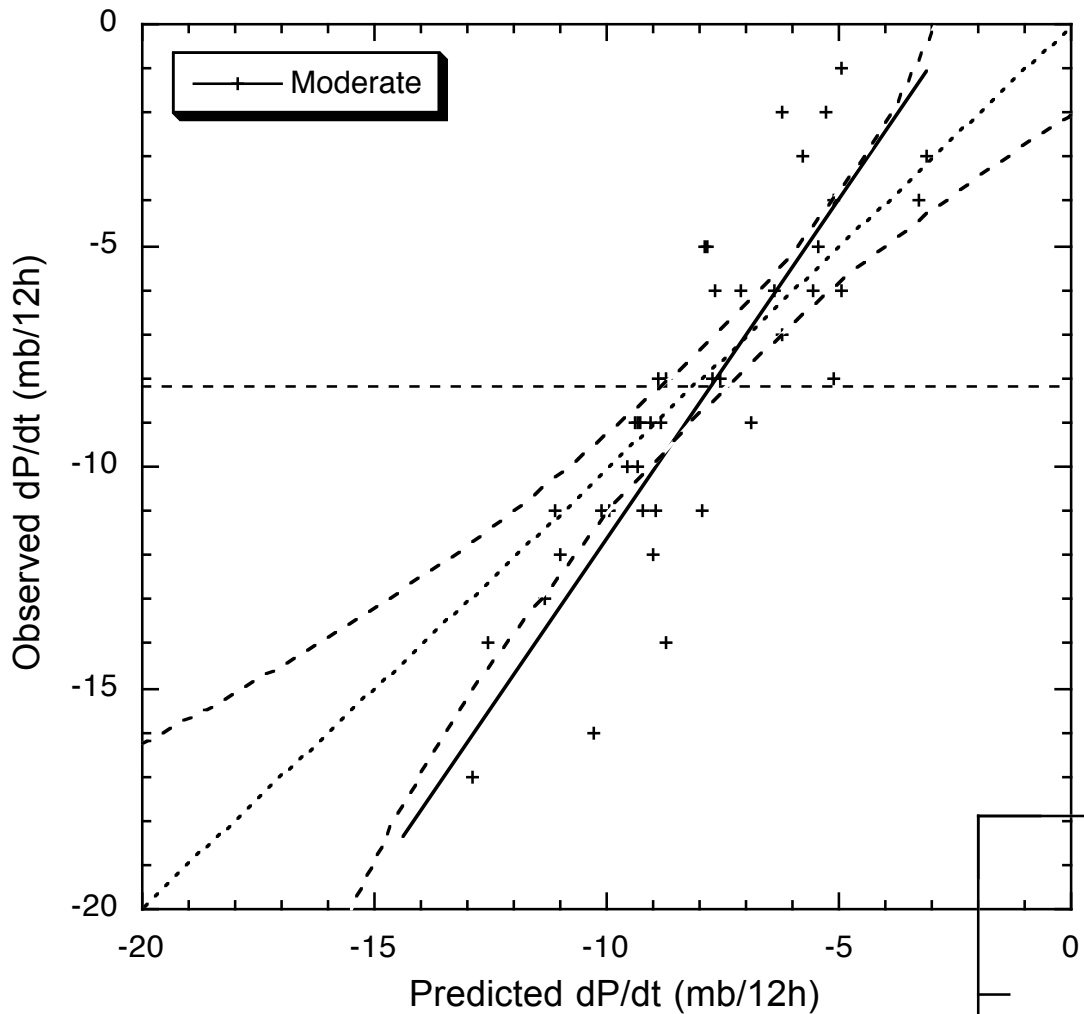


Figure 5.6c. The *moderate* bin's observed deepening rate (mb/12h) of cases from the 1991-2002 data set plotted against the predicted deepening rate (mb/12h) from the updated ASCII regression equation seen in Figure 2. The center line shows a perfect correlation bound on both sides by a 95% confidence interval calculated for the entire data set. The horizontal line marks the mean deepening rate for the entire data set.

ASCII Verification (1991 - 2002)

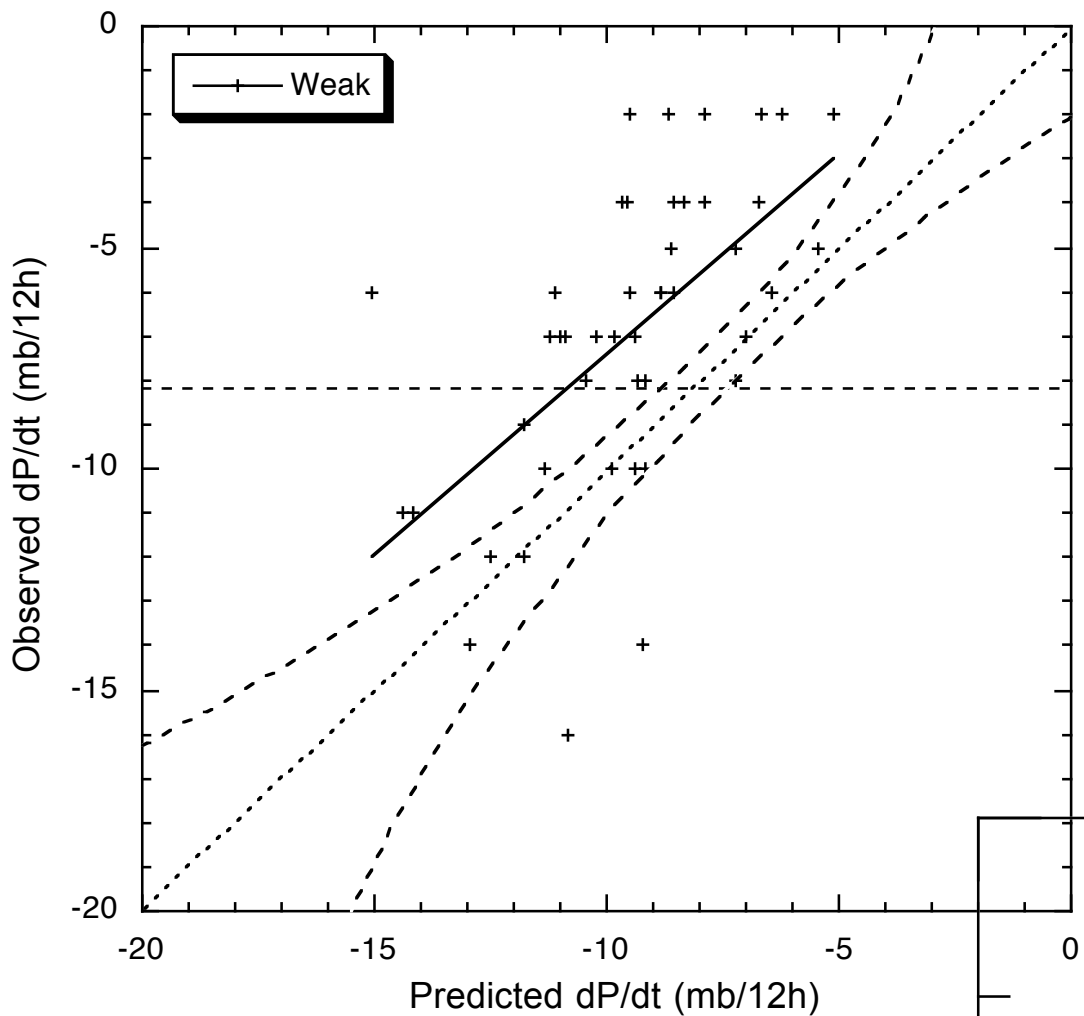


Figure 5.6d. The *weak* bin's observed deepening rate (mb/12h) of cases from the 1991-2002 data set plotted against the predicted deepening rate (mb/12h) from the updated ASCII regression equation seen in Figure 2. The center line shows a perfect correlation bound on both sides by a 95% confidence interval calculated for the entire data set. The horizontal line marks the mean deepening rate for the entire data set.

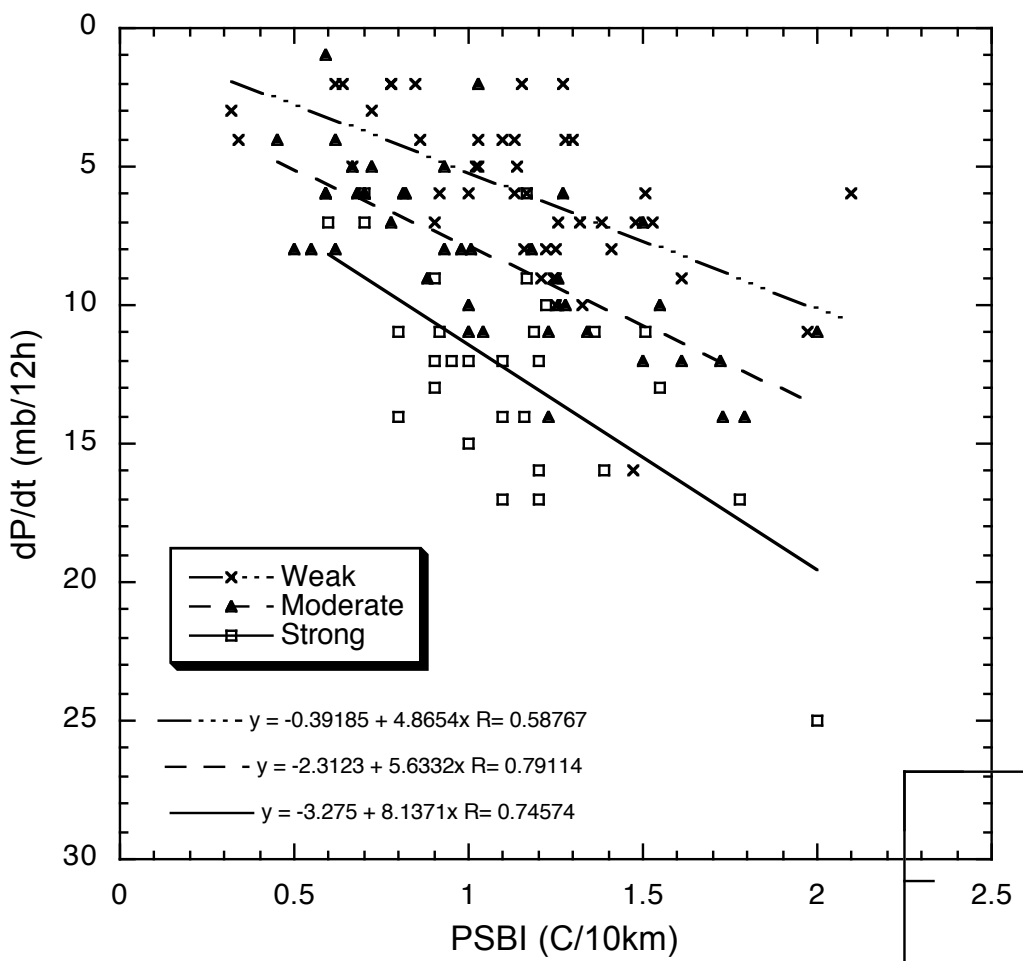


Figure 5.7. The ASCII dataset (1991-2002) of ETC's ($\Delta P/12h$ vs. PSBI) broken down into bins of 500-mb positive vorticity advection(s^{-2}).

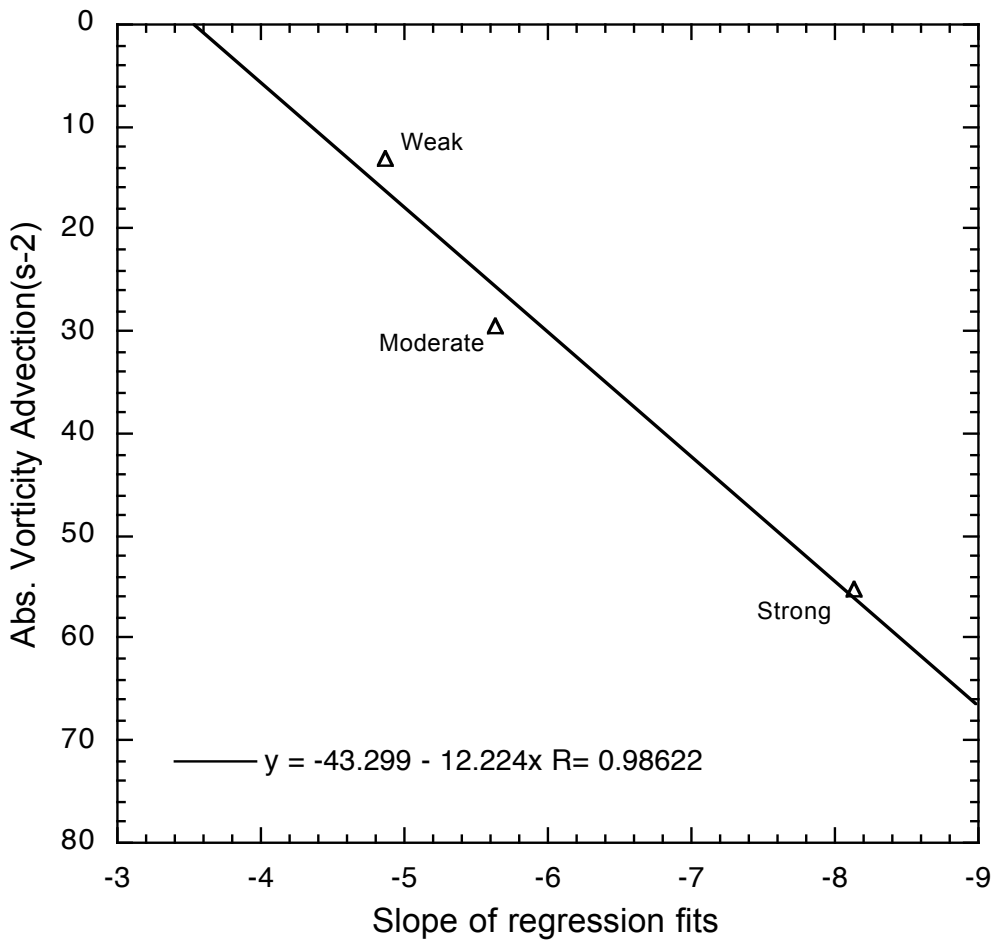


Figure 5.8. The maximum absolute vorticity advection (s^{-2} , averaged for each bin) plotted against the corresponding slope of the linear regressions seen in Figure 5.7.

The corrected predictions for the deepening rates using the separate regression equations of the respective bins are seen in Figure 5.9. Since the entire 1991-2002 data set (a) has the same regression, this prediction was unchanged. However, the "weakly forced" (b), "moderately forced" (c), and "strongly forced" (d) deepening rates are independently verified. Although the scatter within each bin is left mostly unchanged, the trend, discussed above, for ASCII to "over-predict" ("under-predict") the deepening rate of storms involving weak (b) (strong (d)) upper-level forcing has been rectified by the use of the separate regression equations. The prediction improvements of the "moderately forced" cases (Figure 5.6c) are less substantial, although still noticeable, because this bin's separate regression equation is similar to the average of the entire data set.

ASCII Verification (1991-2002)

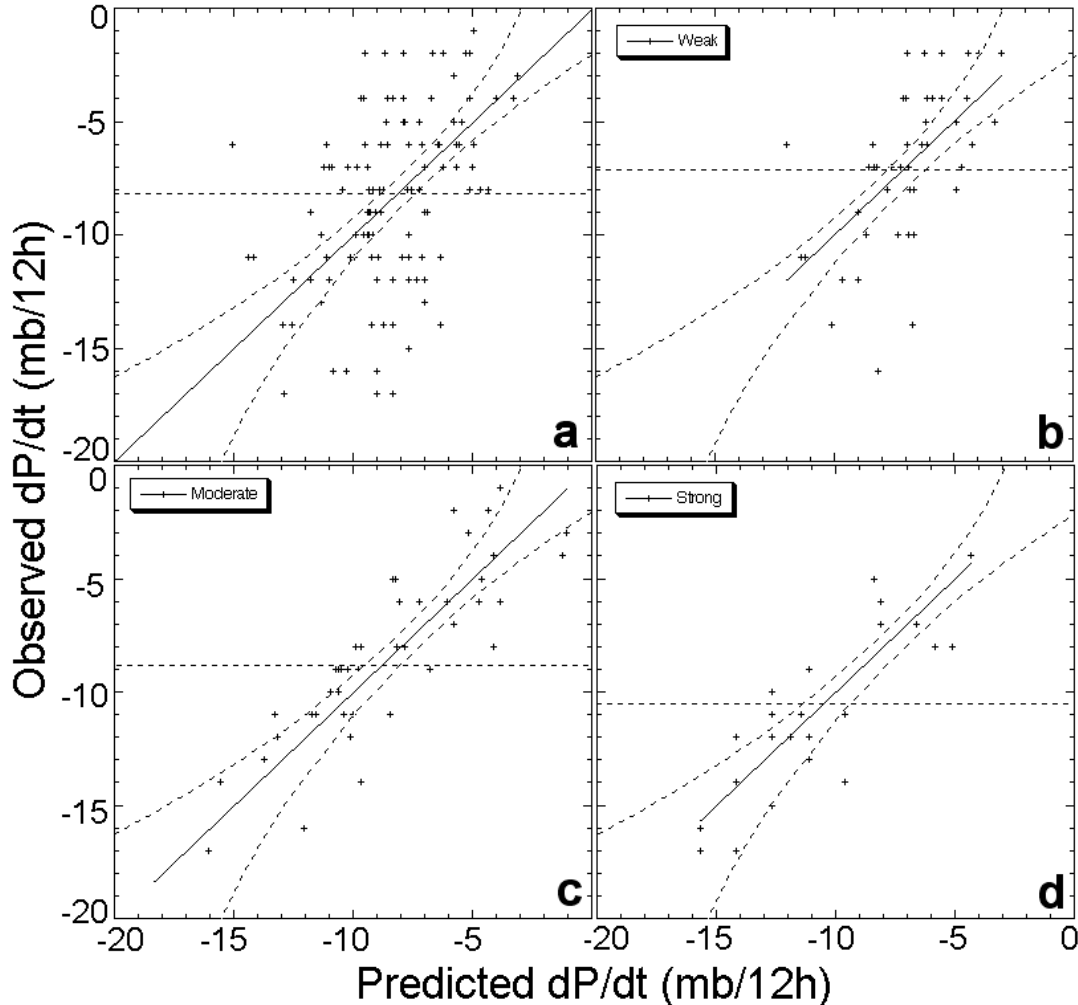


Figure 5.9. The observed deepening rate (mb/12h) of cases from the 1991-2002 data set plotted against the predicted deepening rate (mb/12h) from the separate regression equations of the respective bins. The center line shows a perfect correlation bound on both sides by a 95% confidence interval calculated for the entire data set. The horizontal line marks the mean deepening rate for the entire (a), and the binned (b), (c), and (d) data sets. The full distribution (a), as well as the weakly forced (b), moderately forced (c), and strongly forced (d) bins are shown.

5.5 Summary

The Atlantic Surface Cyclone Intensification Index (ASCII) is a forecast index that quantifies the amount of low-level baroclinicity over the Gulf Stream region east of North Carolina. It is calculated from the temperature difference between the coldest 24-hour average air temperature at Cape Hatteras, or Wilmington, NC, and the temperature at the western boundary of the Gulf Stream. This value is referred to as the pre-storm baroclinic index (PSBI), and is used to predict the deepening rate of the impending extratropical cyclone. The initial ASCII study covered the years 1982-1990. This data set was recently expanded to cover 11 years and 4 months of data from 1991 to 2002, presented in section 5.3, which added 115 storms to the original 10 year (116 storm) data set. The doubling of the original ASCII climatology data verifies threshold values defined in the PSBI by the statistically insignificant changes in the regression fit (1.7%) which explain as much as 30% of the variance in cyclone deepening rate. However, the neglect of upper-tropospheric forcing as a predictor in the original ASCII formulation precludes explanation of a large fraction of the deepening rate variance.

In the second half of this chapter, a modified index is derived in which an approximate measure of upper-level forcing is included. The 1991-2002 cyclone events were separated into bins of “strongly forced”, “moderately forced”, and “weakly forced” based on the strength of the nearest upstream maximum of 500-mb absolute vorticity associated with the surface low. This separation method reduced the scatter and further isolated the contributions of surface forcing versus upper-level forcing on extratropical cyclogenesis. Results of the combined upper-level index and PSBI demonstrate that as much as 74% of the deepening rate variance can be explained for cases with stronger upper-level forcing.

CHAPTER 6: MESOSCALE NUMERICAL MODEL

6.1 Model System Overview

The fifth-generation NCAR/ Penn State Mesoscale Model (MM5) is the latest version of a mesoscale model first used and developed at Penn State in the early 1970's. MM5 is a primitive equation model that uses a non-dimensional σ -vertical coordinate system. The model has been changed so that it now includes multiple-nests, nonhydrostatic dynamics, and a four dimensional data assimilation (FDDA) capability. Model performance has also been enhanced with the development of more physics options and the ability to run the model on several computer platforms. A flow chart showing the MM5 modeling system is shown in Figure 6.1. The flow chart breaks the MM5 modeling system into three components: 1. Main Programs, 2. Data Sets, and 3. Additional Capabilities. TERRAIN, REGRID, RAWINS, INTERP, and MM5 are the main programs included in the MM5 model. Programs TERRAIN and REGRID interpolate terrestrial and isobaric atmospheric data in a latitude-longitude mesh to a variable high-resolution model domain. Projection options for the model domain include Mercator, Lambert Conformal, or Polar Stereographic. Mesoscale detail is added to the REGRID data with surface and upper air observations from the standard global network of surface and rawinsonde stations in the RAWINS program. Atmospheric data is then interpolated using the INTERP program from pressure levels to the vertical sigma coordinate system employed by MM5. MM5 is the final main program, and is the numerical weather prediction component of the model. The MM5 program includes the various physics options and the governing equations.

The MM5 Modeling System Flow Chart

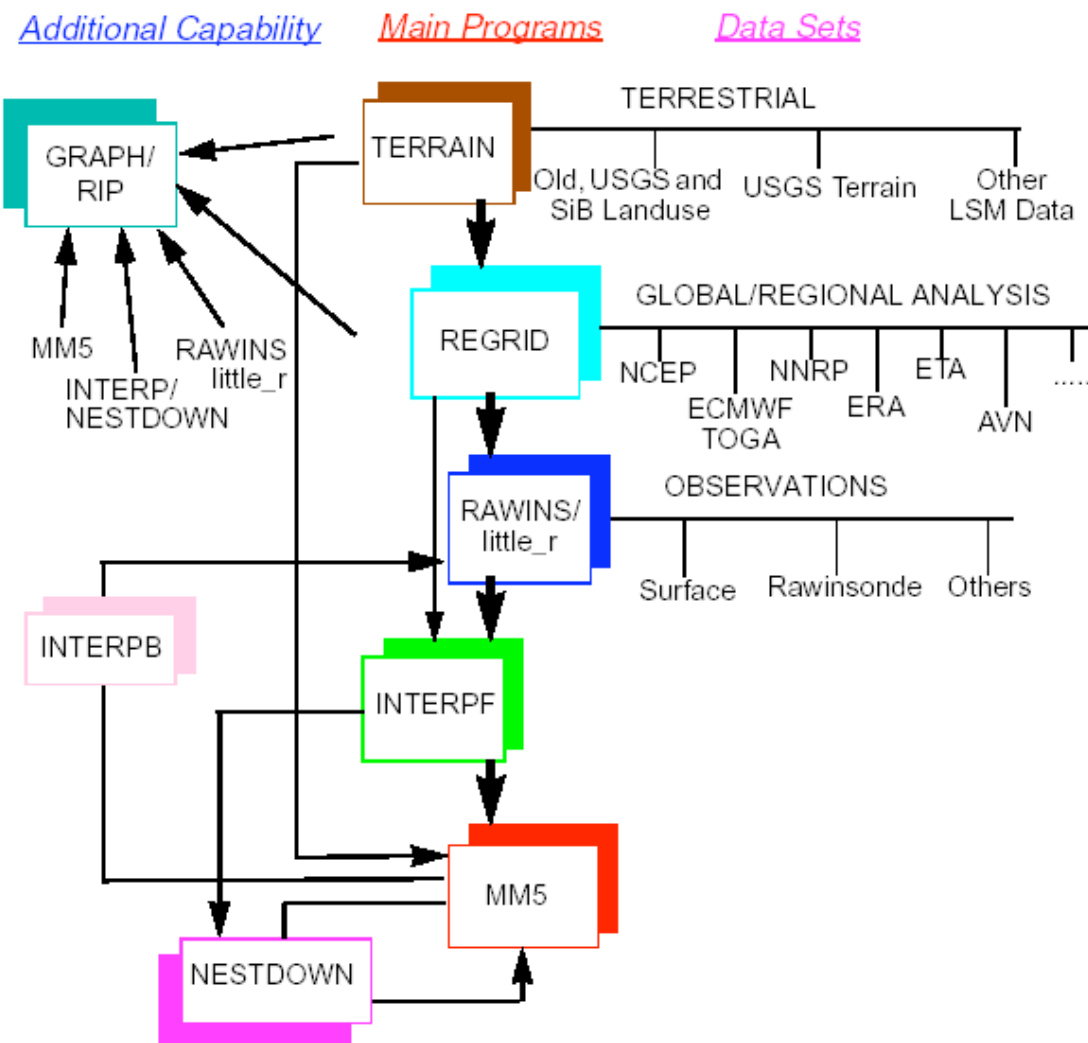


Figure 6.1. Flow chart of the MM5 routines within the modeling system (Grell et al. 1994).

A single model domain is created in TERRAIN and used for the model run. The area coverage of the domain, as well as the resolution is specific to the simulation, and is discussed later in the respective chapters.

Atmospheric data interpolated in the REGRID and RAWINS programs must be converted from pressure levels to the sigma terrain following coordinate system. The formula for the dimensionless sigma level is given by:

$$\sigma = \frac{(p - p_t)}{(p_s - p_t)} \quad (6.1)$$

where p is the pressure, p_t is a specified constant top pressure, and p_s is the surface pressure.

Vertical sigma levels used for this study are shown in Figure 6.2.

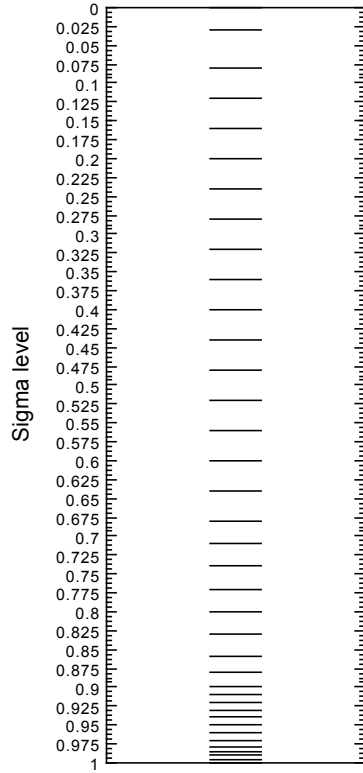


Figure 6.2. Vertical sigma levels within the model domain used in all the experiments in this study.

In all the simulations, the domain has 38 vertical σ levels between 1000 mb and 100 mb with 18 of the levels below 850 or 1.5 km. Numerous sigma levels are located in the lowest 1.5 km of the atmosphere because fluxes of heat, moisture, and momentum occur in the planetary boundary layer.

6.2 Initialization and Boundary Conditions

Operational analysis from the Eta-212 grid was used to initialize all the simulations. The above data are interpolated onto the model grid to serve as initial values and to provide lateral boundary conditions for the model. The specifics of each data set used will be discussed in the respective chapters.

MM5 uses data from the United States Geological Survey (USGS) database for terrain and landuse initialization. The domain was initialized with high resolution 30 second (.9km) terrain and landuse files. Initialized topography for the model domain is shown in Figure 6.3. Initialized terrain files include landuse files with 24 categories as shown in Table 6.1.

Table 6.1. USGS-24 land-use file identification for model domain initialization

No	Description
1	Urban and Built-Up Land
2	Dryland Cropland and Pasture
3	Irrigated Cropland and Pasture
4	Mixed Dryland/Irrigated Cropland and Pasture
5	Cropland/Grassland Mosaic
6	Cropland/Woodland Mosaic
7	Grassland
8	Shrubland
9	Mixed Shrubland/Grassland
10	Savanna
11	Deciduous Broadleaf Forest
12	Deciduous Needleleaf Forest
13	Evergreen Broadleaf Forest
14	Evergreen Needleleaf Forest
15	Mixed Forest
16	Water Bodies
17	Herbaceous Wetland
18	Wooded Wetland
19	Barren or Sparsely Vegetated
20	Herbaceous Tundra
21	Wooded Tundra
22	Mixed Tundra
23	Bare Ground Tundra
24	Snow or Ice

The landuse categories are given values for albedo, moisture availability, emissivity, roughness length, and thermal inertia. Variables for land-use are given different values for summer and winter to account for changes in the landuse characteristics. The land-use file used for initializing the model outer domain is shown in Figure 6.4. As with topography, landuse is diverse in the model domain and presents a challenge for the model to perform in such a complex environment.

6.3 Model Equations

The model's governing equations are found in the MM5 program, which is the numerical weather prediction part of the mesoscale modeling system. MM5's equations and physics options allow for research on large and small scales. Large-scale atmospheric phenomenon such as monsoons and tropical systems and small-scale events such as fronts, land-sea breezes, and urban heat islands can all be simulated using MM5.

The equations for the nonhydrostatic model's basic variables excluding moisture in terms of terrain following coordinates (x, y, s) are as follows:

Pressure

$$\frac{\partial p'}{\partial t} - \rho_0 g w + \gamma p \nabla \cdot \bar{V} = -\bar{V} p' + \frac{\gamma p}{T} \left(\frac{Q}{c_p} + \frac{T_0}{\theta_0} D_\theta \right) \quad (6.2)$$

Momentum (x-component)

$$\frac{\partial u}{\partial t} + \frac{m}{\rho} \left(\frac{\partial p'}{\partial x} - \frac{\sigma}{p^*} \frac{\partial p^*}{\partial x} \frac{\partial p'}{\partial \sigma} \right) = -V \cdot \nabla u + v \left(f + u \frac{\partial m}{\partial y} - v \frac{\partial m}{\partial x} \right) - ew \cos \alpha - \frac{uw}{r_{earth}} + D_u \quad (6.3)$$

Momentum (y-component)

$$\frac{\partial v}{\partial t} + \frac{m}{\rho} \left(\frac{\partial p'}{\partial y} - \frac{\sigma}{p^*} \frac{\partial p^*}{\partial y} \frac{\partial p'}{\partial \sigma} \right) = -V \cdot \nabla v - u \left(f + u \frac{\partial m}{\partial y} - v \frac{\partial m}{\partial x} \right) - ew \sin \alpha - \frac{vw}{r_{earth}} + D_v \quad (6.5)$$

Momentum (z-component)

$$\begin{aligned} \frac{\partial w}{\partial t} + \frac{\rho_0}{\rho} \frac{g}{p^*} \frac{\partial p'}{\partial \sigma} + \frac{g}{\gamma} \frac{\partial p'}{p} &= -V \cdot \nabla w + g \frac{p_0}{p} \frac{T'}{T_0} - \frac{g R_d}{c_p} \frac{p'}{p} \\ &+ e(u \cos \alpha - v \sin \alpha) + \frac{u^2 + v^2}{r_{earth}} + D_w \end{aligned} \quad (6.6)$$

Thermodynamics

$$\frac{\partial T}{\partial t} = -V \cdot \nabla T + \frac{1}{\rho c_p} \left(\frac{\partial p'}{\partial t} + V \cdot \nabla p' - \rho_0 g w \right) + \frac{Q}{c_p} + \frac{T_0}{\theta_0} D_\theta \quad (6.7)$$

Advection terms can be expanded as

$$V \cdot \nabla A = mu \frac{\partial A}{\partial x} + mv \frac{\partial A}{\partial y} + \xi \frac{\partial A}{\partial \sigma} \quad (6.8)$$

where

$$\xi = -\frac{\rho_0 g}{p^*} w - \frac{m\sigma}{p^*} \frac{\partial p^*}{\partial x} u - \frac{m\sigma}{p^*} \frac{\partial p^*}{\partial y} v. \quad (6.9)$$

The divergence term can be expanded as

$$\nabla \cdot V = m^2 \frac{\partial}{\partial x} \left(\frac{u}{m} \right) - \frac{m\sigma}{p^*} \frac{\partial p^*}{\partial x} \frac{\partial u}{\partial \sigma} + m^2 \frac{\partial}{\partial y} \left(\frac{v}{m} \right) - \frac{m\sigma}{p^*} \frac{\partial p^*}{\partial y} \frac{\partial v}{\partial \sigma} - \frac{\rho_0 g}{p^*} \frac{\partial w}{\partial \sigma} \quad (6.10)$$

6.4 MM5 Surface Flux Calculations

The surface heat flux, H_s , and the surface moisture flux, E_s , within MM5 are dependent on the PBL scheme chosen. Initial simulations using MM5 version 3.4 used the bulk-aerodynamic method as discussed in sections 3.3.2 and 3.3.4 (Deardorff 1972). After migrating to MM5 version 3.5 and 3.6, both MRF and Blackadar, which share almost identical flux parameterizations, were employed (Zhang and Anthes 1982). The differences arise with the mixing interactions of Resiner versus the Simple Ice microphysics scheme choices, as well as the OSU LSM (MRF) versus 5-layer LSM (Blackadar) option. However, the LSM choice, as discussed later, exhibits a negligible difference on this winter event simulation due to the lack of vegetation and vast snow cover.

It is the Zhang and Anthes (1982) version of the Blackadar PBL scheme which is

detailed below because its combination with the 5-layer LSM proved most realistic in the simulation of the 24-25 January 2000 winter storm case. Within the Blackadar PBL scheme, the surface flux calculations of heat and moisture are based on the Monin-Obukhov similarity theory. This scheme has four stability cases; stable, mechanically driven turbulence, and forced convection which are handled with a first-order closure, while the unstable (free convection) is treated with a non-local closure (Blackadar 1976, 1979). The friction velocity is defined as:

$$u_* = \text{MAX} \left(\frac{kV}{\ln \frac{z_a}{z_0} - \varphi_m}, u_{*0} \right) \quad (6.11)$$

where u_{*0} is 0.1 ms^{-1} over land (zero over water), z_0 is the roughness parameter, z_a is the height of the lowest sigma level, and $V = (V_a^2 + V_c^2)^{\frac{1}{2}}$ where V_a is the wind speed at the lowest sigma level and V_c is the convective velocity. MAX refers to the option within the code to chose the greater of the two values presented. φ_m and φ_h are nondimensional stability parameters that are functions of the bulk Richardson number,

$$R_{IB} = \frac{g z_a}{\theta_a} \frac{\theta_{va} - \theta_{vg}}{V^2}, \quad (6.12)$$

where θ_v is the virtual potential temperature, and the subscripts “a” and “g” represent the lowest sigma-level and ground level respectively. The surface heat flux is defined as:

$$H_s = -c_{pm} \rho_a k u_* T_* \quad (6.13)$$

where c_{pm} is the specific heat at constant pressure for moist air, ρ_a is the density of air, and

$$T_* = \frac{\theta_a - \theta_g}{\ln \frac{z_a}{z_0} - \varphi_h}. \quad (6.14)$$

6.4.1 Stability Cases

The first stability regime is for the stable case where $R_{IB} > 0.2$, $u_* = u_{*0}$, and

$$\varphi_m = \varphi_h = -10 \ln \frac{z_a}{z_0}. \quad (6.15)$$

For the stable case, the surface heat flux is defined as the larger of the two flux values defined in the model as:

$$H_s = MAX\left(-250Wm^{-2}, -c_{pm}\rho_a k u_* T_*\right) \quad (6.16)$$

The second case, for $0 \leq R_{IB} \leq 0.2$, is the mechanically driven turbulence case where

$$\varphi_m = \varphi_h = -5 \left(\frac{R_{IB}}{1.1 - 5R_{IB}} \right) \ln \frac{z_a}{z_0}. \quad (6.17)$$

There are two unstable regimes. The first unstable case is for forced convection, $R_{IB} < 0$, where $|h/L| \leq 1.5$, so that when the PBL height (h) = z_a , $|R_{IB} \ln(z_a/z_0)| \leq 1.5$, and $\varphi_m = \varphi_h = 0$.

The Monin-Obukhov length is defined as

$$L = -\frac{c_{pm}\rho_a \theta_a u_*^3}{kgH_s}. \quad (6.18)$$

The second unstable case is for free convection, $R_{IB} < 0$, where $|h/L| > 1.5$. Here

$$\varphi_h = -3.23 \left(\frac{z_a}{L} \right) - 1.99 \left(\frac{z_a}{L} \right)^2 - 0.474 \left(\frac{z_a}{L} \right)^3, \quad (6.19)$$

and

$$\varphi_m = -1.86 \left(\frac{z_a}{L} \right) - 1.07 \left(\frac{z_a}{L} \right)^2 - 0.249 \left(\frac{z_a}{L} \right)^3, \quad (6.20)$$

so that $z_a/L \geq -2.0$. According to Zhang and Anthes (1982) and Grell (1995), z_a/L is approximated by

$$\frac{z_a}{L} = R_{IB} \ln \frac{z_a}{z_0} \quad (6.21)$$

to avoid computing iterative solutions for φ_m , while maintaining continuity with the bulk Richardson number.

The surface moisture flux is defined by Carlson and Boland (1978) as

$$E_s = M \rho_a I^{-1} (q_{vs}(T_g) - q_{va}), \quad (6.22)$$

and

$$I^{-1} = k u_* \left[\ln \left(\frac{k u_* z_a}{K_a} + \frac{z_a}{z_l} \right) - \varphi_h \right]^{-1}, \quad (6.23)$$

where the molecular diffusivity, $K_a = 2.4 \times 10^{-5} \text{ m}^2\text{s}^{-1}$, and z_l equals 0.01 over land, (z_0 over water). According to Grell (1995), the roughness length, z_0 , over land is a function of the land-use category shown in Table 6.1. The roughness length over water is defined by Delsol et al. (1971) as $z_0 = 0.032 u_*^2 g^{-1} + z_{0c}$, where z_{0c} is on the order of $1 \times 10^{-4} \text{ m}$.

6.4.2 PBL Regimes

There are two PBL regimes within the Blackadar scheme, a nocturnal regime, and a free convection regime. The three first-order closure cases of stable, mechanically driven turbulence, and forced convection, discussed above, fit into the nocturnal regime. Within the nocturnal regime, the surface stress, τ_s , is a function of the friction velocity from Equation 6.11,

$$\tau_s = \rho u_*^2, \quad (6.24)$$

and can be broken into x and y components based on the wind speed at the lowest sigma level, V_a , so that

$$\tau_{sx} = u\tau_s V_a^{-1}, \quad (6.25)$$

and

$$\tau_{sy} = v\tau_s V_a^{-1}. \quad (6.26)$$

The prognostic equations for the surface layer variables are defined as:

$$\frac{\partial \theta_a}{\partial t} = \frac{-(H_1 - H_s)}{(\rho_a c_{pm} \bar{z}_1)}, \quad (6.27)$$

where H_1 is the heat flux at the top of the surface layer, and the surface heat flux, H_s , is calculated from Equation 6.13;

$$\frac{\partial q_{va}}{\partial t} = \frac{-(E_1 - E_s)}{(\rho_a z_1)}, \quad (6.28)$$

where E_1 is the moisture flux at the top of the surface layer, and the surface moisture flux, E_s , is calculated from Equation 6.22; and

$$\frac{\partial u_a}{\partial t} = \frac{(\tau_{1x} - \tau_{sx})}{(\rho_a \bar{z}_1)}, \quad (6.29)$$

$$\frac{\partial v_a}{\partial t} = \frac{(\tau_{1y} - \tau_{sy})}{(\rho_a \bar{z}_1)}, \quad (6.30)$$

$$\frac{\partial q_{ca}}{\partial t} = \frac{-F_1}{(\rho_a \bar{z}_1)}, \quad (6.31)$$

where F can be the flux of momentum, heat, or moisture. Above the surface layer, these variables are computed at full sigma-levels using K-theory equations for vertical diffusion (Richtmeyer 1957; Zhang and Anthes 1982).

In the PBL regime for free convection, the last of the four cases discussed above, the prognostic variables are solved for analytically. Since the lower troposphere is considered to be unstable for this case, vertical mixing is computed based on the mixed layer thermal

structure (opposed to the K-theory used in the nocturnal regime). Prognostic variables, between the lowest level (subscript “a”) and the top of the surface layer (subscript “1”), are computed from the equation:

$$A_a^{\tau+1} = A_a^{\tau-1} + \left(\frac{F_s z_1}{\bar{m} h^2} - \frac{F_s}{\bar{m} h} + \frac{F_1}{\bar{m} h} \right) \times \left[\exp\left(-\frac{\bar{m} h \Delta t}{z_1}\right) - 1 \right] + \frac{F_s \Delta t}{h} \quad (6.32)$$

where the mixing coefficient is defined as

$$\bar{m} = H_1 \left[\rho_a c_{pm} (1 - \varepsilon) \int_{z_1}^h [\theta_{va} - \theta_v(z')] dz' \right]^{-1}, \quad (6.33)$$

A is any prognostic variable, and F is the flux of moisture, momentum, or heat. The entrainment coefficient, ε , is equal to 0.2, and H_1 , is

$$H_1 = \rho_a c_{pm} z_1 (\theta_{va} - \theta_{v_{1.5}})^{\frac{3}{2}} \left(\frac{2g}{27\theta_{va}} \right)^{\frac{1}{2}} \frac{1}{z_1} \left[z_1^{-\frac{1}{3}} - (2z_{1.5})^{-\frac{1}{3}} \right]^{-\frac{3}{2}}. \quad (6.34)$$

The subscript “1.5” refers to the next highest half-sigma level.

The general prognostic equations above the surface layer are defined as:

$$\frac{\partial A_i}{\partial t} = \bar{m} (A_a - A_i) \quad (6.35)$$

where A represents the potential temperature, θ , the water vapor mixing ratio, q_v , or the cloud water mixing ratio, q_c , and

$$\frac{\partial B_i}{\partial t} = w \bar{m} (B_a - B_i) \quad (6.36)$$

where B represents u or v, and $w = 1 - z/h$. Grell et al. (1995) notes that since the top of the mixed layer may not coincide with a model level, the weighting function, w, can result in unrealistic drops in reduced mixing.

6.5 Model Physics Schemes

Model physics are included in the MM5 program in the modeling system and can be changed according to the user's desire. There were two microphysics schemes used in the studies below, and each will be further discussed in respective sections. The Simple Ice scheme is used in the case studies for the purpose of saving memory on the CPU. The model uses explicit equations for cloud water, rainwater, ice and water vapor. The Simple Ice scheme was used to account for the ice phase processes. There is no supercooled water and immediate melting of snow below the freezing level. The Reisner 2 scheme was also chosen, but produced numerous core-dumps due to the extensive computations involved in winter storms. The Kain-Fritsch cumulus parameterization was chosen, as well as the Eta M-Y planetary boundary layer model: (1.5 order TKE closure). This was also switched for Blackadar PBL depending on the simulation (discussed below). Kain-Fritsch cumulus parameterization scheme was used to account for sub-grid scale convection (Kain *et al.*, 1993). The Kain-Fritsch parameterization is complex cloud-mixing scheme that is capable of solving for entrainment or detrainment. The scheme also removes the available buoyant energy in the relaxation time. Updraft and downdraft properties are also predicted. The influence of shear effects on the precipitation efficiency is also considered by the Kain-Fritsch scheme. The Advanced Cloud Radiation Scheme was used for radiation parameterization. The cloud-radiation scheme was used to account for the interaction of shortwave and longwave radiation with clouds and the clear air. The scheme is useful in simulating the atmospheric temperature tendencies. Surface radiation fluxes are also used as a boundary condition for the cloud-radiation scheme. Various land surface models (LSM) were tested including: Noah Model (except for Blackadar PBL), and OSU LSM. This scheme

is capable of resolving diurnal temperature variations that result in a more rapid response from the surface temperature (Dudhia et al. 1996). Real time high resolution (1.1 km) SST data ingestion from NOAA's Coastwatch program was used as the basis for these simulations. The use and manipulation of these files will be discussed in the following chapters.

CHAPTER 7: 24-25 JANUARY 2000 CASE

7.1 Introduction

A comparison based on sea surface temperature (SST) grid resolution is performed in this chapter to investigate air-sea heat exchange and its horizontal gradient, and the processes that contribute to the formation of surface cyclones along the east coast of the United States. The objective of this study is to investigate the role of the Gulf Stream in the development of east coast extratropical cyclones using the 24-25 January 2000 storm. A numerical weather model was employed to perform a control and an experimental simulation of this winter storm. The parameters for the control and experimental simulations were identical with the exception of the SST input data set. The SST data for the initialization of the control simulation were derived from the National Centers for Environmental Prediction (NCEP) 2.5° data. The experimental simulation was initialized with 1.1 km high resolution data obtained from NOAA's Coastwatch program. The differences in these simulations are analyzed to acquire an understanding of the importance that small-scale Gulf Stream features have on extratropical cyclogenesis.

The overall performance of the experimental simulation was better than the control simulation for this major event. The most significant improvements were seen in the forecast deepening rate and track where the lowest sea-level pressure in the experimental simulation was 6 mb lower than the control simulation, and the largest differences in forecast position were more than 150 km closer to the actual track. In the control simulation, the reduced development compared to the experimental simulation may be due to the coarse grid SST representation which fails to capture key thermal gradient features of the Gulf Stream.

Evidence suggests that the high resolution SST data did affect the track by changing the location of the frontal boundaries through enhanced surface-level convergence. It is the enhanced effectiveness of vortex stretching associated with the convergence along this frontal boundary that can explain the tendency for a stronger storm in the experimental simulation. This coastal front, which formed above the tight marine thermal gradient of the Gulf Stream's western boundary, is not seen in the control simulation. Thus, the control simulation's poor forecast may be linked, in part, to the weakly defined Gulf Stream Front during model initialization.

7.2 Background

The southeasterly facing coastline of the Carolinas yields a favorable angle for the perpendicular offshore flow typical of the winds from a cold-air outbreak (Wayland and Raman 1989). These winds further enhance the already large thermal contrast resulting in large marine boundary layer baroclinicity. Studies have shown that pre-storm destabilization may act to significantly increase the likelihood for subsequent rapid cyclogenesis (e.g., Holt and Raman 1990; Kuo et al. 1990; Fantini 1991; Vukovich et al. 1991). This is discussed in greater detail in the preceding chapters.

Within a hundred kilometers offshore of the coast lies the Gulf Stream, which in the fall, winter, and spring months, has a sea surface temperature warmer than that of the near coastal waters. Large horizontal temperature gradients occur during winters off the mid-Atlantic coast because of the presence of the Gulf Stream with a sea surface temperature of 24 to 28°C. Coastal waters have surface temperatures typically in the range of 6 to 9°C during the winter months (Wayland and Raman 1989). During the occurrence of coastal

fronts and cold-air outbreaks, air temperatures generally range from -5 to 5°C, which can result in a large cross-shelf atmospheric thermal gradient.

A CAO occurs when strong northerly winds force cold air southward. Vukovich et al. (1991) observed that the largest values and strongest gradients of total heat flux during a cold-air outbreak offshore to the north and east of Cape Hatteras, NC. This is because the geographical setting allows for very little time and distance for the colder continental air mass to modify before encountering the much warmer waters offshore. This region is highly baroclinic in the Marine Boundary Layer (MBL) especially when the Gulf Stream is closer to the coast. The degree of MBL baroclinicity is dependent on the ratio of the offshore-onshore air temperature difference to the distance of the Gulf Stream Front to the coast. These strong horizontal thermal gradients, when combined with a cold landbreeze, can result in the rapid and intense destabilization of the MBL within the Gulf Stream region thus increasing convection (Cione et al. 1998). The enhanced baroclinic energy and reduced static stability, can result in rapidly deepening winter cyclones (e.g., Bunker 1976; Kocin and Uccellini 1985a,b; Chou et al. 1986; Reed and Albright 1986; Dirks et al. 1988; Raman and Riordan 1988; Holt and Raman 1990; Kuo et al. 1990; Warner et al. 1990; Vukovich et al. 1991; Cione et al. 1993; Cione et al. 1998; Xie et al. 1999).

Cione et al. (1993) show that the pre-storm baroclinicity, which includes the pre-storm Gulf Stream front (GSF) position, sea surface temperatures, and average coastal air temperatures, is correlated to the intensification of coastal cyclones. Results from the Cione et al. (1993) study reveal that both the thermal structure of the continental airmass and the position of the GSF, in relation to land, are linked to the rate of surface cyclonic intensification.

The distance of the GSF from the coast can fluctuate significantly. Lateral meandering of the GSF makes these distances vary, such that at Cape Hatteras, NC, offshore distance to the GSF can vary from 15 to 120 km from the coast, while offshore of Wilmington, NC, the front can vary between 100 and 300 km (Cione et al. 1993). These variations are caused by the lateral or cross shelf meandering of the GSF. Meandering of the Gulf Stream is essentially a manifestation of the down stream propagation of topographic Rossby waves created at the site of a topographic bump or hill-like bottom feature offshore of Charleston, SC located at 32N and 79W; also known as the Charleston "bump" (Brooks and Bane 1978; Pietrafesa et al. 1978; Rooney et al. 1978; Pietrafesa et al. 1985).

The interaction of upper-level potential vorticity anomalies with the lower-level thermal advection can induce cyclogenesis. However, in the Gulf Stream region, it is important to know to what degree these factors promote storm development. The objective of this study is to investigate the role of the Gulf Stream in the development of east coast extratropical cyclones using the 24-25 January 2000 east coast storm.

7.3 Baroclinicity and ASCII

Although it is assumed that baroclinic processes are the single most important factor in the development of cyclones (e.g., Rogers and Bosart 1986; Sanders 1986a), evidence shows that surface heat fluxes and their horizontal gradient, as discussed above, work in conjunction with baroclinicity for the explosive growth of a marine cyclone (e.g., Kuo and Reed 1988; Holt and Raman 1990; Huang and Raman 1990; Kuo and Low-Nam 1990; Cione et al. 1993; Cione et al. 1998; Xie et al. 1999).

The mutual interaction of upper-tropospheric cyclonic disturbances and lower-

tropospheric thermal gradients forms the basis of the Sutcliffe-Petterssen self development paradigm for extratropical cyclones (e.g., Sutcliffe and Forsdyke 1950; Uccellini 1990). From a potential vorticity (PV) perspective, self development can be described as the mutual amplification of counter-propagating thermal waves on the tropopause and lower boundary (Hoskins et al. 1985; Morgan and Nielsen-Gammon 1998). The strength of the interaction is determined not only by the characteristics of the boundary disturbances themselves, but is also related to the static stability of the intervening tropospheric air and to the character and strength of lower-tropospheric, diabatically generated PV maxima (e.g., Davis and Emanuel 1991; Davis et al. 1993; Stoelinga 1996).

The Gulf Stream's influence on the overlying atmosphere is a significant factor in determining the nature of the cyclogenesis process. Cione et al. (1993) show that the pre-storm baroclinicity, which includes the pre-storm GSF, sea surface temperature, and coastal air temperature, has a correlation coefficient of 0.56 to the sea-level intensification rate of coastal cyclones. Results from this study reveal that both the thermal structure of the continental air-mass and the position of the GSF, in relation to land, are linked to the rate of surface cyclonic intensification, and can explain as much as 31% of the storm deepening rate variance.

The Atlantic Surface Cyclone Intensification Index (ASCII) is a forecast index that quantifies the amount of low-level baroclinicity off the coast of the Carolinas during a CAO, and is covered in greater detail in Chapter 5. ASCII is based on the gradient between the coldest 24 hour average air temperature at the coast during a CAO and the temperature of the GSF. The resulting pre-storm baroclinic index (PSBI) is used to forecast the probability that a cyclone in the domain will exhibit rapid cyclogenesis. PSBI values less than $1.0^{\circ}\text{C}/10\text{km}$

indicated that a storm in the domain would be unlikely to undergo explosive development while values greater than $1.7^{\circ}\text{C}/10\text{km}$ indicated that there is a strong chance for rapid cyclogenesis (Cione et al. 1998), providing that an upper-tropospheric disturbance is approaching the area.

7.4 24-25 January 2000 Case Background

Four days prior to the 24 January 2000 storm development, a small coastal low tracked northeast from Cape Hatteras, NC. A high pressure system extended southeastward behind this first coastal low, and strong northwesterly winds advected a cold air mass off the coast of the Carolinas and over the Gulf Stream. The 24-h temperature observations beginning 12Z Jan 20 decreased as much as 15°C in the coastal region between Wilmington, NC (station KILM) and Morehead City, NC (station CLKN7). This offshore flow remained in place through most of Jan 23, after which it slowly dissipated, and set the stage for an intense winter storm that formed off the southeastern coast of the United States on 24 Jan 2000. Figures 7.1a-d show METAR (a french acronym for "aviation routine weather report") and ship / buoy observations overlaid the most recent corresponding GOES8 imagery during the formation and deepening of the coastal storm. Anomalously high SST values can be seen in these readings which will later serve to justify the warm-core filament seen in the SST initialization data set. In Figure 7.1a, valid 06Z Jan 23, a 24°C SST observation can be seen east of Cape Hatteras marked by the green circle. The surface circulation can be seen east of Charleston, SC in Figure 7.1b, valid 00Z Jan 25, as well as a 23°C SST observation (green circle) can be seen south of Cape Hatteras. Although the rotation may not be distinguishable within the cloud cover, the wind observation show a surface wind circulation. The land

temperatures range from 2 to 3°C while the surface air temperatures have increased almost 8°C east of the low's center. In Figure 7.1c, valid 12Z Jan 25, the red circle shows the heavy snow report for RDU, and the green circle highlights a 22°C SST observation that coincides with a 4°C surface air temperature. This is almost a 14°C drop in surface air temperatures in 12 h as the center of circulation approached Cape Hatteras, NC. The wind observations in Figure 7.1c place the low almost due east of Cape Hatteras. Two more regions of 22°C and 24°C SST are seen in Figure 7.1d (green circles), valid 18Z Jan 25, as well as substantial low-level convection resulting from the offshore flow east of South Carolina.

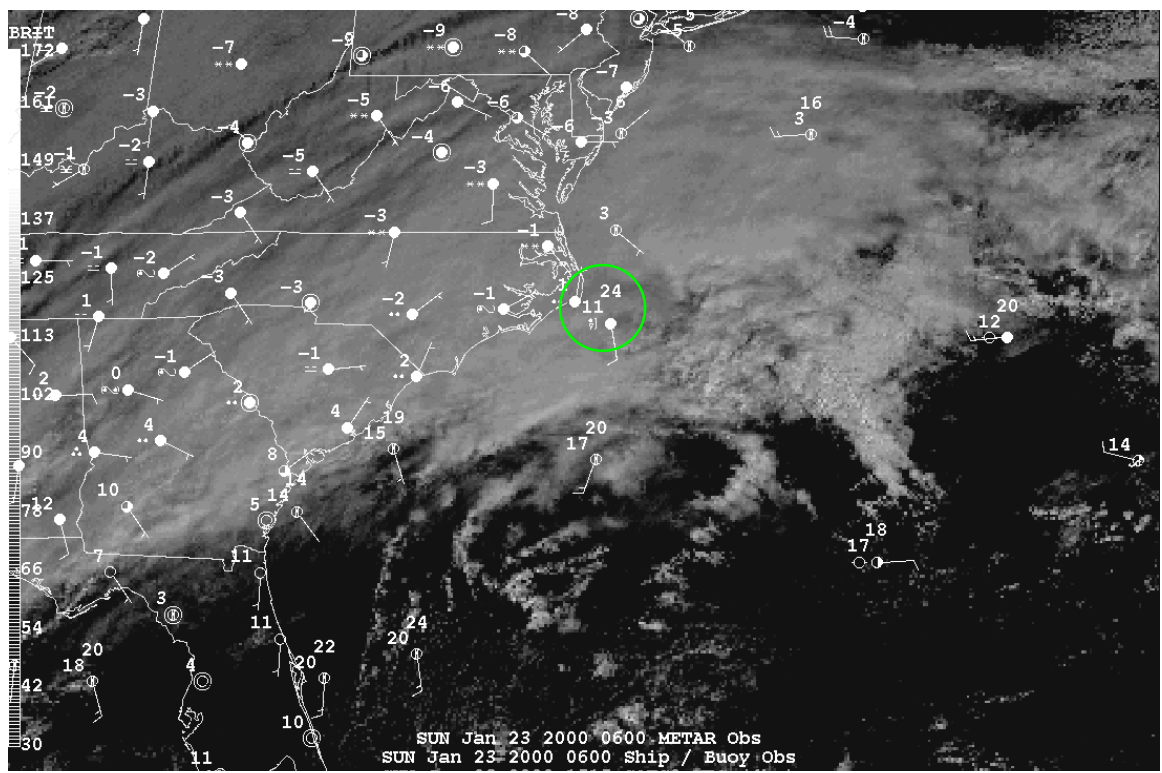


Figure 7.1a Metar obs and Ship/buoy obs (SST is the top value) valid 06Z 23 Jan 2000 overlaid the most recent corresponding GOES8 imagery.

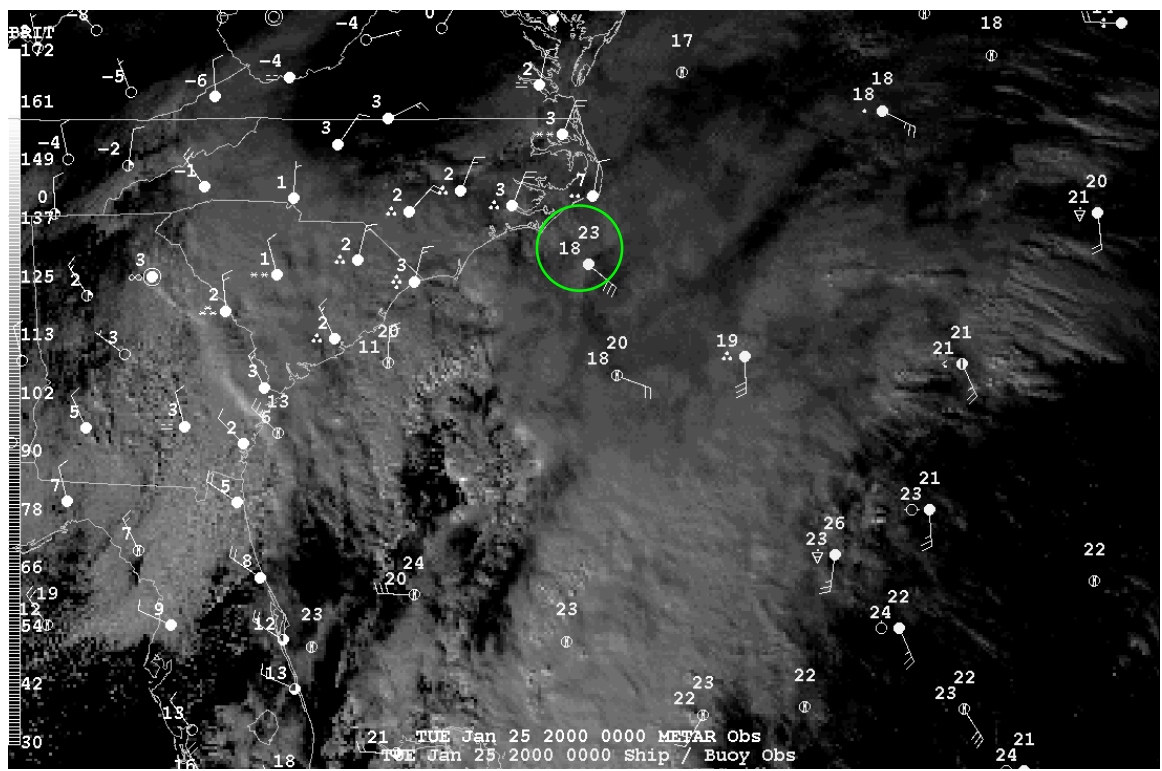


Figure 7.1b Metar obs and Ship/buoy obs (SST is the top value) valid 00Z 25 Jan 2000 overlaid the most recent corresponding GOES8 imagery.

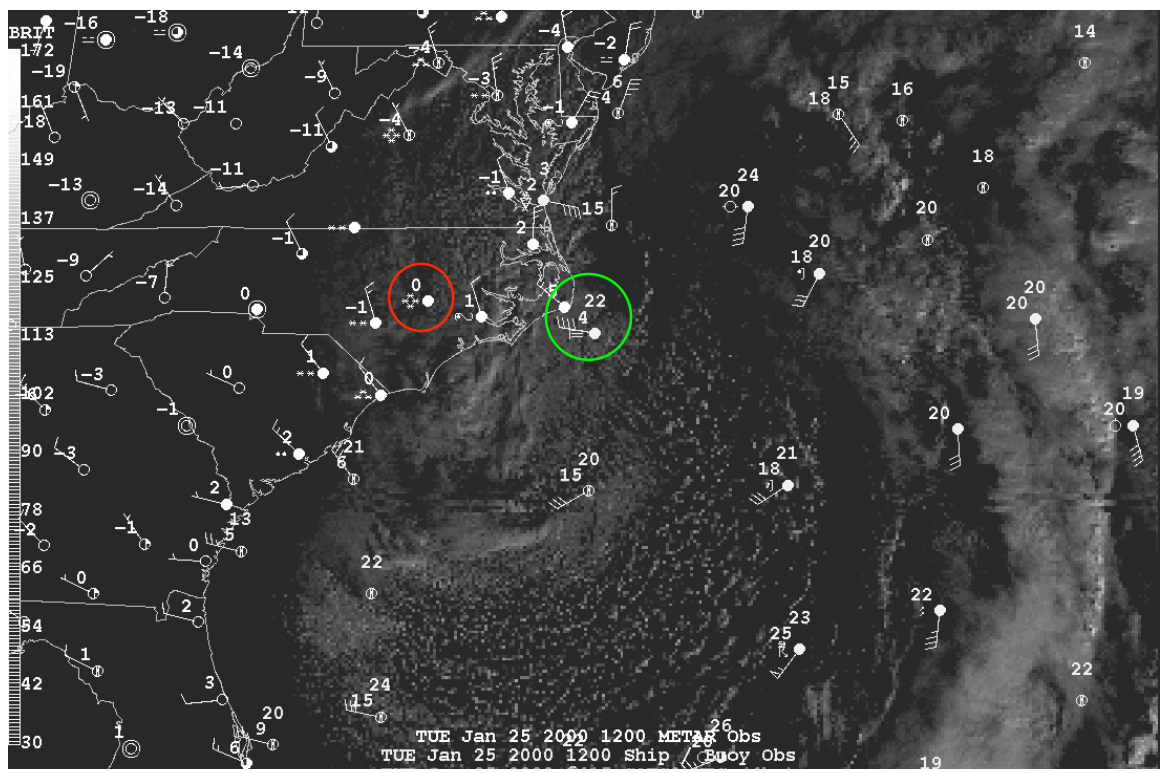


Figure 7.1c Metar obs and Ship/buoy obs (SST is the top value) valid 12Z 25 Jan 2000 overlaid the most recent corresponding GOES8 imagery.

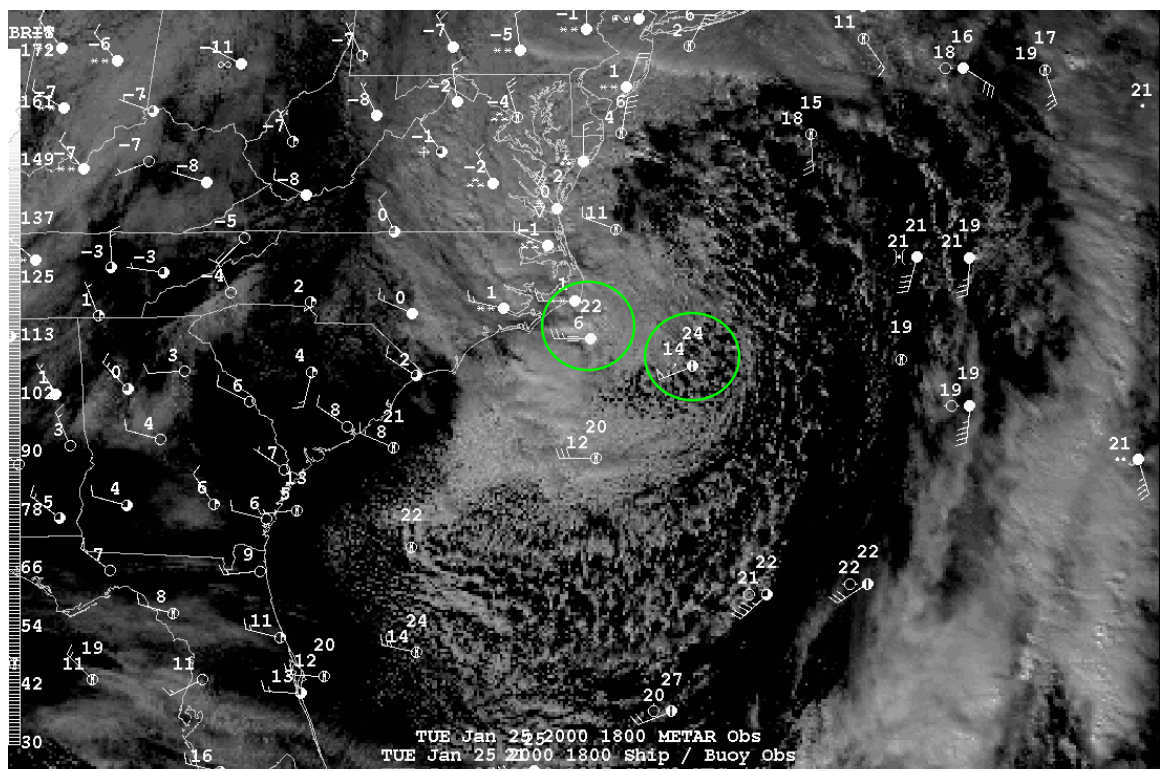


Figure 7.1d Metar obs and Ship/buoy obs (SST is the top value) valid 18Z 25 Jan 2000 overlaid the most recent corresponding GOES8 imagery.

Figure 7.2 plots sea-level pressure (mb, solid lines) and 500-mb geopotential height (dashed lines) valid 12Z 24 Jan (a), 00Z 25 Jan (b), and 12Z 25 Jan (c). The surface low began to form along a stationary coastal front northeast of Florida, and downstream from an upper-level trough on 24 January 2000 (Figure 7.2a). The surface low formed in the northern Gulf of Mexico, and began to track along a stationary coastal front northeast of Florida, and downstream from an upper level trough on 24 January 2000. As it moved over the Gulf Stream from Charleston, SC to Cape Hatteras, NC, the pressure dropped at a rate in excess of 1.3 mb h^{-1} (Figures 7.2b,c).

The closed circulation was located east of South Carolina around 15Z on Jan 24, and moved northeast along the coast following a frontal boundary that set up along the temperature gradient formed by the western boundary of the Gulf Stream. The surface low continued to move north and was located east of New England by 00Z Jan 26. The winter storm brought heavy snowfall from the Carolinas through the New England region. Record snow amounts fell across central North Carolina with the Raleigh-Durham (RDU) airport reporting a snowfall accumulation in excess of 20 inches. Radar imagery (NOWRAD 2 km base reflectivity) captures can be seen in Figures 7.3a,b,c which correspond to the times seen in Figure 7.2. Figure 7.3a, valid 12Z Jan 24 (a), shows two areas of precipitation, one offshore, and another region moving from AL to GA. This second area of precipitation, missed by most operational model's initializations, produced a diabatically generated PV anomaly which was responsible for the enhanced banding seen in Figures 7.3b,c (Brennan and Lackmann 2004). This event broke the previous snowfall record for a single storm and established a new monthly total accumulation record for RDU, as well as several other nearby locations. A snowfall total map can be seen in Figure 7.4.

Prior to the explosive development, the Eta, MRF, and AVN model runs failed to accurately predict not only the track, but the deepening rate and the precipitation amount for the event (e.g., Buizza and Chessa 2002; Zhang et al. 2002; Zupanski et al. 2002). Additional studies have been conducted on this case in an attempt to understand the sources of forecast error (e.g., Tracton and Du 2001; Langland et al. 2002; Zupanski et al. 2002; Jang et al. 2003; Brennan and Lackmann 2004). Most forecasts placed the storm to far to the east by as much as 200 km and called for less than 4 to 6 inches of accumulated snowfall in the central North Carolina region. Although the models listed above showed the development of a nor'easter type storm, the intensity and precipitation were grossly under predicted. During this event, the GSF was less than 50-60 km off the shoreline. As a result, the ASCII index was predicting rapid cyclogenesis. The pre-storm baroclinic index was estimated to be greater than $2^{\circ}\text{C}/10\text{km}$ which corresponds to a forecasted pressure drop of 15 mb/12h. This was not far from the observed 17 mb drop during the 12 hours of greatest deepening.

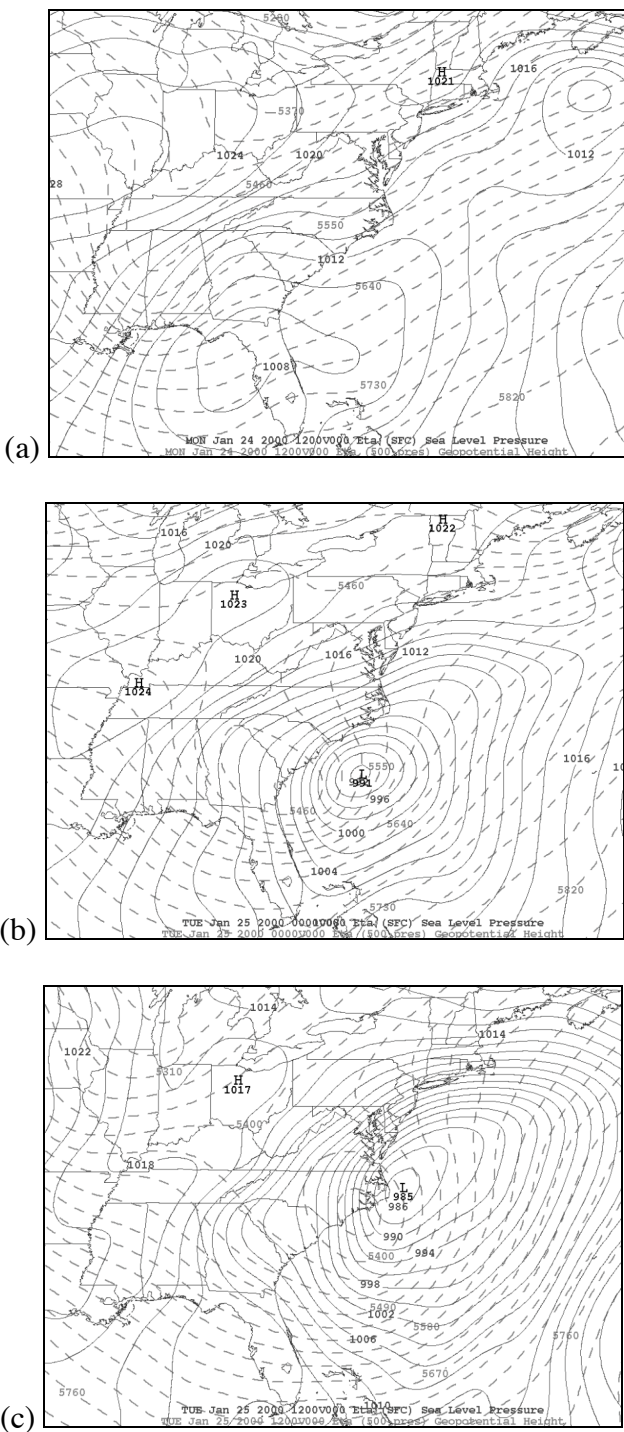


Figure 7.2 Observations of sea-level pressure (mb, solid lines) and 500-mb geopotential height (dashed lines) valid 12Z 24 Jan (a), 00Z 25 Jan (b), and 12Z 25 Jan (c).

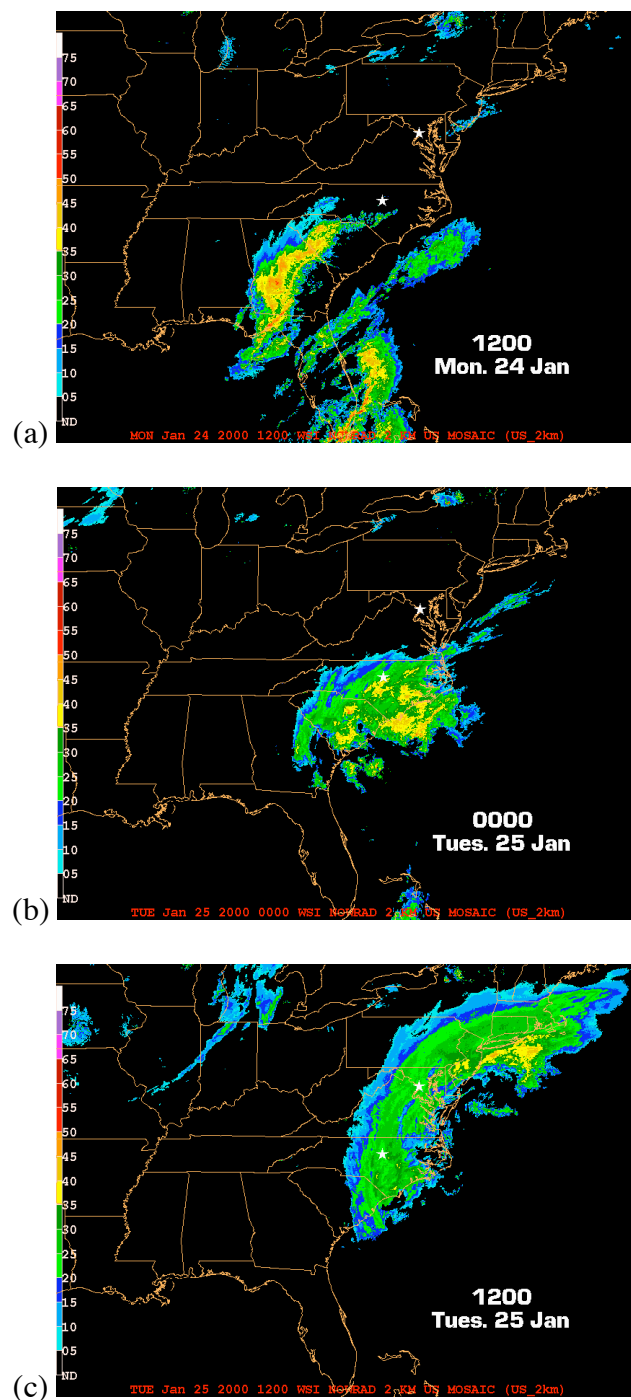


Figure 7.3 NOWRAD 2 km base reflectivity valid 12Z Jan 24 (a), 00Z Jan 25 (b), and 12Z Jan 25 (c).

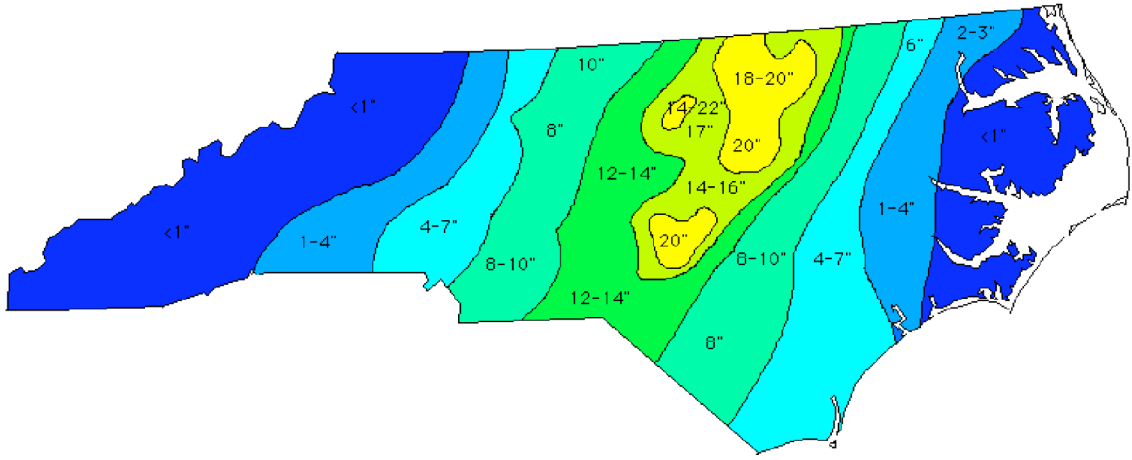


Figure 7.4 North Carolina snowfall totals for the 24-25 January 2000 winter storm (NWS Raleigh, NC).

7.5 Experiment Design

7.5.1 Model background and simulation history

Several versions of MM5.3 were used during this project beginning with v5.2.1 and moving through to the final version 5.3.6. Although some of the changes were minor, other larger changes in PBL schemes and physics schemes were tested. The Mellor-Yamada PBL scheme was the final choice in version 3.6 mainly because it was a required option when running the OSU LSM. Multiple test runs were done on a silicone graphics machine (SGI) using the Blackadar PBL combined with no LSM. This was mainly because Blackadar is not compatible with the OSU LSM. Results from this combination were very similar to the M-Y

PBL and OSU combination. Some studies have found the opposite results (e.g. Pleim and Chang 1992; Mironov et al. 1999; Bright and Mullen 2002); however, these studies were conducted over regions of dense vegetation. The combinations used in these simulations found minimal impact because of the lack of vegetation during January and the ground cover initialization which included large areas of snow cover that blocked the soil moisture fluxes. These finding were in agreement with sensitivity studies conducted by Zhang et al. (2003).

Several pitfalls were encountered when switching from a SGI to a LINUX environment. One of which was the inability to process Blackadar with the 2.0 version of the Portland Group complier. This was attempted on multiple processors and a single processor. After months of changing the dreaded "-byteswapio" flag back and forth, the decision was made to stick with a single 3 GHz processor LINUX machine, and run the simulations "in house" (State Climate Office of North Carolina). This environment, combined with the new release of the Portland Group compiler, proved to be very stable. However, with only 2 Gigabytes of RAM, the size and resolution of the domain were very limited. A final run which tested the Kain-Fritsch 2 cumulus parameterization proved to be an insignificant change, so the original KF1 was the ultimate choice.

Several simulations were done using the Resiner microphysics scheme, and were very promising. The QPF was much more in line with the observations. However, when switching to the "in house" LINUX machine, this option proved to be far too memory intensive. Runs (9 attempts in all) would time-out around the 42 h mark in the simulation (initialized 00Z 24 Jan 2000). This happened to correspond to the maximum intensification point in the surface low pressure, as well as the QPF, and resulted in one-too-many calculations followed by a "core dump". After several attempts, the choice was made to

move back to the Simple Ice scheme as this was the most stable. The bottom line is as long as all the parameters (not including SST) were the same for both the control and experimental simulations, it really didn't matter which parameters were chosen.

7.5.2 Model description

The control and experimental simulations were done using NCAR/PSU MM5 version 3.6 (e.g., Dudhia 1993; Grell et al. 1994; Haagenson et al. 1994). A single 10 km domain was initialized at 00Z 24 January 2000 with NCEP's operational analysis from the Eta-212 (40 km) grid. In both simulations, the domain has 38 vertical σ levels between 1000 hPa and 100 hPa with 18 of the levels below the 850 hPa level. Numerous sigma levels are located in the lowest 1.5 km of the atmosphere because fluxes of heat, moisture, and momentum occur in the planetary boundary layer. The model forecast was run to 48 hours (00Z Jan 26).

The Kain-Fritsch cumulus parameterization was chosen, as well as the Eta M-Y planetary boundary layer model: (1.5 order TKE closure). The Kain-Fritsch cumulus parameterization scheme was used to account for sub-grid scale convection (Kain et al. 1993). The advanced cloud radiation scheme was used for radiation parameterization, and the simple ice scheme was used for cloud physics. The model uses explicit equations for cloud water, rain water, ice and water vapor. There is no supercooled water and immediate melting of snow below the freezing level.

The Oregon State University (OSU) land surface model (LSM) was chosen for both simulations. However, previous testing of various land surface models showed no significant differences. Sensitivity studies suggest that snow cover and the lack of vegetation during the

winter months reduce the LSM's effect on the atmospheric surface layer (Chen and Dudhia 2001).

The experimental simulation was conducted using the same MM5 version with the identical domain as the control. The model was also initialized at 00Z 24 January 2000 with NCEP's operational analysis from the Eta-212 grid, and used the same land surface, PBL, microphysics, and cumulus parameterization schemes. The model was integrated for 48 hours just as in the previous control simulation. Unlike the control simulation's SST data shown in Figure 7.5a, high resolution SST data were prescribed for the experimental simulation (Figure 7.5b). The improvement to the SST data was the only difference between the control and experimental simulations.

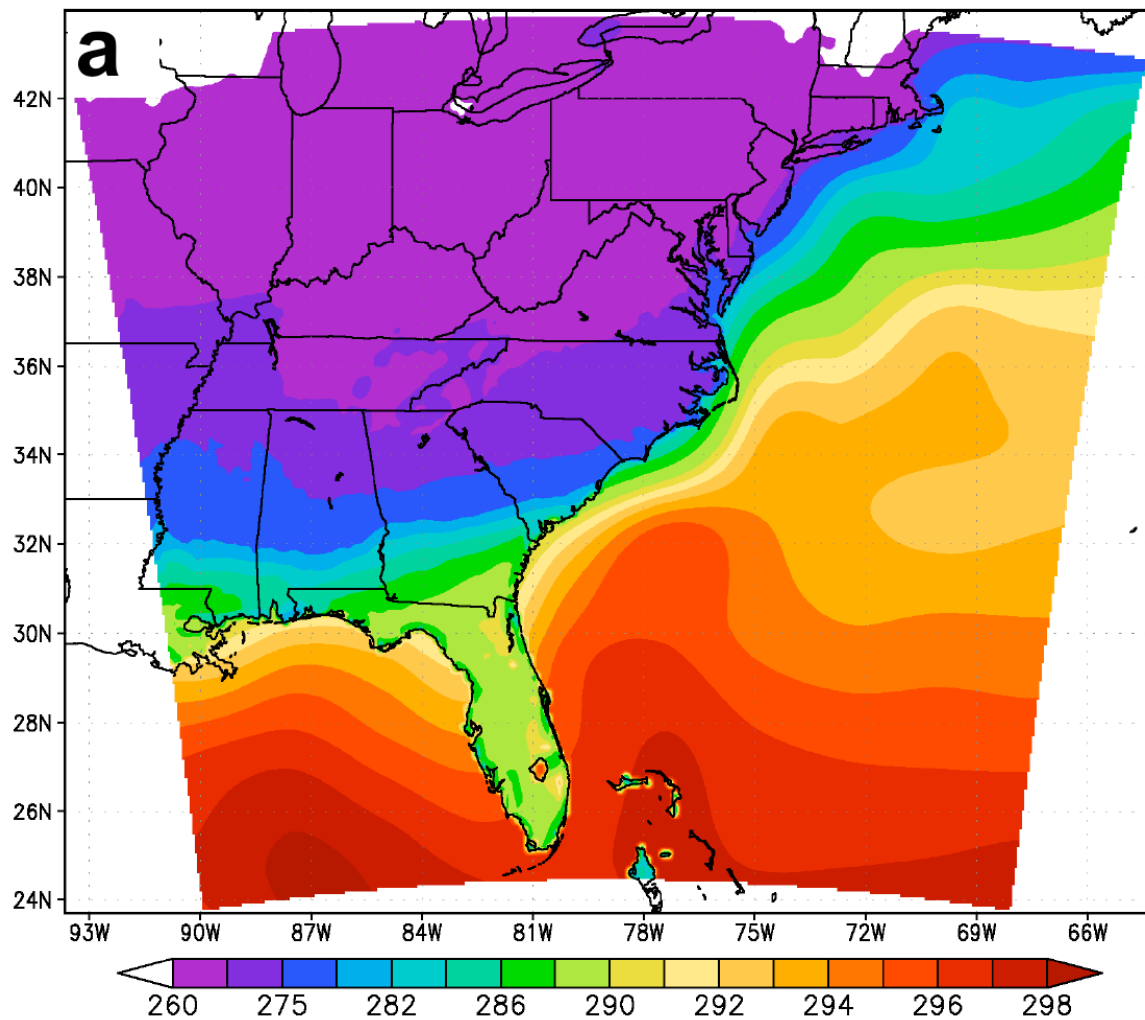


Figure 7.5a The model's domain showing sea surface temperatures regridded to 10 km for the control simulation using NCEP's 2.5° resolution data.

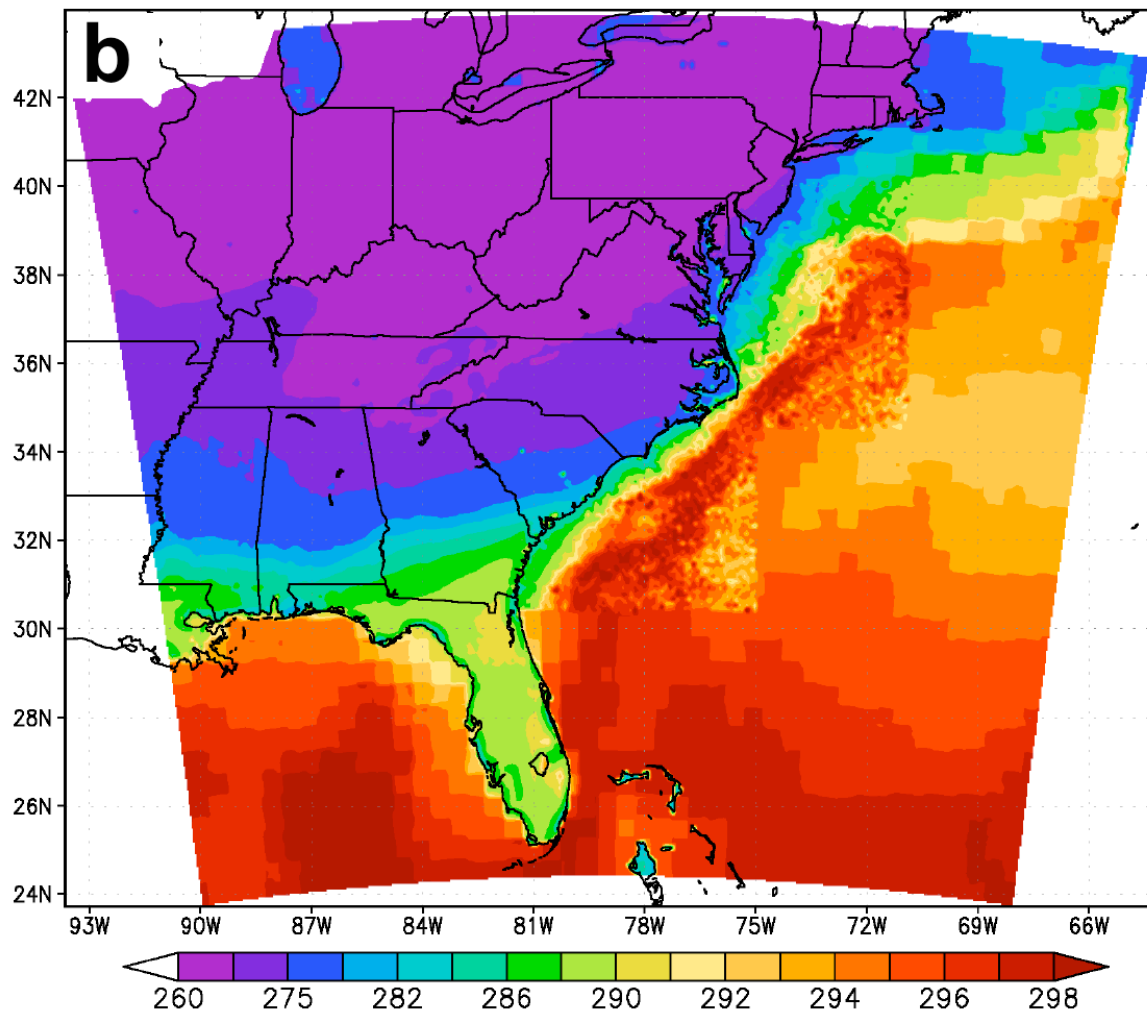


Figure 7.5b The model's domain showing sea surface temperatures regridded to 10 km for the experimental simulation using 1.1 km grid spacing data.

7.5.3 SST data pre-processing methods

The evolution of the SST ingestion method into MM5's REGRID subroutine began with a very crude method of converting the GRIB SST file into a matrix in IDL. Once the matrix was formed, the chosen SST values were typed in by hand. It is a very complex task to selectively map over parts of the Gulf Stream because, if the data set is based on a lat / lon grid, there will be gaps of data missing near the coastline because of the irregular southwest to northeast shape. Obviously, if the coastline was a smooth line running north to south, this would be a simple task.

The first simulation, with the manually entered SST data proved somewhat successful, so the choice was made to experiment with coding the data import methods. The high resolution data acquired from Coastwatch was in a different format than what MM5's REGRID could read. The first task was to convert the data to a Lambert conformal grid. Then write over the SST GRIB file data for the corresponding grid points. It should go without saying, that in this step, the SST GRIB file's matrix must be larger than the high resolution data to be mapped over. Otherwise, it will extend beyond the domain size and REGRID will not run. Once this method was running smooth, several simulations were conducted.

There was however, one large problem: the high resolution data was corrupted with clouds. Inevitably, when looking for SST data preceding a winter storm, there will be low-level convection over the Gulf Stream. This is the whole premise behind the "pre-storm conditioning period" discussed in Chapter 5. The MM5 program equations were reading the numerical values for cloud tops as a very warm SST value. In the SST data set, beyond the limits of realistic SST values, the corresponding numbers for very warm and very cold were

the same. Thus, MM5 would default to values exceeding 40°C causing unrealistic jumps in sensible heat flux and vertical motion. To fix this problem, several various cloud filters were devised. The first version was FORTRAN code run in IDL, but due to the convenience of MATLAB, the code was switched over to C. The general logic behind the filter is to set a particular upper limit for a realistic SST value (e.g. 28°C for the upper GSF) in the region of concern. All values exceeding this limit would be flagged. Then, all the flagged values would be interpolated based on the nearest non-flagged values on all sides. For example: the SST grid point which needs to be calculated can be defined as $A_{(i,j)}$, where i and j are the coordinates of A's matrix location. Two values for $A_{(0,0)}$ must be calculated, one in the vertical axis ($Y_{(0,0)}$), and one in the horizontal axis ($X_{(0,0)}$). By choosing points on either side of the flagged value and averaging them so that $X_{(0,0)} = (X_{(-1,0)} + X_{(1,0)}) / 2$, and $Y_{(0,0)} = (Y_{(0,-1)} + Y_{(0,1)}) / 2$, a value for $A_{(0,0)}$ can be calculated using the equation: $A_{(i,j)} = (X_{(i,j)} + Y_{(i,j)}) / 2$. If the nearest $i, j = \pm 1$ value is also flagged, then the $i, j = n \pm 1$ is applied until a non-flagged value is found, and the averaging loops back to the $A_{(0,0)}$ point.

To find a quality data set where the interpolating could be kept to a minimum, manual searches were done looking at imagery starting with the most recent passes. After a cloud free data set was constructed, the matrix was fed into REGRID by changing the script that would normally call the SST GRIB file. This was the method that proved most useful for this experiment.

Since this experiments completion, the code has been rewritten once again in PERL, and is fully automated to download, filter, and run the simulation. However, at the time this was written, the NESTDOWN program has not been configured to regrid the new SST matrix for a nested domain model. The NESTDOWN code will have to be rewritten to

accept the matrix. This is why all the simulations used in this experiment are a single domain.

7.5.4 SST ingestion for the 24-25 January 2000 case

To create the experimental SST grid file, the file used to initialize the control simulation (Figure 7.5a), was combined with the Eta-212 SST and the new 1.1 km high resolution data. The new SST data were derived from digital images acquired by the Advanced Very High Resolution Radiometer (AVHRR) carried onboard the NOAA-12 and NOAA-14 polar orbiting satellites. First, a single pass 1.1 km resolution data set was found by looking at imagery prior to the cold-air outbreak with as little cloud cover as possible. The chosen imagery was from 22 January 2000, less than 2 days prior to the start of the simulation. This was soon enough to reveal the dominant features of the Gulf Stream, but prior to the increase in cloud cover. This image was less than 10% corrupted with clouds. To fix this problem of cloud cover, an interpolation routine was used to plot grid points based on the closest non-flagged values on all four sides. This was done for all the cloud fringe data as well.

Once the cloud free SST data set was constructed, it was mapped over the corresponding grid points in the Eta-212 SST data set, and then mapped over the Control run's NCEP SST data. The final SST file used to initialize the experimental simulation is

shown in Figure 7.5b¹. The mapping covered the zone extending beyond the southern edge of the Gulf Stream to include most of the region containing the storm track, and also beyond the northern edge of the Gulf Stream to include GSF features. Ship and buoy observations were compared against the imagery in the data set to validate the SST off the southeast coast of NC. Figure 7.5c shows observations of SST for 06Z 23 Jan 2000. Large SST values of 24°C east of Cape Hatteras, NC, and 23°C southeast of Frisco, NC were recorded, and thus validate the warm-core filament seen in the imagery of Figure 7.5b.

¹ This mapping process involved multiple 512x512 matrices, the eastern boundaries of which are distinguishable in Figure 7.5b. The raw data for one of the matrices is also seen in Figure 7.5c.

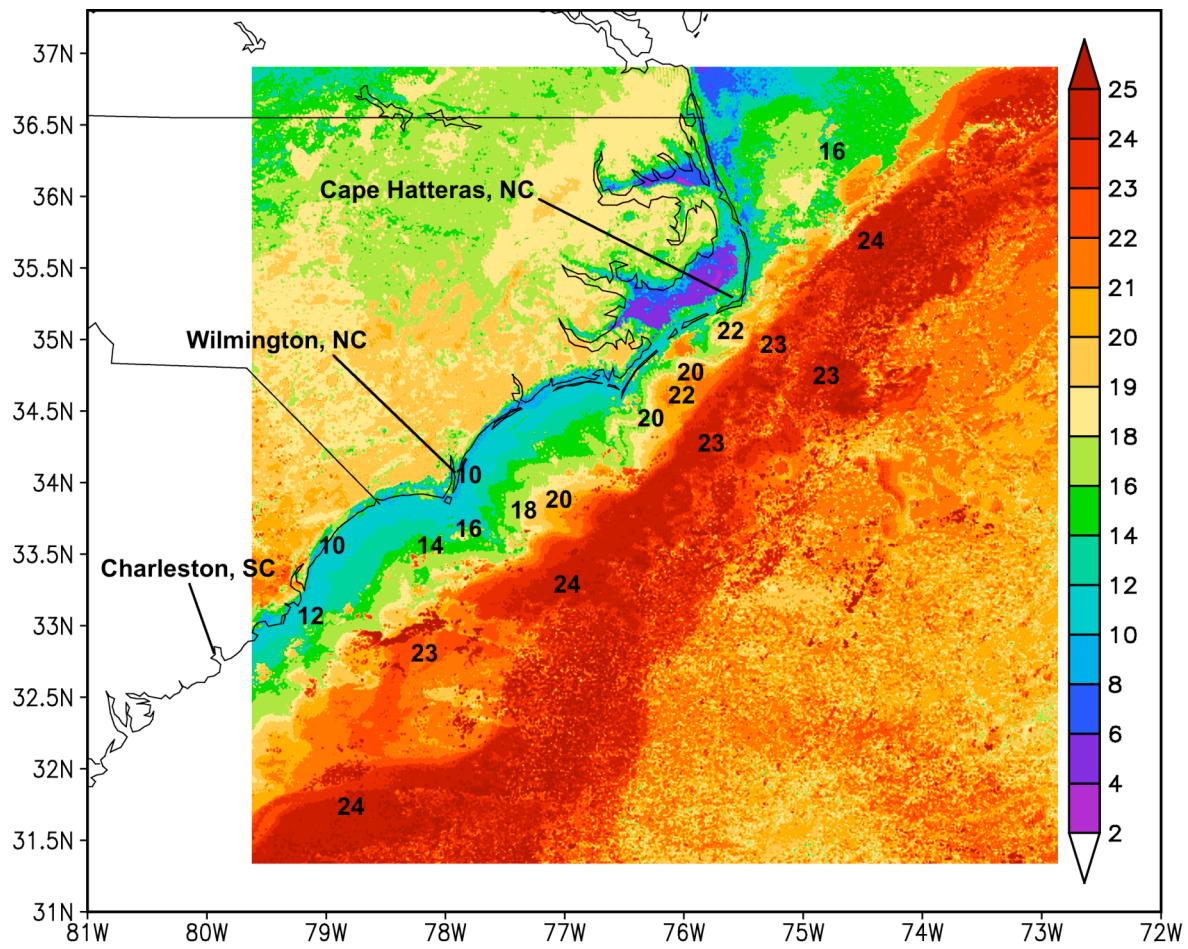


Figure 7.5c Ship and buoy observations of SST valid 23 Jan 2000 overlaid the post-cloud-filtered 1.1 km raw SST data valid 22 Jan 2000 (°C).

7.6 Results

The results discussed below include the change in track and intensity for both the control and the experimental simulations in response to the respective SST gradients associated with the Gulf Stream. The tracks and sea-level pressures of the experimental simulation (dashed), control simulation (dotted), and observations² (solid) are shown in Figure 7.6. Corresponding positions of each storm are marked with the respective times. The sea-level pressures at those times are listed in a table within Figure 7.6. In both simulations, the sea-level pressure had no significant variation from the observations until 21Z Jan 24. After 03Z Jan 25, the motion, or speed of the center of the low in the experimental simulation was faster and closer to the observed position.

The first major pressure differences between the simulations begin around 06Z Jan 25. Three hours later at 09Z Jan 25, the experimental simulation's sea-level pressure is 2 mb lower than the control simulation. At the time when the 3-mb pressure drop begins, the experimental simulation is tracking the center of the low pressure system closer to the GSF, located at 35N, 75.5W comparing Figure 7.6 to Figure 7.5b. However, in the control simulation, the low is not accelerating at the same rate, nor does it experience the abrupt pressure decrease. The lateral position of the storm in the experimental simulation was to the west of the control simulation, and closer to the observed track. At the point when the storm is passing east of Cape Hatteras, NC from 09Z to 16Z Jan 25, the control simulation's position of the center of circulation is about 100 km east of that in the experimental

² The surface analysis was performed by the staff at the National Weather Service Weather Forecast Office, Raleigh, NC (NWS WFO RAH).

simulation. The sea-level pressure for the experimental simulation at 16Z Jan 25 is 982 mb. This is 6 mb lower than that in the control simulation, and 4 mb higher than the analyzed pressure of 978 mb. By 16Z Jan 25, the experimental simulation's position, located 37.5N, 74W, is within 25 km of the observed low pressure's position. However, the control simulation begins to lag the forward speed of both the experimental simulation and the observed storm. Once the tracks progress beyond 37N, the control simulation veers further to the east. During this time, the experimental simulation follows a track much closer to that of the observed storm. By 23Z Jan 25, the control simulation's central low pressure is 150 km southeast of the experimental's center, located 39N, 72W, which is only about 50 km south of the observed low, and following a similar track.

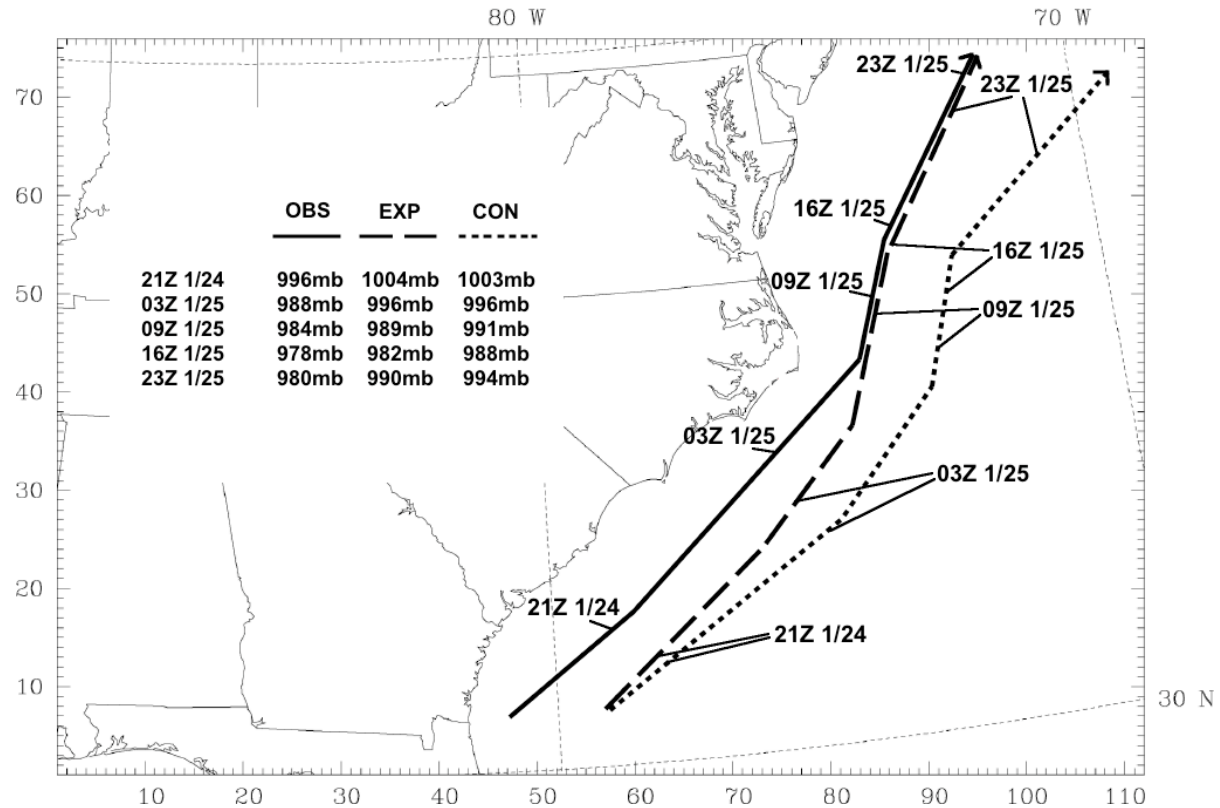


Figure 7.6. Tracks for 24-25 January 2000 winter storm. The solid line is the observed track (surface analysis performed by staff at the NWS WFO RAH), dashed is the experimental simulation, and the dotted line is the control simulation. Both simulations were initialized at 00Z Jan 24. Various positions of the storms are marked on the tracks with the corresponding times. Sea-level pressures are shown in the table inset for the respective times.

Since the western edge of the GSF is not adequately resolved in the control simulation, there is a lack of surface level convergence in the region above where the GSF would be located. Plots of 10-m wind vectors and 2-m temperatures show typical convergence extending off the northeast quadrant of the low pressure system in both simulations. Six hours after initialization (06Z Jan 24) there are minimal differences in the wind field and some evidence of 2-m temperature influence (Figures 7.7a,b). The largest temperature differences are over the water where the SST was changed. Figures 7.8a and 7.8b, valid 12Z Jan 24 for control and experimental simulations respectively, show a noticeable 2 to 4°C difference in the 2-m temperatures primarily north and east of Cape Hatteras around 37N, 72W. A line of convergence along a frontal boundary extending off the northeast quadrant of a central area of low pressure located 32.5N, 76.5W, or about 200 km east-southeast of Charleston, SC is seen in both simulations. At this time, the differences in 10-m wind vectors are negligible. However, a noticeable difference in the 2-m air temperatures can be seen in the region located 35N, 74W to 38N, 69W (circled) where the experimental simulation, shown in Figure 7.8b, has values averaging 4°C higher than the control simulation (Figure 7.8a). Since the convergence is following the 293 K isotherm in both simulations, there is minimal difference in the front's position. This is likely due to the fact that it is just 12 h into both simulations which were initialized with the same atmospheric data.

The 10-m wind vectors and 2-m temperatures, valid 21Z Jan 24, are shown in Figure 7.9. More significant differences in the 2-m temperature fields can be seen between the control simulation (Figure 7.9a), and the experimental simulation (Figure 7.9b). The simulated 10-m air temperatures in the experimental simulation continues to exceed that in

the control by about 4°C in the same location (circled) 35N, 74W to 38N, 69W. However, this region (circled) has extended farther to the south in the experimental simulation (Figure 7.9b) where values are actually 2-3°C cooler than in the control simulation. The previous region of convergence from Figure 7.8, beginning at 33N, 75W and extending northeast to 36N, 70W, is still seen in the control simulation of Figure 7.9a (arrow), but has shifted southeast towards 32N, 72W in the experimental simulation (Figure 7.9b, arrow "A"). The surface circulation at 31N, 76W is still evident in both simulations, as well as a new area of convergence (arrow "B") in the experimental simulation, located along the 291 K isotherm, beginning at 32N, 77W (Figure 7.9b) along a rapidly forming coastal front. This coastal front, which is more pronounced in the experimental simulation, spans the entire length of the Gulf Stream's western boundary. Slightly stronger winds, 2 m/s greater than the control, west of the coastal front in the experimental simulation seem to be driving the area of cooler air temperatures further south. The difference in 2-m temperatures below the region of the coastal front in the experimental simulation is more than 8°C greater in the experimental compared to the control simulation.

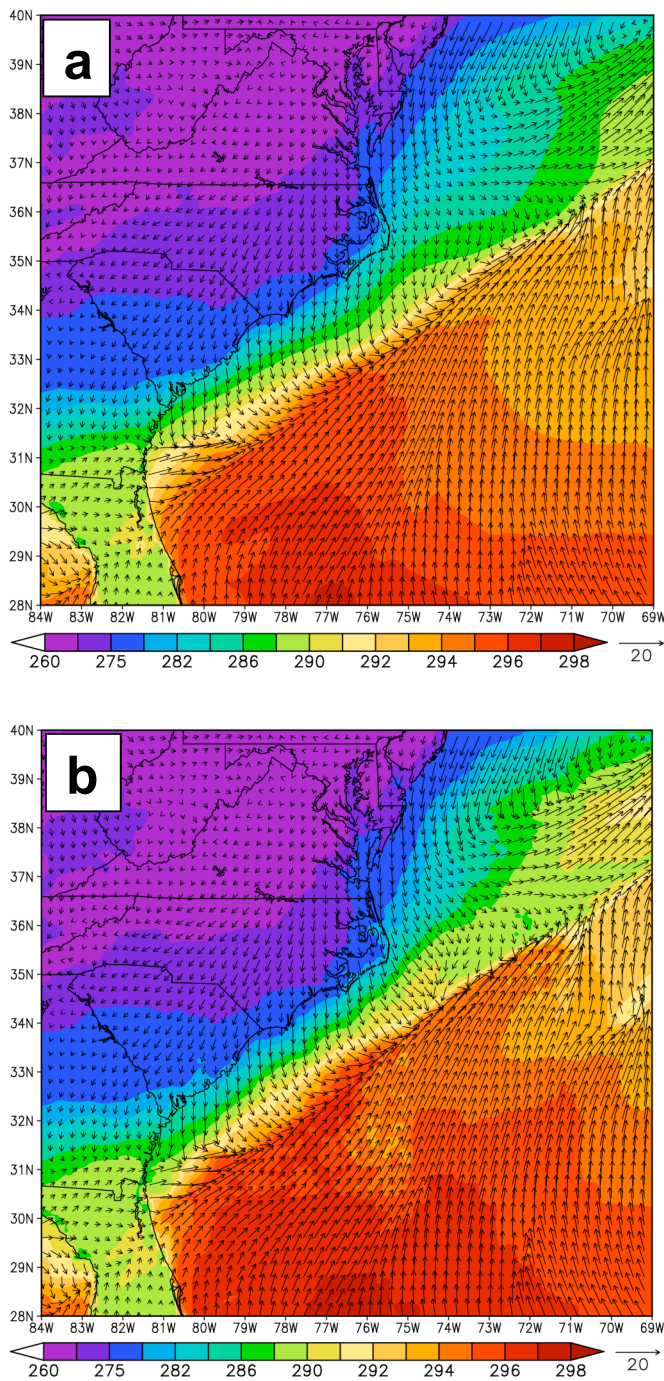


Figure 7.7 Plots of 2-m temperatures (K) and 10-m winds vectors (m/s) for (a) the control simulation and (b) the experimental simulation valid 6Z 24 Jan (6h after initialization).

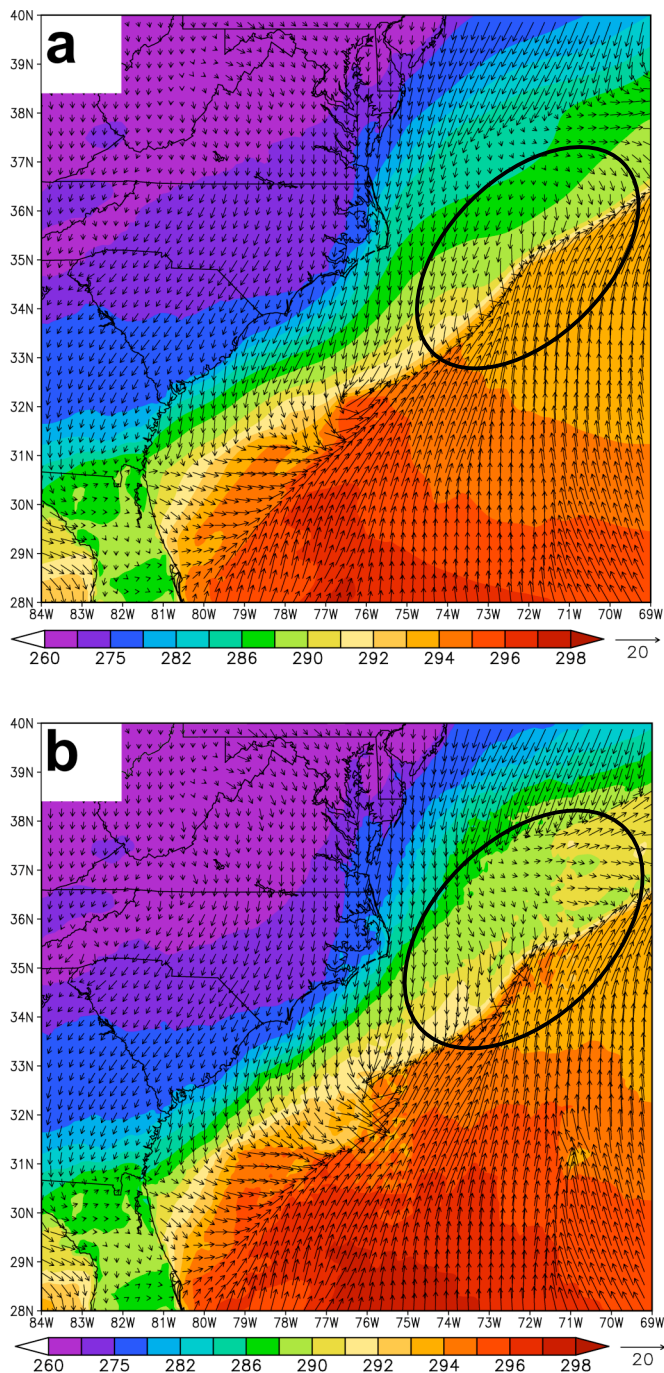


Figure 7.8 Plots of 2-m temperatures (K) and 10-m wind vectors (ms^{-1}) for (a) the control simulation and (b) the experimental simulation valid 12Z Jan 24 (12 h after initialization). The circle indicates regions to compare features.

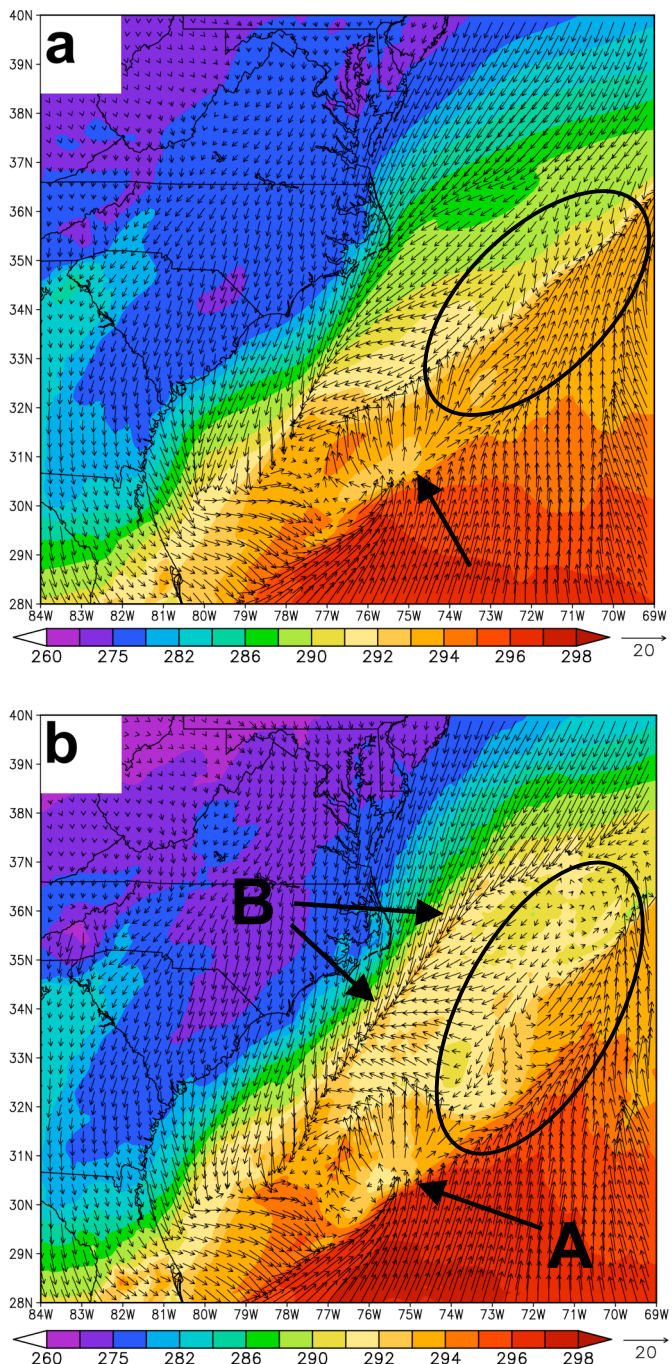


Figure 7.9 Plots of 2-m temperatures (K) and 10-m wind vectors (ms^{-1}) for (a) the control simulation and (b) the experimental simulation valid 21Z Jan 24 (21 h after initialization). The circle indicates regions to compare features.

Plots of convergence at the 10-m wind level (Figure 7.10) have values of $2 \times 10^{-4} \text{ s}^{-1}$ extending off the northeast quadrant of the low pressure system in both simulations located at 36.5N, 73W. Although, in the experimental simulation, the convergence extends much further along the coast above the GSF region, particularly between 18Z and 24Z. Figures 7.10a,b, valid 06Z Jan 24, show minor differences (less than $1 \times 10^{-4} \text{ s}^{-1}$) which are likely due to the initialization conditions, since the SST has had minimal time to influence the lower atmosphere. The 10-m convergence, valid 00Z Jan 25, is shown in Figure 7.11. Elevated values greater than $4 \times 10^{-4} \text{ s}^{-1}$ are seen extending off the northeast quadrant of the low pressure system in both simulations located at 32N, 77W. The convergence in the control simulation (Figure 7.11a) is much shorter and less defined as compared to the experimental simulation. The control simulation has maximum values reaching $6 \times 10^{-4} \text{ s}^{-1}$ in the region of 32N, 77W near the vicinity of the low-level circulation. The surface level convergence for the experimental simulation is shown in Figure 7.11b, where maximum values of $9 \times 10^{-4} \text{ s}^{-1}$ parallel the coastline for a greater distance along the thermal gradient of the GSF from 31.5N, 77.2W to 38N, 71.5W. This region, which corresponds to the location of the coastal front, is verified by the 10-m wind field shown in Figure 7.9b. The convergence in the region of the low-level circulation located at 32N, 77W shares the same position and value as the control simulation. However, the maximum value of $9 \times 10^{-4} \text{ s}^{-1}$ in the experimental simulation located 320 km north of the low-level circulation at 35.5N, 75.4W, corresponds to a warm core surface filament seen in Figure 7.5b and 7.5c. The coastal front is even more evident in the 10-m convergence difference field (Figure 7.11c) of the experimental minus the control simulation where the values of convergence in the experimental simulation exceed the control simulation by $4 \times 10^{-4} \text{ s}^{-1}$ along the frontal boundary.

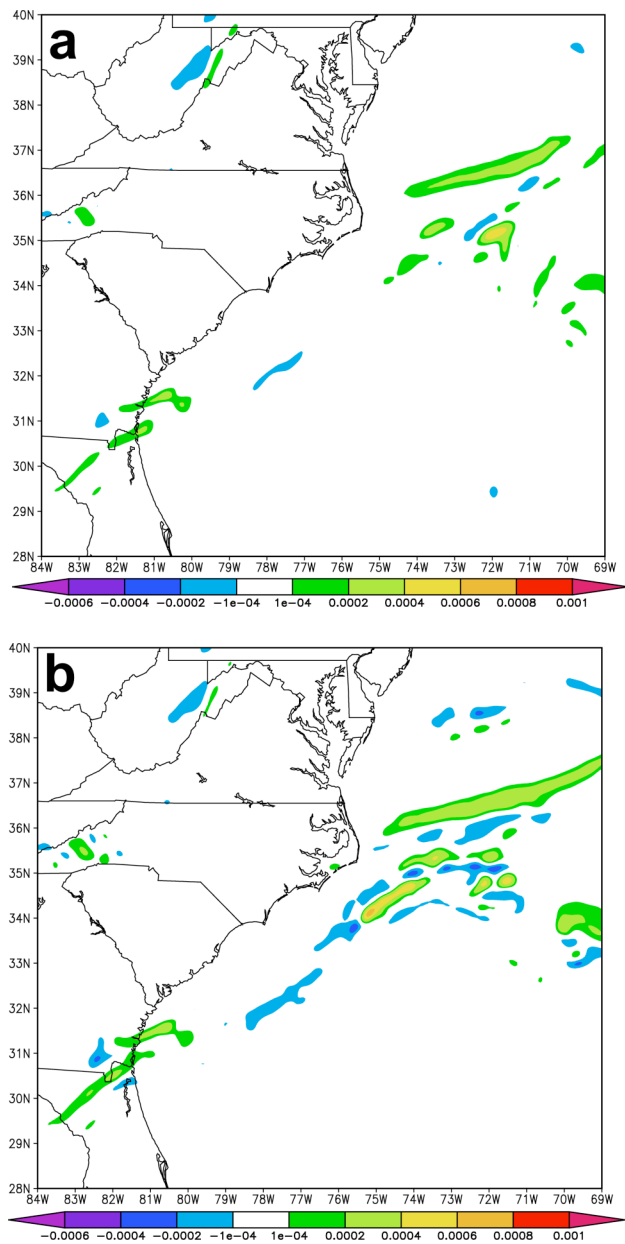


Figure 7.10 Plots of 10-m convergence (s^{-1}) for (a) the control simulation and (b) the experimental simulation valid 6Z 24 Jan (6h after initialization).

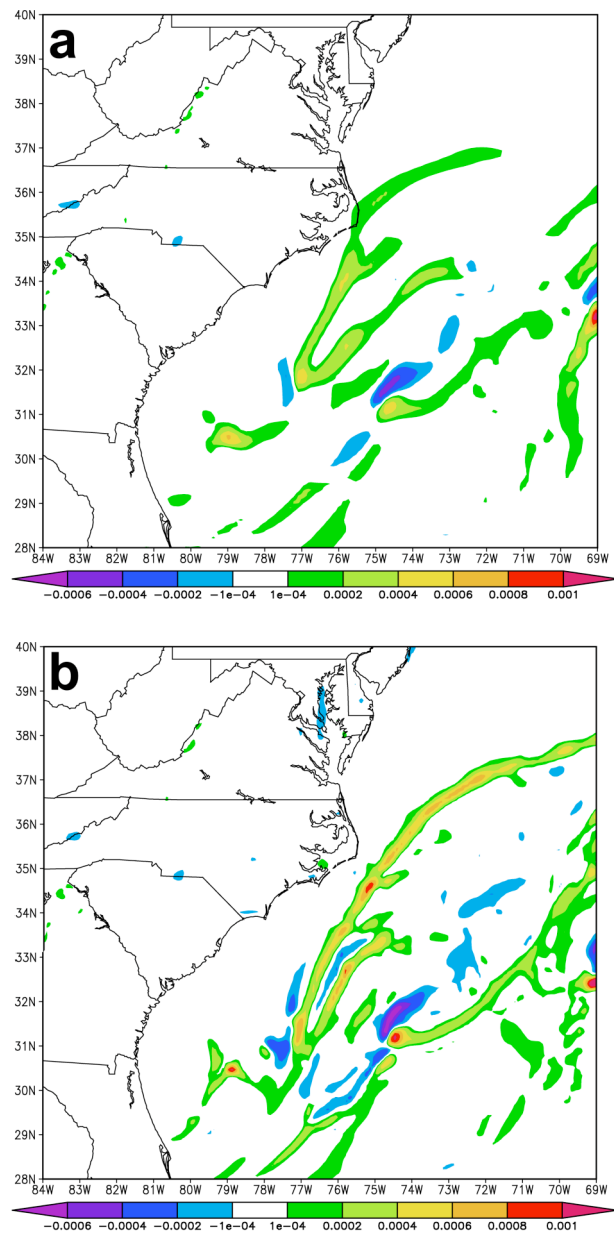


Figure 7.11 Plots of 10-m convergence (s^{-1}) valid 00Z Jan 25 (24 h after initialization) for the control simulation (a), the experimental simulation (b).

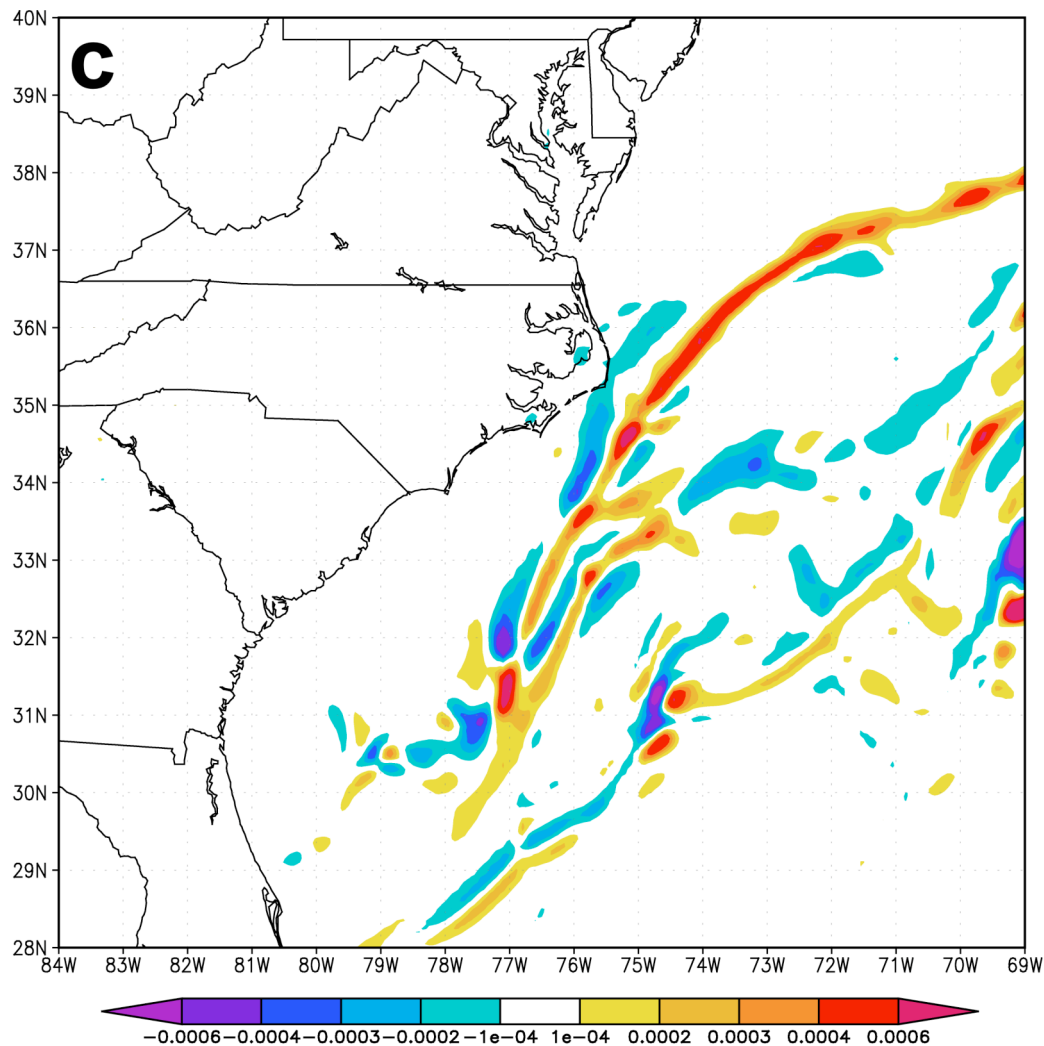


Figure 7.11c Plots of 10-m convergence (s^{-1}) valid 00Z Jan 25 (24 h after initialization) for the experimental simulation minus the control simulation difference field (c).

The largest values of sensible heat flux near the center of circulation in the control simulation never exceed 200 Wm^{-2} . However, in the experimental simulation, values are in excess of 500 Wm^{-2} . This is partly because of the lack of storm development, but more a factor of position and weak SST data. In both simulations, large values can be seen to the southwest side of the circulation in the wake of the surface low. This is typical of the advection of cold offshore winds, but is not considered a direct factor in storm intensification (e.g., Nuss and Anthes 1987, and Kuo, Reed, and Low-Nam 1990).

Sensible heat flux valid 12Z Jan 24 for the control simulation (Figure 7.12a) show regions of 100 Wm^{-2} to 200 Wm^{-2} off the southeast coast of the Carolinas and east of the Delaware region. These same regions show increased sensible heat flux in the experimental simulation valid 12Z Jan 24 (Figure 7.12b), however the values are almost twice that of the control. In addition to those shared regions around $33\text{N}, 79\text{W}$, and $40\text{N}, 72\text{W}$, the experimental simulation shows the zone of 200 Wm^{-2} off the Carolinas extending well northeast of Cape Hatteras to $36\text{N}, 74.5\text{W}$.

Surface sensible heat flux in Wm^{-2} valid 00Z Jan 25 for the control simulation is shown in Figure 7.13a. There is a large region with heat flux values of greater than 250 Wm^{-2} located off the southeast coast of the Carolinas at $33\text{N}, 79\text{W}$. The sensible heat flux values in the experimental simulation, shown in Figure 7.13b, valid 00Z Jan 25, are more than three times that of the control simulation (Figure 7.13a) located off the Carolinas at $33.5\text{N}, 76.5\text{W}$ extending well northeast of Cape Hatteras, NC to $36\text{N}, 74.5\text{W}$. It is evident that the well defined GSF of the experimental simulation is influencing the surface-level dynamics. Values of sensible heat flux from 300 to 400 Wm^{-2} can be seen in Figure 7.13b along the western Gulf Stream boundary parallel to the coastline. The largest difference between the

experimental and control simulation of 325 Wm^{-2} (Figure 7.13c) is located at about 100 km south of Cape Hatteras, NC at 34N, 75.5W. Sea-level pressure contours shown in Figure 7.13b (particularly 1004 to 1008 mb) also align with regions of elevated sensible heat flux along the GSF due to the increased winds extending northeast of Cape Hatteras, NC.

By 12Z Jan 25 (36 h after initialization), the fully developed storm is following a track northeast of Cape Hatteras, NC shown in Figure 7.14. In both simulations elevated sensible heat flux values greater than 325 Wm^{-2} can be seen off South Carolina (33N, 78W) as a result of the cold dry air advecting over the warm water (Figure 7.14a and 7.14b). In the region slightly northeast of this, located at 33.5N, 78W, the experimental simulation's values exceed those in the control simulation by 50 Wm^{-2} to 100 Wm^{-2} (Figure 7.14c). However, north and west of the preceding edge of the center of circulation located at 38N, 73W, and 36N, 74W respectively, the sensible heat flux in the experimental simulation is 400 Wm^{-2} larger than the control simulation. This is likely a result of a more defined gradient corresponding to the location of a warm core filament which can be seen off the Delmarva peninsula (38.5N, 72W, Figure 7.5b), as well as the elevated SSTs ($>22^\circ\text{C}$) within that filament. The SST gradient preceding the storm's position at 12Z Jan 25 also corresponds to the region of convergence (31.5N, 77.2W to 38N, 71.5W, Figure 7.11b), as well as the future track of the storm. Figures 7.15a,b show the largest values of sensible heat flux, not only because of the cold air advecting south behind the low pressure, but also because Figure 7.15 is valid 18Z Jan 25 (2pm EDT), so radiation effects can be seen over land. The effects of the cold air advecting over the warm water behind the low pressure are verified by the satellite imagery in Figure 7.1d. This enhanced sensible heat flux which is driving this low-level convection is responsible for the low-level cloud formation east of GA and SC.

The largest values of sensible heat flux near the center of circulation in the control simulation never exceed 200 Wm^{-2} . However, in the experimental simulation, values are in excess of 500 Wm^{-2} . This is partly because of the lack of storm development in the control simulation, but more a factor of position and weak SST data. In both simulations, large values can be seen to the southwest side of the circulation in the wake of the surface low. This is consistent with strong cold advection, but is not considered a direct factor in storm intensification (e.g., Nuss and Anthes 1987, and Kuo et al. 1990).

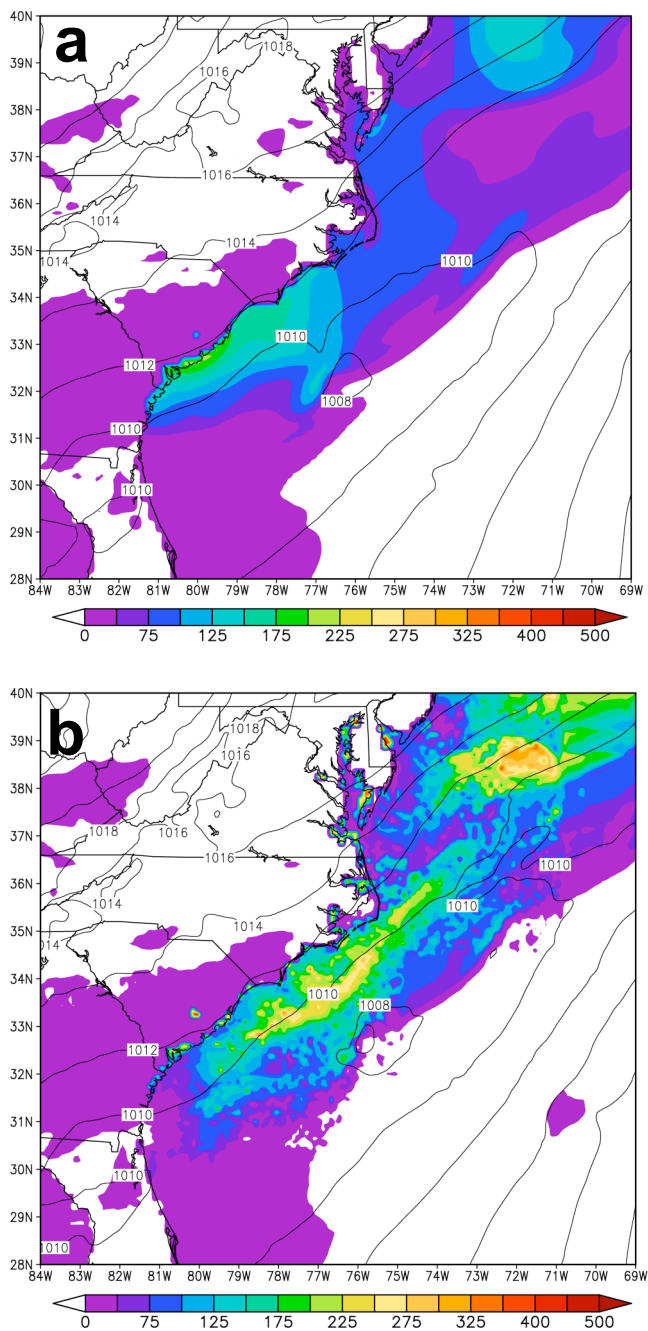


Figure 7.12 Plots of surface-level sensible heat flux (W/m^2) and pressure (mb) for (a) the control simulation and (b) the experimental simulation valid 12Z 24 Jan (12h after initialization).

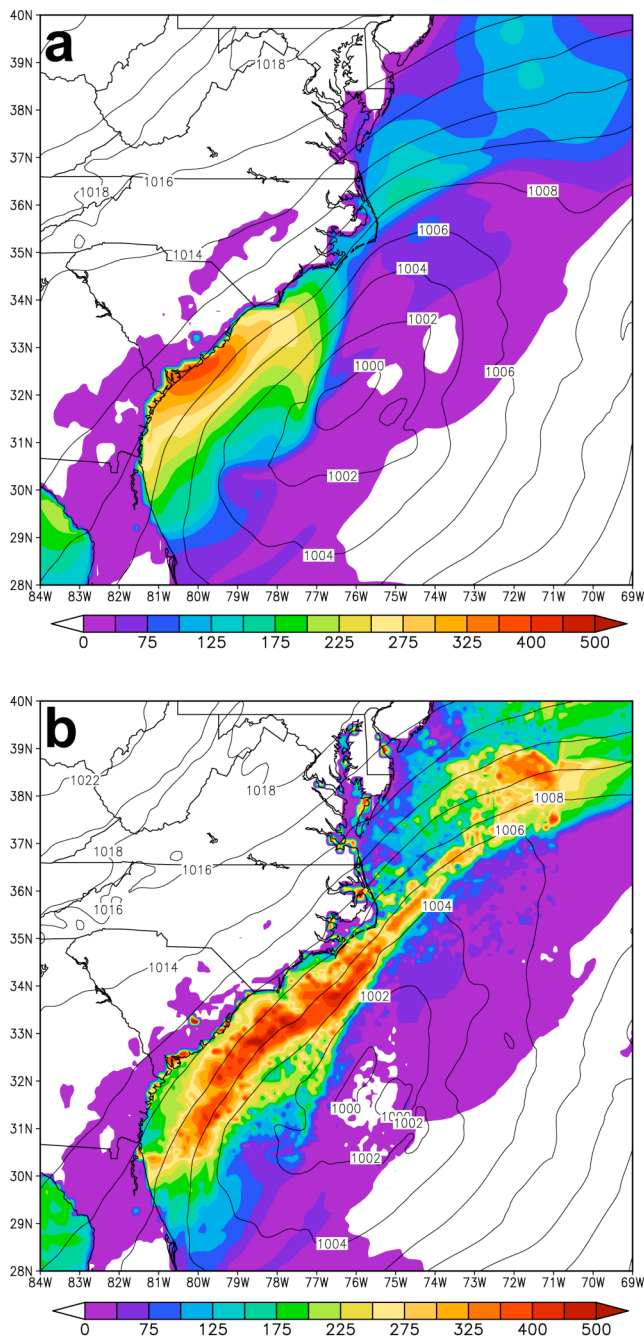


Figure 7.13 Plots of surface-level sensible heat flux (Wm^{-2}) and sea-level pressure (mb) valid 00Z Jan 25 (24 h after initialization) for the control simulation (a), the experimental simulation (b).

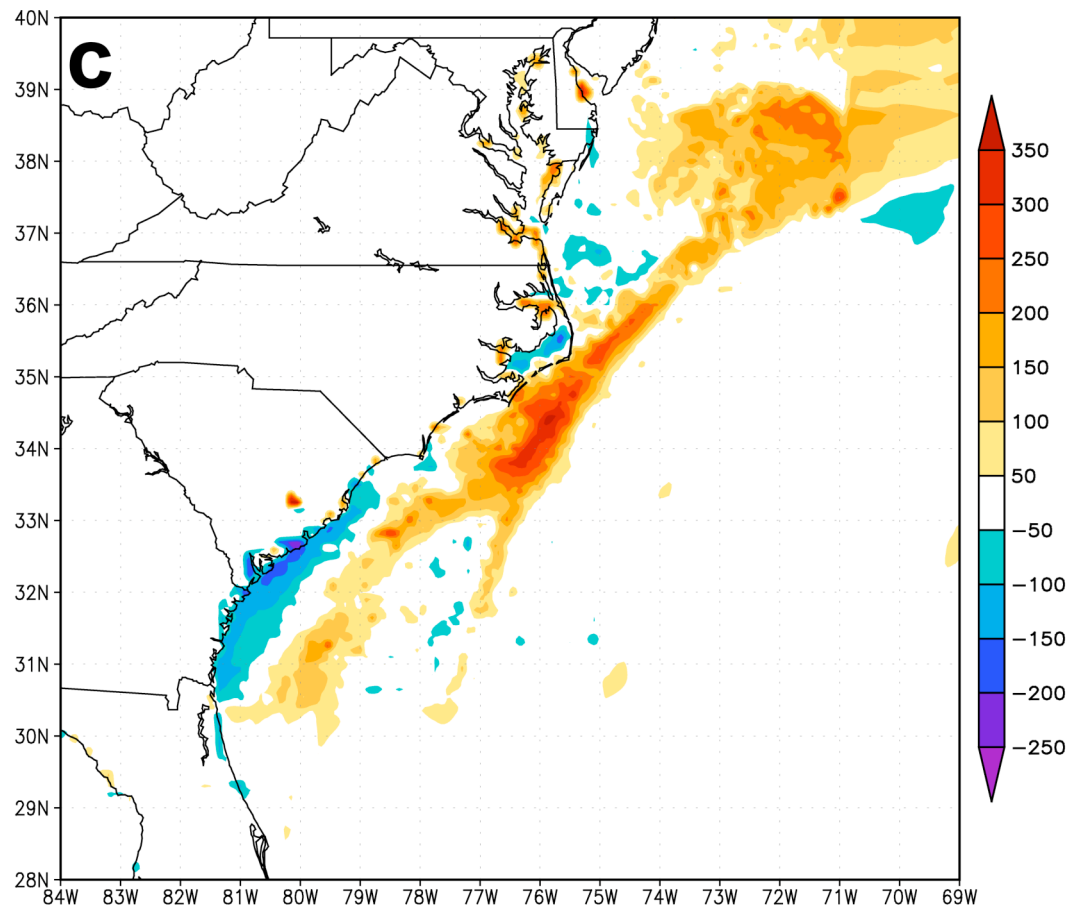


Figure 7.13c Plots of surface-level sensible heat flux (Wm^{-2}) and sea-level pressure (mb) valid 00Z Jan 25 (24 h after initialization) for the experimental simulation minus the control simulation difference field (c).

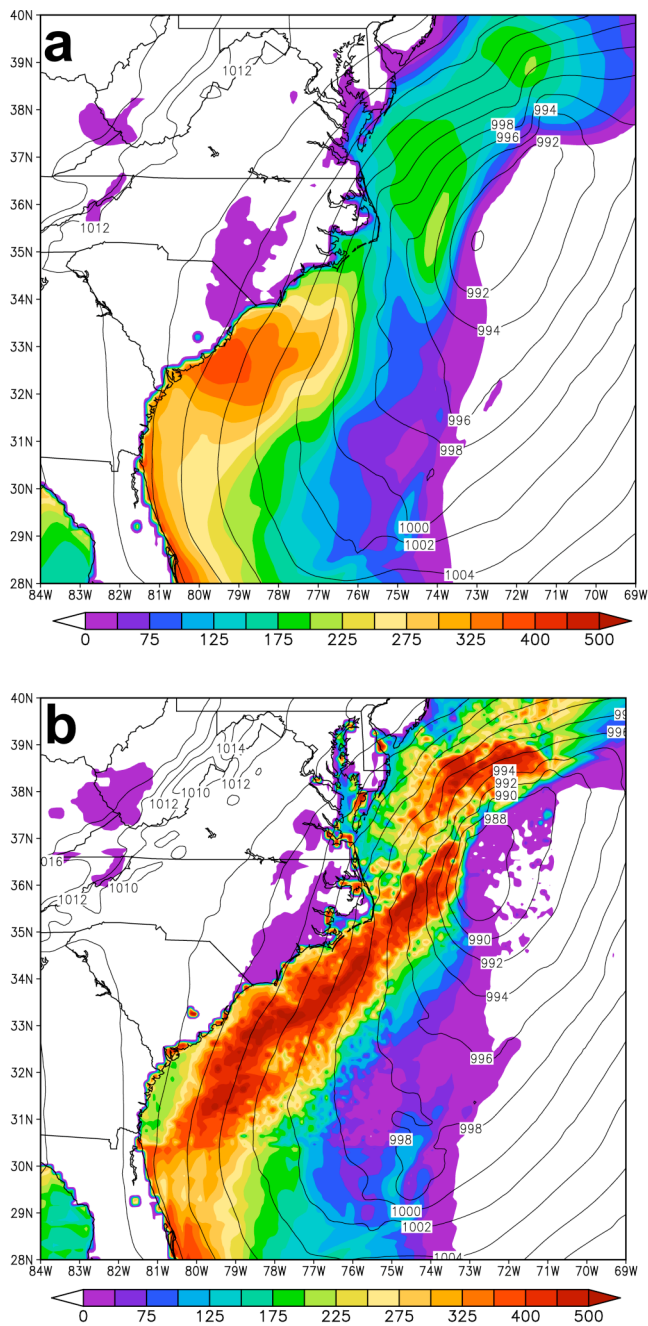


Figure 7.14 Plots of surface-level sensible heat flux (W m^{-2}) and sea-level pressure (mb) valid 12Z Jan 25 (36 h after initialization) for the control simulation (a), the experimental simulation (b).

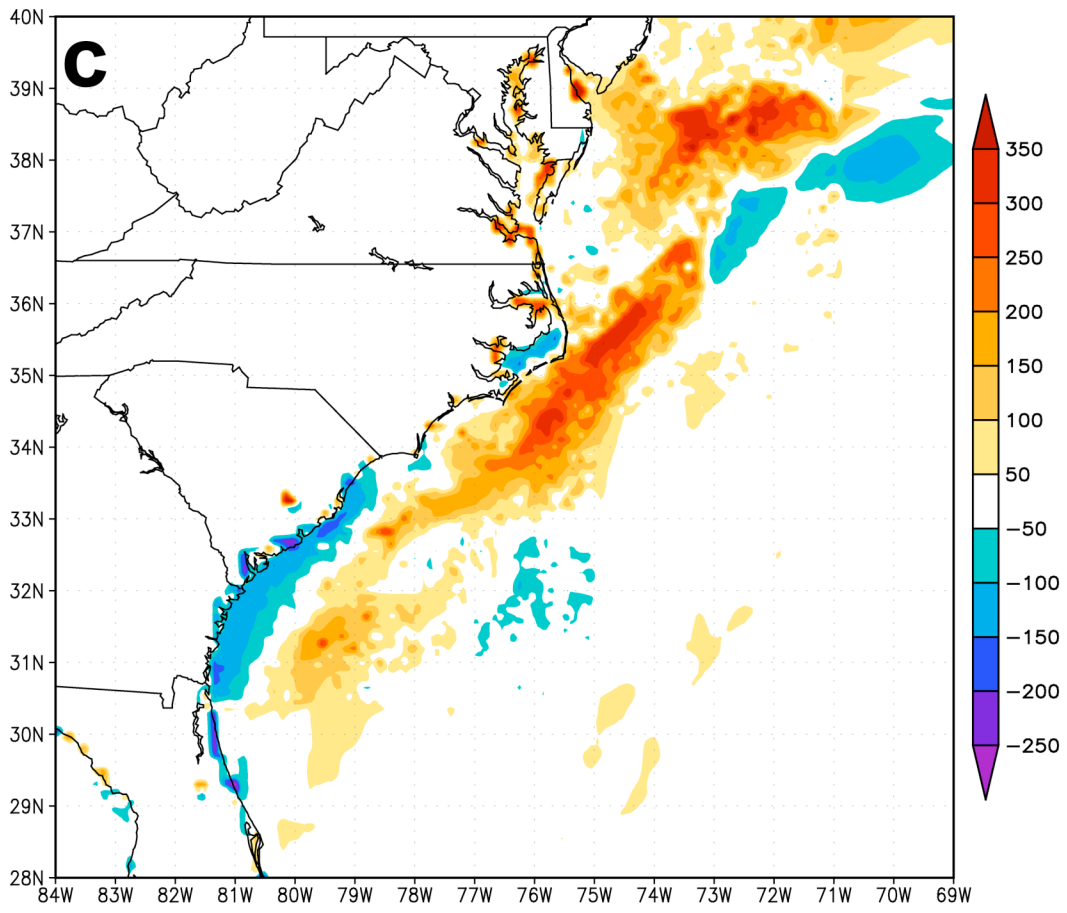


Figure 7.14c Plots of surface-level sensible heat flux (Wm^{-2}) and sea-level pressure (mb) valid 12Z Jan 25 (36 h after initialization) for the experimental simulation minus the control simulation difference field (c).

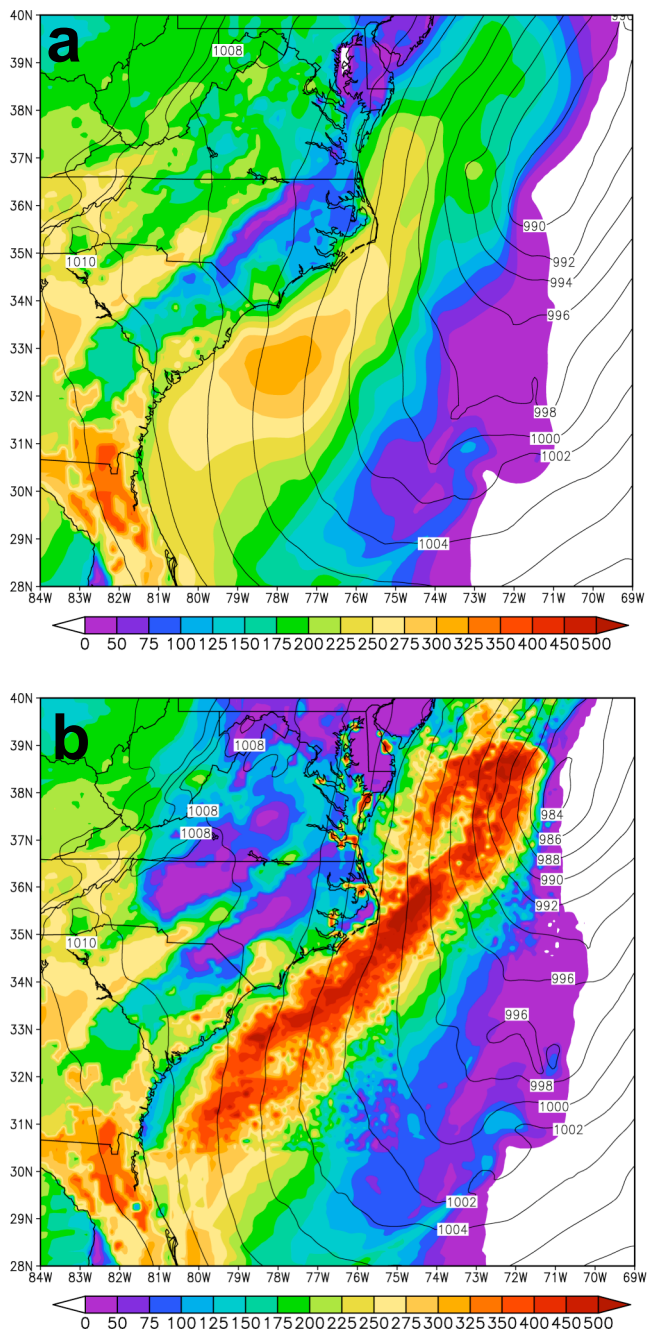


Figure 7.15 Plots of surface-level sensible heat flux (W/m^2) and pressure (mb) for (a) the control simulation and (b) the experimental simulation valid 18Z (2pm EDT) 25 Jan (42h after initialization).

Figures 7.16a and 7.16b, valid 12Z Jan 24, show minor localized areas of increased winds located at 32.5N, 76W where the magnitudes in the experimental are 6 to 7 ms^{-1} greater, but there is minimal difference corresponding to the GSF region because the coastal front did not begin to form for another 6-8 hours. Directly around the center of the low pressure, the winds in the experimental are slightly stronger (6 m/s), but the wind field of the control simulation southeast of Cape Hatteras has almost twice the fetch of winds exceeding 10 ms^{-1} .

The coastal frontogenesis, evident by 21Z Jan 24, is taking place along a line 32N, 77W to 37N, 72W in Figure 7.17b of the experimental simulation more so than Figure 7.17a of the control simulation. The coastal front seen in the experimental simulation (Figure 7.17b) has winds 2-4 ms^{-1} larger than those in the control simulation which are verified by the 10-m wind vectors in Figure 7.9b, and convergence contours of Figure 7.11b which are 4e-4 s^{-1} larger in the experimental simulation. Values of wind speed just east of the front in Figure 7.17b are 4 to 6 ms^{-1} lower than the control seen in Figure 7.17a. More importantly, the transition where the winds decrease east of the front in Figure 7.17b is more abrupt for the experimental simulation. Both figures are valid 21Z Jan 24 (21 h into the simulation), and share almost identical wind velocity values of 8 ms^{-1} (16 kts) over the region east of South Carolina located at 32.5N, 79.5W. Northeast of Cape Hatteras, NC, the experimental simulation (Figure 7.17b) shows a slightly larger 12 ms^{-1} (23 kts) fetch with a few small areas of 14 ms^{-1} . In addition to the regions of increased wind velocity west of the coastal front, the experimental simulation shows a region of velocities 4 ms^{-1} (8 kts) less than that of the control simulation east of the front around 36N, 72W.

Thirty six hours into the simulation (12Z Jan 25), the fully developed low pressure

system of the control, shown in Figure 7.18a, is located about 180 km due east of Cape Hatteras, NC. The experimental simulation's position of the low, shown in Figure 7.18b, located at 37N, 73W, is about 80 km to the north-northwest of the control's position. In Figures 7.18a and 7.18b, minor differences can be seen along the Gulf Stream region east of GA to southeast NC with most of the wind velocities in the 12 ms^{-1} (23 kt) range. East of Cape Hatteras, NC near the coastline, both simulations share similar regions of $20\text{-}22 \text{ ms}^{-1}$ (39-43 kts) from about 36N to 37N. However, closer to the center of circulation, the experimental simulation's 10-m winds (Figure 7.18b) exceeded the control simulation's winds by about 4 ms^{-1} (8 kts) with maximum values approaching 50 kts. The region of greatest sensible heat flux difference located just off the southeast coast of North Carolina (35N, 74W) presented earlier in Figure 7.14b is likely a result of the high resolution SST because the corresponding regions shown in Figures 7.18a and 7.18b have values that differ less than 1 ms^{-1} . In the experimental simulation, in the wake of the low behind the cold front 31.5N, 73 to 75W, the winds are 4-5 ms^{-1} less than the control simulation. This region in Figure 7.18b corresponds to a zone of high resolution SST, shown in Figure 7.5b, east of the Gulf Stream at 31.5N, 75W which has values $3\text{-}4^\circ\text{C}$ less than those in the control simulation.

Although the track of the experimental simulation is slower by about 3 h and 50 km east of the observed position at 12Z Jan 25, the values of wind speed over land from 2 to 8 m/s, as well as the larger values seen between Cape Hatteras, NC and the low pressure are verified, by the observations seen in Figure 7.1c.

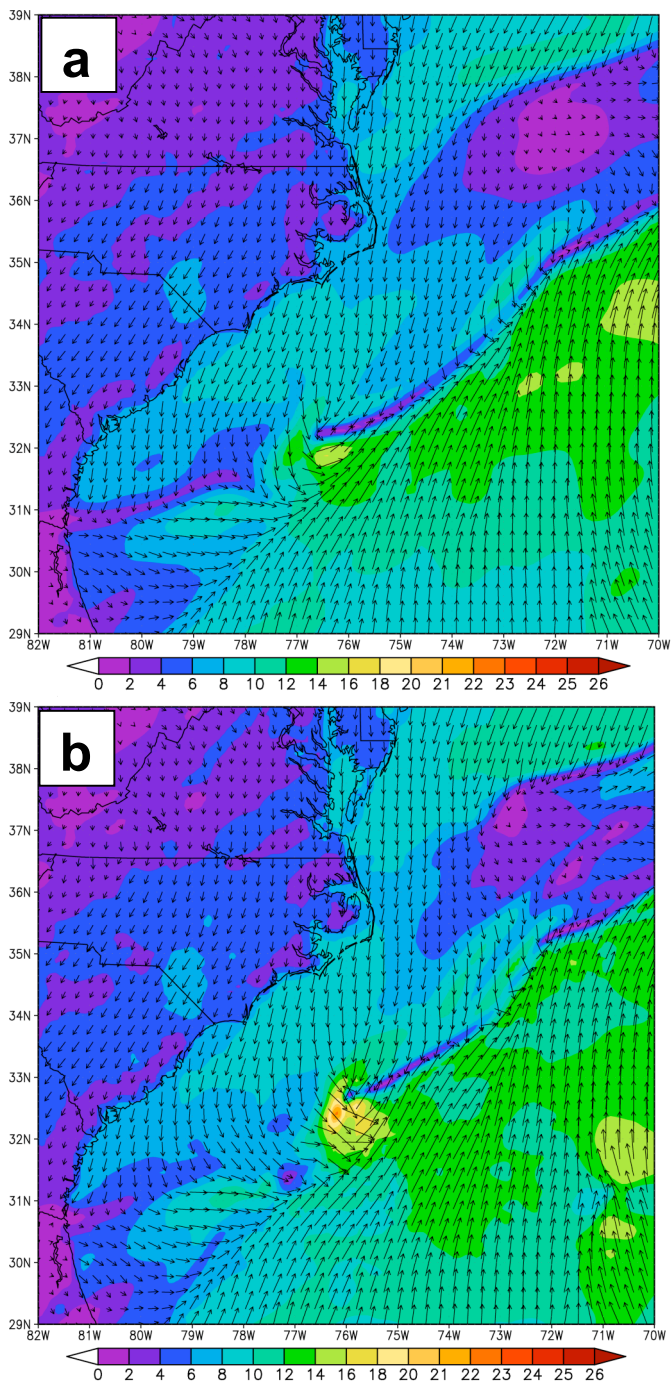


Figure 7.16 Surface-level wind field plots (m/s) for (a) the control simulation and (b) the experimental simulation valid 12Z 24 Jan (12h after initialization).

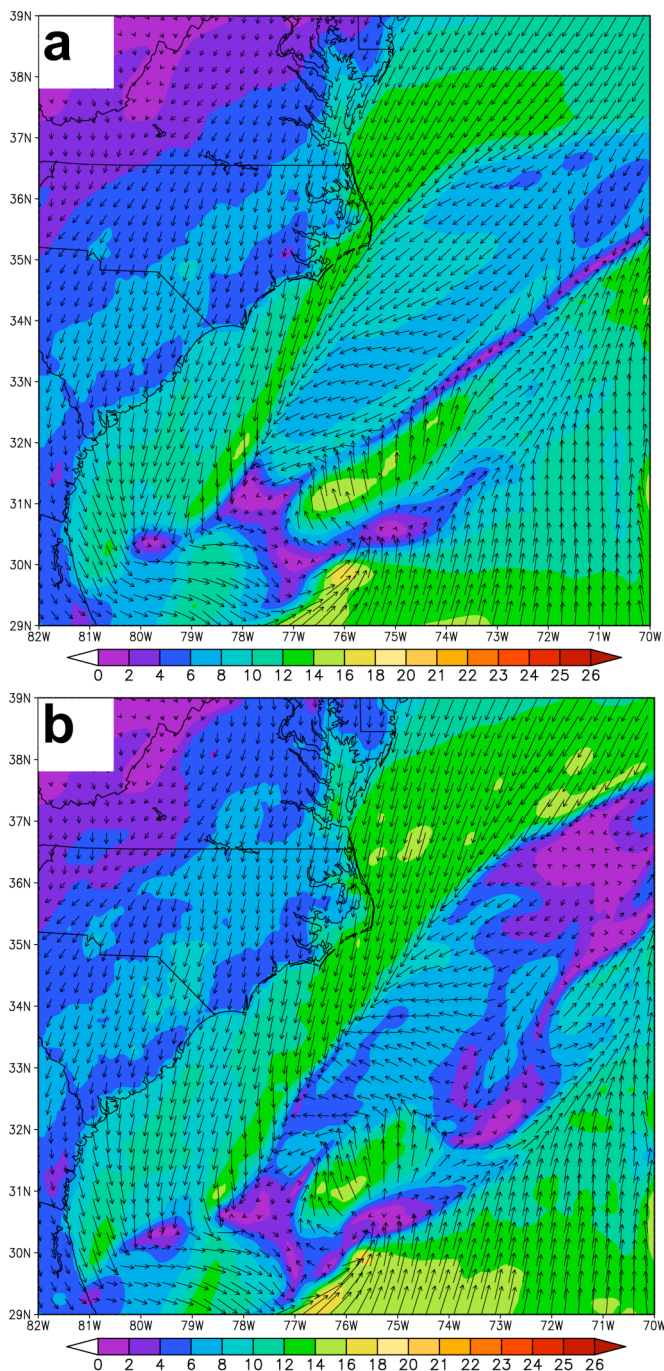


Figure 7.17 10-m wind field (ms^{-1}) and vectors for (a) the control simulation and (b) the experimental simulation valid 21Z Jan 24 (21 h after initialization).

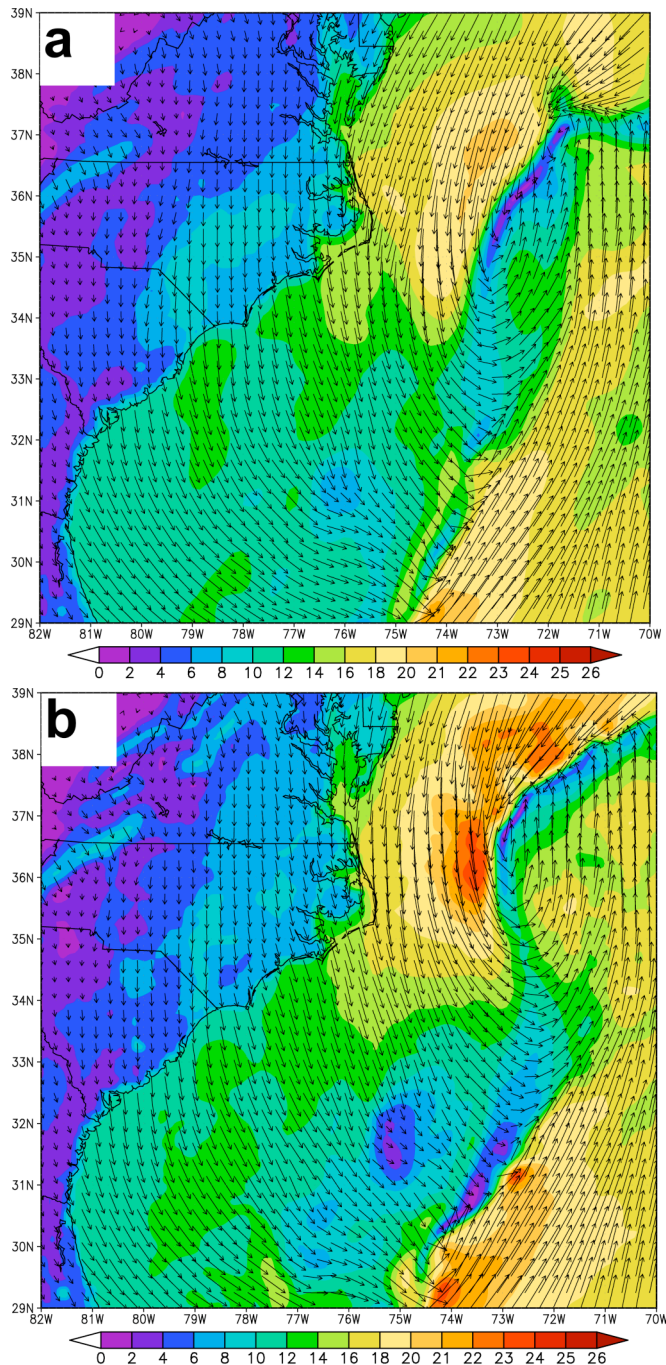


Figure 7.18 10-m wind field (ms⁻¹) and vectors for (a) the control simulation and (b) the experimental simulation valid 12Z Jan 25 (36 h after initialization).

The low-level (950-hPa) vortex stretching (s^{-2}) valid 21Z Jan 24 is shown in Figure 7.19 for the control simulation (a), the experimental simulation (b), and the experimental simulation minus the control simulation difference field (c). The stretching was calculated via term three in Equations 4.6 and 4.7, or essentially $\xi_a(\nabla \cdot \vec{V})$. In both simulations, there are two adjacent swaths of elevated stretching linked to the coastal frontogenesis. In the control simulation (Figure 7.19a) the region, located 32N, 76W, has maximum values of $3 \times 10^{-7} \text{ s}^{-2}$, while there is a slightly weaker line about 200 km to the west which crosses the tip of Cape Hatteras, NC. The ultimate path of the low pressure system in the control simulation was along a line between these two regions and slightly closer to the stronger swath to the east (Figure 7.6). In the experimental simulation (Figure 7.19b) the line of enhanced vortex stretching is split in two, similar to the control simulation; however, it is the swath further to the west which is significantly more pronounced. This line has values exceeding $6 \times 10^{-7} \text{ s}^{-2}$ which extend well past the latitude of Cape Hatteras, NC. The track of the storm in the experimental simulation (Figure 7.6) did not veer from this path until beyond 18Z Jan 25. A difference field of the experimental minus the control simulation's vortex stretching is shown in Figure 7.19c. Values where the control simulation exceeds the experimental simulation, when plotted on a symmetrical scale, are nearly negligible compared to the enhanced stretching seen in the experimental simulation. Along the region where the coastal frontogenesis in the experimental simulation (Figures 7.19b and 7.11b) occurred, the magnitude of the vortex stretching is $4 \times 10^{-7} \text{ s}^{-2}$ greater than the control simulation.

Plots of 950-hPa vortex stretching, valid 12Z Jan 25, are shown in Figure 7.20. At this time, the surface low pressure has deepened significantly and is located east of Cape Hatteras, NC. The maximum values of stretching in the control simulation (Figure 7.20a) are

much larger than those in the previous Figure 7.19a, but still further east of those in the experimental simulation (Figure 7.20b). The horizontal position difference in the two regions can be seen in Figure 7.20c (located 37N, 72W), as well as the significantly larger values ($>4 \times 10^{-7} \text{ s}^{-2}$) of the experimental simulation.

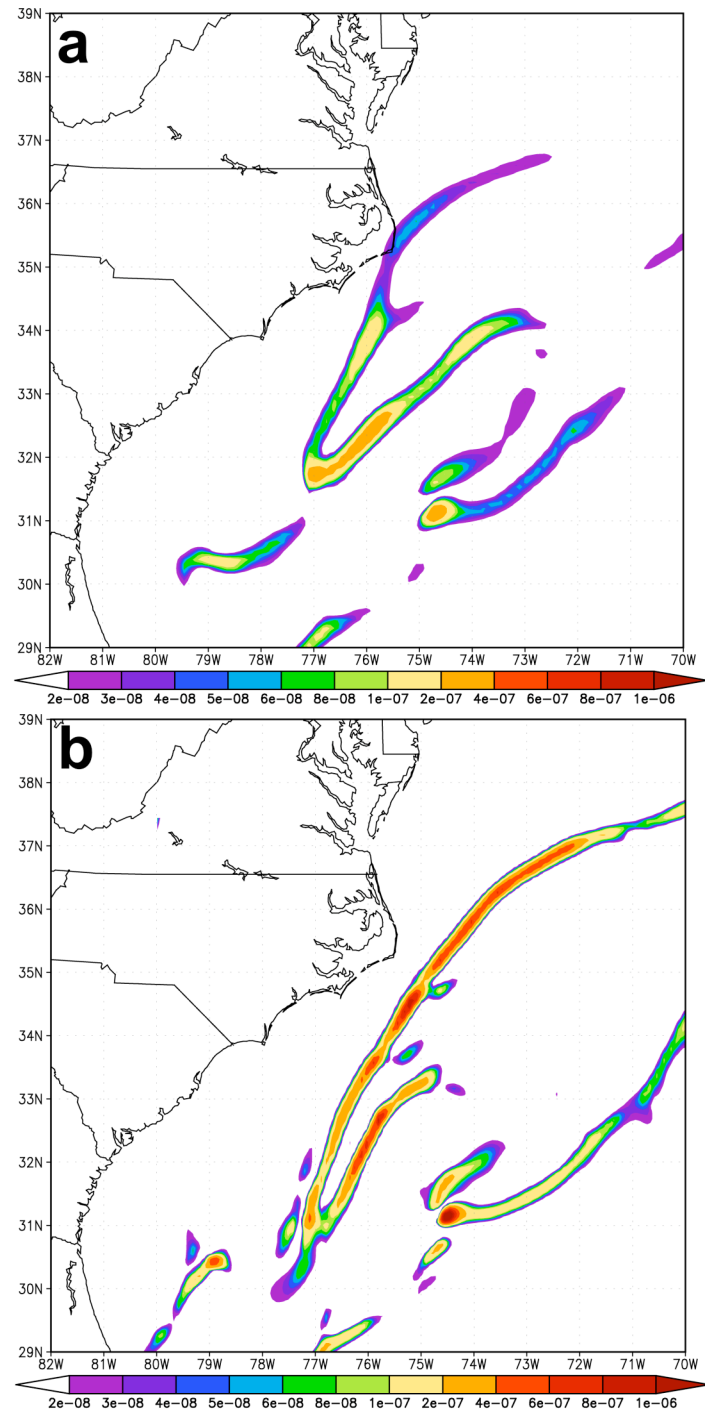


Figure 7.19 Plots of 950-hPa stretching (s^{-2}) valid 21Z Jan 24 (21 h after initialization) for the control simulation (a), the experimental simulation (b).

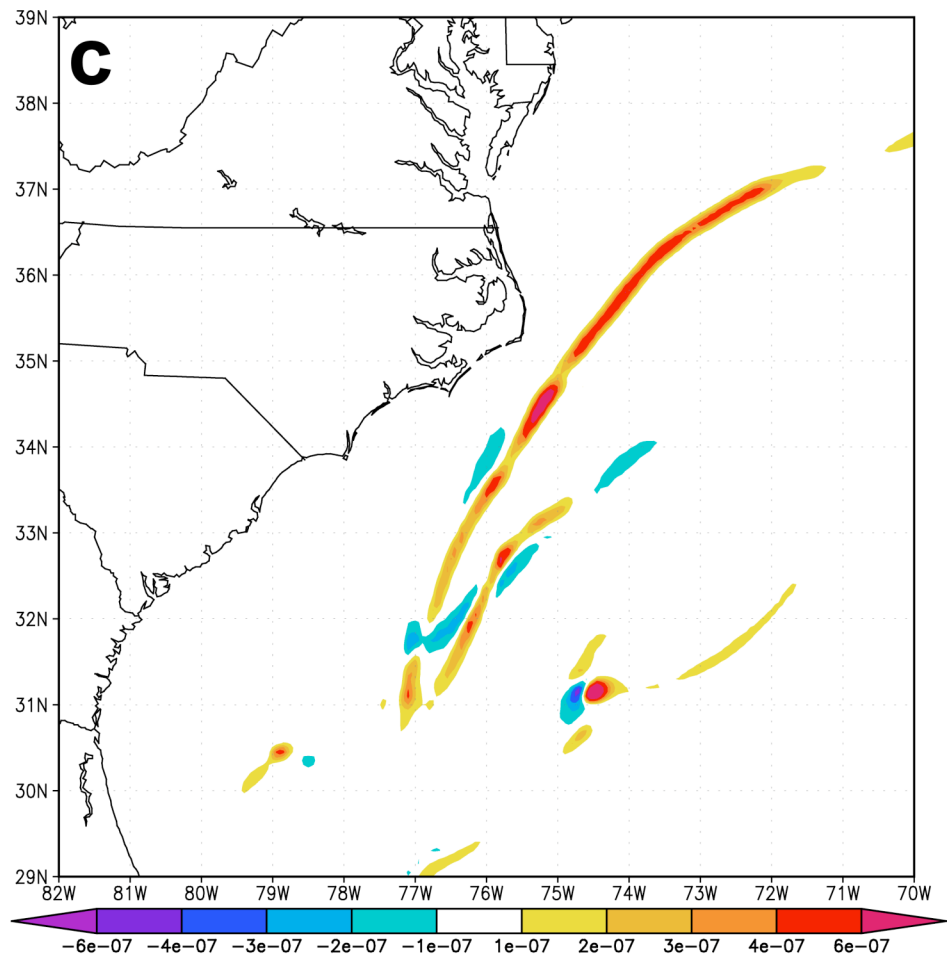


Figure 7.19c Plots of 950-hPa stretching (s^{-2}) valid 21Z Jan 24 (21 h after initialization) for the experimental simulation minus the control simulation difference field (c).

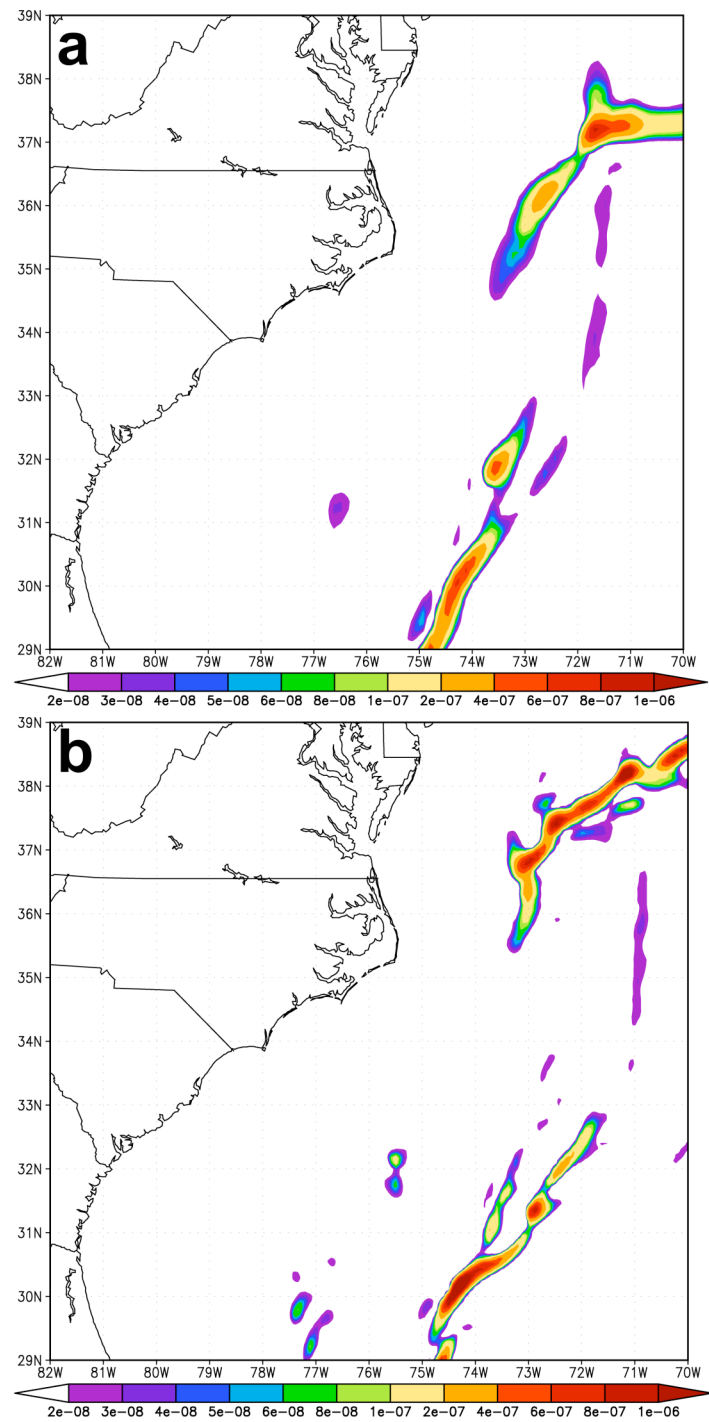


Figure 7.20 Plots of 950-hPa stretching (s^{-2}) valid 12Z Jan 25 (36 h after initialization) for the control simulation (a), the experimental simulation (b).

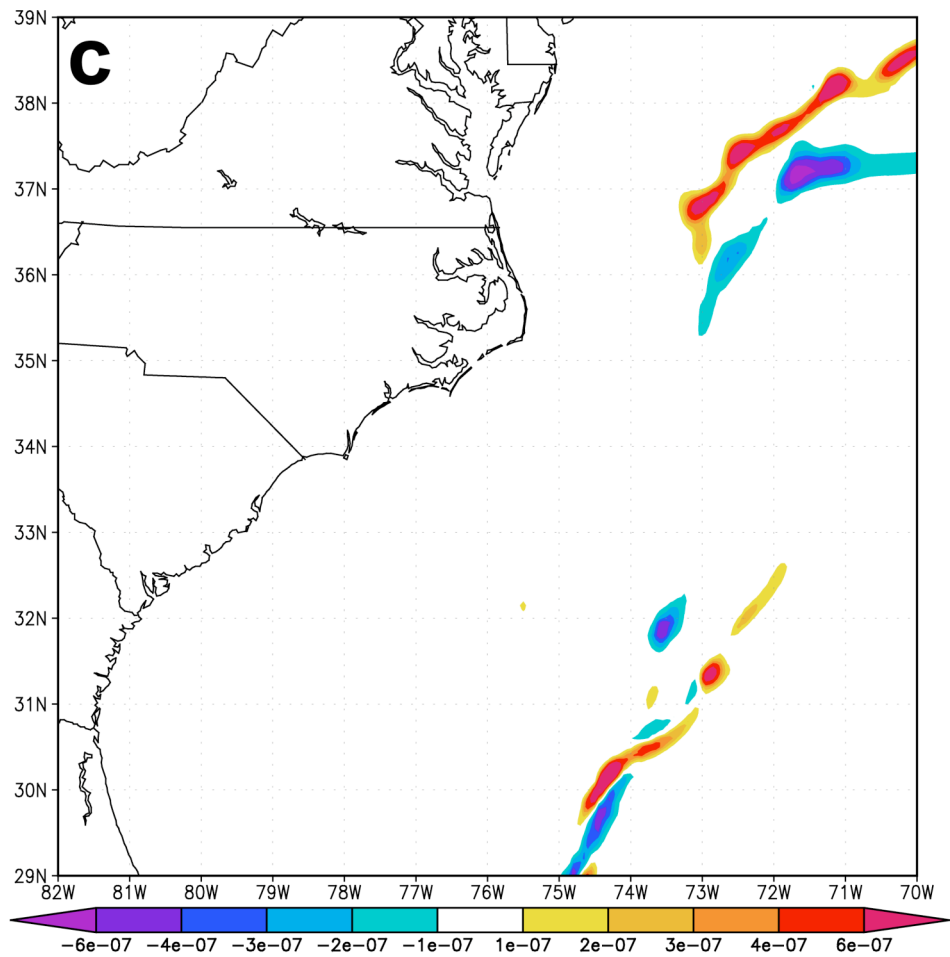


Figure 7.20c Plots of 950-hPa stretching (s^{-2}) valid 12Z Jan 25 (36 h after initialization) for the experimental simulation minus the control simulation difference field (c).

Sea-level pressure time series for the control simulation (blue) and experimental simulation (red), are shown in Figure 7.21. Significant differences between the control and experimental simulations are not evident until 30 h. The largest differences in the simulated pressures occur between 30 h and 44 h, and continue beyond 12Z Jan 24. At this time, the experimental simulation is tracking the center of the low pressure system along the GSF, and deepening at a rate of 1.2 mb h^{-1} until 08Z Jan 25. A sharp 3-mb pressure drop occurs at 33 h into the simulation which corresponds to the time where the experimental simulation's low pressure center crossed over the warm-core filament located east of Cape Hatteras, NC. In the control simulation (blue), the low is not accelerating at the same rate, nor does it experience the abrupt pressure decrease by 09Z Jan 25. When the track of the experimental simulation shown in Figure 7.6 (06Z - 09Z Jan 25) crosses the warm Gulf Stream region located at 36N, 74.5W (Figure 7.5b), the corresponding pressure drop is shown in Figure 7.21 (32 h). The increased deepening rate of the experimental simulation's surface low is likely due to enhanced vortex stretching along the frontal boundary seen in this region more so than the control simulation. The largest difference in pressure when the experimental simulation is 6 mb lower than the control occurs 42 h into the simulation (18Z Jan 25). As the storm in the experimental simulation moves off the region of high resolution SST (beyond 44 h), the sea-level pressure differences between the two simulations decrease. Not only do the differences decrease, but the pressures rise in both simulations as the occluded storm begins to weaken.

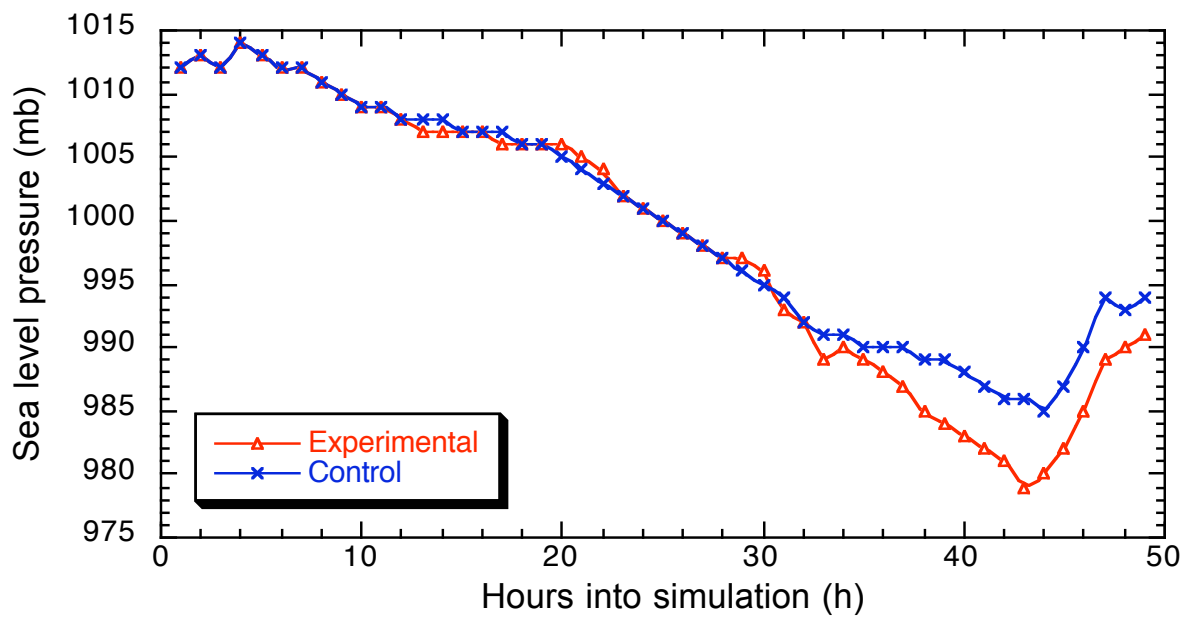


Figure 7.21 Time series of sea-level pressure (mb) for experimental simulation (red) and control simulation (blue). Initialization 00Z 24 Jan 2000 (0 h into simulation) through 00Z 26 Jan 2000 (48 h into simulation).

Figures 7.22 through 7.27 show accumulated precipitation (mm) for the entire storm event. The precipitation is contoured for the liquid equivalent and does not include the addition of the second MM5 convective precipitation parameter. Although there are differences in the quantitative precipitation forecast (QPF) for the simulations, the values seem to only be distantly related to the enhancement of the surface low pressure as shown in previous studies (e.g. Griffith et al. 1978; Wylie 1979). Brennan and Lackmann (2004) show that a diabatically generated PV anomaly was likely responsible for the enhanced precipitation banding in the January 2000 case.

In Figure 7.22, the difference between the control and the experimental simulations is very minor. There is a slightly larger area of precipitation measuring less than 2 mm over east GA. However, this is one hour after initialization, so it can be seen that the model was not initialized with any precipitation fields. Six hours later, Figure 7.23, valid 06Z Jan 24, the experimental simulation has slightly more precipitation off the coast of GA and FL, and the extension of a band over Cape Hatteras. Other than these differences, which are within 2-4 mm of each other, the simulations are still following identical trends. These trends extend through 12Z JAN 24, where the only noticeable difference in the accumulated precipitation (Figure 7.24) is a region over SC which is not seen in the control simulation. Although the difference is >2 mm, this time marks the point where the simulations begin to follow slightly different tracks. Figure 7.24 is 12 hours into the simulation, and some of these effects could be a function of the higher resolution SST on both the east and west coast of FL.

There is a moderate increase in QPF beginning 00Z Jan 25, 24 h into the experimental simulation (Figure 7.25b). In Figure 7.25a, the precipitation southeast of the SC / NC border is actually greater than the experimental; however, the landfalling precipitation is greater in

the experimental simulation. Part of this is a factor of the track, and part of it is related to the position: the low pressure in the experimental at 00Z Jan 25 is further north, as well as west, when compared to the control simulation at the same time.

The band of precipitation continues to widen through the 36 h mark (12Z Jan 25, Figure 7.26). In Figure 7.26b, the experimental simulation, the band crosses Cape Hatteras with storm totals exceeding 35 mm. In the control, Figure 7.26a, the same location posts values in the 14 to 16 mm range. Further south along the coastline centered around 35N, 77.5W, the experimental simulation has accumulated precipitation values over 30 mm which is 3 times larger than the control, but once again, this likely just a factor of the track being slightly more westward.

Beyond this point, the control simulation's QPF actually produces more landfalling precipitation than the experimental in the regions north of the NC / VA border. This is seen mainly in regions north of the Carolinas moving into the Delmarva region of VA. Figure 7.27, valid 00Z Jan 26, is the total accumulated precipitation for the entire simulations. The overall increase in QPF seen in the experimental simulation is likely more of a factor of the track than the resolution of the SST. Although some is undoubtedly from an increase in convection, the fact that the experimental simulation was closer to the coast shifted the precipitation fields to the west as well. It is odd that the last few hours of the control simulation produce more landfall precipitation despite the center of the low pressure taking a more eastward track (Figure 7.6). However, this is consistent with the plots of dBZ presented later.

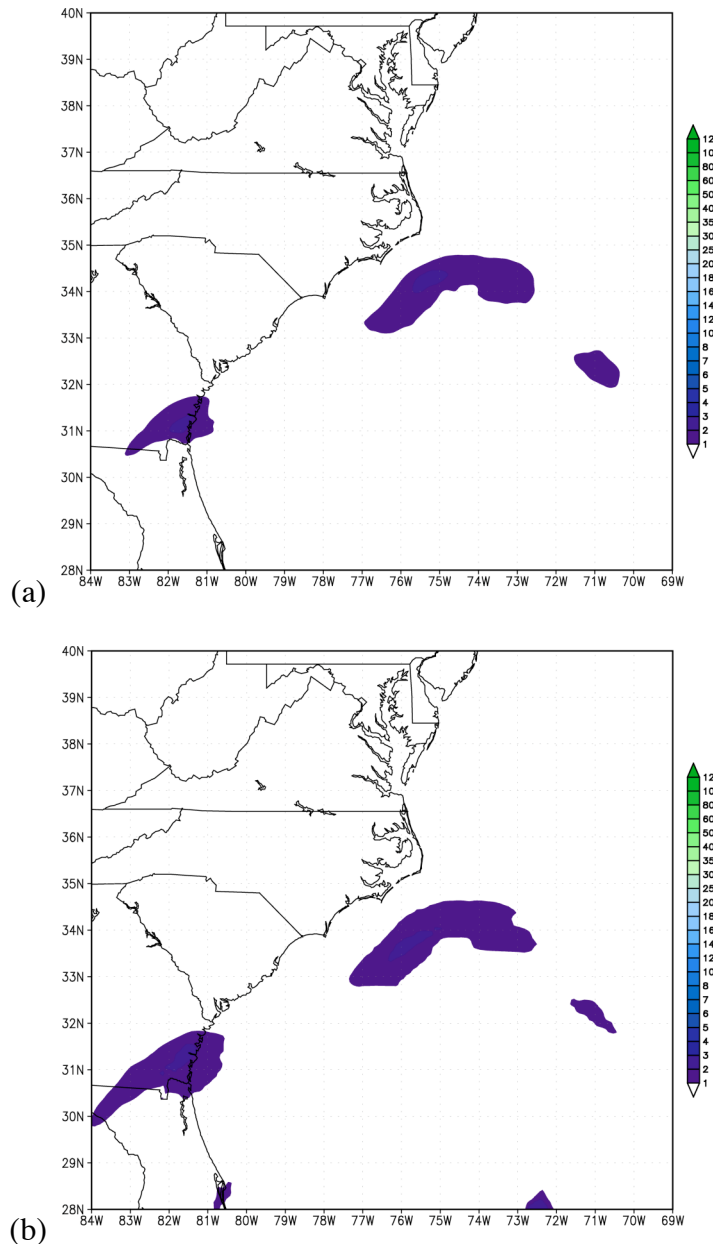


Figure 7.22 Cumulative precipitation (mm) valid 01Z 24 Jan 2000 (1h into simulation) for control simulation (a) and experimental simulation (b) initialized 00Z 24 Jan 2000.

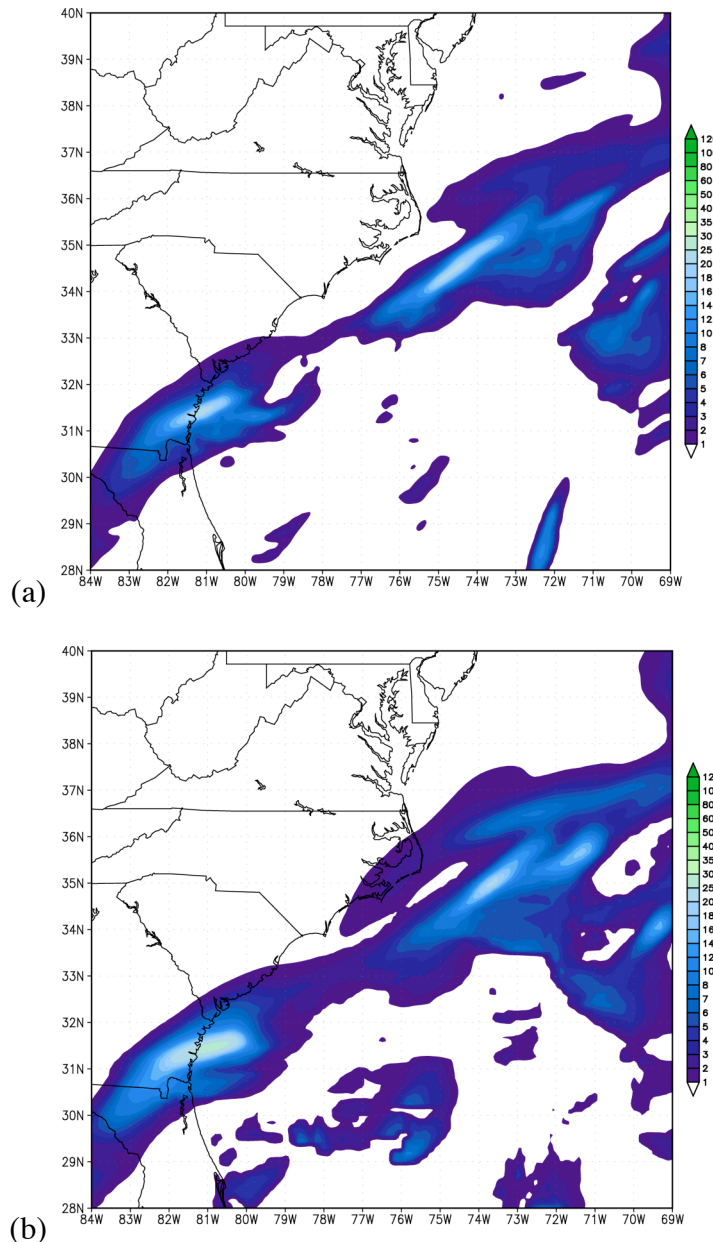


Figure 7.23 Cumulative precipitation (mm) valid 06Z 24 Jan 2000 (6h into simulation) for control simulation (a) and experimental simulation (b) initialized 00Z 24 Jan 2000.

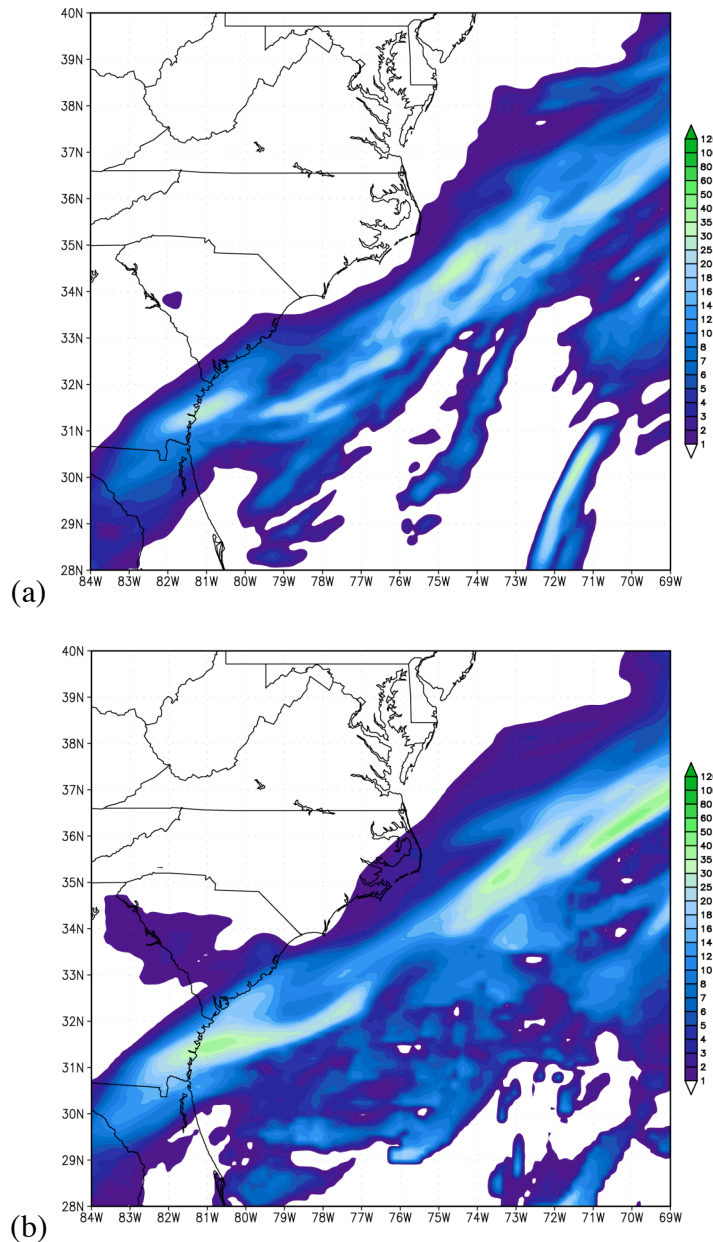


Figure 7.24 Cumulative precipitation (mm) valid 12Z 24 Jan 2000 (12h into simulation) for control simulation (a) and experimental simulation (b) initialized 00Z 24 Jan 2000.

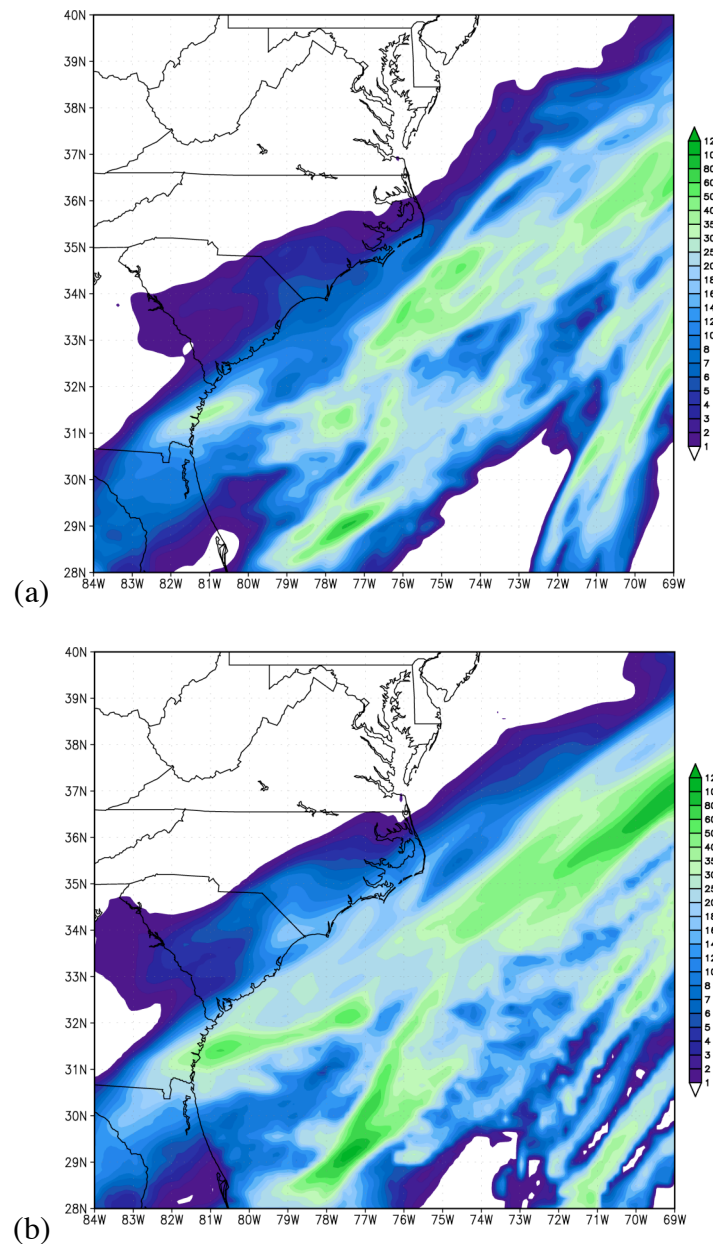


Figure 7.25 Cumulative precipitation (mm) valid 00Z 25 Jan 2000 (24h into simulation) for control simulation (a) and experimental simulation (b) initialized 00Z 24 Jan 2000.

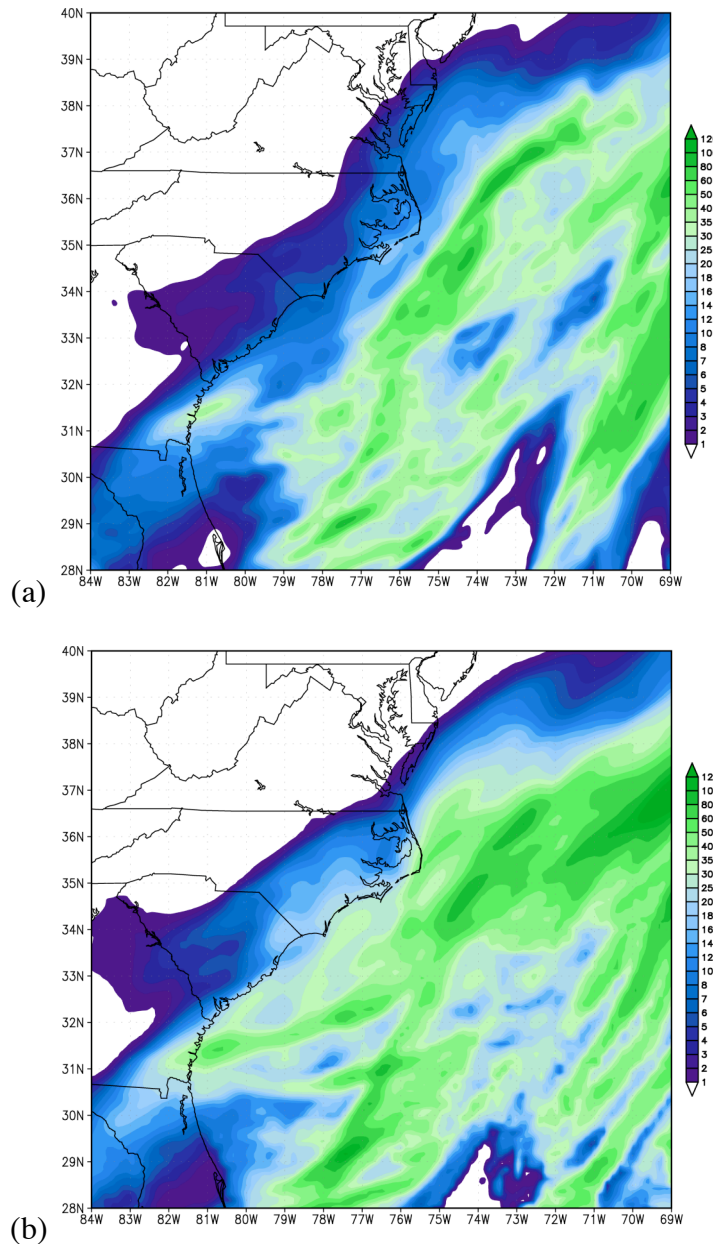


Figure 7.26 Cumulative precipitation (mm) valid 12Z 25 Jan 2000 (36h into simulation) for control simulation (a) and experimental simulation (b) initialized 00Z 24 Jan 2000.

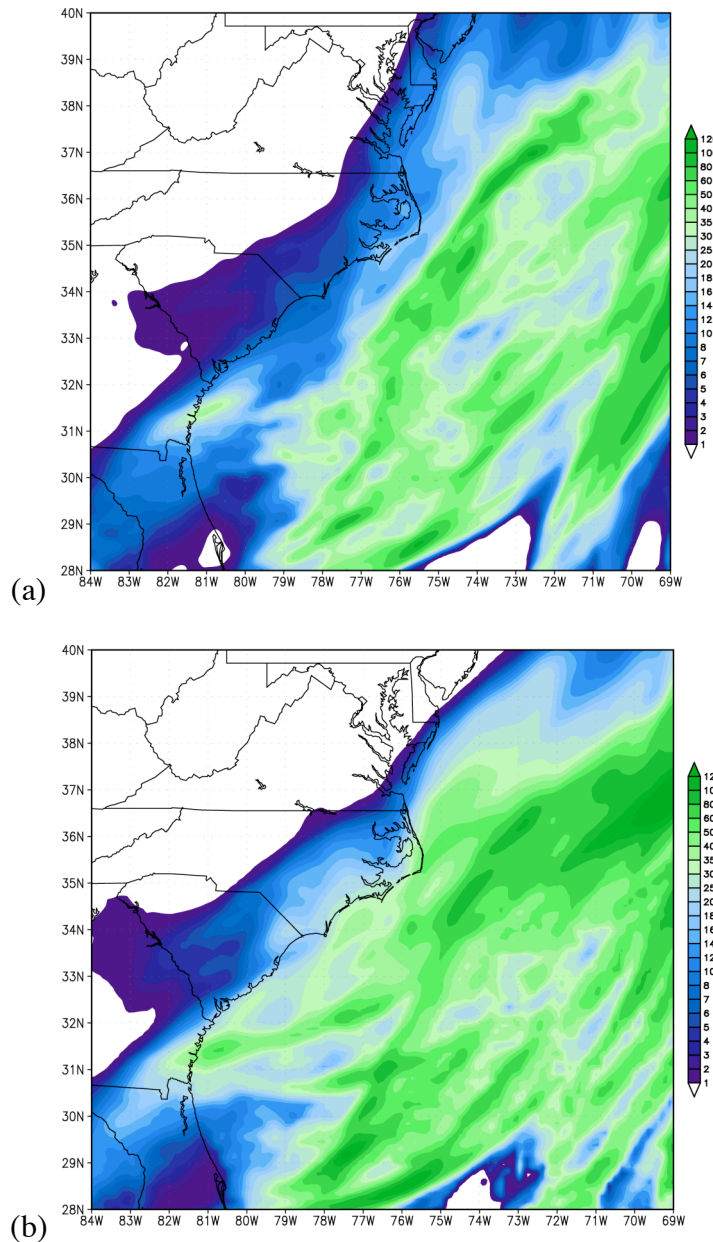


Figure 7.27 Cumulative precipitation (mm) valid 00Z 26 Jan 2000 (48h into simulation) for control simulation (a) and experimental simulation (b) initialized 00Z 24 Jan 2000.

Figure 7.28 Shows the simulated dBZ for the control (left) and experimental (right). The simulated reflectivity in Figure 7.28a,b, valid 12Z Jan 24, corresponds well with localized areas of surface winds seen in Figure 7.16, as well as the 12 h accumulated precipitation of Figure 7.24. When comparing Figures 7.28c,d (valid 00Z Jan 25) and Figures 7.28e,f (valid 12Z Jan 25) to the QPF in Figures 7.25 and 7.26, it is interesting to see that the largest areas of simulated reflectivity do not necessarily correspond to the largest values of accumulated liquid precipitation. However, the regions of development do agree with the convergence, most noticeably in the experimental's Figure 7.28d, as compared to Figure 7.11 (the convergence valid 00Z Jan 25). To some degree, Figure 7.28 verifies the QPF, but more importantly, it establishes the lack of link to the intensity of the surface low pressure. It is most interesting to compare Figure 7.28 to the Figure 7.3, the NOWRAD 2 km base reflectivity. The simulated banding features agree quite well with the observations in Figures 7.3b,c. However, the simulated dBZ of Figures 7.28a,b completely misses the region of precipitation moving from GA into SC (Figure 7.3a). Not capturing this region of precipitation during initialization is the likely cause of the "bust" in the snowfall forecast (Brennan and Lackmann 2004). Since the Figures in 7.28 were captured at the same times during the simulation, there is a slight difference between the values based on the position of the storm. For example, Figure 7.28f shows a lower dBZ than 7.28e partly because the storm is progressing faster up the coast, and has already begun to move away from the North Carolina coastline. Regardless, it is interesting to see that the dBZ, on average, is larger in the control simulation than in the experimental simulation even though the surface low pressure at 36 h (12Z Jan 25, Figure 7.28e and 7.28f) is 5 mb lower for the experimental simulation.

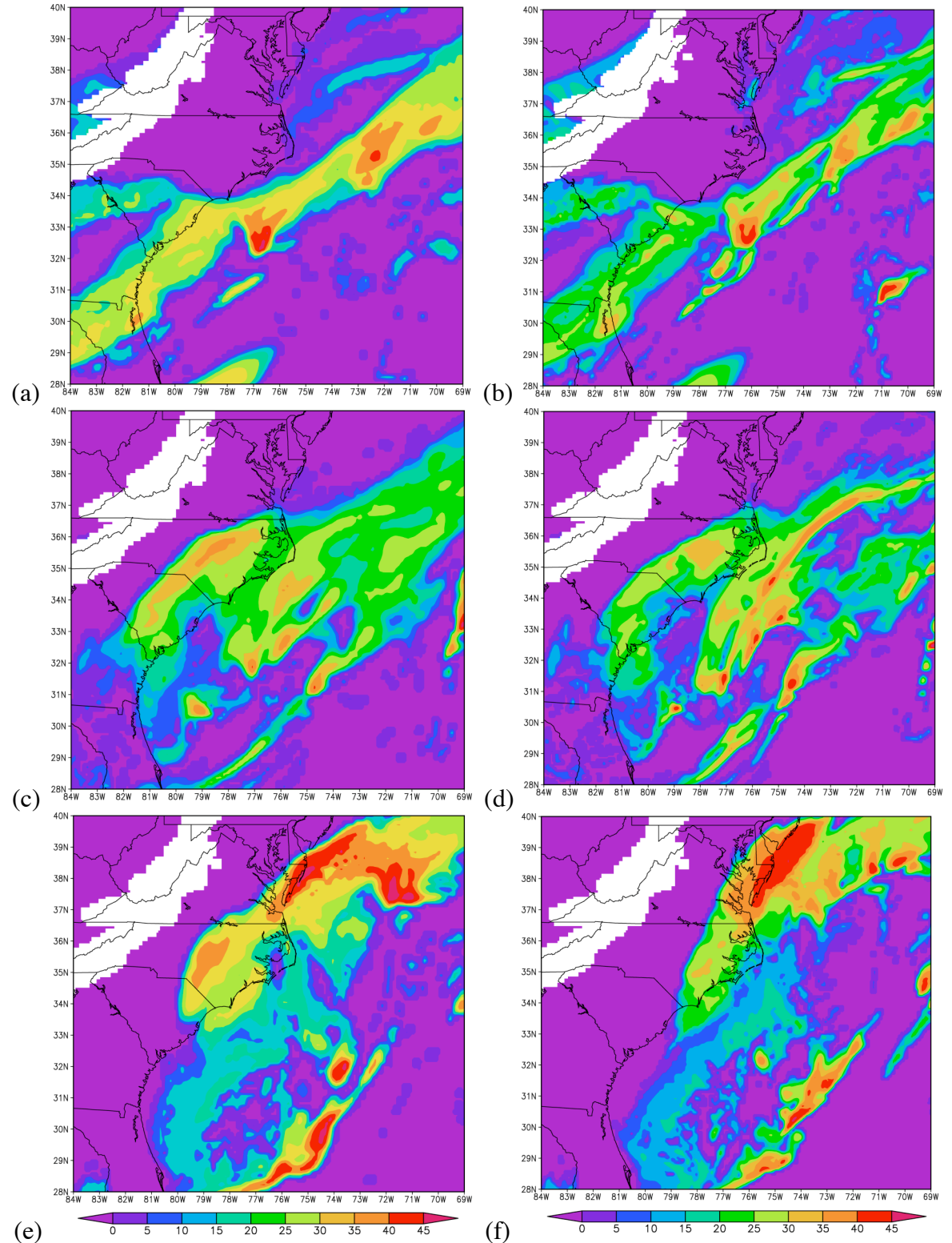


Figure 7.28 Simulated dBZ for the control / experimental valid 12Z 24 Jan 2000 (a/b, 12 h), 00Z 25 Jan 2000 (c/d, 24 h), and 12Z 25 Jan 2000 (e/f, 36 h).

Cross sections of vorticity (10^{-5} , s-1) seen in Figure 7.29 are taken at latitude 34.5N, and cover longitudes 78W to 72W . Since this is a fixed location cross section, there is some variability in time as to the peak storm (crossing the transect) comparison from the control (left) to the experimental (right). Regardless, larger values of vorticity are seen in the experimental simulation. This verifies the argument that the increased deepening rate was a result of vortex stretching along the frontal boundary which sets up in the middle of the transect (~74.5W). It is hard to draw conclusions from a side by side comparison because of the storm lag, but when observing a side by side change between four plots, the implied development can be observed. The change in vorticity of the control simulation's Figure 7.29c to 7.29e, valid 00Z Jan 25 to 06Z Jan 25, shows an increase of 0.008×10^{-5} , s-1. Whereas, the experimental simulation's vorticity change, seen in Figures 7.29d and 7.29f, valid for the same time, increases by 0.010×10^{-5} , s-1. This is still somewhat misleading, as the experimental simulation's vorticity was much greater, almost twice that of the control's near the surface, with a maximum value of 0.016×10^{-5} , s-1 at 06Z Jan 25. It is interesting to see that the control simulation, mainly in Figure 7.29c and 7.29e, position the vorticity further to the west than the experimental. This is actually the case, and can be seen in Figure 7.11b's convergence along 34.5N. There is a region in Figure 7.11a that marks the peak in surface vorticity seen in Figure 7.29c which is valid for the same time, 00Z Jan 25. Likewise, Figure 7.11b has a region of convergence along 34.5N that corresponds to the 0.0006×10^{-5} s-1 value of vorticity located at 74.7W. Although the control simulation is further west, its track is more northeastward as compared to the experimental simulation. Thus, as the storms track north of 34.5N and beyond the cross section, the experimental takes a track closer to the coast.

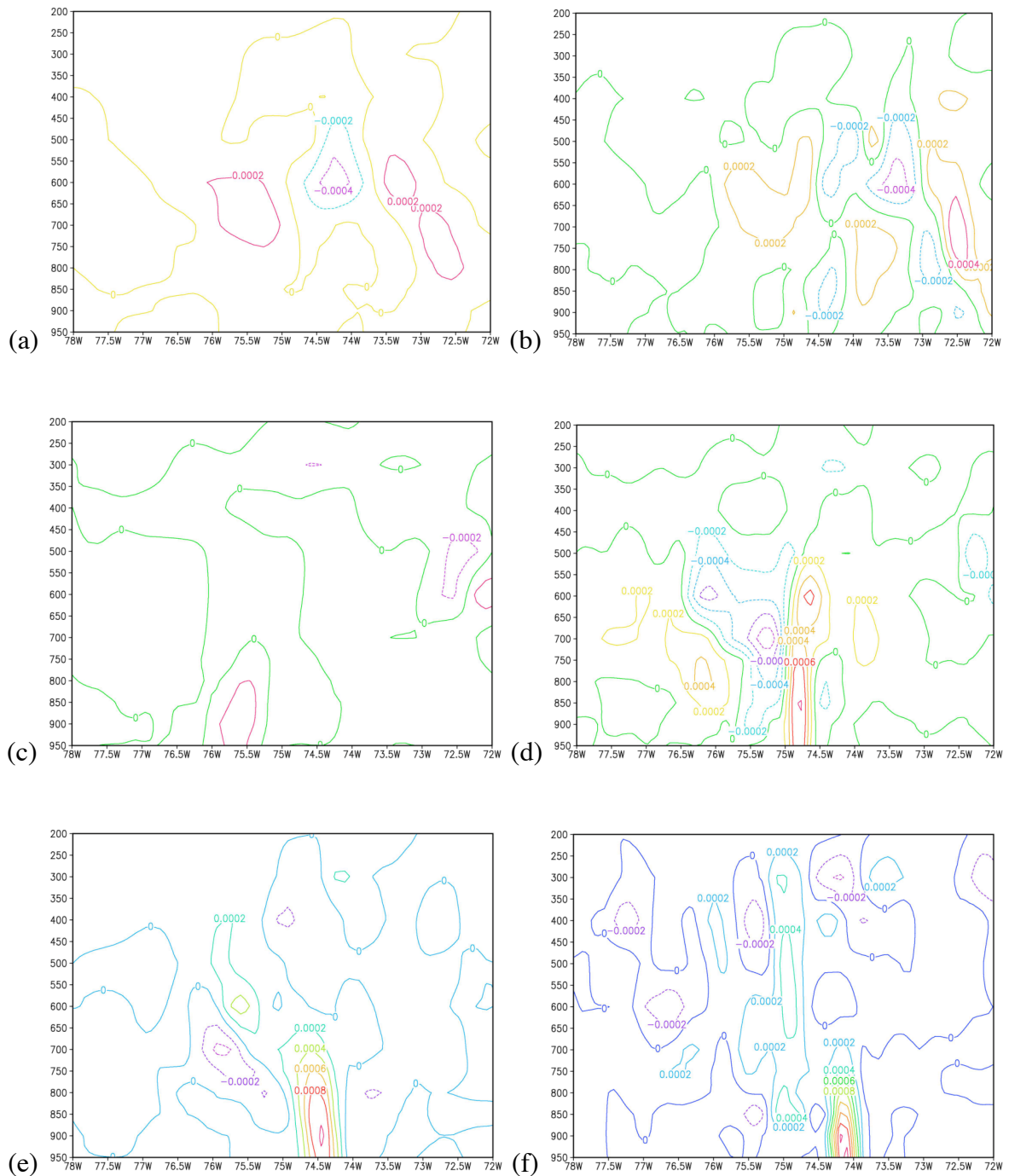


Figure 7.29 Cross sections of vorticity (10^{-5} , s^{-1}) at latitude 34.5N, and covering longitudes 78W to 72W for control / experimental valid 18Z 24 Jan 2000 (a/b), 00Z 25 Jan 2000 (c/d), and 06Z 25 Jan 2000 (e/f).

Along these same lines, cross sections of potential vorticity (Figure 7.30) also show higher values for the experimental simulation. The cross section was taken in the same location as the transect in Figure 7.29 (latitude 34.5N, and longitudes 78W to 72W). The 6 h time window corresponds to the passage of the center of the surface low pressure. However, as in the previous cross sections, the control simulation's low is lagging the experimental simulations low pressure by an hour or so, thus Figure 7.30a does not show significant development. When comparing Figure 7.30c (control) to Figure 7.30d (experimental) differences can be noted throughout the vertical structure of the storm. Both figures are valid 06Z Jan 25. It is not surprising that the experimental is 6 pvu at the surface, 2 pvu higher than the control. What is interesting is that there is a noticeable difference in PV all the way up to the 200 mb level. These influences are quite large even considering it is 30 h into the simulation.

Figures 7.31 through 7.33 illustrate a different perspective of the simulations using Vis5D. This is part of the MM5 ported to OS X project explained in Appendix A. Although the "still" figures are more for visualization than information, the ability to see 3-D animations of storm development opens a new door for air-sea analysis.³ Unfortunately the animations cannot be shown in the text. The plots show cloud moisture which is colored to temperature (height). In Figure 7.31, valid 12Z Jan 24, only slight differences can be seen between the control and experimental simulations. There are two areas of enhanced surface-

³ For an even greater Vis5D experience, turn down the green in the RGB color slide window in the side panel while leaving the red and blue high, and view the animation with 3-d "movie" glasses.

level convection directly south of Cape Hatteras and further offshore. There are even less differences between plots in Figure 7.32 which is 24 h into the simulation (00Z Jan 25). This is most likely a factor of the chosen perspective. There is noticeable noise from grid spacing feeding back into the model from the SST data. However, the perspective when comparing the control to the experimental is not exactly the same. This misalignment accounts for most of the isosurface smoothing, particularly in the control. The experimental simulation in Figure 7.33 (12Z Jan 25) has increased amounts of cloud moisture at the surface-level; however, it is seen along a much narrower swath. This is likely a result of the increased surface sensible heat flux, and agrees quite well with the plot of sensible heat flux valid 12Z Jan 25 seen in Figure 7.14b. As stated earlier, this type of plot is more for the visualization during animation, so obtaining numerical values from Vis5D still images is second to GrADS.

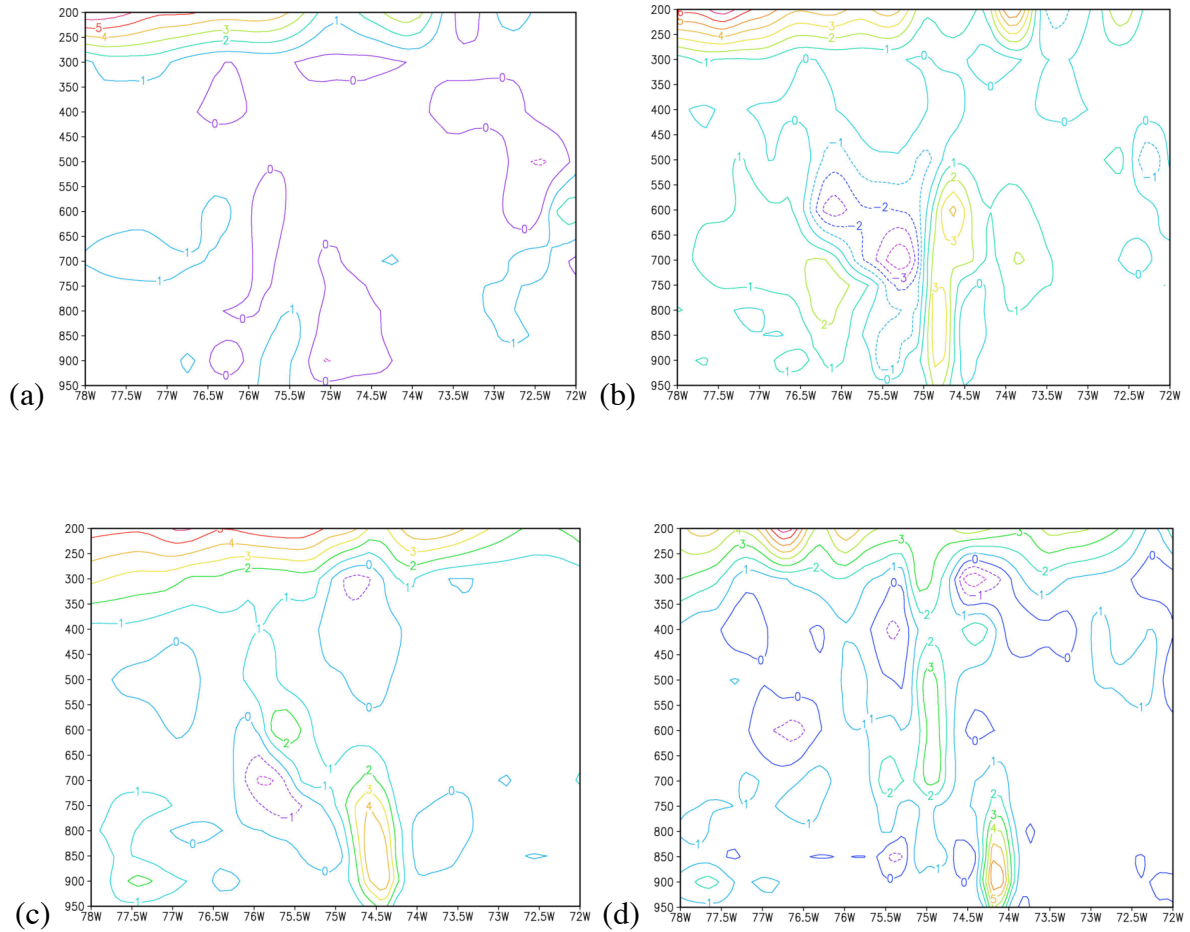


Figure 7.30 Cross sections of potential vorticity (pvu) at latitude 34.5N, and covering longitudes 78W to 72W for control / experimental simulations valid 00Z 25 Jan 2000 (a/b), and 06Z 25 Jan 2000 (c/d).

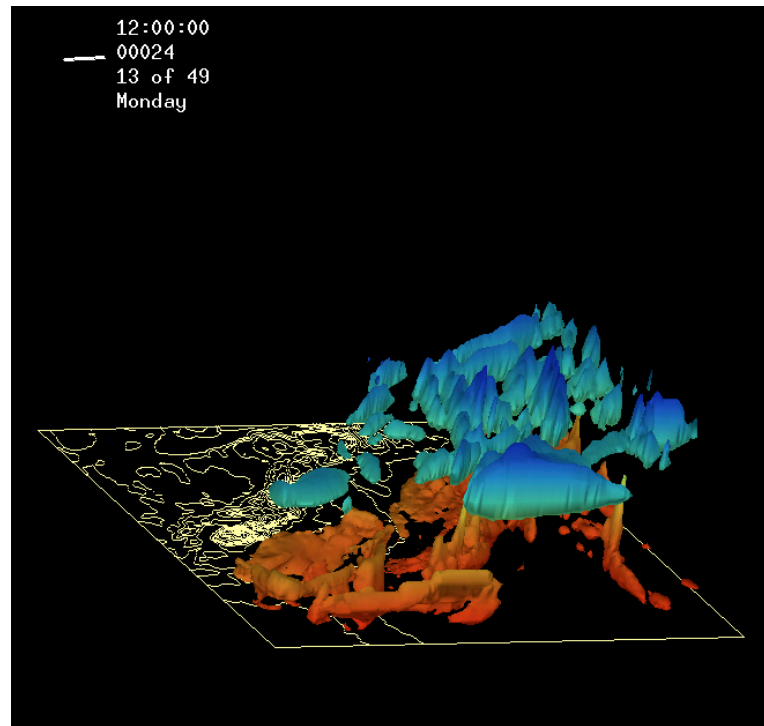
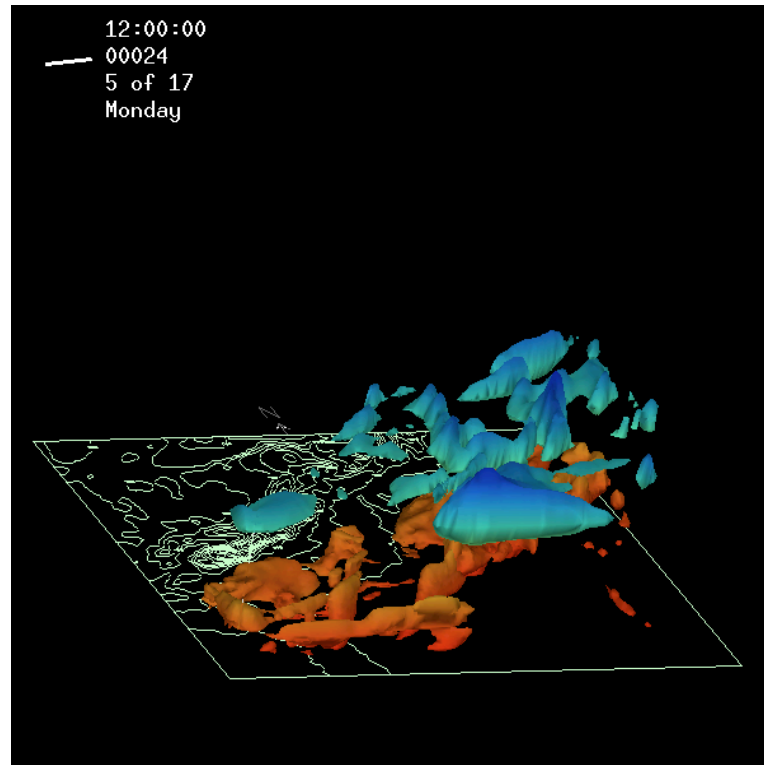


Figure 7.31 Cloud moisture colored to temperature (height) valid 12Z 24 January 2000. The control is on the top, and the experimental is on the bottom.

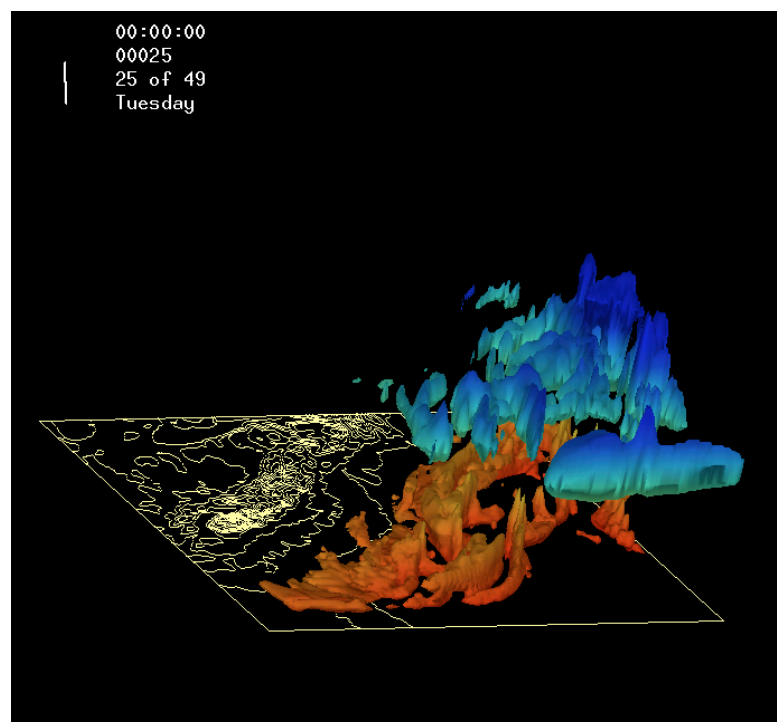
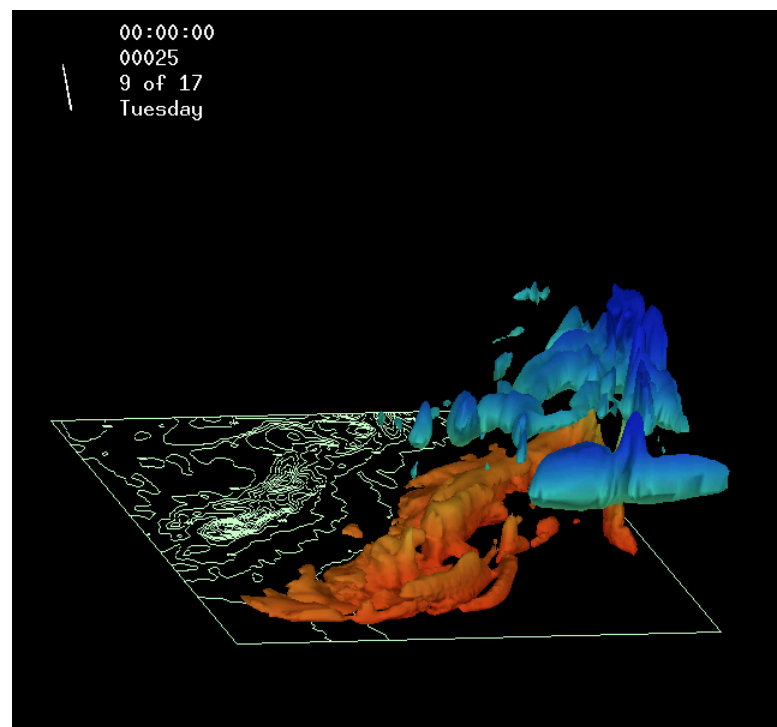


Figure 7.32 Cloud moisture colored to temperature (height) valid 00Z 25 January 2000. The control is on the top, and the experimental is on the bottom.

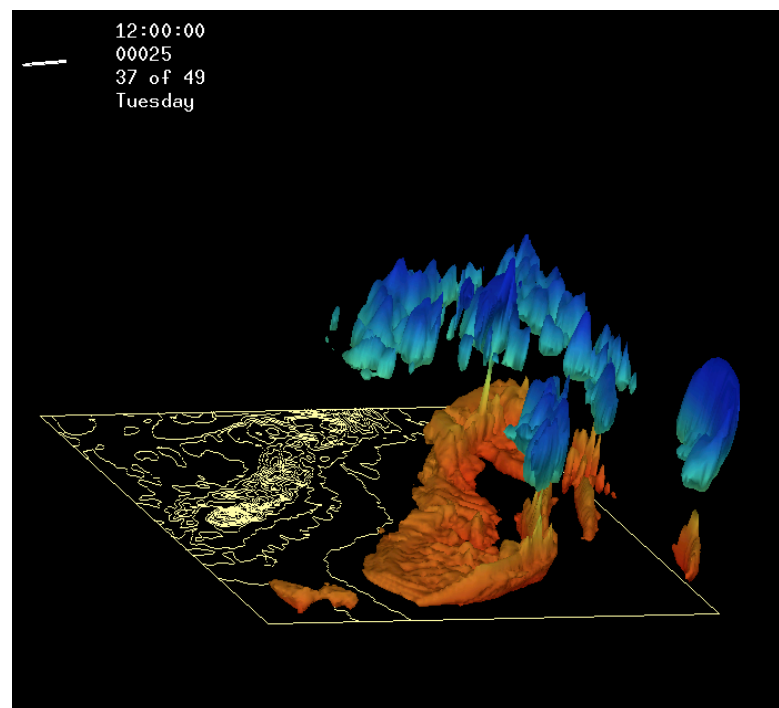
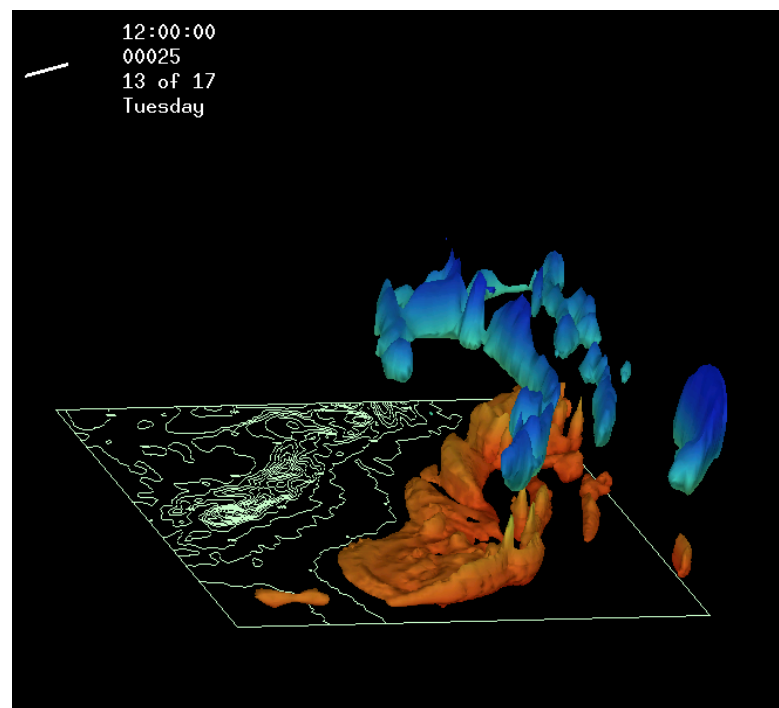


Figure 7.33 Cloud moisture colored to temperature (height) valid 12Z 25 January 2000. The control is on the top, and the experimental is on the bottom.

7.7 Summary

The general purpose of this study was to investigate the role of the Gulf Stream in the development of east coast extratropical cyclones using the 24-25 January 2000 east coast storm. A specific objective was also to test the hypothesis that the forecast "busts" in track and deepening rate were linked, in part, to forecast model's initialization with low resolution SST data.

A comparison based on SST grid resolution was performed using MM5 to simulate the 24-25 January 2000 case. The parameters for the control and experimental simulations were identical with the exception of the SST input data set. The SST data for the initialization of the control simulation were derived from the NCEP 2.5° data, and the experimental simulation was initialized with 1.1 km SST data from 22 January 2000, less than two days prior to the start of the simulation. This was soon enough to reveal the influencing features, but prior to the increase in cloud cover. It was this data that revealed a more defined GSF, as well as two warm core surface filaments with SST values 5-7 C greater than that of the control's SST data set. This image had less than 10% clouds over the Gulf Stream region. To fix this problem of cloud cover, an interpolation routine was used to plot grid points based on the closest non-flagged values without clouds on all four sides. Once the cloud free SST dataset was constructed, it was mapped over the corresponding grid points in the SST dataset of the control run and then used to initialize the experimental simulation. Ship and buoy observations were compared against the imagery in the dataset to validate the abnormally high SST region off the southeast coast of NC.

In general, the performance of the experimental simulation was better than the control simulation. In the control simulation, the reduced development compared to the

experimental simulation may be due to the improper SST representation. Evidence suggests that the high resolution SST data did affect the track by changing the strength and location of the frontal boundaries. Thus, the control simulation's poor forecast may be linked in part to the weakly defined Gulf Stream Front during model initialization.

The track of the experimental simulation was much closer to the observed track than the control simulation, more so during the final 12 h of the simulations. The low pressure system in the experimental simulation tracked further west, as well as slightly faster than the control simulation. However, both simulations begin to lag the observed forward speed of the low pressure. When the control and experimental tracks begin to separate, the experimental's central low pressure experiences a sharp decrease.

Large areas of convergence along the GSF are seen in the experimental simulation. This convergence is more defined along a rapidly forming coastal front, which is far more evident in the experimental simulation. Wind vectors point to increased frontogenesis in a line paralleling the GSF. The other areas of convergence are shared by both simulations.

The largest values of sensible heat flux near the center of circulation in the control simulation never exceed 200 Wm^{-2} . However, in the experimental simulation, values are in excess of 500 Wm^{-2} . These large differences in sensible heat flux are partly a result of the increased wind velocities seen in the experimental simulation; however, the regions where the wind was slightly greater were quite localized. The majority of the coastal region seen in both simulations had wind velocities that differed less than 6-8 kts. This is partly because of the lack of storm development, but more a factor of position and weak SST data.

Both simulations share similar regions of 10-m wind velocities; however, closer to the center of circulation, the experimental simulation's 10-m winds exceeded the control's winds by about 8 kts with maximum values approaching 50 kts.

Comparisons of QPF, dBZ, and the NOWRAD 2 km base reflectivity verify that the intensity of the surface low pressure may not be linked the increased QPF. Although the QPF was larger for the experimental simulation, it was more a factor of the westward position than enhanced deepening rate.

Larger values of vorticity are seen in the experimental simulation which suggest that the increased deepening rate was a result of vortex stretching along the frontal boundary which sets up in the center of the transect. Although the time lag in forward motion of the control's surface low pressure affected the cross section's values, the 6-h change of near-surface vorticity for the control's simulation was much less than the experimental's values.

CHAPTER 8: SENSITIVITY TO BOUNDARY LAYER BAROCLINICITY

8.1 Introduction and Motivation

This experiment was devised in an attempt to isolate the contributions of the sea surface temperature's thermal gradient on extratropical cyclogenesis. In Chapter 5, the Atlantic Surface Cyclone Intensification Index (ASCII) data set was verified by adding 11 years and 4 months of new data to more than double the number of storms. Findings show that the regression fit of the new data changed less than 2%. This suggests that surface baroclinicity, quantified by the Pre-storm Baroclinic Index (PSBI), does contribute to the development of coastal cyclones. Not only is it a contributing factor, but when the storms were binned based on upper-level 500-mb vorticity, a nearly linear relationship of the amount of contribution was revealed. In Chapter 7, simulations were conducted on the 24-25 January 2000 winter storm case where a true high resolution SST input file was used to initialized the model instead of the coarse grid time-averaged file currently provided in the NCEP GRIB data sets. A significant increase in the deepening rate was found in response to the formation of a coastal front which was not seen in the control simulation. In this Chapter, both previous experiments are combined in a sensitivity case study using the 24-25 January 2000 case to verify the PSBI. This is done by systematically damping the effects of the SST gradient to test the hypothesis that numerical simulations of the 24-25 January 2000 case will follow deepening rates predicted by the PSBI. All other model initialization parameters are left unchanged with the exception of the SST file.

8.2 Model Configuration and Methods

Three different simulations were run in this experiment with the only change being the SST initialization file. These simulations will be referred to as (a), (b), and (c), and the significance of their corresponding SST inputs will be discussed below.

The basic model configuration was left unchanged from the case study of Chapter 7 with the exception of the variation in the SST discussed below, and the domain size. The simulations were done using NCAR/PSU MM5 version 3.6. A single 10 km-grid domain (Figure 8.1) was initialized at 00Z 24 January 2000 with NCEP's operational analysis from the Eta-212 grid. For all simulations, the domain has 38 vertical σ levels between 1000 mb and 100 mb with 18 of the levels below 850 mb or 1.5 km. More sigma levels are located in the lowest 1.5 km of the atmosphere because fluxes of heat, moisture, and momentum occur in the planetary boundary layer. The model forecast was run to 48 hours, which simulated the storm through, and well beyond the inner domain and the maximum precipitation for the event.

As in the high resolution 24-25 January 2000 case (Chapter 7), the Kain-Fritsch cumulus parameterization was chosen, as well as the Eta M-Y planetary boundary layer model: (1.5 order TKE closure). Kain-Fritsch cumulus parameterization scheme was used to account for sub-grid scale convection (Kain *et al.*, 1993). The Advanced Cloud Radiation Scheme was used for radiation parameterization. The Simple Ice Scheme is used to reduce the number of processor calculations and decrease the model run times. The model uses explicit equations for cloud water, rain water, ice and water vapor. There is no super-cooled water and immediate melting of snow below the freezing level. The Oregon State University land surface parameterization (OSU) was chosen for the LSM.

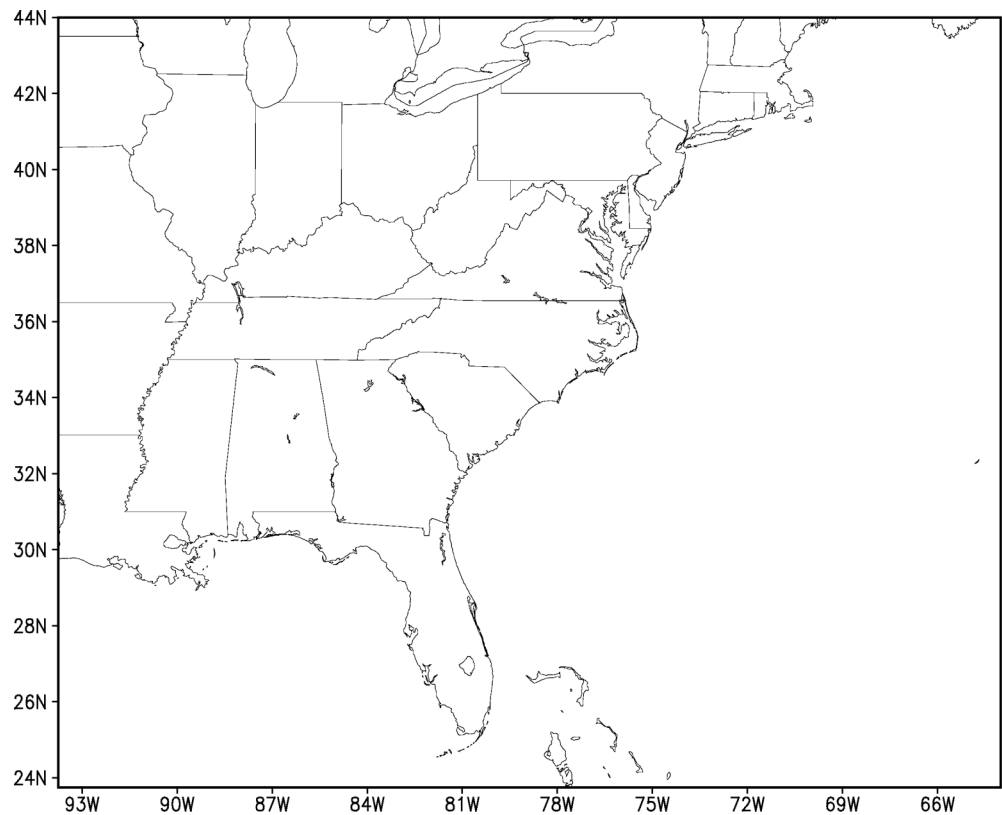


Figure 8.1 The SST sensitivity simulation's single outer domain of 10 km grid spacing. This domain was chosen based on the balance between having a domain large enough to minimizes forcing from boundary conditions, and the CPU memory limitations of a high resolution grid file with 38 sigma levels.

The systematic changing, or smoothing of the Gulf Stream SST was the only change within the simulations. This was done beginning with the unchanged SST data file (Figure 8.2a) used in simulation (a). This file is part of the standard initialization files from NCEP's operational analysis on the Eta-212 grid. The equation for the smoothing that simulations (b) and (c) underwent (Figures 8.2b and 8.2c) is expressed as:

$$T = T_c + \frac{1}{2}(T_0 - T_c) \quad (8.1)$$

where T is the calculated SST, T_c is the SST of the near coast (beach front), and T_0 is the initial SST. In order to only have this algorithm applied to the SST, and leave the land temperatures unchanged, a lower limit of 290 K was placed on T_c and T_0 . For example, in simulation (b), if $T_c = 290$ k and $T_0 = 298$ K, then the new SST (T) would be 294 K. If this "new" $T = 294$ K was then said to be the T_0 for simulation (b), the T for simulation (c) would be 292 K. This process is repeated until $T_c = T_0 = 290$ K, where upon the thermal gradient of the SST is completely eliminated. This method changes the PSBI systematically, but does change the GSF-coast distance as well as the GSF temperature. Therefore, a separate dependence can not be identified between the horizontal distance and the temperature of the GSF. However, the objective of this experiment is to verify ASCII using a mesoscale model simulation. Since the PSBI (Equation 5.5) includes both parameters, whether the numerator is increased, or the denominator is decreased, yields the same PSBI values as seen by the ASCII regression fit forecast method. The post-smoothed SST input files can be seen in Figure 8.2. Simulation (a) has the largest SST gradient, and simulation (c) has the smallest gradient.

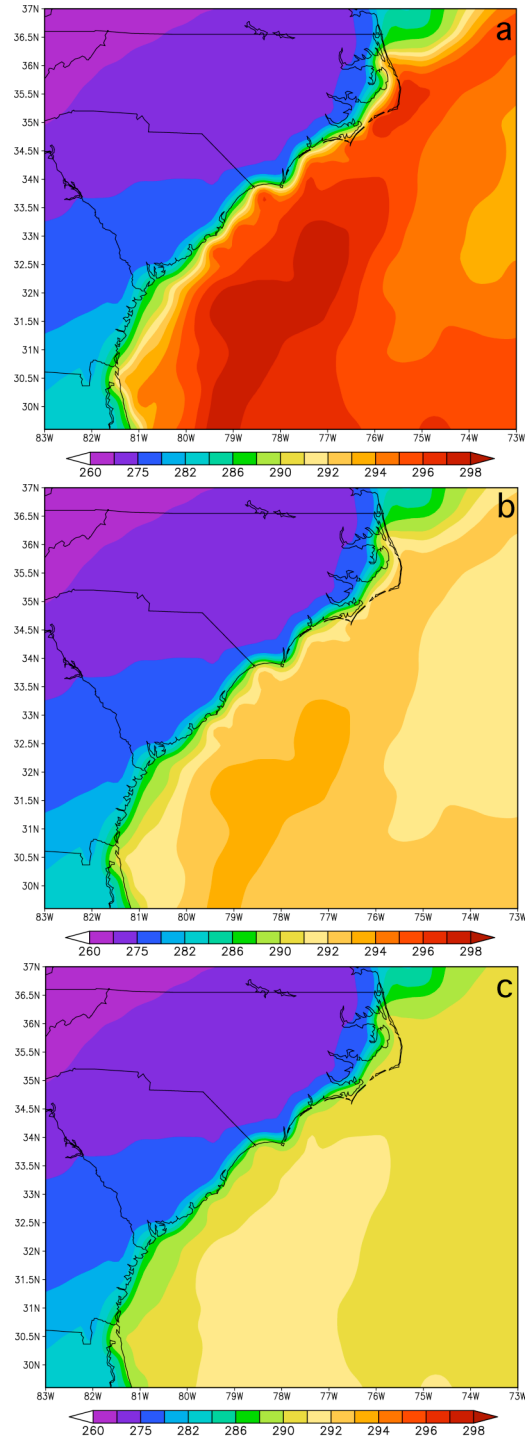


Figure 8.2 The three SST input files used in the simulations where (a) is the SST file with the largest gradient (with almost unrealistic values for January), (b) is the product of the first smoothing run, and (c), the weakest gradient, a product of the second smoothing run. The PSBI values are $2.8^{\circ}\text{C}/10\text{km}$, $1.8^{\circ}\text{C}/10\text{km}$, $1.2^{\circ}\text{C}/10\text{km}$ for (a), (b), and (c) respectively.

The deepening rate was defined by the largest 12-h pressure drop as the surface low passed through the ASCII domain (Figure 5.1) which is the same method employed for the ASCII study when using the re-analysis maps. There was also an attempt made to group the (a), (b), and (c) simulations into a bin based on the 500-mb vorticity, however, this posed an inherent problem in trying to separate the surface disturbance from the upper-level forcing. Although the only change made was to the SST initialization file, which altered the surface low development, the effects of the change extended throughout the upper mid-troposphere. At the time the surface low entered the ASCII domain, the simulation was well underway (26-28 h into simulation). The variations in intensity at the surface were altering the 500-mb vorticity through mutual feedback. However, the changes were minor, and did not extend beyond the limits of the bin (using the 3-bin method seen in Chapter 5).

8.3 Results

8.3.1 Sea-level pressure comparison

The deepening rate, or change in sea-level pressure, was of most concern because of its use in the ASCII forecast. As a result, several plots of sea-level pressure can be seen on the following pages for the purpose of marking the peak deepening rate for the ASCII calculations, as well as observing the differences in growth of the cyclone. The first figure (8.3a,b, and c) valid 12Z Jan 24 (12 h into simulation) shows conditions preceding the development of the main storm. The simulations (a), (b), and (c) correspond to the same (a), (b), and (c) of the SST plots in Figure 8.2. This will be the case for all of the following figures as well. The circulation seen is a small area of low pressure which formed along the coastal front preceding the main storm around 33N, 76W. At this point, simulation (b) shows

the deepest value of central pressure at 1005 mb, but this could also be due to adjustments occurring close to the initialization. The minimum pressure seen in Figures 8.3a and 8.3c is 1008 mb.

Figure 8.4 shows the development six hours later (18Z Jan 24) where the initial stages of the cyclone development can be observed. In simulations (b) and (c), the low pressure's center appears from the south after forming off the coast of Florida above 77W. Simulation (a), seen in Figure 8.4a, shows the same area of low pressure, but the forward motion has already surpassed that in the other simulations and is located 31N, 78W to 34N, 75W. The central pressure of (a) is the same as (b), and 1 mb lower than (c).

By 00Z Jan 25 (Figure 8.5, 24 h into simulation), the low pressure is beginning to strengthen rapidly. This is most noticeable in Figure 8.5a where the convergence extends over the warm-core eddy off Cape Hatteras (seen in Figure 8.2a) as a result of the elongated central low pressure running north to south at 75.2W. Simulations (b) and (c) are more closely matched, although minor differences can be seen. The pressure of (a), at 00Z Jan 25 is 1 mb lower than (b), and 2 mb lower than (c). The isobars along the northwest side of simulation (c) are more curved matching the more diluted SST gradient seen in Figure 8.2c. Simulation (b)'s contours align more with the SST gradient (Figure 8.2b), but nowhere near the curvature that is observed in simulation (a) (Figure 8.2a).

Figure 8.6, valid 06Z Jan 25, (30 h into simulation) illustrates the largest difference in position seen between the runs where (a) is much closer to the coast than (b) and (c). The central pressures are 988 mb, 992 mb, and 993 mb for (a), (b), and (c) respectively. Simulation (a) is still trying to hold on the double-low structure as the upper of the two low pressure centers will eventually take over. This transfer in central low pressure location adds

to the apparent forward motion of (a). At 06Z Jan 25, the low center in simulation (c) is actually further north than in the other simulations, (b) and (c), but is also on a track taking it further east, and away from the coastline.

Thirty six hours into the simulation (valid 12Z Jan 25) the positions of the central low pressures begin to come back together and follow the same track (Figure 8.7). This is likely a result of the lows moving north of the region of SST gradient. However, the difference in sea-level pressure continues to grow where (a) is 980 mb, (b) is 988 mb, and (c) is 991 mb. At this point simulation (a) is obviously a significantly stronger storm with greater wind. The wind pattern of (a) is also more north-south oriented over NC (Figure 8.7a), as well as more tightly wrapped around the center of the low pressure.

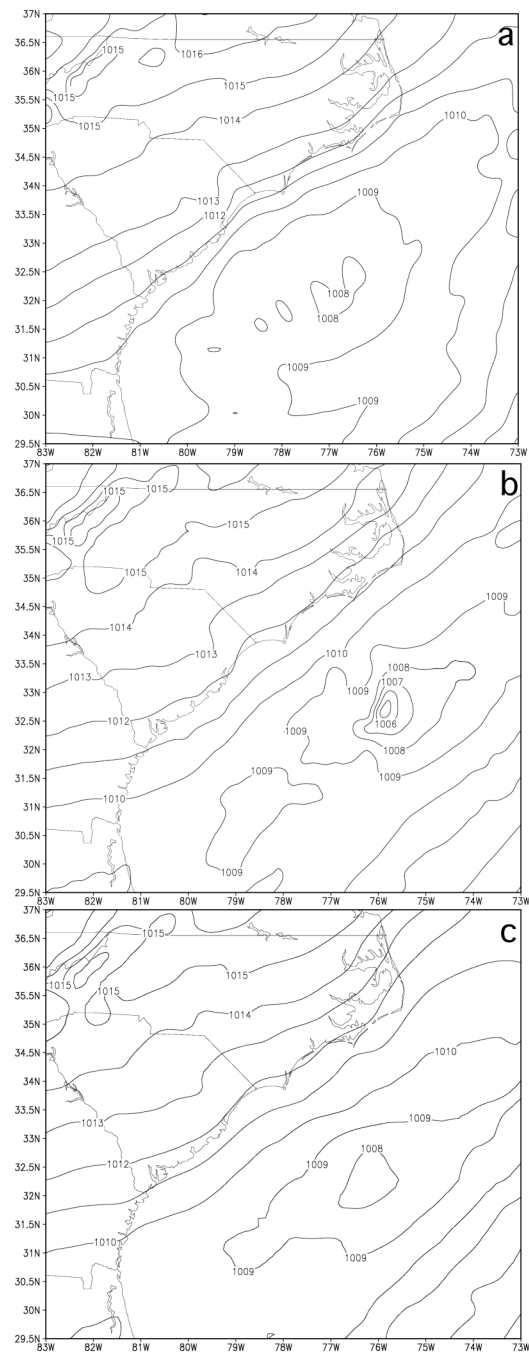


Figure 8.3 Plots of sea-level pressure for simulations (a), (b), and (c) valid 12Z 24 Jan (12 h into simulation). The low pressure seen is a small area of low pressure forming along the coastal front.

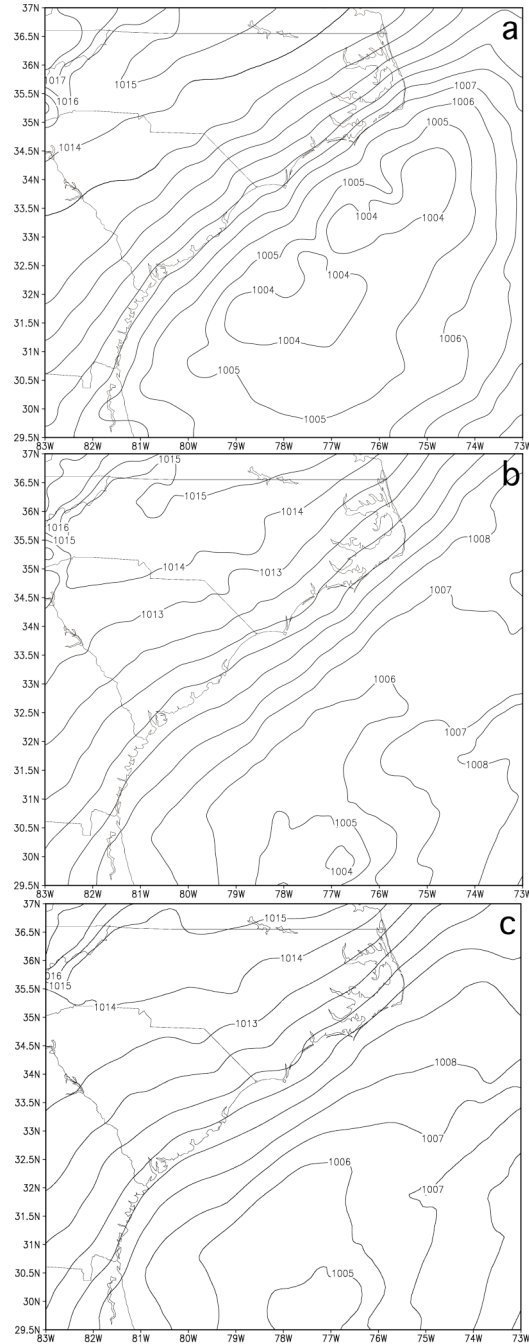


Figure 8.4 Plots of sea-level pressure for simulations (a), (b), and (c) valid 18Z 24 Jan (18 h into simulation). The initial stages of the main coastal storm can be seen.

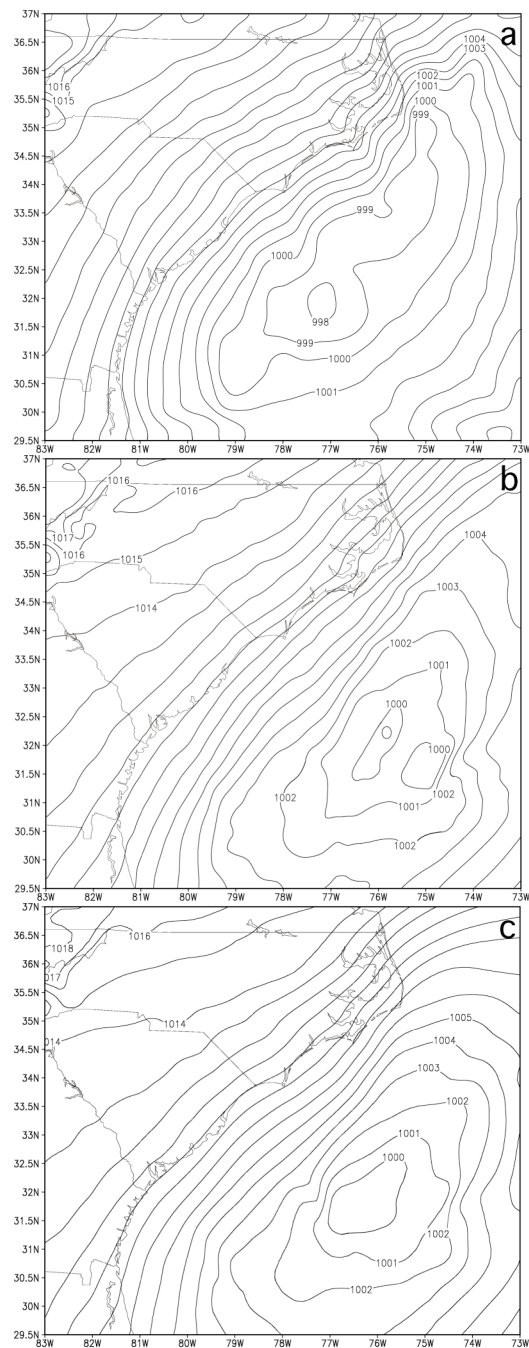


Figure 8.5 Plots of sea-level pressure for simulations (a), (b), and (c) valid 00Z 25 Jan (24 h into simulation).

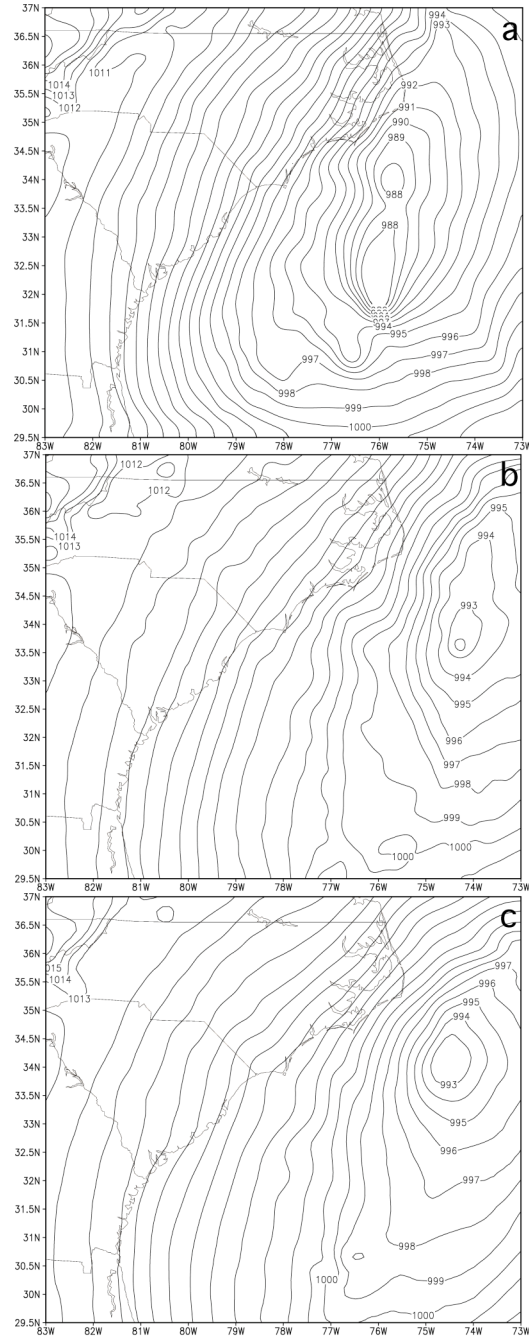


Figure 8.6 Plots of sea-level pressure for simulations (a), (b), and (c) valid 06Z 25 Jan (30 h into simulation).

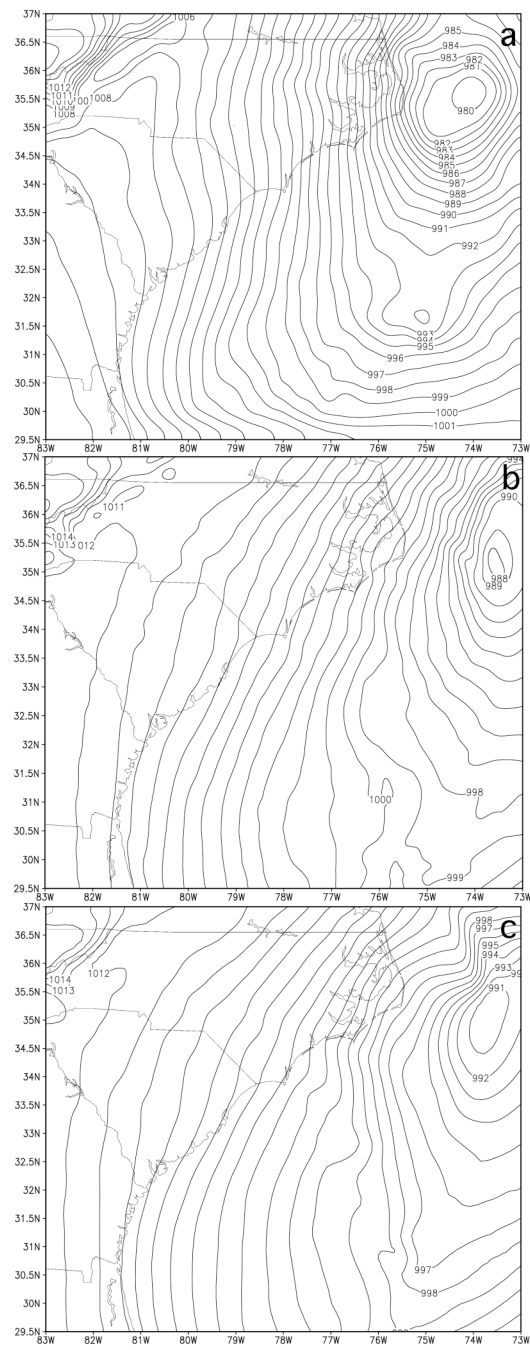


Figure 8.7 Plots of sea-level pressure for simulations (a), (b), and (c) valid 12Z 25 Jan (36 h into simulation).

8.3.2 500-mb absolute vorticity comparison

Plots of the 500-mb absolute vorticity are seen in Figures 8.8, 8.9, and 8.10. These figures show the 12-h evolution of the maximum absolute vorticity zone seen in the final figure (8.10). As mentioned earlier, the feedback from the developing surface low pressure enhanced the upper-level vorticity more in (a) than in (b) and (c). In Figure 8.8, there are minor zones of differing vorticity, but 6 h, and even 12 h later, the regions are much more noticeable. Figure 8.8a, which is valid 00Z Jan 25, has one larger area of negative vorticity ($-5 \times 10^{-5} \text{ s}^{-1}$) located at 36N, 77W which is not seen in Figures 8.8b, and Figure 8.8c. Otherwise, differences in Figure 8.8 are decreasing by about $1 \times 10^{-5} \text{ s}^{-1}$ as comparing (a) to (b), and (b) to (c).

In Figure 8.9a, the vorticity is significantly enhanced along the edge of the new center of low pressure forming in response to the warm-core eddy. As a result, large pressure falls occurred in (a) between 06Z and 12Z Jan 25 (Figures 8.6a and 8.7a). Figure 8.9a, the simulation with the largest SST gradient, has values of 500-mb vorticity exceeding $16 \times 10^{-5} \text{ s}^{-1}$ over a region south of Cape Hatteras at 34N, 77.7W. This was $3 \times 10^{-5} \text{ s}^{-1}$ greater than simulation (b), and almost double the values seen in simulation (c) for the same time and location.

The 500-mb vorticity values in Figure 8.10a, of $17 \times 10^{-5} \text{ s}^{-1}$ over a region northeast of Cape Hatteras (36.5N, 74.5W) exceeded simulation (b)'s vorticity by $5 \times 10^{-5} \text{ s}^{-1}$, and again, doubled the values seen in simulation (c).

This vorticity response would typically be expected; however, it posed an inherent problem when trying to apply the same binning methods to the (a), (b), and (c) simulations. The fact that the surface disturbance cannot be separated from the upper-level forcing (that it

is influencing) results in 3 different storms, which differ through the upper mid-troposphere, and not just at sea-level.

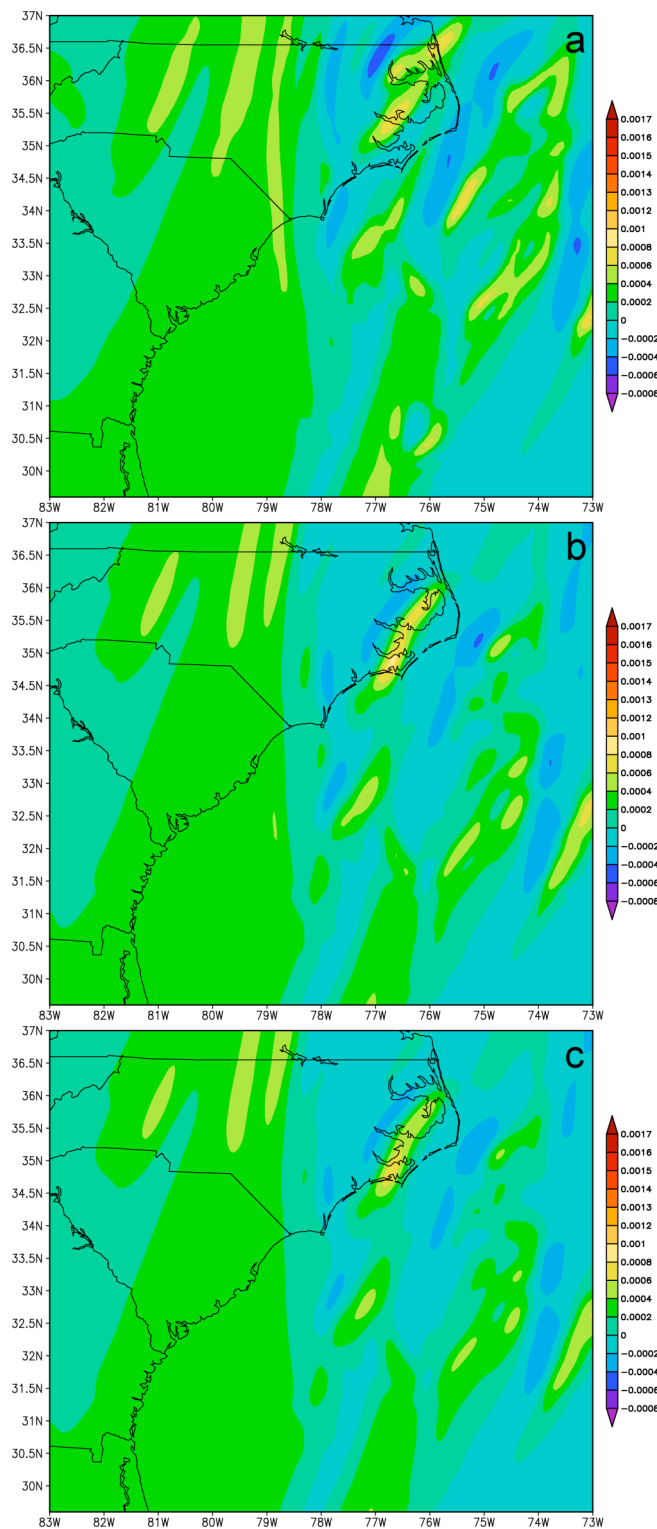


Figure 8.8 Plots of 500-mb vorticity (10^{-1} s^{-1}) for simulations (a), (b), and (c) valid 00Z 25 Jan 2000 (24 h into simulation).

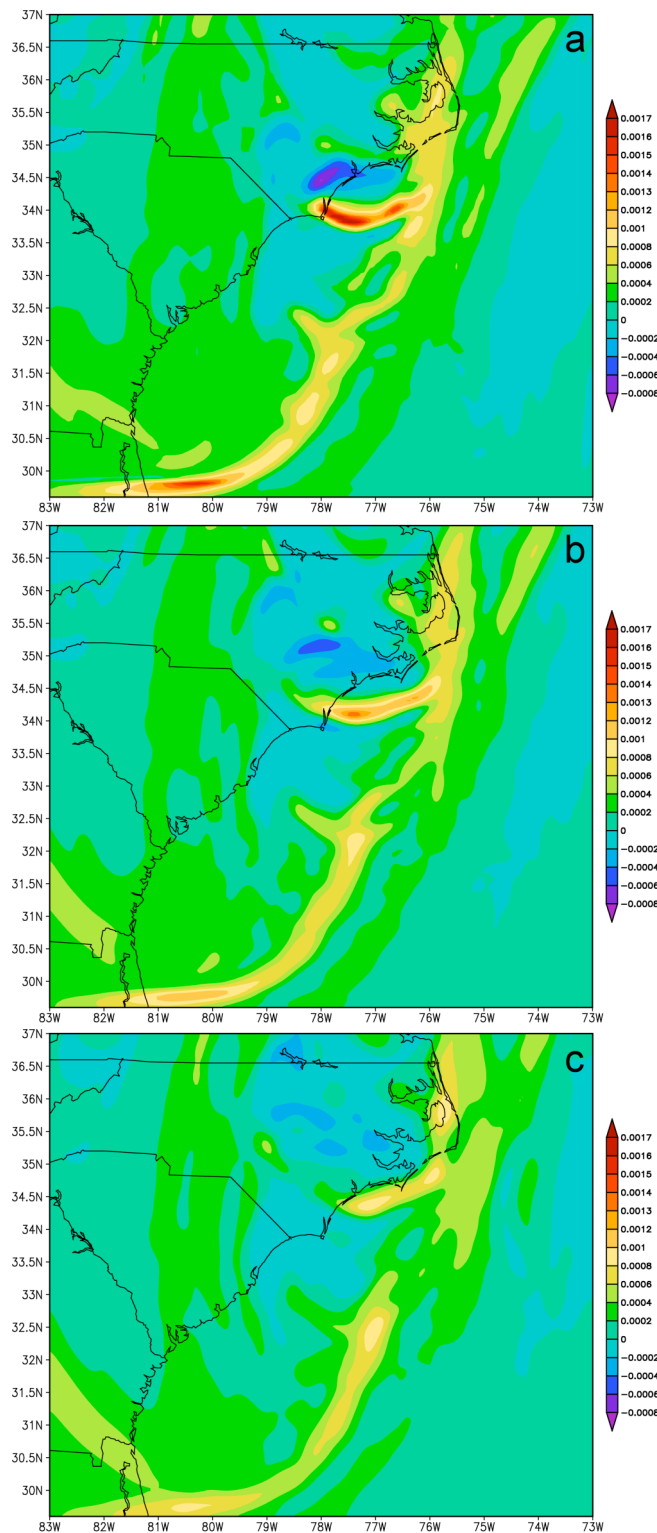


Figure 8.9 Plots of 500-mb vorticity (10^{-1} s^{-1}) for simulations (a), (b), and (c) valid 06Z 25 Jan 2000 (30 h into simulation).

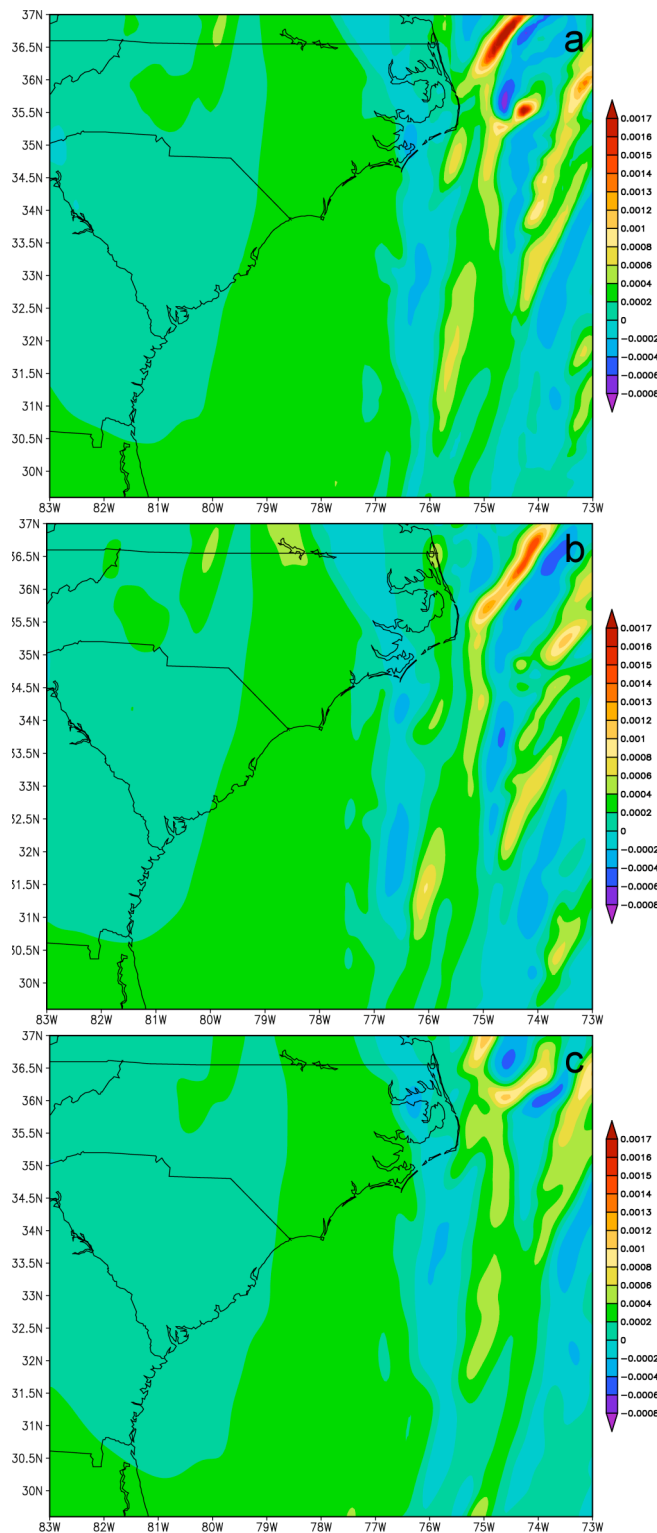


Figure 8.10 Plots of 500-mb vorticity (10^{-1} s^{-1}) for simulations (a), (b), and (c) valid 12Z 25 Jan 2000 (36 h into simulation).

8.3.3 PSBI comparison

Calculations for the PSBI, according to the simulations, used the same equation (Equation 5.5) discussed in Chapter 5. The results were computed from numerical gridded output files and accurate to within 5 km (half the grid space difference). $T_l = 5.6^\circ\text{C}$ was recorded during the initialization (24 h prior to development), and is the same for (a), (b), and (c). For simulation (a), $T_{GSF} = 25^\circ\text{C}$, and $d = 70$ km resulting in a PSBI value of $2.8^\circ\text{C}/10\text{km}$. This PSBI value is much higher than the PSBI value of $2.1^\circ\text{C}/10\text{km}$ calculated using the actual observations (discussed in Chapter 7). For simulation (b), $T_{GSF} = 20^\circ\text{C}$, and $d = 80$ km resulting in a PSBI value of $1.8^\circ\text{C}/10\text{km}$, and finally, for simulation (c), $T_{GSF} = 19^\circ\text{C}$, and $d = 110$ km resulting in a PSBI value of $1.2^\circ\text{C}/10\text{km}$. These numbers are truncated, and this is an inherent obstacle when plotting model's gridded data. The actual "observed" calculation was done using 1.1 km resolution SST imagery, so not only will the GSF value not be truncated, but the location is accurate to within 1 km.

The sea-level pressure was obtained from Figure 8.5 (valid 00Z Jan 25) to Figure 8.7 (valid 12Z Jan 25). This corresponded to the 12-h period of greatest deepening. For simulation (a), the change in pressure was 18 mb, the largest drop of the 3 simulations. Both (b) and (c) experienced pressure decreases of 11 mb and 18 mb respectively. These values were plotted against the PSBI values, discussed above, in the Figures presented below.

8.3.4 ASCII comparison

As explained in Chapter 5, the 6-bin procedure was conducted based on the strength of the nearest maximum of 500-mb absolute vorticity associated with the surface low (Figure 8.11). The maximum absolute vorticity value for each storm was selected during the same

12 h period used for ΔP in the ASCII dataset. In order to achieve similar quantity in terms of the amount of storms per bin, the absolute vorticity values covered by each bin are greater at both extremes. For example, bin "16" is by itself because there were several storms with a maximum absolute vorticity greater than $15 \times 10^{-5} \text{ s}^{-1}$ and less than $17 \times 10^{-5} \text{ s}^{-1}$. Likewise, bins "21+" and "13-" were grouped because of the lack of storms with maximum absolute vorticities above $20 \times 10^{-5} \text{ s}^{-1}$, and below $14 \times 10^{-5} \text{ s}^{-1}$. Figure 8.11, which shows the ASCII dataset (1991-2002) of ETC's ($\Delta P/12\text{h}$ vs. PSBI) broken down into bins of 500-mb vorticity (10^{-5} s^{-1}), is plotted along with the (a), (b), and (c) sensitivity simulations. Linear regression fits were done for each bin, as well as the sensitivity simulations. Once again, the stratified bin positions, suggest that there is a shifting degree of mutual dependency on surface versus upper-level forcing. It is interesting to see where the simulations fall according to the binned method even though the vorticity was slightly different for each run. It should be mentioned here that the maximum 500-mb vorticity values of $17 \times 10^{-5} \text{ s}^{-1}$ for (a) and $16 \times 10^{-5} \text{ s}^{-1}$ for (b), and (c) were much less than the observed maximum 500-mb absolute vorticity value of $19 \times 10^{-5} \text{ s}^{-1}$. This is a result of less than accurate model initialization fields prior to the "spin-up" which did not properly capture the upper-level trough (e.g. Zhang et al. 2002; Buizza and Chessa 2002).

A final comparison was done with the updated ASCII dataset (1980-2002) of ETC's $\Delta P/12\text{h}$ vs. PSBI (Figure 8.12). The "Storms" (blue) linear regression fit combines both sets of storms (1980-1990 and 1991-2002), and the sensitivity simulations (a), (b), and (c) with regression fit (red). Although there are only three data points to base the regression on, it aligns well with the fit for the ASCII data set. The very high correlation coefficient of 0.986 for the sensitivity simulations fit is a result of only having 3 data points. Even with 3 points,

the simulations (a, red circle), (b, green circle), and (c, black circle) fell in a line that shared a similar slope as the ASCII fit. Since the SST gradient was exponentially decreased in half, the (a) simulation falls much further down the vertical axis than (b) and (c).

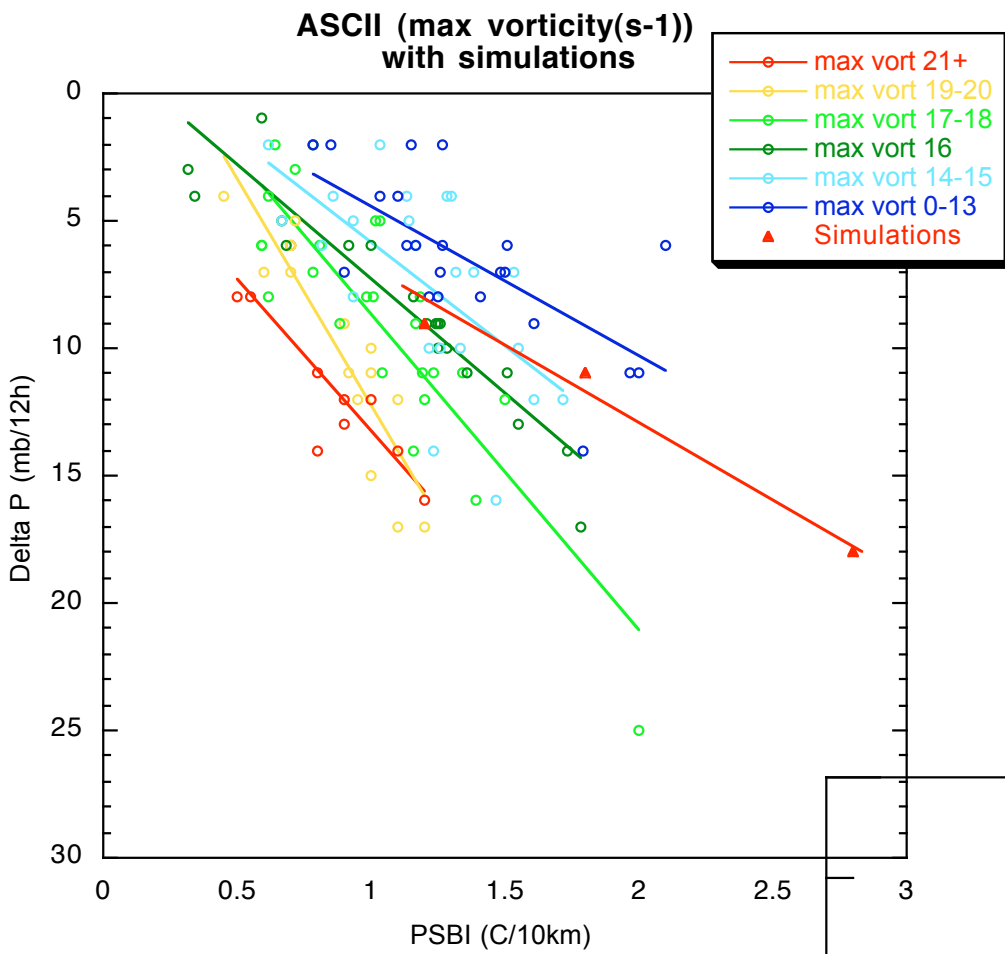


Figure 8.11 The ASCII dataset (1991-2002) of ETC's ($\Delta P/12h$ vs. PSBI) broken down into bins of 500mb vorticity ($10^{-5}s^{-1}$) plotted with the (a), (b), and (c) sensitivity simulations.

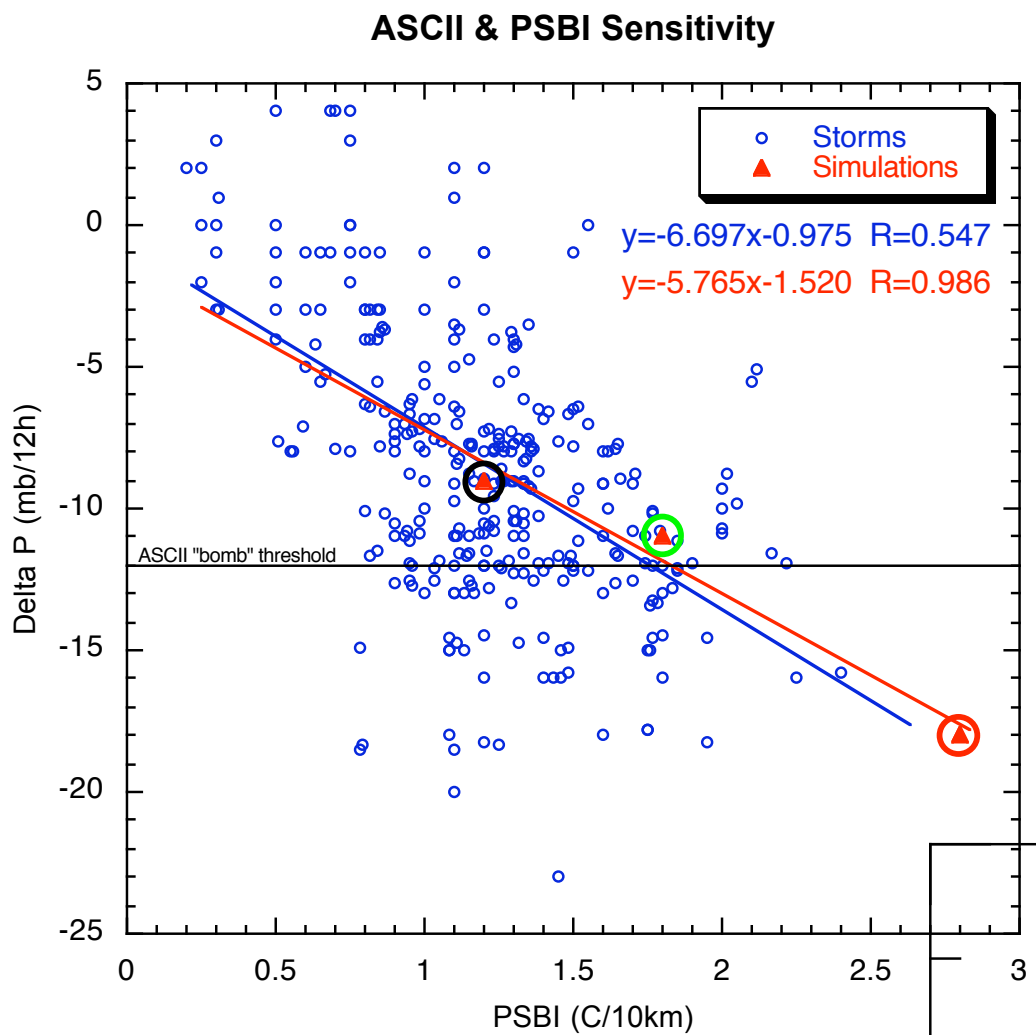


Figure 8.12 The updated ASCII dataset (1980-2002) of ETC's $\Delta P/12h$ vs. PSBI. The "Storms" (blue) linear regression fit combines both sets of storms (1980-1990 and 1991-2002), and the sensitivity simulations (a, red), (b, green), and (c, black) with regression fit (red).

8.4 Summary

Using the mesoscale model MM5 version 3.6, a 48 h simulation was run 3 times. For each consecutive simulation, the SST data input file was systematically altered to decrease the effects of the thermal gradient. There were no other changes to the simulation's initialization grid files. Thus, the three simulations shared the same upper-level forcing characteristics.

The pre-storm baroclinic index (PSBI) was calculated for each storm using the initialization data, and plotted against the deepening rate for the respective storm. The PSBI for simulation (a) was intentionally set to a value much larger than would be observed in nature. Not only was the SST excessively high, but there was essentially no transition from cold near-coast water to the GSF, as the GSF was placed along the coastline. It was the objective of this study to have PSBI values that would separate the data points along the x axis of the ASCII plot, so unrealistically large, as well as small PSBI values were intentionally derived. The graphical results verify the slope of the ASCII discussed in Chapter 5 by the matching slope of the three simulations.

CHAPTER 9: SENSITIVITY TO GULF STREAM POSITION

9.1 Introduction and Motivation

This experiment was devised in an attempt to isolate the contributions of the sea surface temperature's thermal gradient on extratropical cyclogenesis. In Chapter 5, the Atlantic Surface Cyclone Intensification Index (ASCII) data set was verified by adding 11 years and 4 months of new data to more than double the number of storms. Findings show that the regression fit of the new data changed less than 2%. This suggests that surface baroclinicity, quantified by the Pre-storm Baroclinic Index (PSBI), does contribute to the development of coastal cyclones. In Chapter 8, both previous experiments, from Chapter 5 and Chapter 7, were combined in a sensitivity case study using the 24-25 January 2000 winter storm to verify the PSBI by systematically damping the effects of the SST gradient. This was done to test the hypothesis that numerical simulations of the 24-25 January 2000 case will follow deepening rates predicted by the PSBI. As expected, this was the case. However, there was an inherent inability to isolate which factor within the PSBI was responsible for rapid cyclogenesis (i.e. the Gulf Stream's position or Gulf Stream's SST) because the damping reduced the PSBI value as a whole. From Equation 5.5, the resulting value could reflect either a smaller numerator (lower SST values), or larger denominator (greater distance from shore). The objective of this experiment is to isolate the contribution to surface-level forcing based on the position of the Gulf Stream without changing the magnitude of the SST. The hypothesis follows the theory behind ASCII in that a reduction in deepening rate is expected as the position of the Gulf Stream is shifted further away from shore. The reasoning behind this is twofold. First, as shown by ASCII, a weaker thermal

gradient will dampen low-level cyclogenesis by reducing boundary layer baroclinicity. However, a more complex reason, which may be more case specific, is the surface to upper-level trough position offset which can either enhance or reduce the vertical feedback. It is evident from Chapter 7 that the surface low pressure will attempt to track along the frontal boundary formed over the GSF as a result of the preexisting vorticity. In this experiment, the Gulf Stream has been shifted to the east while leaving the unique features and SST values unchanged. The final objective is to verify ASCII from the GSF position parameter, as well as to test the hypothesis that by altering the track of the surface low, the feedback link to the upper-level trough will be weakened thus reducing the surface-level cyclogenesis.

9.2 Model Configuration and Methods

Three different simulations were run in this experiment with the only change being the SST initialization file. These simulations will be referred to as the control simulation (*Cntl* or "a"), the experimental simulation 1 (*Exp-1* or "b"), and the experimental simulation 2 (*Exp-2* or "c"). The significance of their corresponding SST inputs and the horizontal gradients will be discussed below.

The basic model configuration was left mostly unchanged from the numerical experiments of Chapter 8 with the exception of some model physics parameters, and the variation in the SST. The simulations were done using NCAR/PSU MM5 version 3.6. A single 10 km domain (Figure 9.1) was initialized at 00Z 24 January 2000 with NCEP's operational analysis from the Eta-212 grid. The size of this domain has been increased significantly from that in Chapter 7 by adding 60 grid points to the x axis and 40 grid point to the y axis. For all simulations, the domain has 38 vertical σ levels between 1000 hPa and 100

hPa with 18 of the levels below 1.5 km. The model forecast was run to 48 hours to allow ample "spin-up" time.

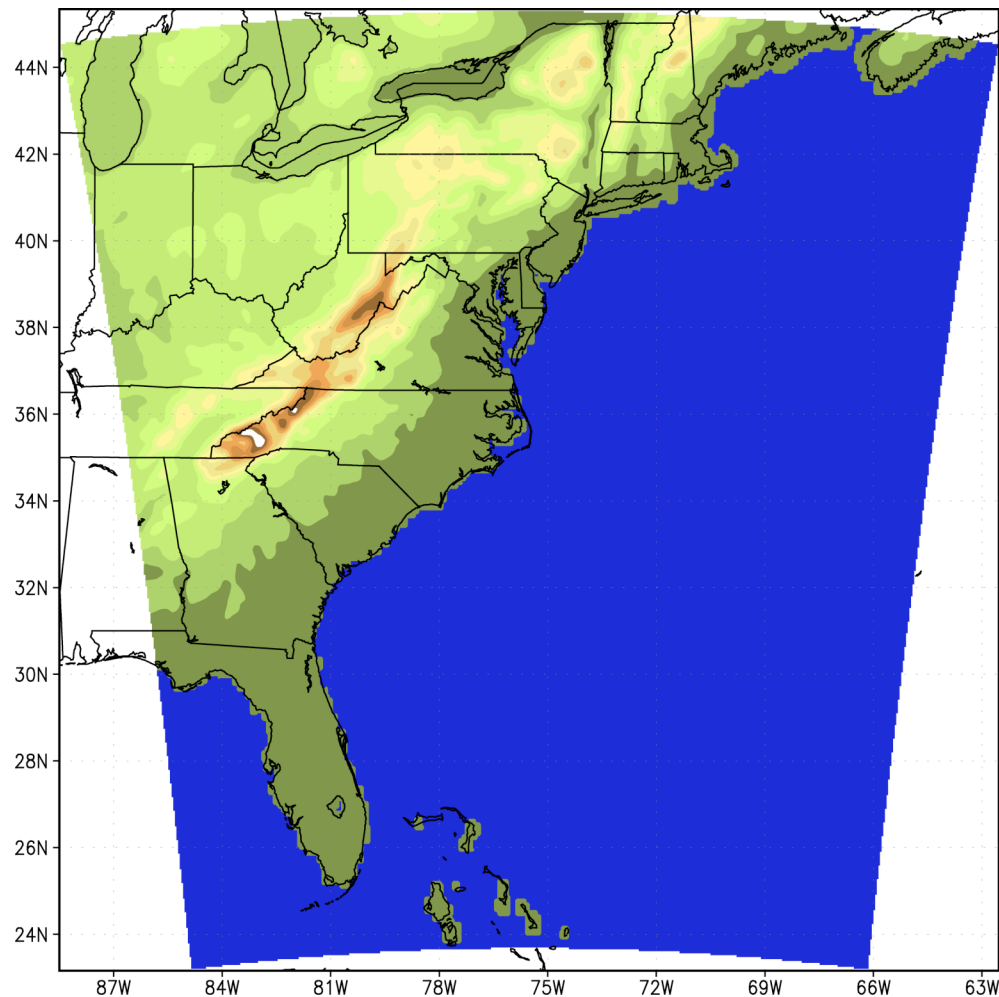


Figure 9.1 The model domain used for all simulations showing the terrain features colored to 100 m contours over the high resolution United States map.

In this experiment the Grell cumulus parameterization was chosen for its handling of convective precipitation at smaller grid scales. The Blackadar planetary boundary layer scheme was chosen because of its successful handling of winter storm systems when paired with the Grell cumulus parameterizations (Grell 1993). The other reason for changing from Kain-Fritch to the Grell/Blackadar combination was the use of the 5-layer soil model. The previous physics options were tied to the use of either the NOAH or OSU LSM which, through numerous sensitivity comparisons, made no significant improvements. This is understandably so for cases in the winter where the influence of vegetation is negligible. In fact, the northern most 30% of the domain for the 24 Jan 2000 case was initialized with snowcover on the ground.

Other physics options include the advanced cloud radiation scheme which was used for radiation parameterization. The simple ice scheme is used to reduce the number of processor calculations and decrease the model run times. Several simulations were conducted using the Reisner 2 microphysics with minimal improvements gained. There is no super-cooled water and immediate melting of snow below the freezing level.

The systematic shifting of the Gulf Stream SST was the only change within the simulations. This was done beginning with the unchanged high resolution SST data file (Figure 9.2a) used in the *Cntl* (a). This file includes the 1.1 km grids that were mapped over the Eta-212 (40 km) grid. The initial mapping procedure was discussed in Chapter 7.

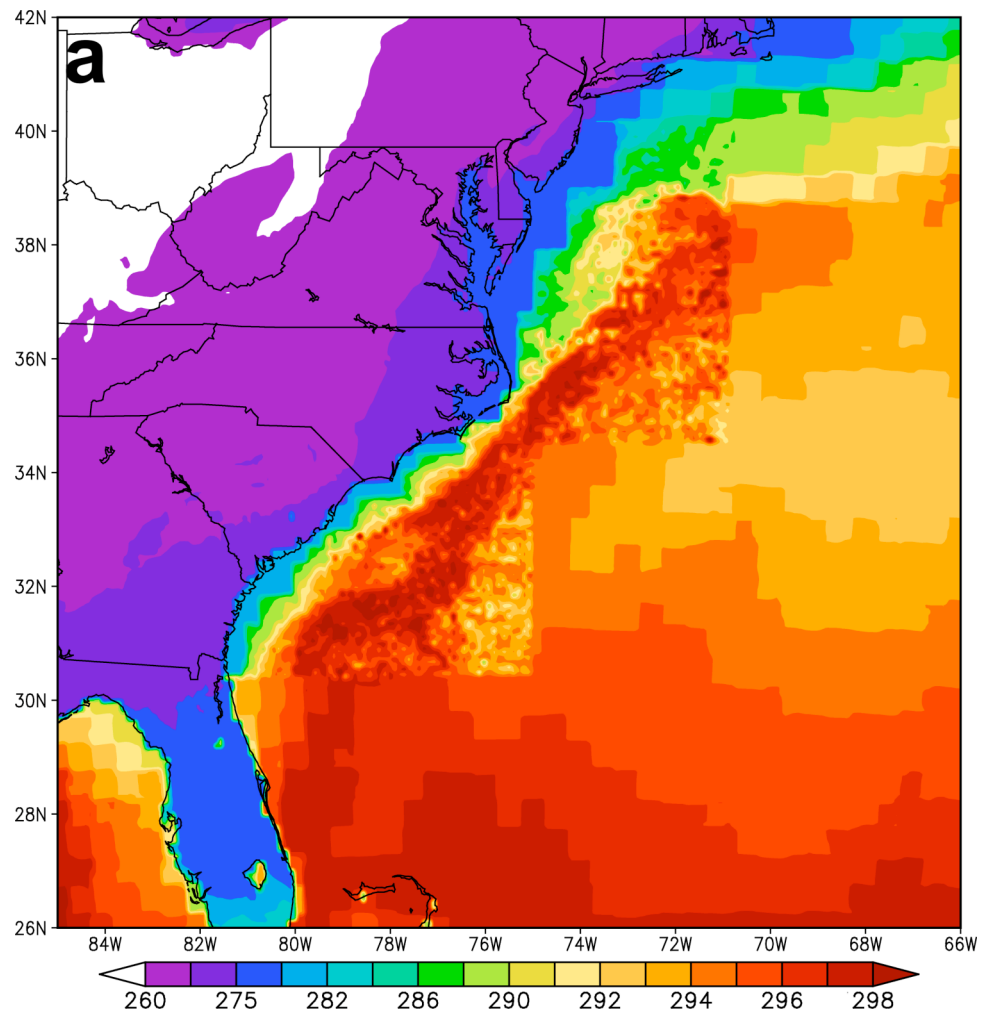


Figure 9.2a The SST initialization file for the *Cntl* simulation. Post regridded to 10 km with no shift to the high resolution data. The high resolution data is from 22 Jan 2000.

9.2.1 SST data pre-processing methods

As discussed in Chapter 7, the evolution of the SST ingestion method into MM5's REGRID subroutine began with a very crude method of converting the GRIB SST file into a matrix in IDL. Once the matrix was formed, the chosen SST values were inserted manually. It is a very complex task to selectively map over parts of the Gulf Stream because, if the data set is based on a lat / lon grid, there will be gaps of data missing near the coastline because of the irregular southwest to northeast shape.

The high resolution data acquired from Coastwatch were in a different format than what MM5's REGRID could read. The first task was to convert the data to a Lambert conformal grid. Then write over the SST GRIB file data for the corresponding grid points.

When looking for SST satellite imagery preceding a winter storm, there will almost always be low-level convection over the Gulf Stream. The REGRID equations were reading the numerical values for cloud tops as very warm SST values causing unrealistic jumps in sensible heat flux and vertical motion. To fix this problem, several various cloud filters were devised. A full description of the cloud filter logic evolution appears in Chapter 7, however the final MATLAB logic is briefly explained below. First, a particular upper limit for a realistic SST value is defined (e.g., 28°C for the upper GSF). All SST values exceeding this limit would be flagged, and then replaced with interpolated values based on the nearest non-flagged grid points on all four sides. For example: the SST grid point which needs to be calculated can be defined as $A_{(i,j)}$, where i and j are the coordinates of A's matrix location. Two values for $A_{(0,0)}$ must be calculated, one in the vertical axis ($Y_{(0,0)}$), and one in the horizontal axis ($X_{(0,0)}$). By choosing points on either side of the flagged value and averaging them so that $X_{(0,0)} = (X_{(-1,0)} + X_{(1,0)}) / 2$, and $Y_{(0,0)} = (Y_{(0,-1)} + Y_{(0,1)}) / 2$, a value for $A_{(0,0)}$ can be

calculated using the equation: $A_{(i,j)} = (X_{(i,j)} + Y_{(i,j)}) / 2$. If the nearest $i, j = \pm 1$ value is also flagged, then the $i, j = n \pm 1$ is applied until a non-flagged value is found, and the averaging loops back to the $A_{(0,0)}$ point.

9.2.2 SST ingestion for the sensitivity to GSF position experiment

The SST files used to initialize the simulations in this experiment are very similar to those in Chapter 7, but not identical. To create the SST input file, the same methods were employed as in the previous experiment where the grids of high resolution data are mapped over the Eta-212 grid. The new SST data file was derived from digital images acquired by the Advanced Very High Resolution Radiometer (AVHRR) carried onboard the NOAA-12 and NOAA-14 polar orbiting satellites. First, a single pass 1.1 km grid data set was found by looking at imagery prior to the cold air outbreak with as little cloud cover as possible. The chosen image was from 22 January 2000, less than 2 days prior to the start of the simulation. This was soon enough to reveal the influencing features, but prior to the increase in cloud cover. This image was less than 10% corrupted with clouds. To fix this problem of cloud cover, the interpolation routine discussed in the previous section, as well as in Chapter 7, was used to plot grid points based on the closest non-flagged values on all four sides. This was done for all the cloud fringe data as well. The difference between this SST file and the file used in Chapter 7 is in the near coastal waters.

For *Exp-1* (Figure 9.2b) and *Exp-2* (Figure 9.2c), the Gulf Stream is shifted east along the x axis (i.e., Δx varies for longitude) 1° and 2.5° of longitude respectively. The differences between the high resolution file seen in Figure 7.5b of Chapter 7 are the values from the edge of the coastline inland. The Coastwatch 1.1 km data includes land and water

temperatures as well as offshore SST. Since the objective is to map these high resolution matrices shifted to the east, that would also be mapping the warmer land temperatures over the ocean. To correct this problem, a MATLAB script was written based on the grid file's land-sea mask. The logic behind the script is as follows: Beginning at a predetermined grid point, the script will map a boundary line moving along the y axis (south) until it intersects a land-sea mask grid point, then it will move east (x axis) until it encounters an SST grid point of 1° warmer than where it was previously located. At this point, the boundary marking loop will turn back south (y axis), and the process is repeated. This loop runs until it reaches 35.2N, where the coastline transitions from facing northeast to facing southeast. South of 35.2N the y axis logic is the same, but the x axis logic is reversed so as to "bounce" between the land-sea mask and the GSF headed west. After the boundary is defined, all grid points to the west along the x axis are adjusted to the same SST as the near-coastal waters. This results in the "step" looking transition of the SST values around 280 K seen in Figure 9.2a, b, and c.

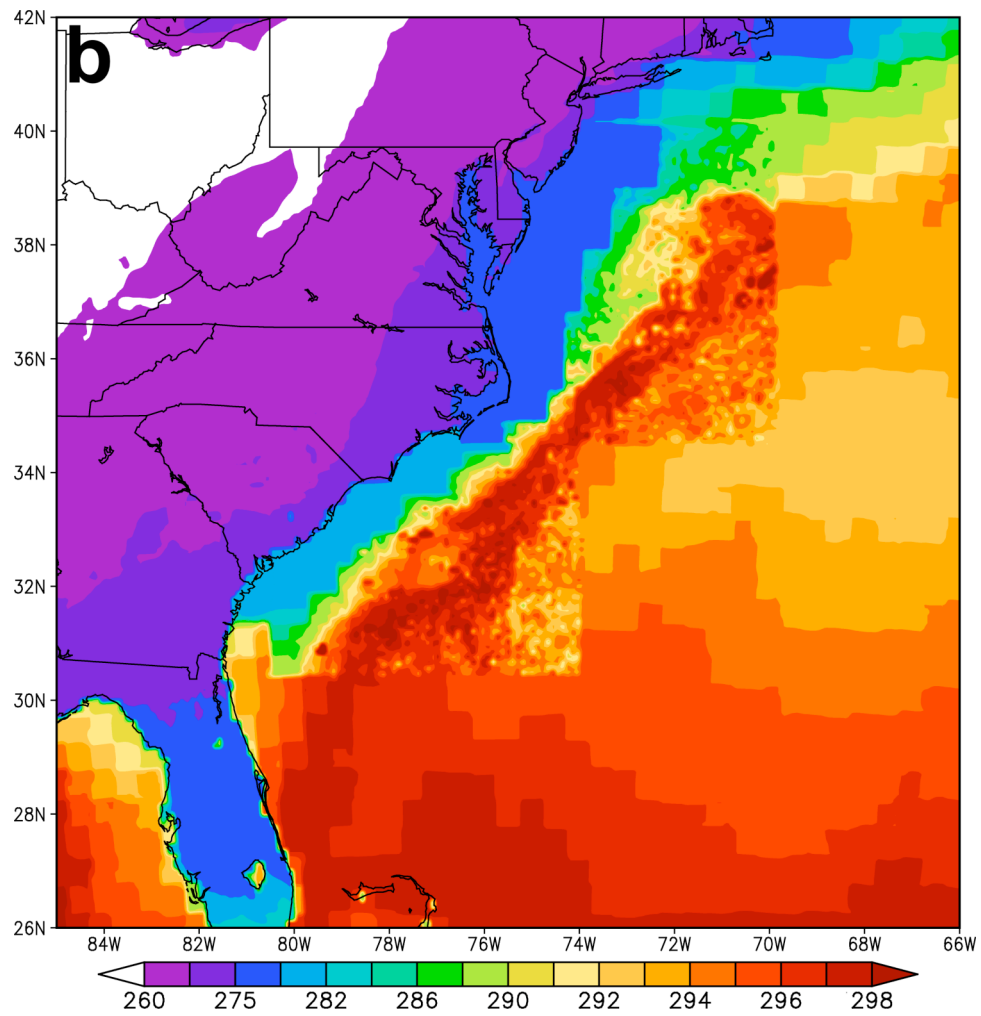


Figure 9.2b The SST initialization file for the *Exp-1* simulation. Post regridded to 10 km with a 1 degree of longitude shift to the high resolution data. The high resolution data is valid 22 Jan 2000.

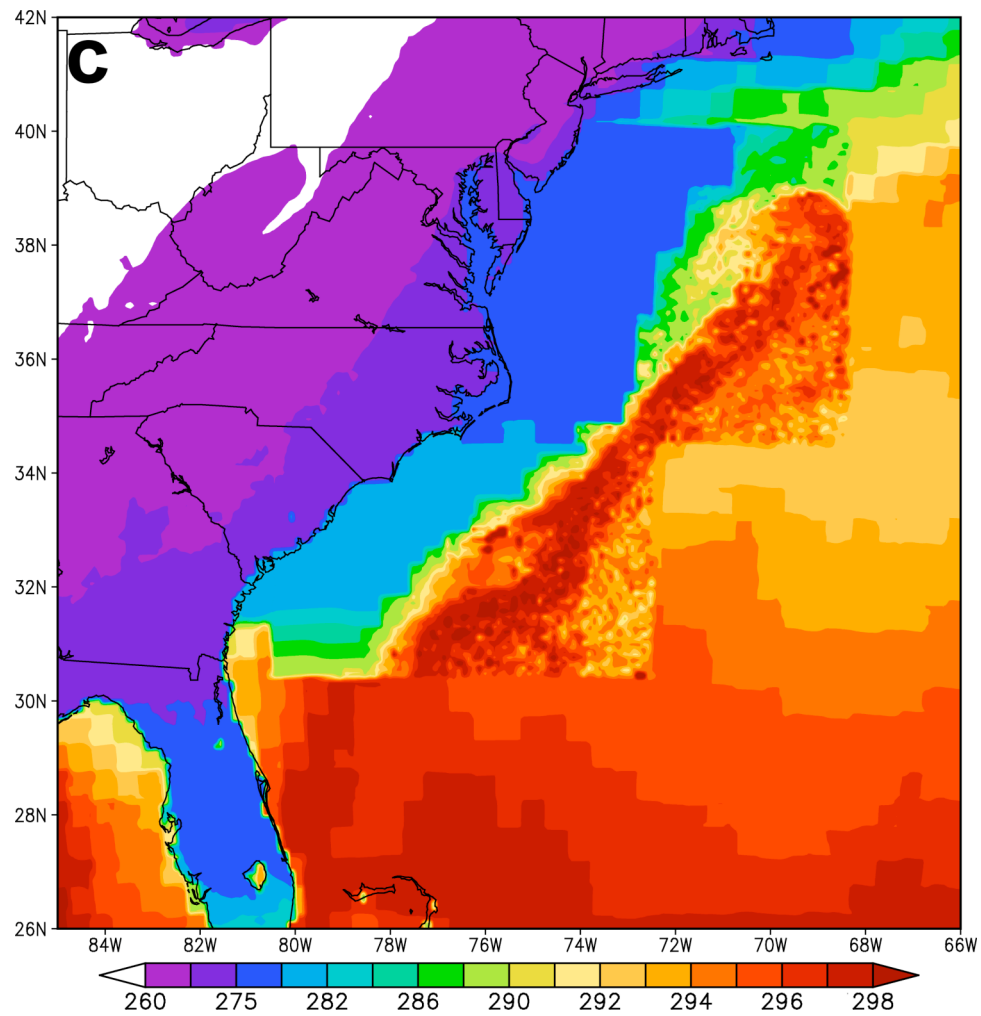


Figure 9.2c The SST initialization file for the *Exp-2* simulation. Post regridded to 10 km with a 2.5 degree of longitude shift to the high resolution data. The high resolution data is valid 22 Jan 2000.

Although this transition is of lower resolution than the adjacent 1.1 km GSF, it is still equal to, or higher, than the resolution of the remaining Eta-212 grid used in the background. Now that the warmer inland values have been changed to the temperature of the near-coastal waters, the matrices are mapped 1° to the east for *Exp-1* (Figure 9.2b), and 2.5° to the east for *Exp-2* (Figure 9.2c). The fact that the new high resolution SST matrices now have cold coastal water temperatures mapped over land (not shown in Figure 9.2) is not important because REGRID will automatically map the land surface temperatures over the SST file (shown in Figure 9.2). These SST data sets are then used to initialize the respective simulations. As mentioned in Chapter 7, ship and buoy observations were compared against the imagery in the data set to validate the very high SST region off the southeast coast of NC (Figure 7.5c).

9.3 Results

9.3.1 Sea-level pressure comparison

The variations in the evolution of the surface low pressure as a result of the different SST initializations files is quite significant, especially later (beyond 24 h) in the simulations. By initializing the simulations at 00Z on January 24, 2000, more than 12 h before the surface low pressure formed, the model's "spin-up" time revealed only minimal differences. The first differences begin to occur around 18Z Jan 24. In Figure 9.3, the *Cntl* (Figure 9.3a) is almost identical to *Exp-1* (Figure 9.3b), however *Exp-2* has sea-level pressure as much as 4 mb higher than in the *Cntl*. This is most noticeable in Figure 9.3d, a sea-level pressure difference field (mb) of *Cntl - Exp-2* (a-c), for two regions east of South Carolina.

Six hours later, the sea-level pressure in the *Cntl*, seen in Figure 9.4a, has dropped to 996 mb and is located 33N, 76W. As in Figure 9.3, the sea-level pressure in *Exp-1* (Figure 9.4b) is almost the same as the *Cntl*, however, the reflectivity is slightly different. The larger reflectivity values in the *Exp-1* simulation northeast of the center of circulation are about 80 km to the east of those in the *Cntl*. Both the *Cntl* and *Exp-1* are much different from the reflectivity seen in *Exp-2* (Figure 9.4c) where almost no convection is seen east of Cape Hatteras, NC. The central sea-level pressure of the storm in *Exp-2* is also 3 mb higher than the *Cntl*. The difference between the *Cntl* and the *Exp-2*, seen in Figure 9.4d, has multiple regions exceeding 5 mb along the forming front where the *Cntl* pressure is significantly lower.

Larger sea-level pressure differences begin to arise between the *Cntl* (Figure 9.5a) and *Exp-1* (Figure 9.5b) by 06Z Jan 25 (30 h into the simulations). The center of the surface low in the *Cntl* is further to the north around 35N, 74.8W and slightly elongated, whereas the surface low in *Exp-1* is located 34.6N, 74.2W, or about 50 km southeast of the *Cntl*. Although the *Cntl* is only 1 mb lower than the *Exp-1*, the region of lower pressure is much larger. The reflectivity in the *Cntl* (Figure 9.5a) is slightly more intense than in the *Exp-1* (Figure 9.5b) over the water, but a significantly heavier band of precipitation can be seen forming over North Carolina to the west of the respective band seen in *Exp-1*. Minimal differences in reflectivity over the ocean are seen in *Exp-2* (Figure 9.5c) when compared to the *Cntl* and *Exp-1*. However, the precipitation band seen in the *Cntl* over North Carolina is almost nonexistent in *Exp-2*. Reflectivity values in the region located at 36.5N, 77W in the *Cntl* are more than twice that of the corresponding region in *Exp-2*. Likewise, major differences in sea-level pressure are also seen between the *Cntl* and the *Exp-2* (Figure 9.5 d)

where the pressure in the *Cntl* is as much as 8 mb lower than the *Exp-2* just east of Cape Hatteras, NC.

Thirty three hours into the simulation (09Z Jan 25) the locations of the central area of low pressure between the *Cntl* (Figure 9.6a) and *Exp-1* (Figure 9.6b) are minimal. The *Exp-1* places the center of the storm about 20 km to the east of the *Cntl*, but it is also favoring a more northward position causing the 987 mb center to split in half forming a "double barrel" feature. The *Cntl* is also catching onto this feature, however, the *Cntl* is favoring the more southern of the two regions (of the 2 double lows) located 35N, 74W. In the *Cntl* (Figure 9.6a), this region is also 1 mb (986 mb) lower than seen in *Exp-1* (Figure 9.6b). The band of precipitation, discussed earlier when comparing the *Cntl* to *Exp-1*, is still further west and much more developed in the *Cntl* (Figure 9.6a). The precipitation band in *Exp-2* (Figure 9.6c) is finally beginning to show signs of development. The reflectivity values in the 35-40 dBZ range are still much lower than the other two simulations. The sea-level pressure is also much weaker in the *Exp-2* simulation. The lowest central pressure of the storm in *Exp-2* is 989 mb, 3 mb higher than in the *Cntl*. The sea-level pressure difference field is seen in Figure 9.6d, valid 09Z Jan 25. A large region, with values exceeding -9 mb (*Cntl* - *Exp-2*) is located 35N, 74.2W which corresponds to the location of the lowest central pressure in the *Cntl* simulation (Figure 9.6a) for the same time (09Z Jan 25). Located 36N, 71W is a region of positive pressure difference because the *Exp-2* simulation's surface low is located much further east (approximately 120 km NE of the *Cntl*).

The sea-level pressure differences at 12Z Jan 25 between *Cntl* (Figure 9.7a) and *Exp-2* (Figure 9.7b) are noticeable in magnitude, but not so much in location. The *Cntl* simulation is still 1 mb lower, or deeper, than *Exp-2*, however, the region covered by the 985

mb isobar is much larger in *Cntl*. The sea-level pressure difference between *Cntl* and *Exp-2* (Figure 9.7c) is most evident in the pressure difference field seen in Figure 9.7d. The same region of -9 mb pressure difference has just shifted to the northeast following the motion of the storms. The most significant developments seen when comparing the simulations in Figure 9.7, valid 12Z Jan 25 (36 h after the initialization) are those of the reflectivity. The *Cntl* (Figure 9.7a), which 6 h before had the heaviest precipitation, now appears to be breaking apart as the storm moves north. However, *Exp-2* (Figure 9.7c) is now showing an abrupt increase in precipitation, more so than in the *Cntl*. *Exp-1* appears to be somewhere in between the other two simulations as far as the timing of the precipitation development. There is not much difference in the horizontal displacement of the precipitation, however there is a substantial difference in the north-south axis. The largest difference between the three simulations is not in location though, it is in the timing. The development of the western band of precipitation followed through the past five figures reveals a temporal delay where the *Exp-1* simulation is lagging the *Cntl*, and the *Exp-2* simulation is lagging the *Exp-1* simulation. This temporal delay is likely a result of the advecting of warm air at the surface-level being delayed from linking with the region of divergence generated by the upper-level trough because the source of the warm moist air has been shifted to the east for each consecutive experimental simulation. Plots of 500-hPa divergence valid 09Z and 12Z Jan 25 are seen in Figures 9.8 and 9.9. Although the divergence fields differ somewhat, the 500-hPa heights are quite similar suggesting that the total wind is not entirely geostrophic. There is a strong correlation, as expected, between the upper-level divergence, and the QPF seen in Figures 9.6 and 9.7, which correspond to 09Z and 12Z Jan 25, respectively. Since the variations in the upper-level flow between the simulations are a result of surface feedback

(i.e., only the SST fields were changed), dynamics above 500-hPa, particularly during the first 24 to 30 h are mostly a function of initialization fields at the respective levels, as well as boundary conditions. As discussed in previous chapters, the pre-existing vorticity along the frontal boundary, which aligns in conjunction with the GSF, plays a key role in the track of the surface cyclone. When comparing the sea-level pressure in Figure 9.8 to Figure 9.9, the difference in deepening rate is likely a factor of weakened feedback in the *Exp-1* and *Exp-2* simulations because the surface-to-upper-trough displacement was increased. This horizontal displacement resulted in a temporal (~ 6 h), and spatial (~ 150 mi NNE) offset of QPF from the *Cntl* to the *Exp-2* simulation.

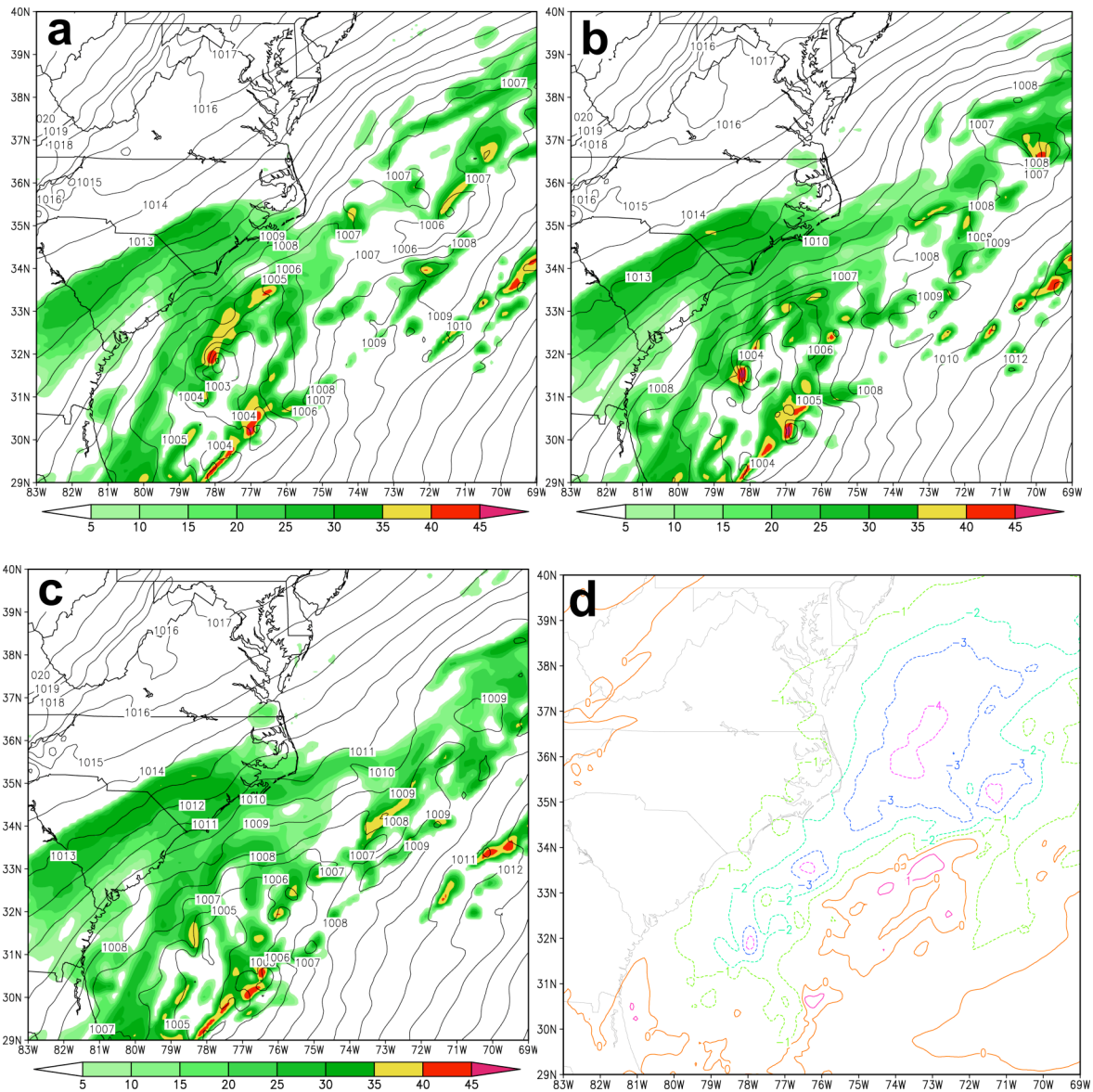


Figure 9.3 Sea-level pressure (mb) and model derived 950-hPa reflectivity (dBZ) valid 18Z Jan 24 (18 h into the simulation) for the *Cntl* (a), *Exp-1* (b), and *Exp-2* (c). A sea-level pressure difference field (mb) of *Cntl* - *Exp-2* (a-c) is shown in (d).

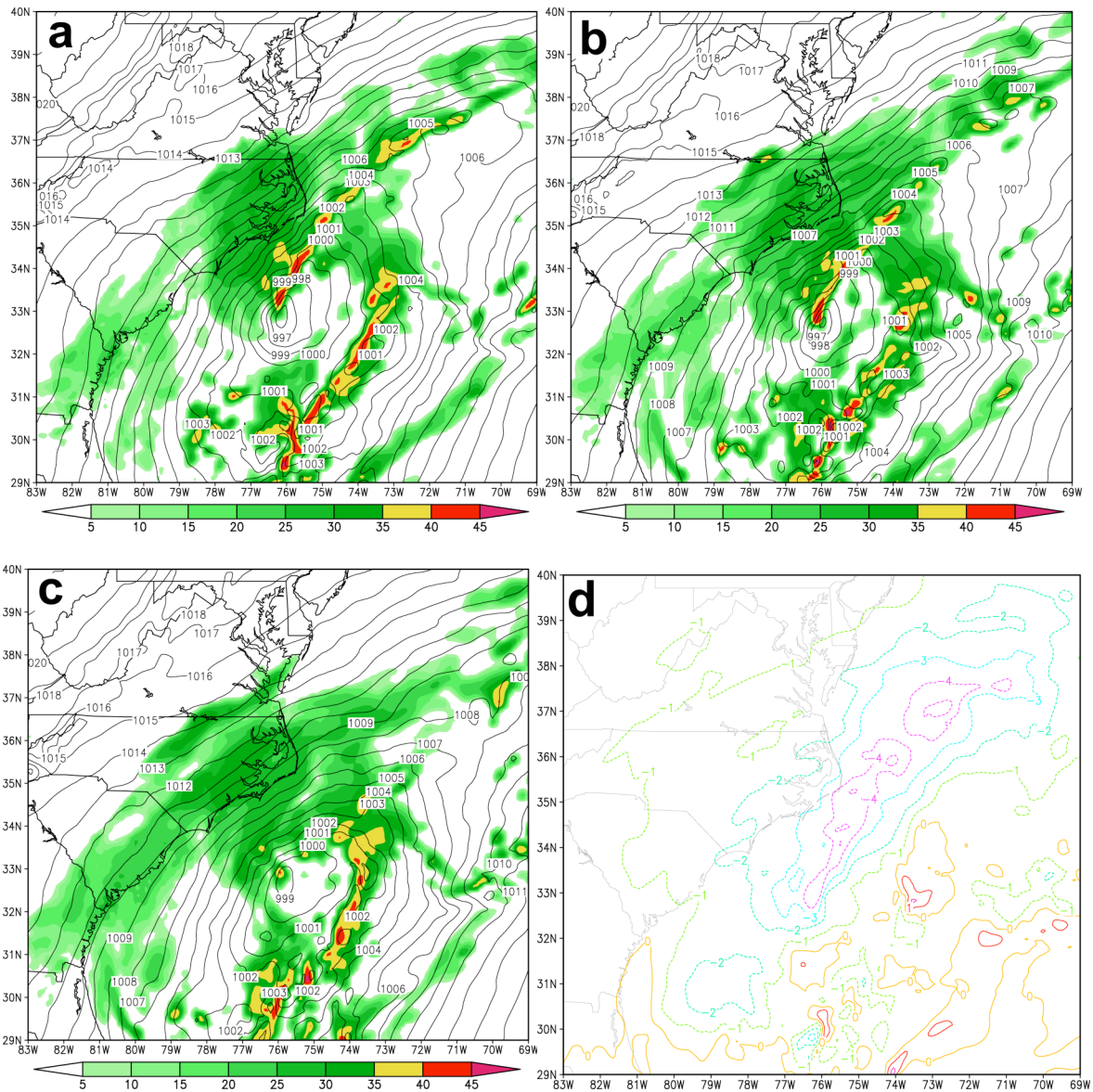


Figure 9.4 Sea-level pressure (mb) and model derived 950-hPa reflectivity (dBZ) valid 00Z Jan 25 (24 h into the simulations) for the *Cntl* (a), *Exp-1* (b), and *Exp-2* (c). A sea-level pressure difference field (mb) of *Cntl* - *Exp-2* (a-c) is shown in (d).

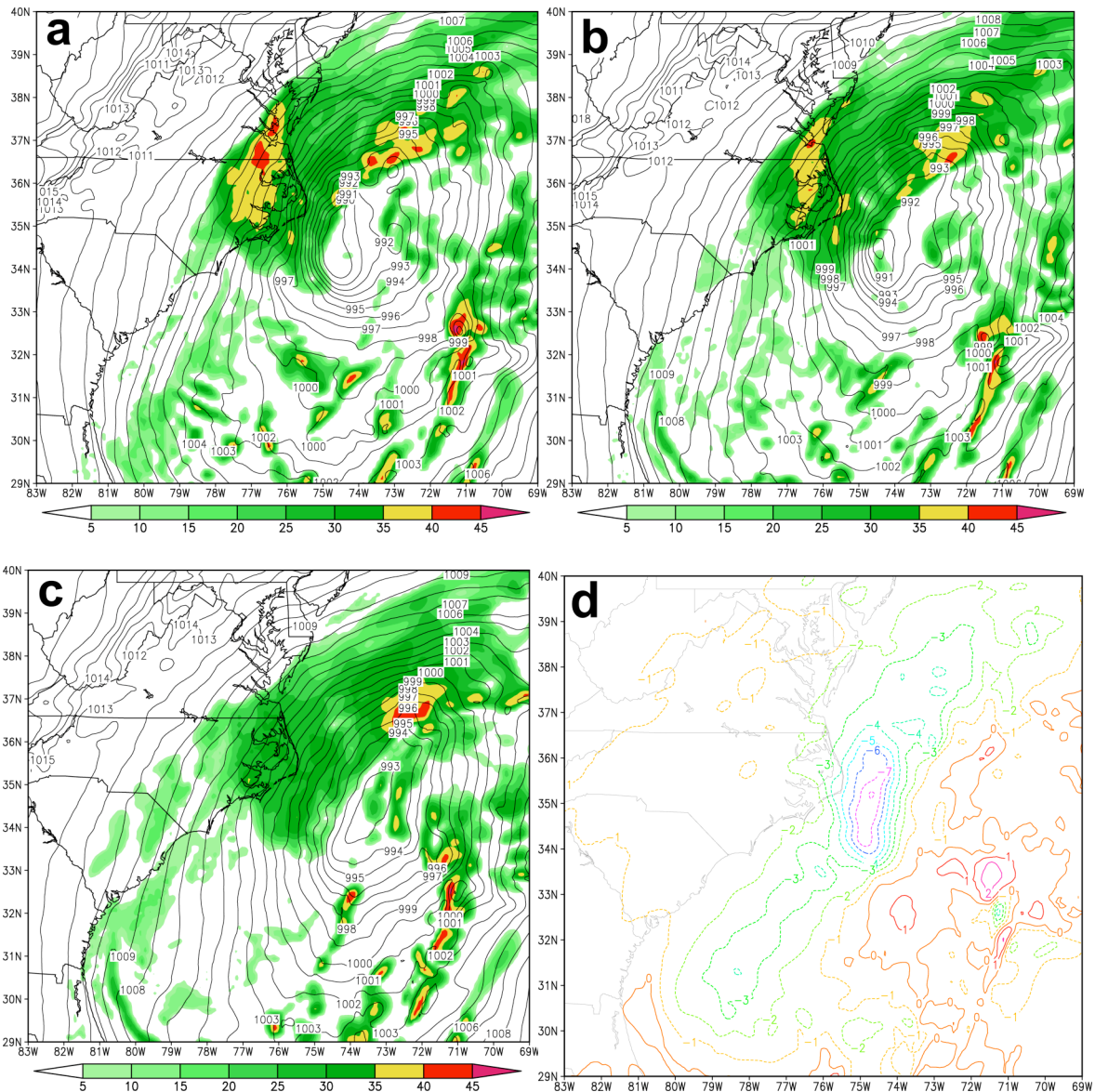


Figure 9.5 Sea-level pressure (mb) and model derived 950-hPa reflectivity (dBZ) valid 06Z Jan 25 (30 h into the simulations) for the *Cntl* (a), *Exp-1* (b), and *Exp-2* (c). A sea-level pressure difference field (mb) of *Cntl - Exp-2* (a-c) is shown in (d).

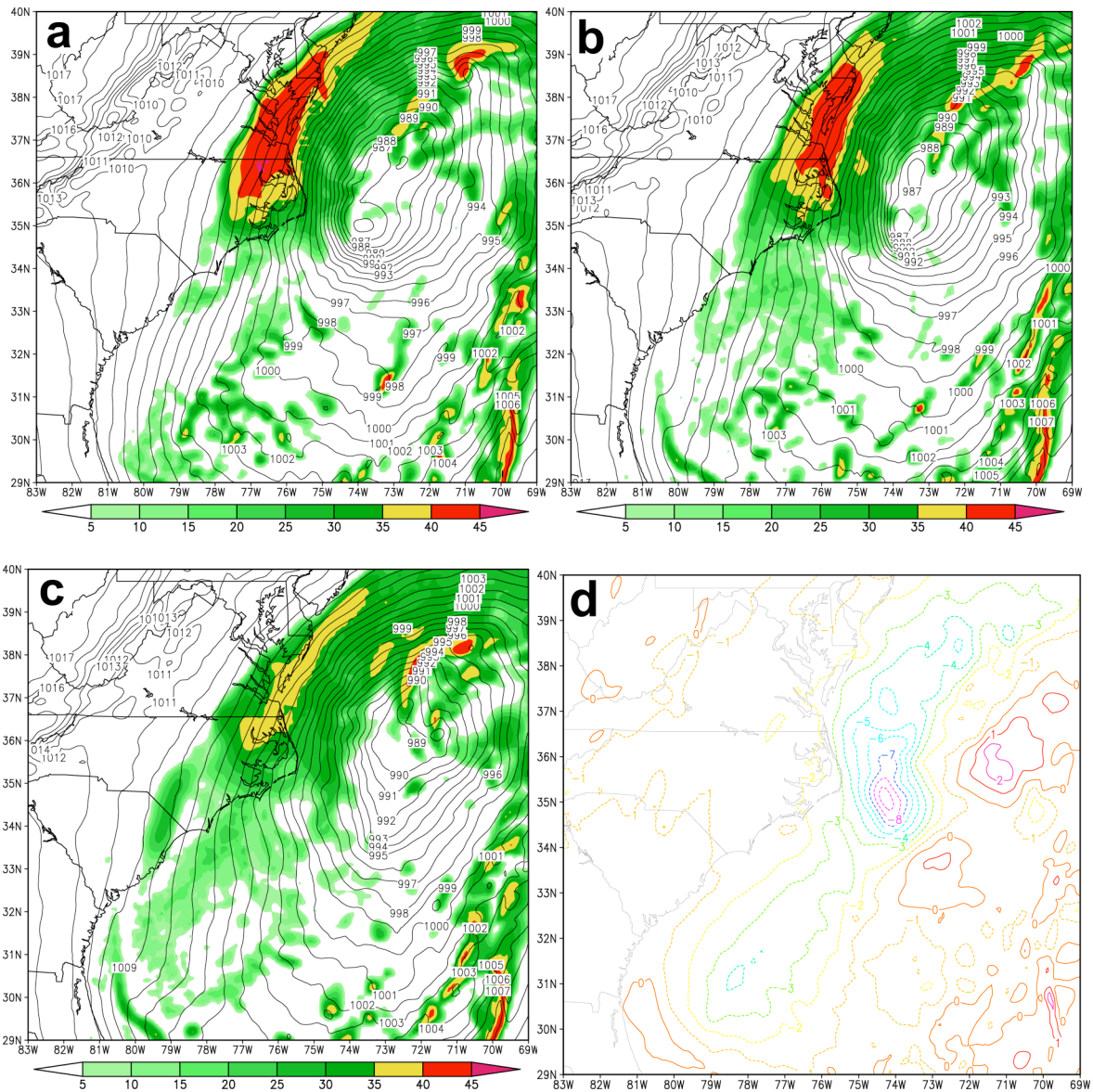


Figure 9.6 Sea-level pressure (mb) and model derived 950-hPa reflectivity (dBZ) valid 09Z Jan 25 (33 h into the simulations) for the *Cntl* (a), *Exp-1* (b), and *Exp-2* (c). A sea-level pressure difference field (mb) of *Cntl* - *Exp-2* (a-c) is shown in (d).

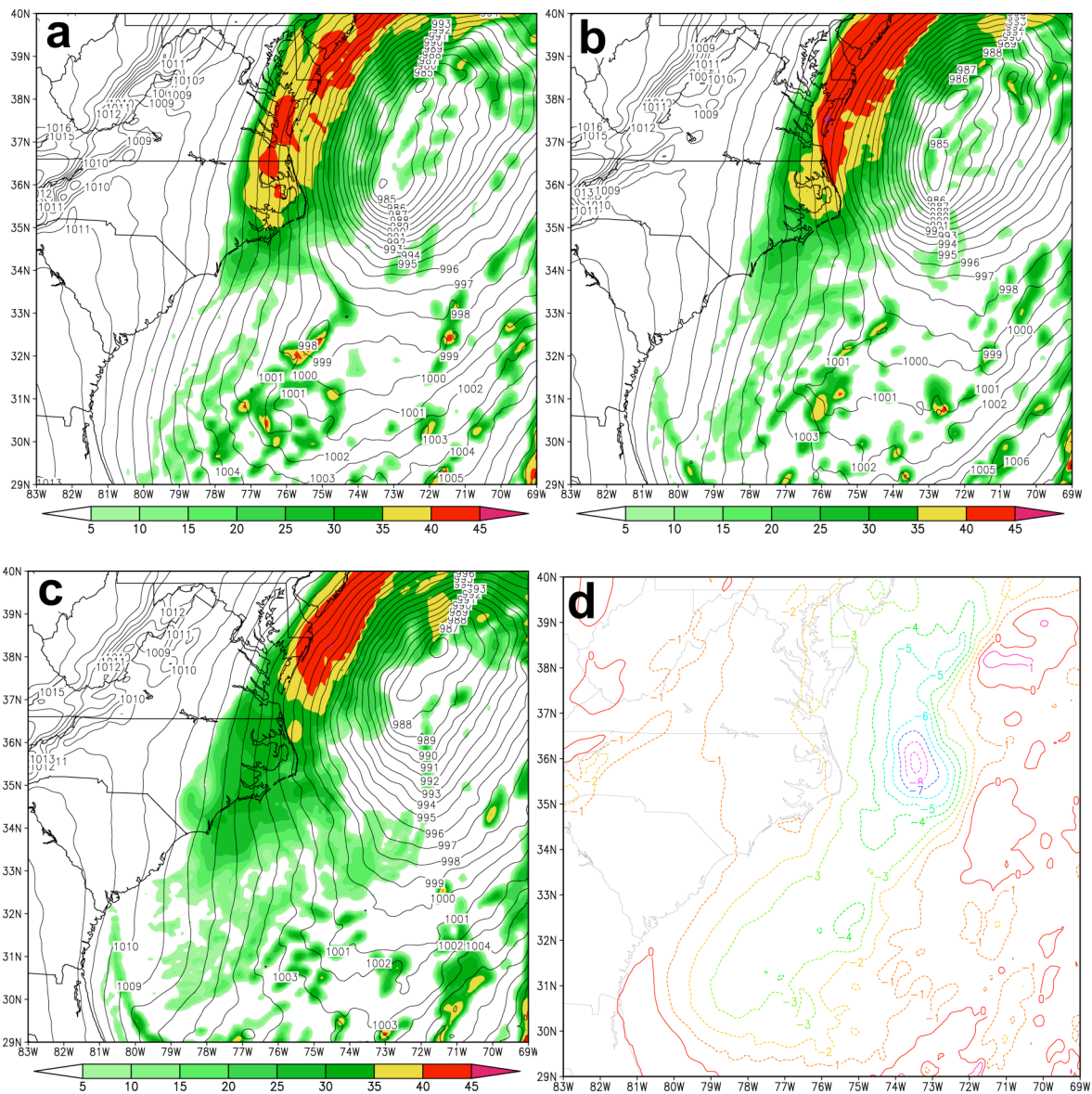
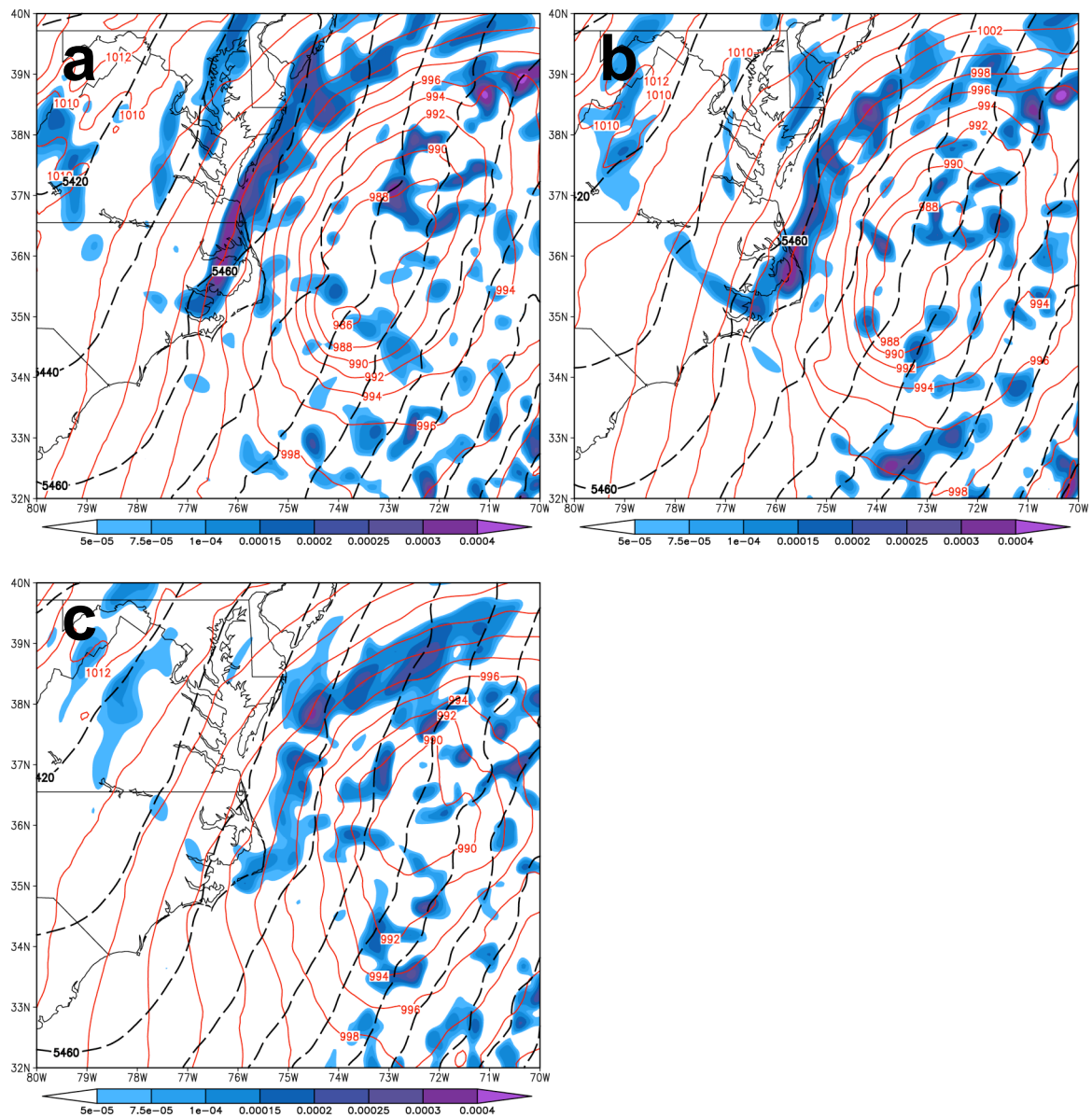


Figure 9.7 Sea-level pressure (mb) and model derived 950-hPa reflectivity (dBZ) valid 12Z Jan 25 (36 h into the simulations) for the *Cntl* (a), *Exp-1* (b), and *Exp-2* (c). A sea-level pressure difference field (mb) of *Cntl* - *Exp-2* (a-c) is shown in (d).



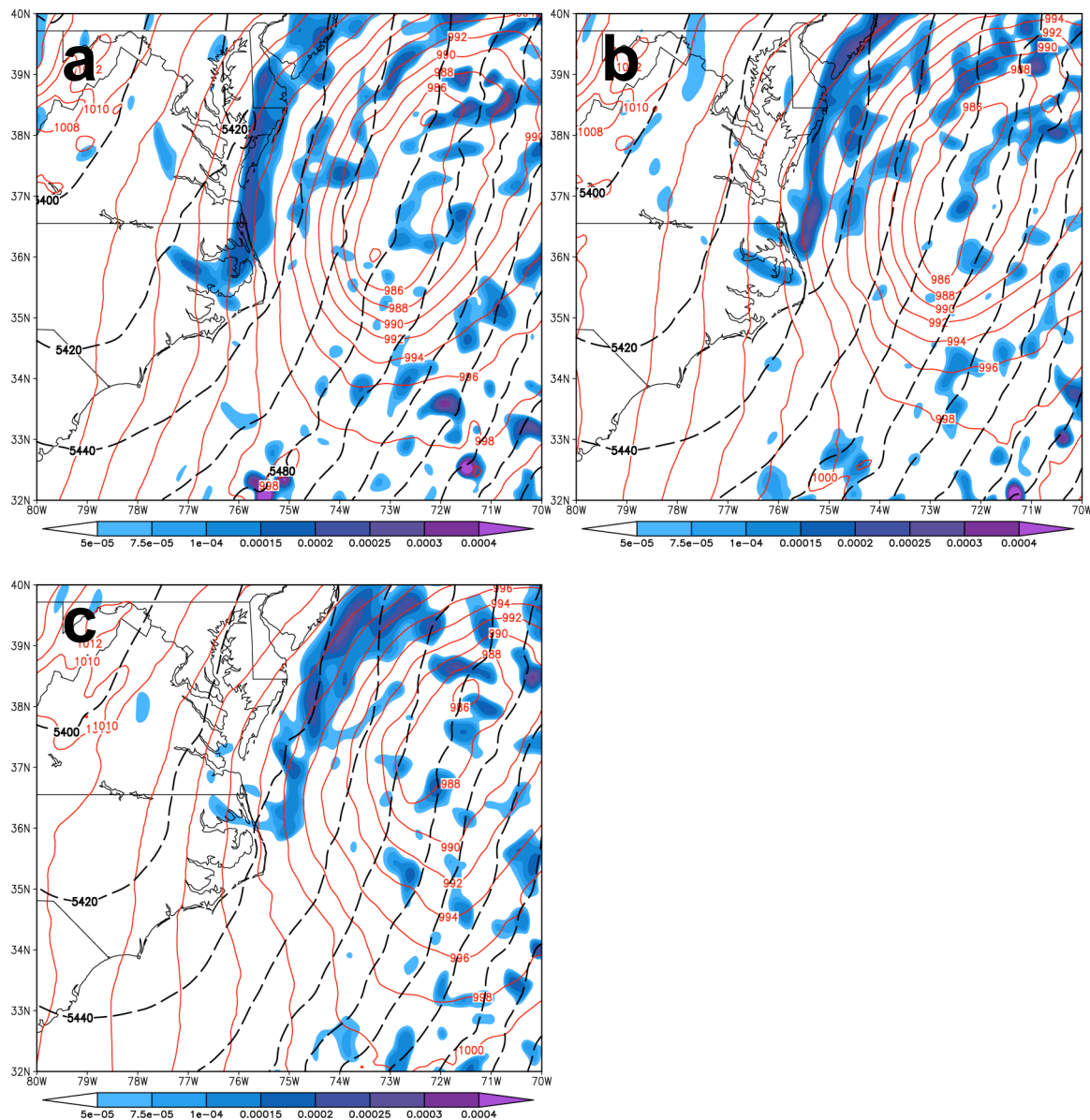


Figure 9.9 Sea-level pressure (mb) and 500-hPa heights and divergence (s^{-1}) valid 12Z Jan 25 (36 h into the simulations) for the *Cntl* (a), *Exp-1* (b), and *Exp-2* (c).

9.3.2 Frontogenesis and surface to upper-level feedback

The lower-level response to the shift in the Gulf Stream's position is most evident when observing the response from the 10-m winds. In Figure 9.10, valid 00Z Jan 25, a comparison can be seen between the simulations 10-m winds and 2-m temperatures. With the exception of the obvious shifting of the temperature to the east as a result of moving the Gulf Stream, the 2-m temperatures are not much different. In the *Exp-1* simulation (Figure 9.10b), there is a 2 K increase in the region of the surface circulation (arrow "A"). This feature is also seen in *Exp-2* (Figure 9.10c) as well as another larger region of increased temperature (arrow "B"). Both of these features are not seen in the *Cntl* simulation (Figure 9.10a). The differences in the 10-m winds are more significant between the simulations. In the *Cntl* simulation (Figure 9.10a), a well defined coastal front can be seen parallel to the GSF along the 291 K isotherm. This convergence is also seen in the 10-m winds of the *Exp-1* simulations (Figure 9.10b), and, like the *Cntl*, is following the 291 K isotherm. However, in the *Exp-1* simulation, the 291 K isotherm, as well as the coastal front, is 1° in longitude further to the east. In the *Exp-2* simulation (Figure 9.10c), the coastal front is not well defined. There is still convergence along the 291 K isotherm from 33N to 36N, however, north of 36N, the winds subside. Following the trends of the first two simulations, the coastal front sets up along the 291 K isotherm, which in *Exp-2* (Figure 9.10c) is 2.5° east of the *Cntl*.

The coastal front, as well as the magnitude of wind speed, can be seen in Figure 9.11a-c. The shape on the coastal front in the *Cntl*, seen in Figure 9.11a, is much like that seen in the *Exp-1* (Figure 9.11b). As discussed earlier, the location of the coastal front in *Exp-1* is about 80-90 km east of the *Cntl*. The magnitudes of the wind speed are almost

identical between the *Exp-1* and *Cntl*. In the *Exp-2* simulation (Figure 9.11c), the coastal front is much weaker and further east. The convergence is more easily seen in by viewing the streamlines, as well as the location 36N, 71W where the winds subside. In the *Exp-2*, there is a $1\text{-}2 \text{ ms}^{-1}$ reduction in wind speed just northwest of the center of circulation, as well as the region southeast of the low pressure.

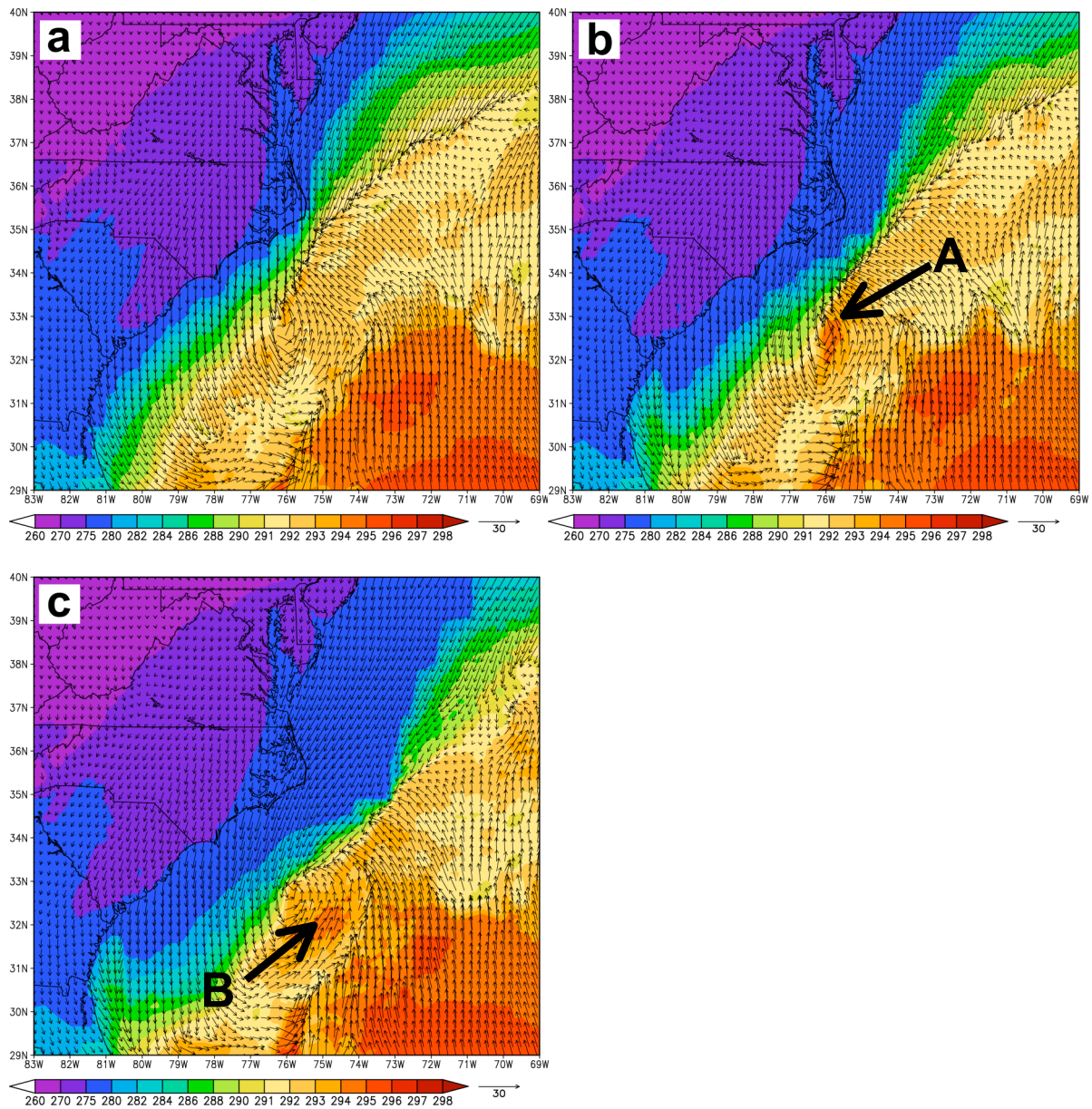


Figure 9.10 Plots of 2-m temperatures (K) and 10-m wind vectors valid 00Z Jan 25 (24 h into the simulations) for the *Cntl* (a), *Exp-1* (b), and *Exp-2* (c).

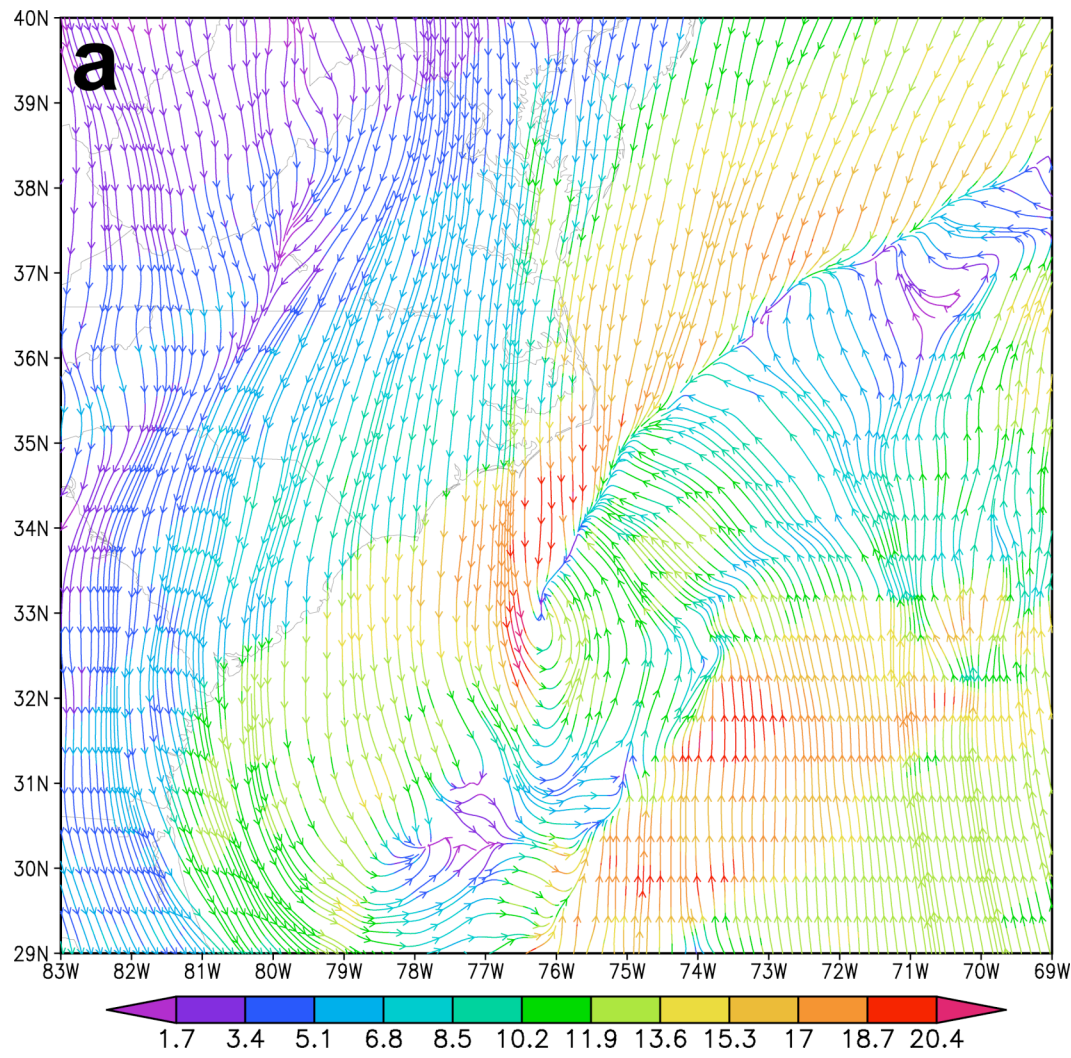


Figure 9.11a Plot of 10-m wind streamlines colored to velocity (ms^{-1}) for the *Cntl* simulation valid 00Z Jan 25 (24 h into the simulation).

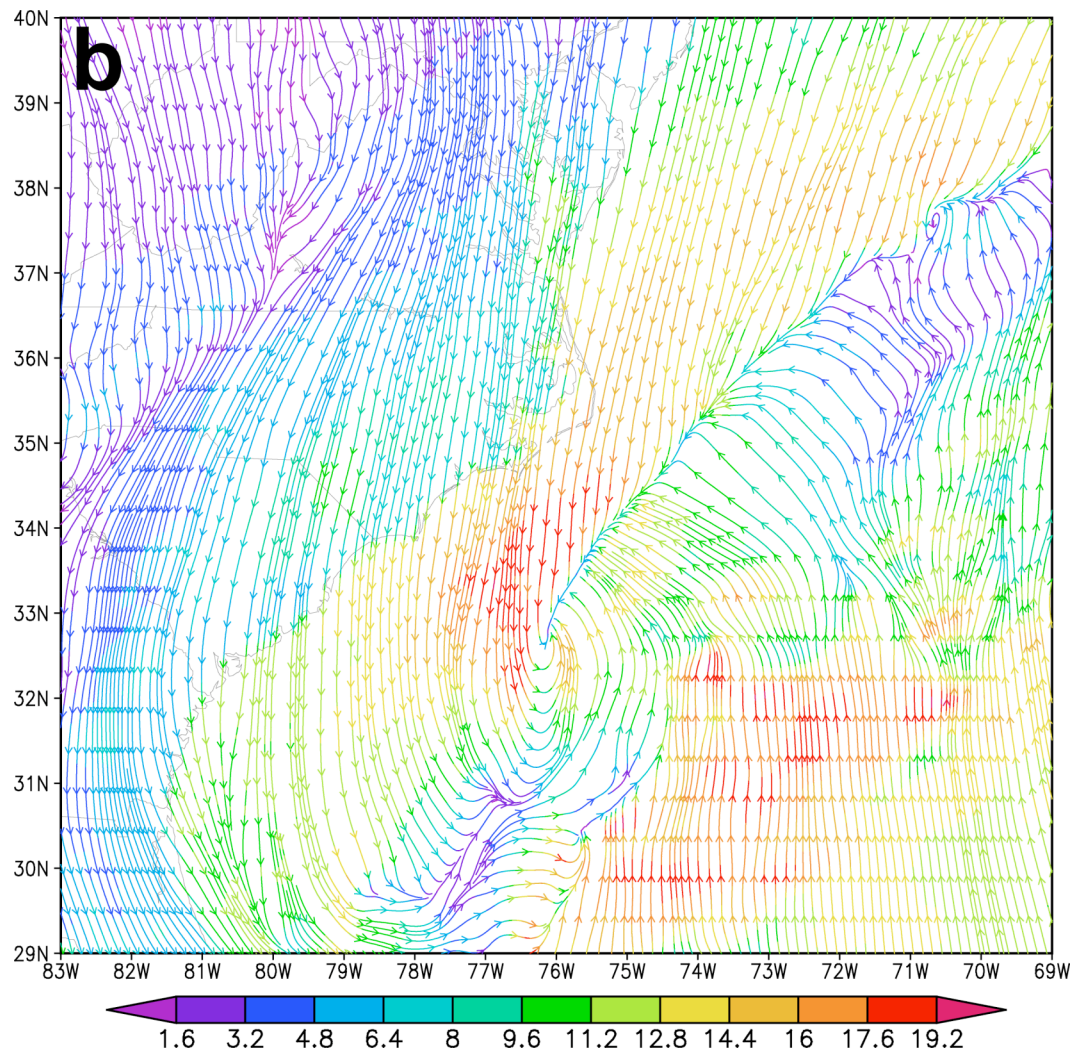


Figure 9.11b Plot of 10-m wind streamlines colored to velocity (ms^{-1}) for the *Exp-I* simulation valid 00Z Jan 25 (24 h into the simulation).

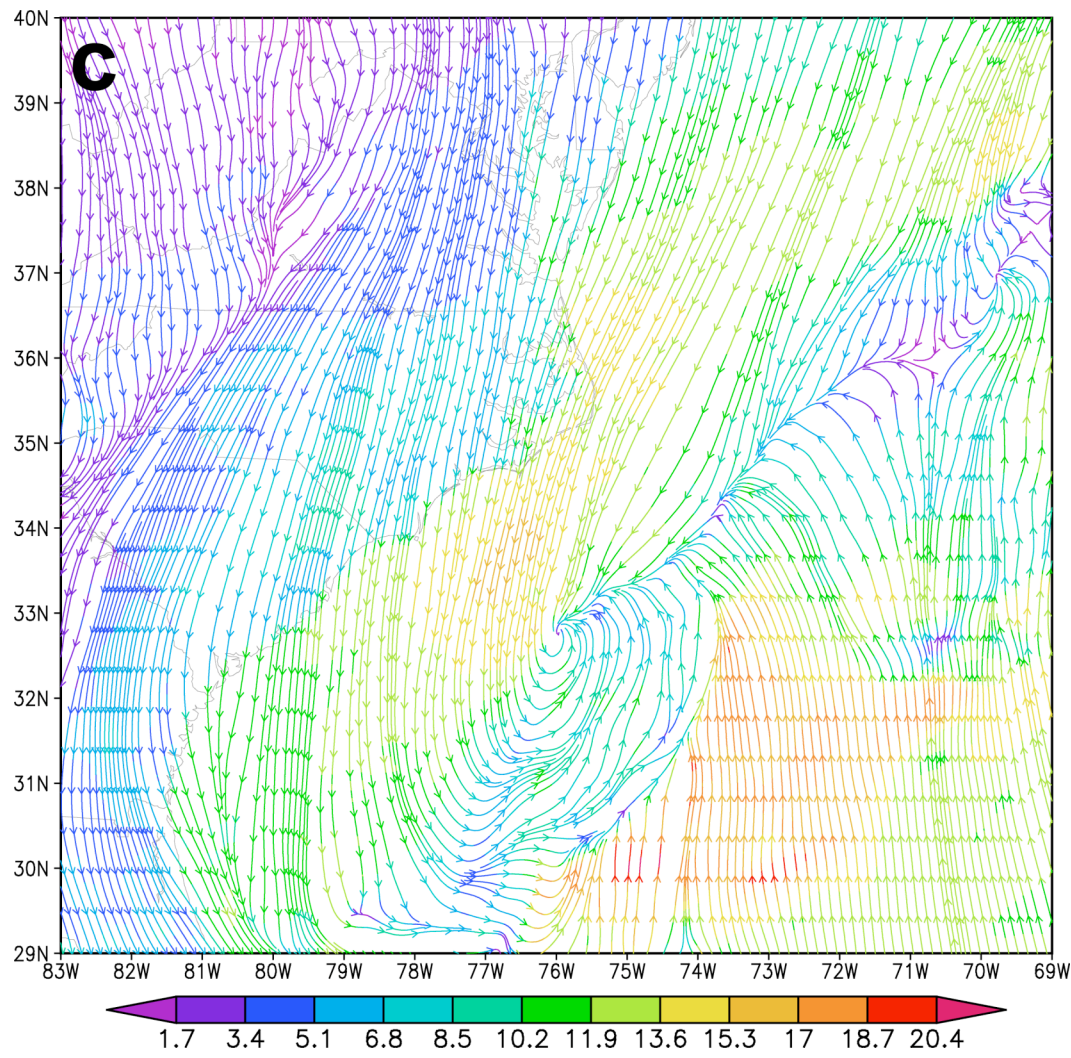


Figure 9.11c Plot of 10-m wind streamlines colored to velocity (ms^{-1}) for the *Exp-2* simulation valid 00Z Jan 25 (24 h into the simulation).

Six hours later (06Z Jan 25) the 2-m temperatures have only marginally changed (Figure 9.12). There is still a well defined difference in the position of the thermal gradient in response to the GSF, which is similar than the gradient at 00Z Jan 25 (Figure 9.10). There are multiple regions of 295 K within the center of circulation of the surface low pressure seen in *Exp-1* (Figure 9.12b) and *Exp-2* (Figure 9.12c), and not seen in the *Cntl* simulation. The region (31.5N, 76.5W) of 290-292 K in the *Cntl*, *Exp-1*, and *Exp-2* gets progressively smaller respectively, which is likely a result of the shifted GSF in conjunction with the northwesterly winds. By 06Z Jan 25, it can be seen, by looking at the 10-m wind vectors, that the circulation center of the *Exp-2* simulation (Figure 9.12c) is almost 200 km NNE of the *Cntl* (Figure 9.12a). At this point in time, this is the largest displacement in surface circulation because beyond 09Z Jan 25, the *Exp-2* slows as the *Cntl* continues to track more quickly. The most probable cause for this (beyond 09Z) is that the storms are exiting the region of the Gulf Stream, thus the low-level steering which is driven by the thermal gradient, does not exhibit the drastic differences as it does south of 38N.

Plots of 10-m wind streamlines valid 06Z Jan 25 (Figure 9.13) also show the location of the frontal boundary. It is evident, as mentioned above, that the circulation in *Exp-2* (Figure 9.13c) is more elongated and positioned NE of the *Cntl*¹ (Figure 9.13a). The convergence along the coastal front in the *Cntl* simulation seen in Figure 9.13a is still more defined than in either experimental simulation. However, the *Exp-2* simulation, seen in

¹ It should be noted that the wind speed color scales in the streamline figures are not the same because of a limitation within the GrADSv1.8 "gxout stream" command which does not read the user defined color scales.

Figure 9.13b, still exhibits a well defined frontal boundary extending off the NE quadrant of the center of circulation. The magnitude of the wind speed in the *Cntl*, particularly in the vicinity of the NW quadrant of the surface-low pressure, is $2\text{-}3 \text{ ms}^{-1}$ greater than *Exp-1*, and $6\text{-}7 \text{ ms}^{-1}$ greater than *Exp-2*.

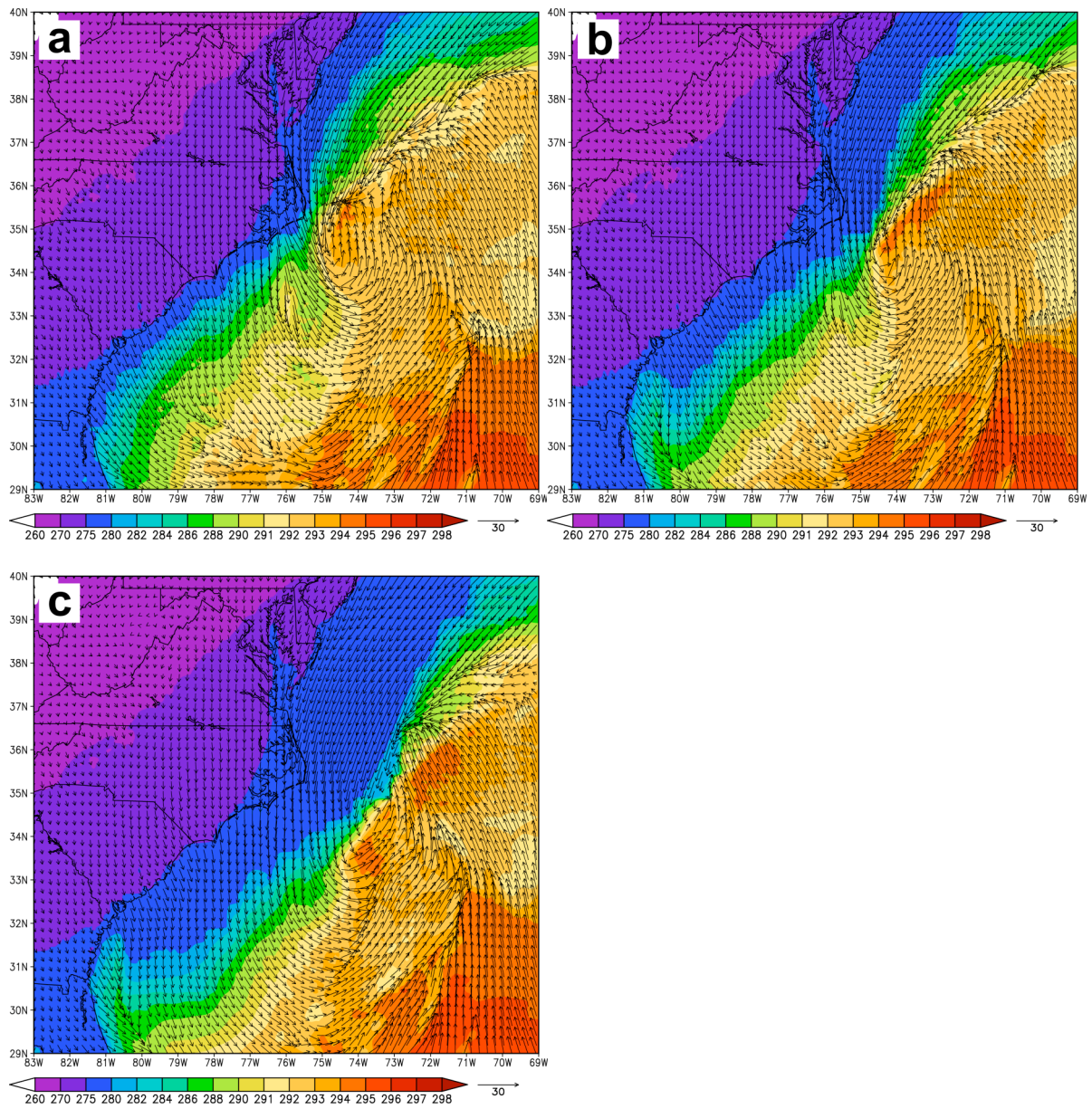


Figure 9.12 Plots of 2-m temperatures (K) and 10-m wind vectors valid 06Z Jan 25 (30 h into the simulations) for the *Cntl* (a), *Exp-1* (b), and *Exp-2* (c).

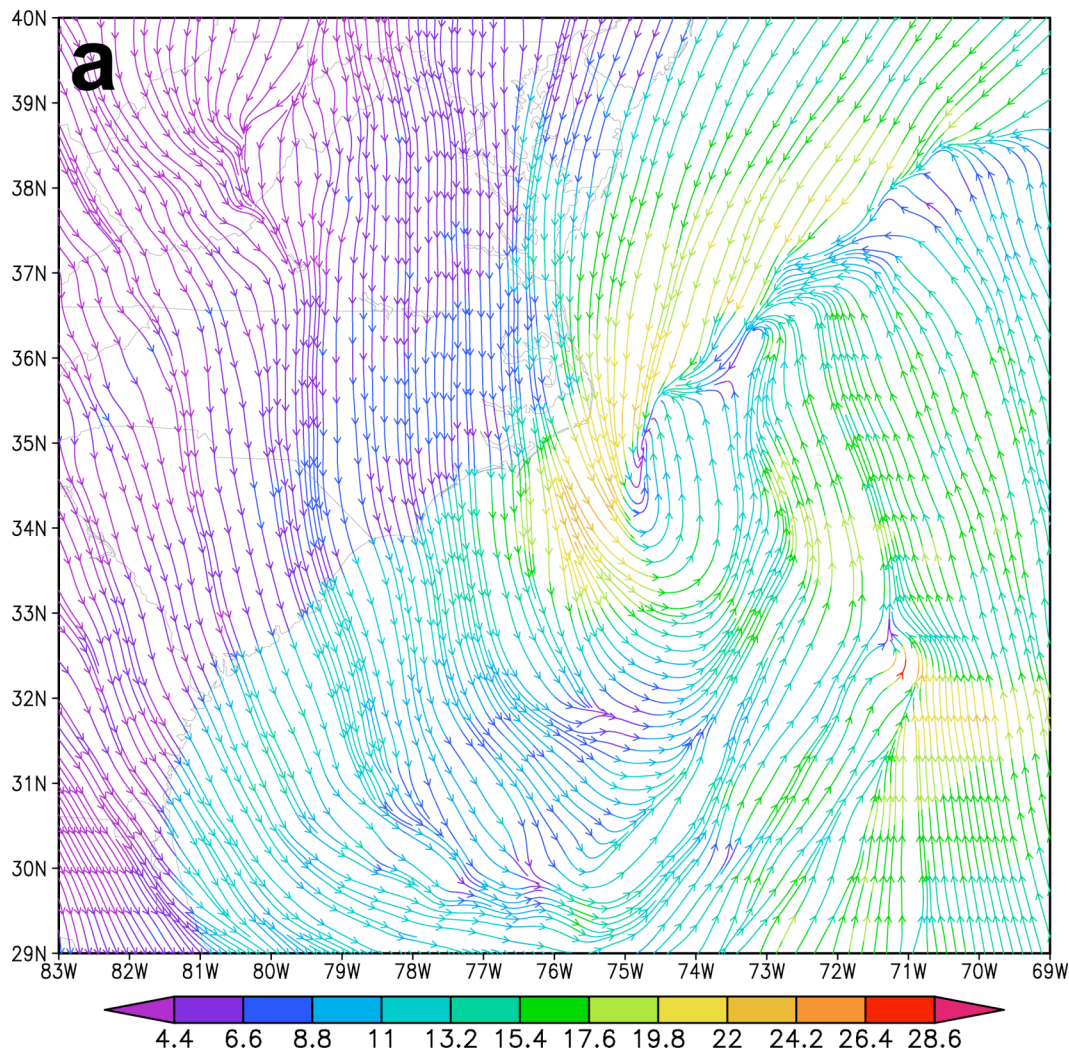


Figure 9.13a Plot of 10-m wind streamlines colored to velocity (ms^{-1}) for the *Cntl* simulation valid 06Z Jan 25 (30 h into the simulation).

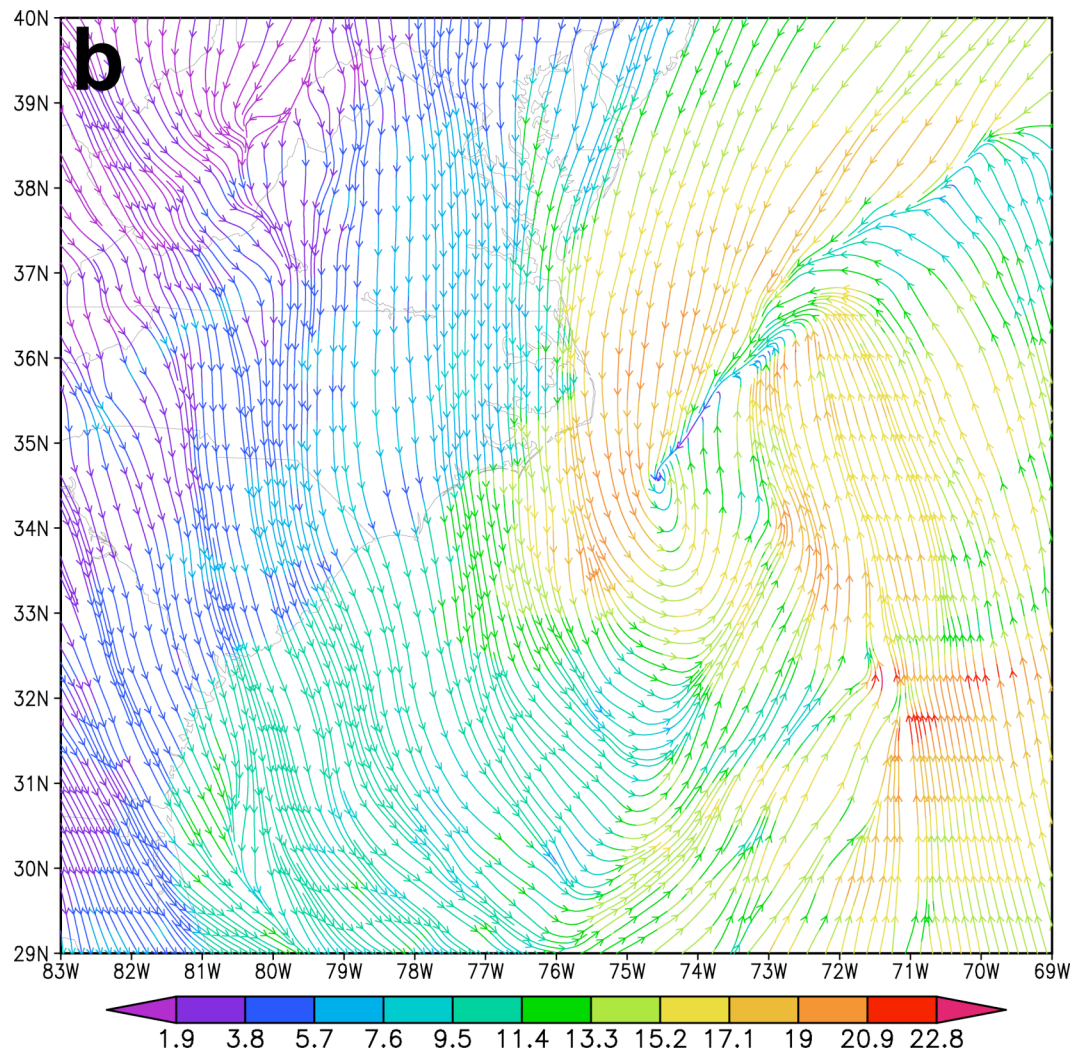


Figure 9.13b Plot of 10-m wind streamlines colored to velocity (ms^{-1}) for the *Exp-I* simulation valid 06Z Jan 25 (30 h into the simulation).

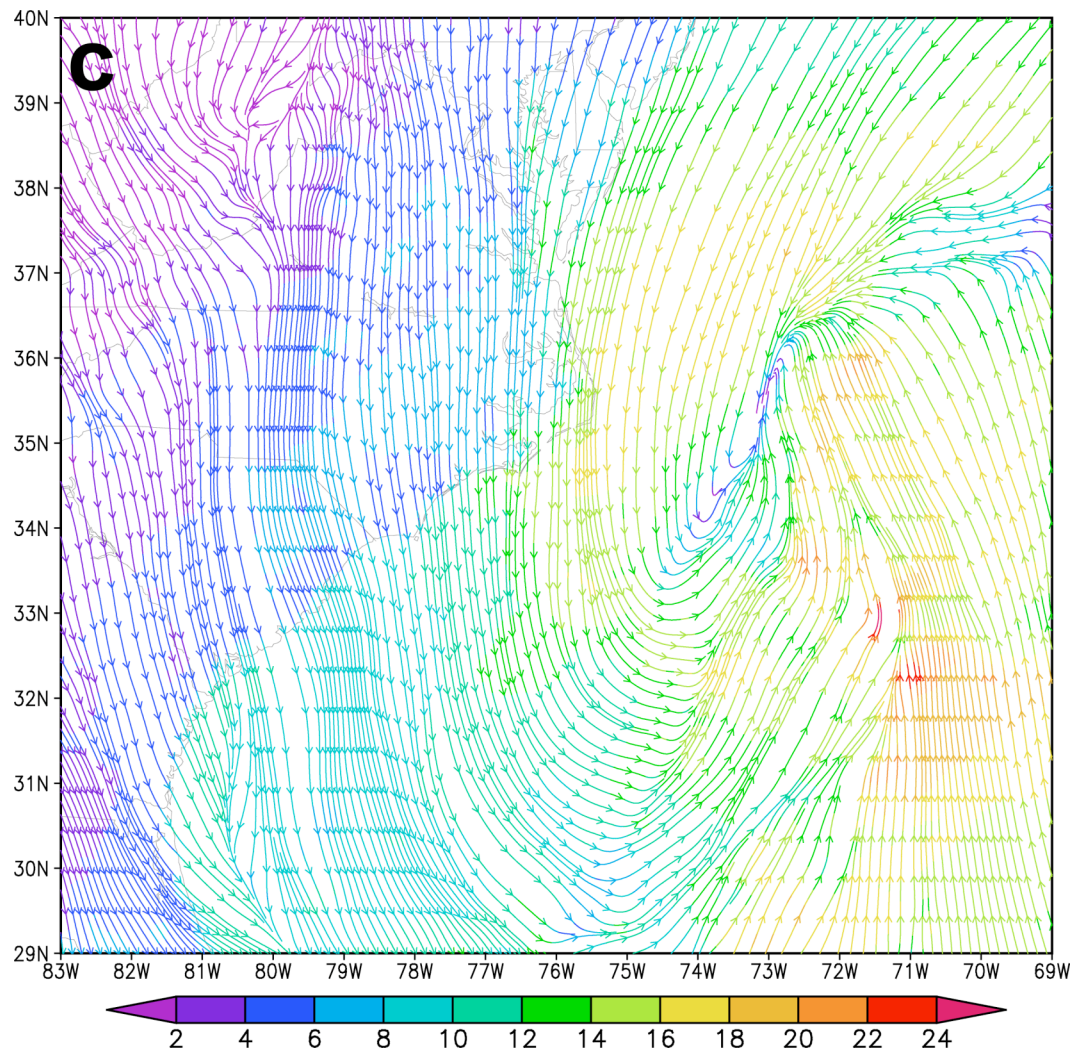


Figure 9.13c Plot of 10-m wind streamlines colored to velocity (ms^{-1}) for the *Exp-2* simulation valid 06Z Jan 25 (30 h into the simulation).

Plots of 950-hPa convergence valid 00Z Jan 25 (24 h into the simulations) are seen in Figure 9.14. When comparing the *Cntl* (Figure 9.14a) with the *Exp-1* (Figure 9.14b), the only notable difference in the position of the line of convergence seen extending from the center of the surface low pressure NE past Cape Hatteras, NC, where the *Exp-1* simulation's maximum values of $8 \times 10^{-4} \text{ s}^{-1}$, is the slight shift to the east. As discussed earlier, there are large differences in the sea-level pressure between the *Cntl* (Figure 9.14a) and the *Exp-2* (Figure 9.14c) simulation. There are also significant differences in location and magnitude of convergence when comparing the *Cntl* to the *Exp-2* simulation, best seen in the difference plot, Figure 9.14d, of the *Cntl - Exp-2*. In the lower portion of Figure 9.14d (arrow "A") the magnitudes of the 950-hPa convergence are quite similar except that the position of the *Exp-2* is slightly shifted to the east, as expected, causing the alternating pattern of positive and negative differences. However, the line of convergence (Figure 9.14d, arrow "B") produced by the *Cntl* simulation, with positive values exceeding $8 \times 10^{-4} \text{ s}^{-1}$, has no negative differences adjacent, or to the east, because there is almost no convergence seen in the *Exp-2* simulation (Figure 9.14c) which corresponds to this location.

The 950-hPa convergence differences between the *Cntl* (Figure 9.15a) and *Exp-1* (Figure 9.15b) 6 h later, 09Z Jan 25 (30 h into the simulation), appear more in the form of divergence in the SW quadrant of the surface low pressure in the *Cntl* simulation. However, this region also appears, to some degree, in the *Exp-1* simulation (Figure 9.15b), and appears more numerically significant than it really is (values are only $-3 \times 10^{-4} \text{ s}^{-1}$) because of the "offset" color scale favoring larger values of convergence opposed to divergence. Larger, yet somewhat noisy values, greater than $6 \times 10^{-4} \text{ s}^{-1}$, appear in the *Cntl* simulation, and stand out in the region NE of Cape Hatteras, NC (arrow "A"), when compared to the *Exp-2* (Figure

9.15d) in the difference plot of the *Cntl - Exp-2* (Figure 9.15d). Significant negative values of $-7 \times 10^{-4} \text{ s}^{-1}$ are seen in Figure 9.15d (arrow "B"), and are caused by positive differences of divergence (i.e., negative convergence) between the *Cntl* and *Exp-2* simulations.

Advancing 6 h to 12Z Jan 25 (Figure 9.16), reveals mainly smaller regions of convergence and divergence less than $\pm 5 \times 10^{-4} \text{ s}^{-1}$ in the area south of 33N and east of 77W. These small scale features weaken, as well as shift further east, as expected, in the *Exp-1* (Figure 9.16b) and *Exp-2* (Figure 9.16c) simulations respectively. More notable differences occur between the *Cntl* (Figure 9.16a) and *Exp-2* simulations, as seen in the difference plot of Figure 9.16d, north of the center of the surface circulation (arrow "A") where the *Cntl* and the *Exp-2* simulation both have convergence exceeding $7 \times 10^{-4} \text{ s}^{-1}$. The difference being that the convergence in *Exp-2* is 80-100 km east of that seen in the *Cntl* simulation.

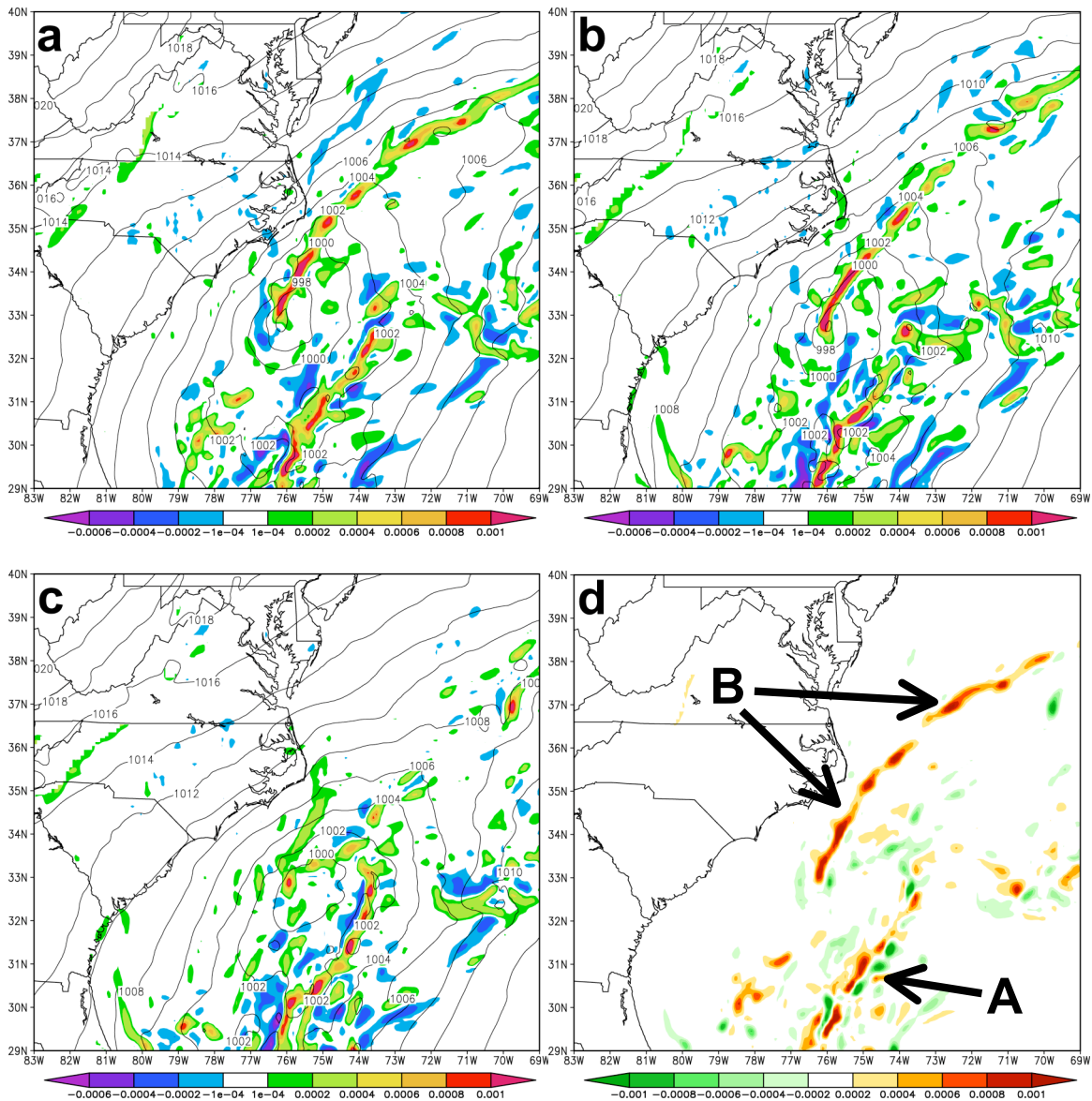


Figure 9.14 Sea-level pressure (mb) and 950-hPa convergence (s^{-1}) valid 00Z Jan 25 (24 h into the simulations) for the *Cntl* (a), *Exp-1* (b), and *Exp-2* (c). A convergence difference field (s^{-1}) of *Cntl* - *Exp-2* (a-c) is shown in (d).

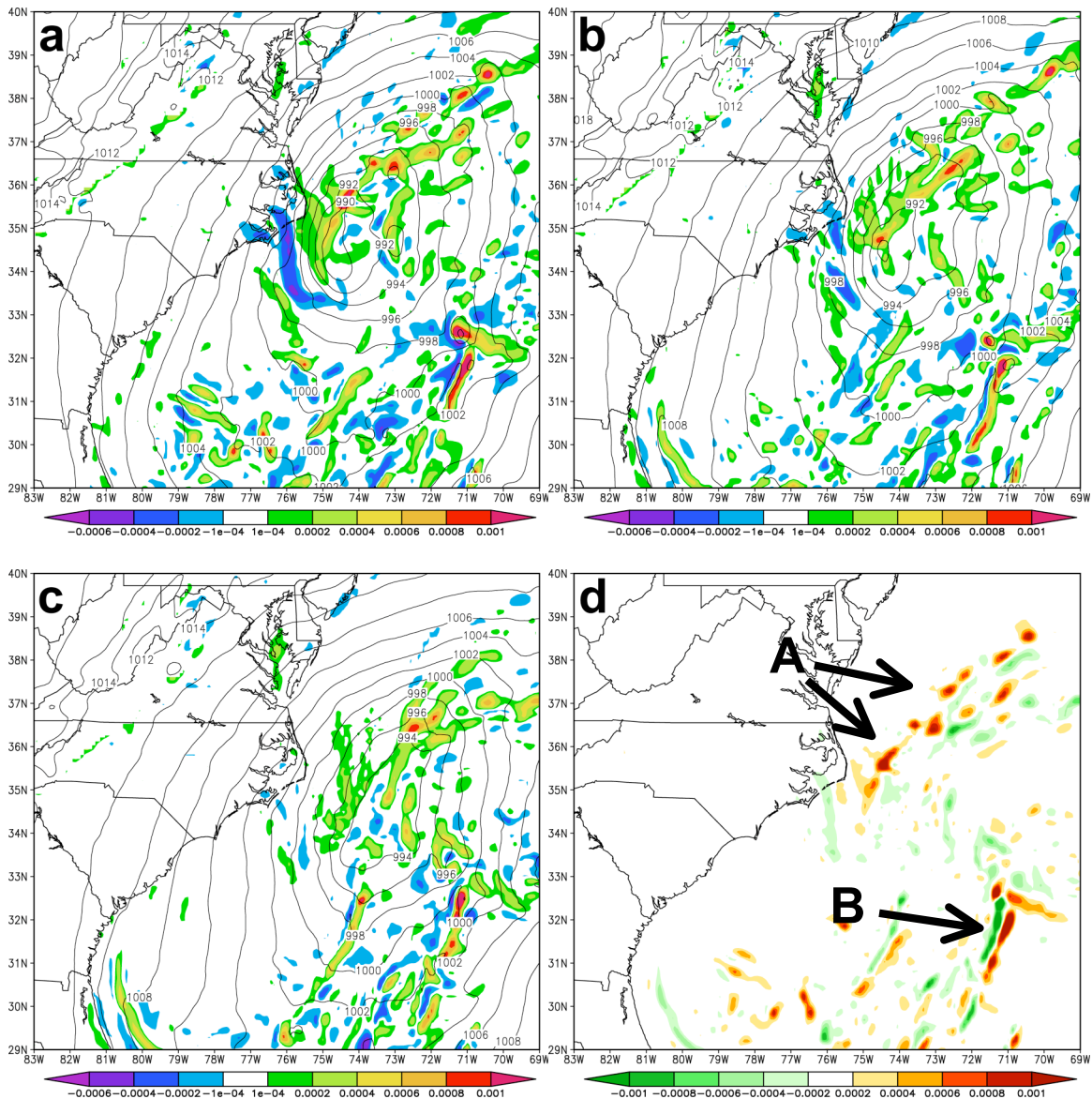


Figure 9.15 Sea-level pressure (mb) and 950-hPa convergence (s^{-1}) valid 06Z Jan 25 (30 h into the simulations) for the *Cntl* (a), *Exp-1* (b), and *Exp-2* (c). A convergence difference field (s^{-1}) of *Cntl* - *Exp-2* (a-c) is shown in (d).

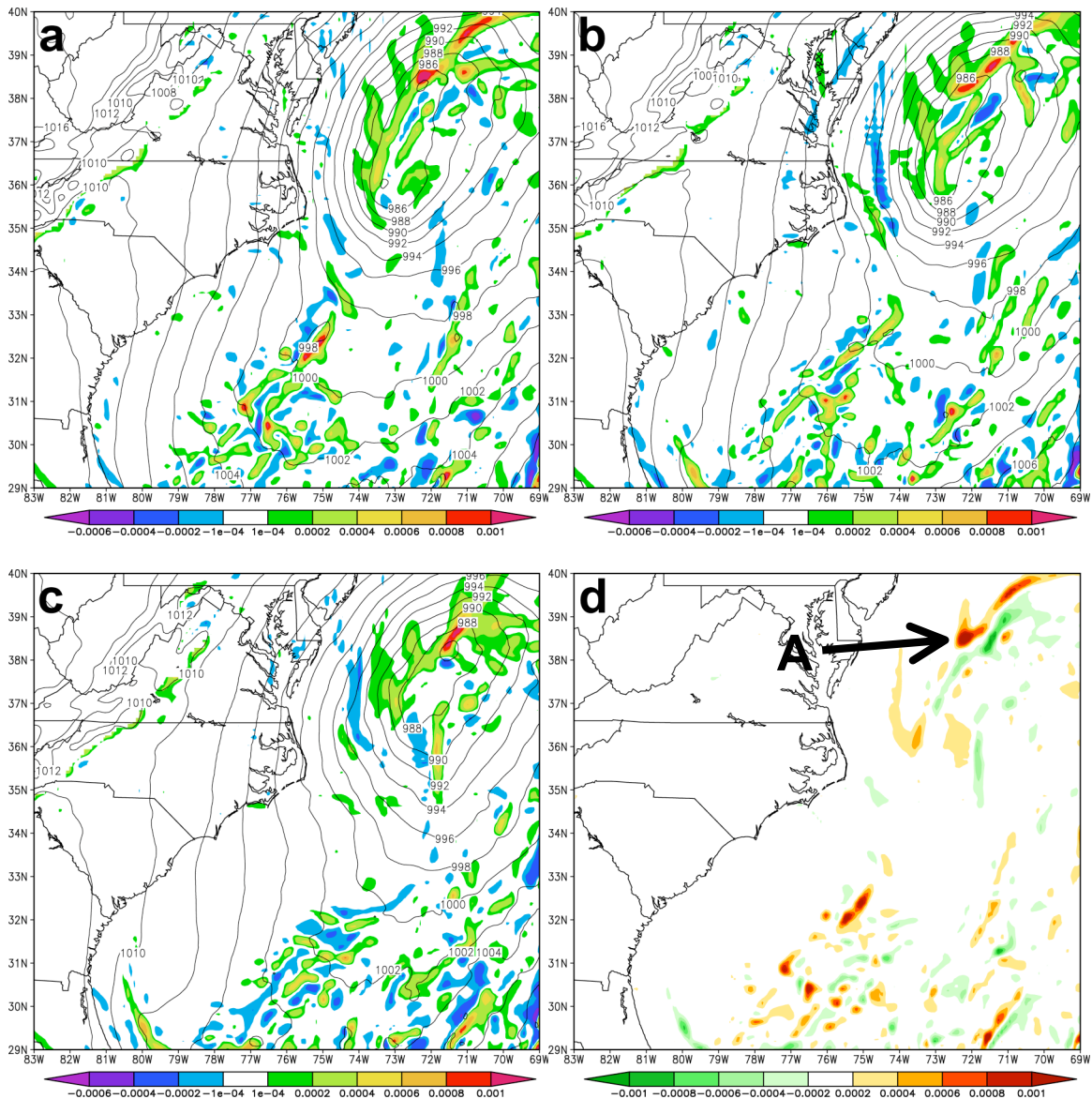


Figure 9.16 Sea-level pressure (mb) and 950-hPa convergence (s^{-1}) valid 12Z Jan 25 (36 h into the simulations) for the *Cntl* (a), *Exp-1* (b), and *Exp-2* (c). A convergence difference field (s^{-1}) of *Cntl* - *Exp-2* (a-c) is shown in (d).

Vertical velocity (ω) at the 850 hPa level along with the sea-level pressure is shown in Figure 9.17 valid 00Z Jan 25. It comes as no surprise that the *Cntl* (Figure 9.17a) and the *Exp-1* (Figure 9.17b) simulation both have a well defined line of upward vertical motion along the location of the frontal boundary. The difference mainly being the eastward shifted position of the *Exp-1*, as the magnitudes, of approximately 1.2 ms^{-1} , are shared by both simulations. The *Exp-2* simulation (Figure 9.17c) has no such region of vertical motion, also made evident by the difference plot seen in Figure 9.17d (arrow "A") of the *Cntl - Exp-2*. This lack of vertical motion at the 850 hPa level is in line with the lower-level convergence seen in the streamline plot (Figure 9.11a), and the convergence plot (Figure 9.14a), both valid 00Z Jan 25. In Figure 9.17d (arrow "B"), the negative values of vertical velocity are actually positive values from the *Exp-2* simulation, which was subtracted from the *Cntl*, and appear just to the east of the *Cntl*'s positive values of equal magnitude ($\sim 1.25 \text{ ms}^{-1}$).

There are evident differences in the 850-hPa vertical velocity fields between the simulations shown in Figure 9.18, valid 06Z Jan 25. In the *Cntl* simulation (Figure 9.18a) values of 1.4 ms^{-1} located at 35.7N, 74.5W, and extending NE to 36.5N, 72.5W, a region which also shares similar values as *Exp-1* (Figure 9.18b). When comparing the *Cntl* simulation to *Exp-2* (Figure 9.18c) differences in vertical velocity, where the *Cntl* exceeds *Exp-2* by more than 1 ms^{-1} , are located $\sim 100 \text{ km}$ east of Cape Hatteras, NC (Figure 9.18d, arrow "A"). Although, this region mainly shows the ω values of the *Cntl*, because the *Exp-2* simulation exhibits no vertical motion in this region. There are also regions of ω shared by all the simulations, best seen in Figure 9.18d (arrow "B"), which are not directly related to the high resolution grids because they appear well to the east of the eastern grid boundary. However, they are shifted in the experimental simulations as a result of the grids causing the

surface low track to shift. This region also corresponds to converging 10-m winds seen in Figure 9.12, as well as heavy precipitation seen in Figures 9.5 and 9.6.

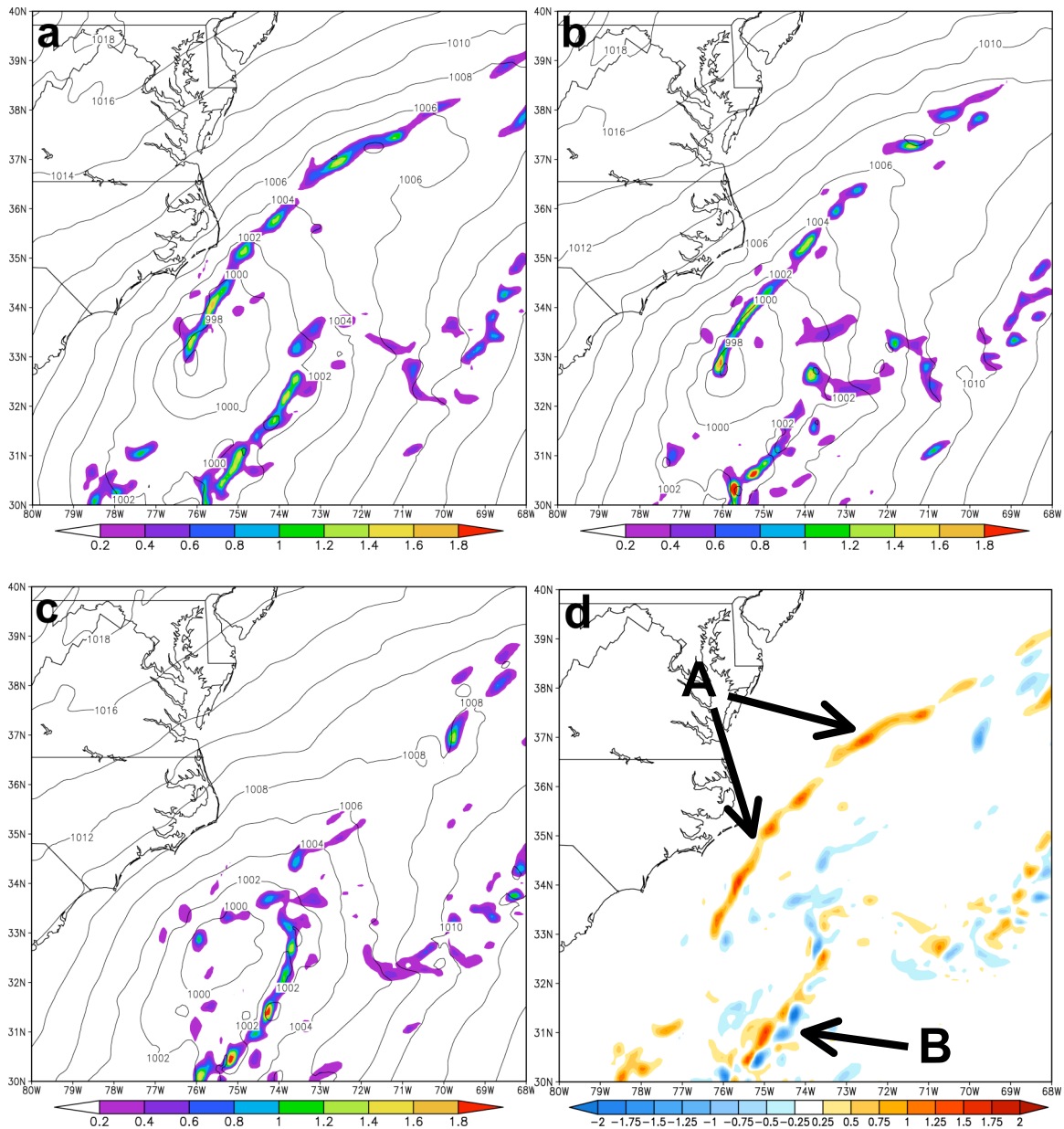


Figure 9.17 Sea-level pressure (mb) and 850-hPa vertical velocity (ω , ms^{-1}) valid 00Z Jan 25 (24 h into the simulations) for the *Cntl* (a), *Exp-1* (b), and *Exp-2* (c). An ω difference field (ms^{-1}) of *Cntl* - *Exp-2* (a-c) is shown in (d).

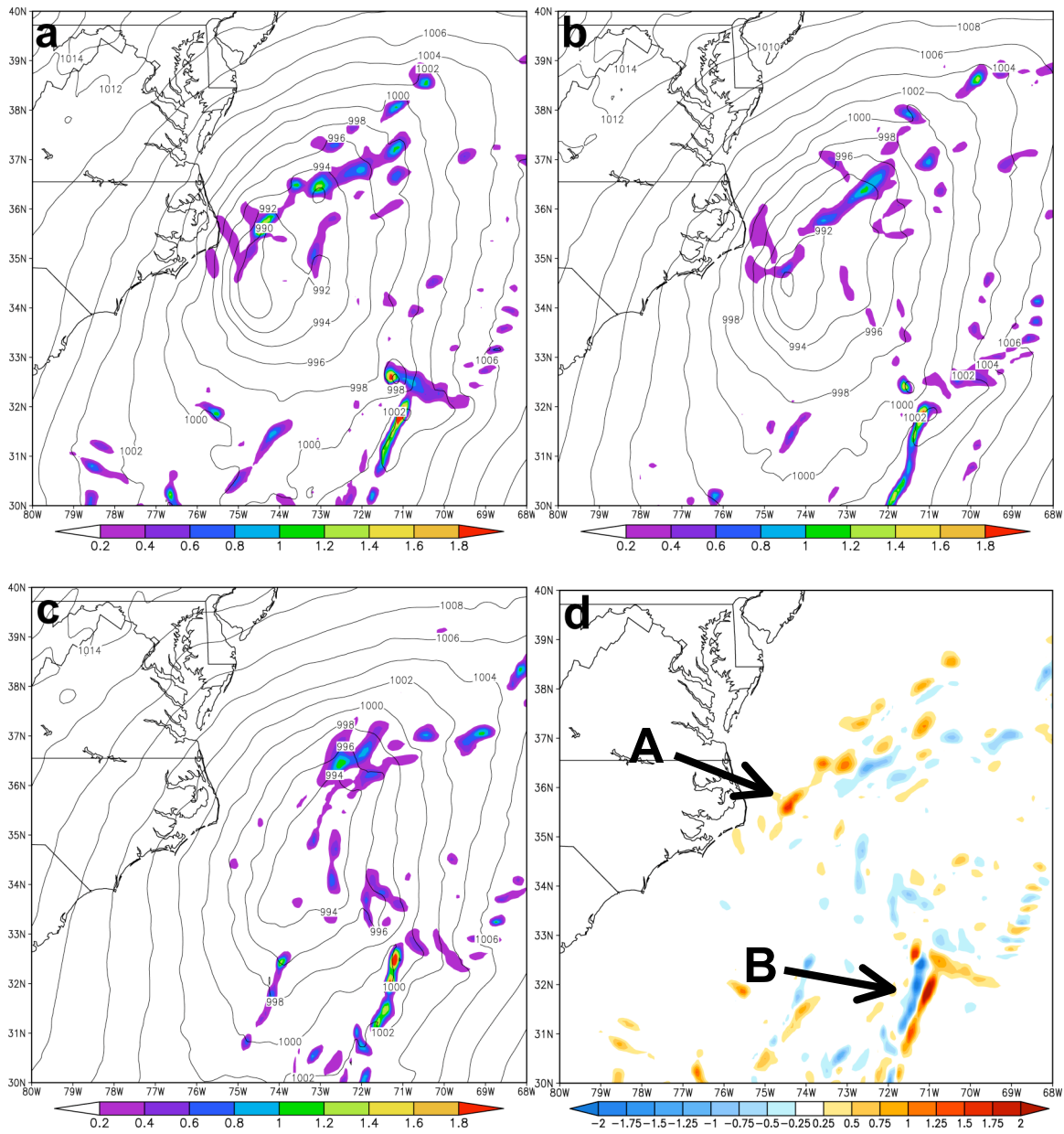


Figure 9.18 Sea-level pressure (mb) and 850-hPa vertical velocity (ω , ms^{-1}) valid 06Z Jan 25 (30 h into the simulations) for the *Cntl* (a), *Exp-1* (b), and *Exp-2* (c). An ω difference field (ms^{-1}) of *Cntl* - *Exp-2* (a-c) is shown in (d).

Cross sections of vorticity reveal significant differences which verify the contrasting degrees of frontogenesis between the simulations. The transects are generated at varying latitudes to follow the evolution of the coastal low pressure system. The vorticity profile, valid 00Z Jan 25, along the latitude 33.2N is seen in Figure 9.19. In the *Cntl* simulation (Figure 9.19a), the maximum values of vorticity below the 850 hPa level exceeded $1.8 \times 10^{-3} \text{ s}^{-1}$ centered over longitude 76.3W. This same response in the *Exp-1* simulation, seen in Figure 9.19b, is much weaker ($< 1.3 \times 10^{-3} \text{ s}^{-1}$), and also occurs 0.2-0.3 degrees of longitude further east than the *Cntl*. When comparing the *Cntl* to the *Exp-2* simulation (Figure 9.19c), this response is almost a nonexistent ($\sim 5 \times 10^{-4} \text{ s}^{-1}$) order of magnitude smaller than the other simulations, as well as located 0.5 degrees of longitude to the east of the *Cntl*. Conversely, there is an increased region of vorticity ($\sim 1 \times 10^{-3} \text{ s}^{-1}$) that appears the greatest in the *Exp-2* simulation (73.8W), and less so in the *Cntl*, but not seen at all in the *Exp-1* simulation (Figure 9.19b).

Vorticity cross sections, which are taken along the 34.7N latitude axis, are seen in Figure 9.20, valid 06Z Jan 25, and are in better longitudinal agreement, with respect to the expected "shift". The *Cntl* simulation, seen in Figure 9.20a, has maximum vorticity values of $1.7 \times 10^{-3} \text{ s}^{-1}$ located at 74.6W below 850-hPa, and values exceeding $1 \times 10^{-3} \text{ s}^{-1}$ which extend to the 750 hPa level. In the *Exp-1* simulation (Figure 9.20b), vorticity values of $1 \times 10^{-3} \text{ s}^{-1}$ barely extend beyond the 900 hPa level, and are 0.4 degrees of longitude east of the *Cntl*. The largest differences in vorticity profiles between simulations occur between the *Cntl* and the *Exp-2* simulations (Figure 9.20c), as expected, and are seen both in location and magnitude. The maximum values of $9 \times 10^{-4} \text{ s}^{-1}$ are located at 73.6W, a full degree of longitude to the east of the *Cntl* (Figure 9.20a). These values, seen in *Exp-2*, are an order of

magnitude smaller than the *Cntl*. Although the difference in magnitude is not as great when the *Exp-2* is compared to the *Exp-1* simulation, the *Exp-2* simulations' vorticity of $7 \times 10^{-4} \text{ s}^{-1}$ extends almost as high as the respective value in the *Cntl*.

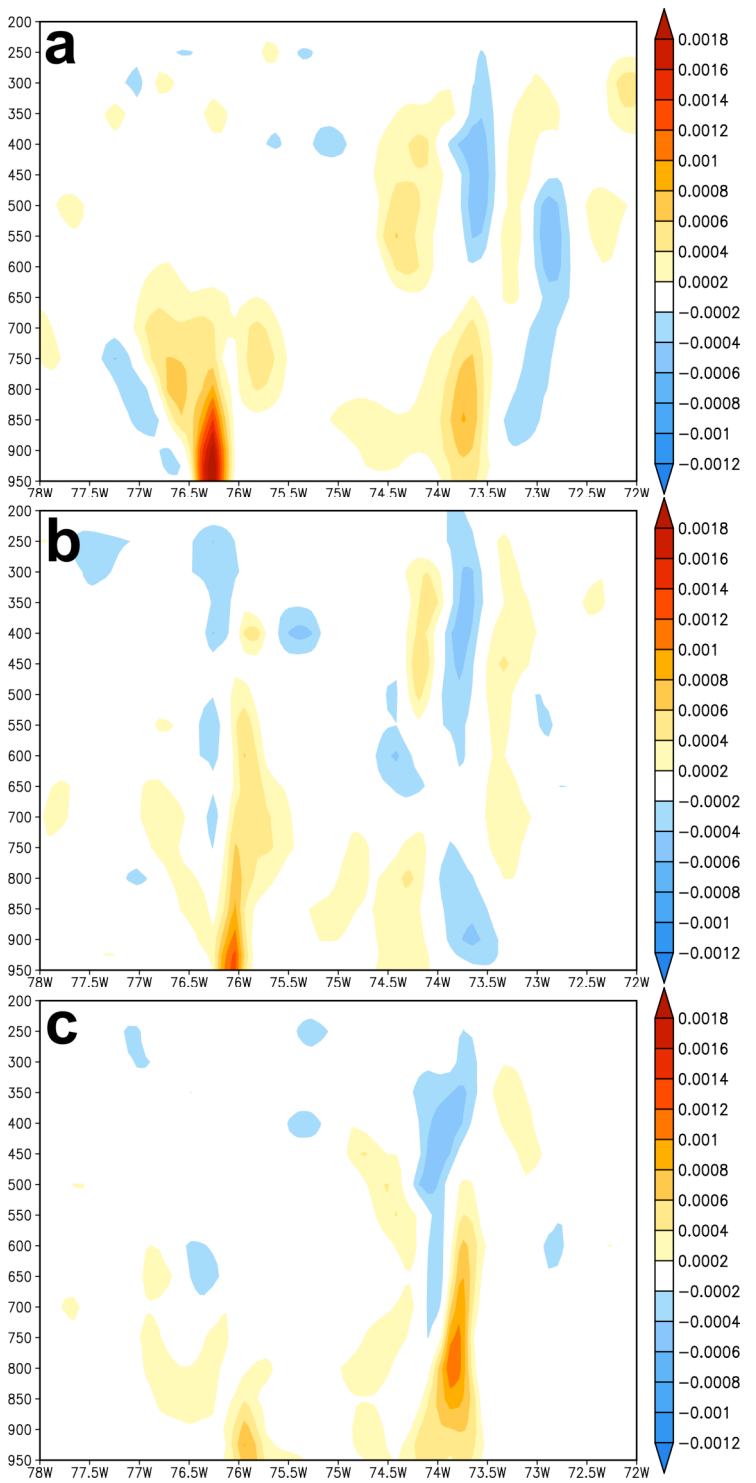


Figure 9.19 Cross sections of vorticity (s⁻¹) along latitude 33.2N valid 00Z Jan 25 (24 h into the simulations) for the *Cntl* (a), *Exp-1* (b), and *Exp-2* (c).

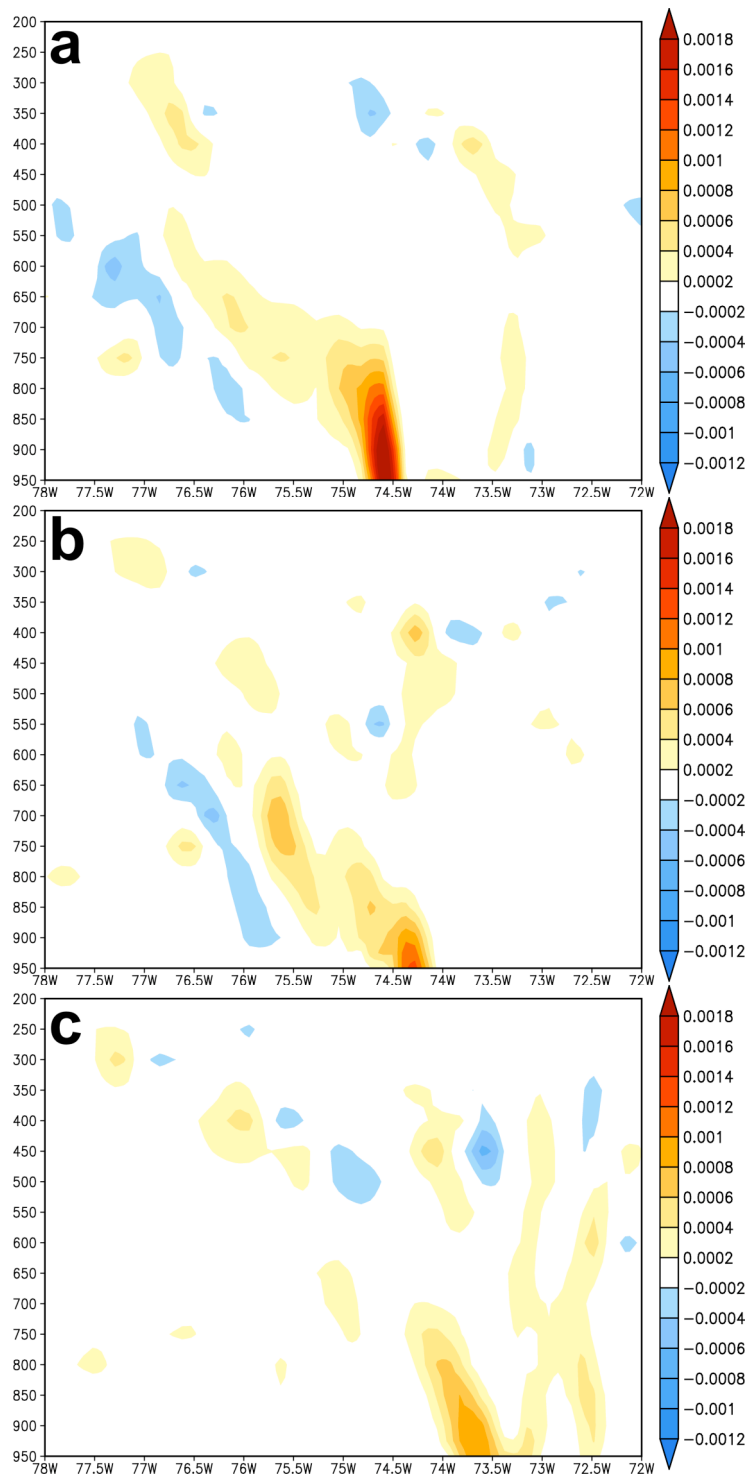


Figure 9.20 Cross sections of vorticity (s^{-1}) along latitude 34.7N valid 06Z Jan 25 (30 h into the simulations) for the *Cntl* (a), *Exp-1* (b), and *Exp-2* (c).

9.3.3 PSBI and ASCII comparison

Calculations for the PSBI, according to the simulations, used the same equation (Equation 5.5) discussed in Chapter 5. The results were computed from numerical gridded output files and accurate to within 5 km (half the grid space difference). Both $T_l = 6^{\circ}\text{C}$, and $T_{GSF} = 24^{\circ}\text{C}$ were recorded during the initialization (24 h prior to development), and are the same for the *Cntl*, *Exp-1*, and *Exp-2*. Only Δx , the longitudinal position of the GSF, varies in this experiment. The values for Δx are taken from an average of two measurements, one from Cape Hatteras, NC, and one from Wilmington, NC. For the *Cntl* simulation $\Delta x = 78$ km, which yields a PSBI value of $2.3^{\circ}\text{C}/10\text{km}$. The *Exp-1* simulation's $\Delta x = 186$ km resulting in a PSBI of $1.0^{\circ}\text{C}/10\text{km}$, and the *Exp-2* simulation's $\Delta x = 352$ km yields a PSBI of $0.5^{\circ}\text{C}/10\text{km}$. These PSBI values are used below to predict the deepening rate for each of the simulations. The simulated sea-level pressure time series is shown in Figure 9.21. Where the lowest sea-level pressures within the domain are plotted each hour for the *Cntl* (red), *Exp-1* (green), and *Exp-2* (blue). Prior to hour 20, the lowest sea-level pressures varied due to localized small scale features over the GSF. Between hours 20 and 32, the surface low pressure began to rapidly develop. Although the *Cntl* and *Exp-1* have lower pressures than the *Exp-2* simulation, the deepening rates are roughly the same. Between hour 32 and hour 42, the *Cntl* continues to rapidly strengthen, while *Exp-2* slowly strengthens, and *Exp-1* falls in between. Beyond hour 42, all the simulations converge to approximately the same pressure as the storm begins to weaken. The most rapid deepening for the simulations after the center of the low pressure entered the domain began at 05Z Jan 25, and was recorded for 12 h. The *Cntl* had a $dP/dt = 12\text{mb}/12\text{h}$, *Exp-1* had a $dP/dt = 9\text{mb}/12\text{h}$, and *Exp-2* had a $dP/dt = 8\text{mb}/12\text{h}$. These values, seen in Figure 9.22, are compared to the deepening rate as

predicted by PSBI (above). The three simulations appear as *Cntl* "A", *Exp-1* "B", and *Exp-2* "C", and the respective deepening rate are averaged per 12 h. It is evident that the trends, although linear, do not correlate very well. Since the simulated 500-hPa vorticity, as discussed in Chapter 8, is lower than the analyzed value, the storm would also fall in the "moderate" bin. The equations from both the "moderate" and "strong" bins were applied with equally skewed results. These results are not particularly surprising since the actual thermal gradient was not changed, just its horizontal location.

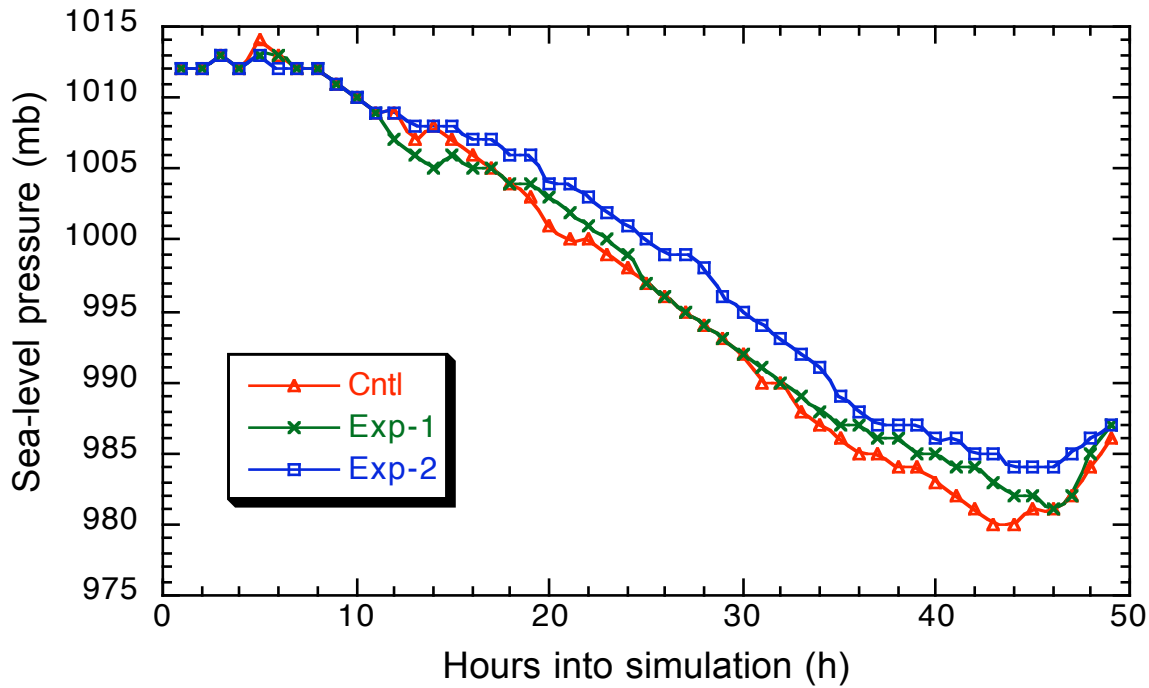


Figure 9.21 Time series of the lowest central sea-level pressure for the *Cntl* (red), *Exp-1* (green), and *Exp-2* (blue) simulations. The hours into the simulation run from hour 1 to hour 49, and correspond to 00Z Jan 24 to 00Z Jan 26.

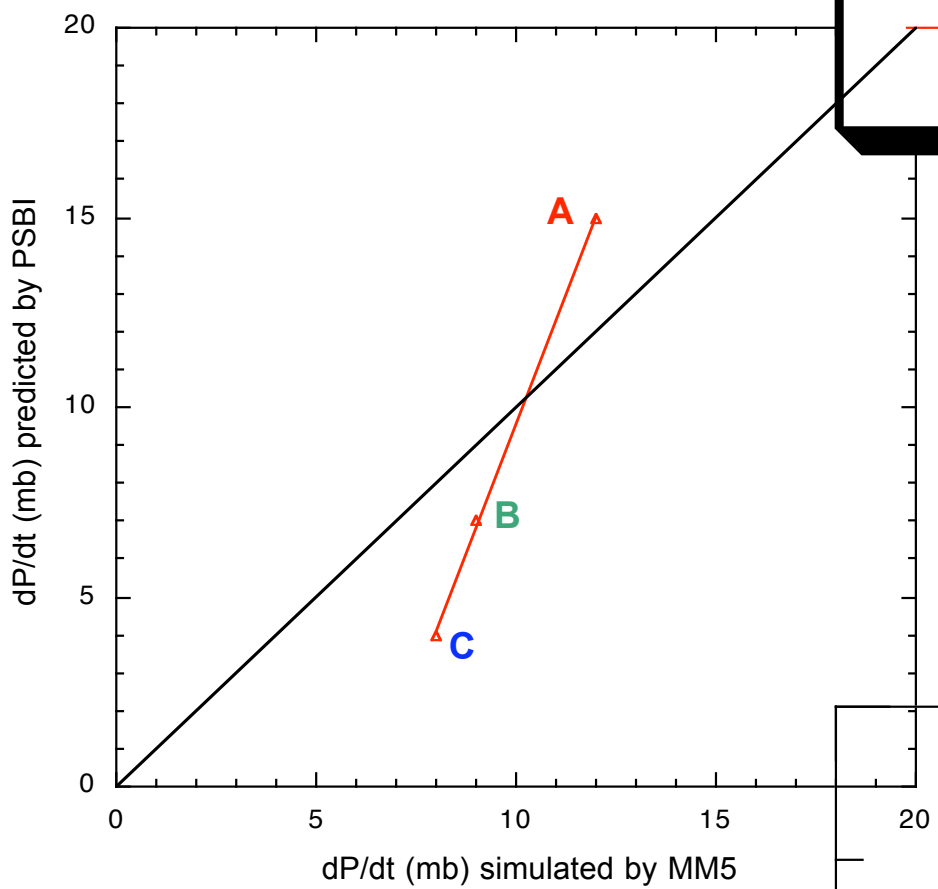


Figure 9.22 Comparison between the deepening rate as predicted by PSBI to the deepening rate simulated by MM5. The three simulations appear as *Cntl "A"*, *Exp-1 "B"*, and *Exp-2 "C"*, and the respective deepening rate are averaged per 12 h.

9.4 Summary

The motivation for this experiment was to isolate the contributions of the location of the SSTs thermal gradient on extratropical cyclogenesis. In Chapter 8, a sensitivity case study was performed using the 24-25 January 2000 case to verify the PSBI by systematically damping the effects of the SST gradient to test the hypothesis that numerical simulations of the 24-25 January 2000 case will follow deepening rates predicted by the PSBI. However, there was an inherent inability to isolate which PSBI variable was responsible for rapid cyclogenesis because the damping reduced the PSBI value as a whole. The objective of this experiment was to isolate the contribution to surface-level forcing based on the position of the Gulf Stream without changing the magnitude of the SST.

Three different simulations were performed in this experiment with the only change being the SST initialization file. The *Cntl* used 1.1 km high resolution SST data which was gridded in its proper location according to the observed conditions on 22 Jan 2000. The *Exp-1* simulation shifted the high resolution SST grids to the east by 1 degree of longitude, and the *Exp-2* simulation shifted them 2.5 degrees of longitude to the east.

The 2-fold hypothesis stated in the beginning of the chapter held true with the exception of one aspect: the definition of "gradient". The hypothesis stated: *First, as shown by ASCII, a weaker thermal gradient will dampen low-level cyclogenesis by reducing thermal advection.* Which is obviously the case, but in this experiment, the gradient was not changed, it was just shifted east. Thus, the "low-level cyclogenesis" in response to the thermal gradient was not significantly damped, but relocated to the east. The hypothesis further states: *However, a more complex reason, which may be more case specific, is the surface to upper-level trough position offset which can either enhance or reduce the vertical*

feedback. This aspect of the experiment was made evident by plots of ω and vorticity profiles. The shift in storm track, as seen in the various 10-m wind plots, was caused by the relocation of the coastal front. The offset likely played a roll in the temporal delay of maximum precipitation which is discussed further in the conclusions section.

CHAPTER 10: CONCLUSIONS

10.1 The Atlantic Surface Cyclone Intensification Index

Inclusion of 11 years and 4 months of data from 1991 to 2002 added 115 storms to the original 10 year (116 storm) ASCII data set compiled by Cione et al. (1993). Application of the same methods employed by Cione et al. (1993) for the first climatological study verify the original regression fit. The slope of the fit (-6.7 mb/12h) was 0.1 mb/12h less than that in the original study. The correlation coefficient of the new 231 storm data set was 0.55. This decreased the explained variance by an insignificant 1.7%. Doubling the size of the original ASCII data set verifies threshold values defined in the Pre-Storm Baroclinic Index by the statistically insignificant changes in the regression fit. However, the variance explained by the PSBI remains low, approximately 30%. In this study, we addressed a major limitation inherent in the original ASCII study by adding an approximate measure of upper-tropospheric forcing.

The additional grouping of storms within the 1991-2002 data set based on 500-mb vorticity significantly reduced the scatter, and further isolated the contributions of surface forcing versus upper-level forcing on extratropical cyclogenesis. The decrease in slope for cases with less upper-level forcing, as well as the stratified bin positions, suggest that there is a shifting degree of dependency on surface-level forcing. Correlation coefficients for the “strongly forced”, “moderately forced”, and “weakly forced” storms are, 0.84, 0.86, and 0.59 respectively. However, all these values are higher than the non-binned correlation coefficient of 0.55. There is a definite trend for stronger correlation among the storms that are linked to larger upstream upper-level vorticity maxima, as demonstrated by the less

substantial improvement in correlation for “weakly forced” storms. Additionally, as much as 74% of the variance can be explained for stronger upper-level forcing cases. This is a marked improvement over the 30% of explained variance from the original ASCII data set, as well as the entire updated climatology.

Employment of the 500-mb vorticity parameter in an operational setting would require the analysis of 24 to 48-h 500-mb forecasted fields of absolute vorticity on a coarse grid (e.g., $2.5 \times 2.5^\circ$) to ensure consistency with the current study, and to reduce noise. To determine the correct bin, an automated script can radially search for the region of maximum absolute vorticity. Following the binning procedure, the correct forecast regression fit of "strongly forced", "moderately forced", or "weakly forced" can be used to predict the deepening rate of the impending storm.

10.2 24-25 January 2000 Case Study

The overall performance of the experimental simulation (with high resolution SST) was better than the control simulation in most aspects of simulating this major storm. In the control simulation, reduced development of the storm may be due to coarse and average SST representation. The control simulation's poor forecast in track position may be linked to the weakly defined GSF. In the experimental simulation, the surface low tracked farther west along the more accurately represented GSF. This track is apparently the result of the surface low pressure following a zone of preexisting vorticity along the coastal front.

Large areas of convergence along the GSF are simulated in the experimental simulation. The areas of convergence further offshore, as well as the minor divergent patterns along the coast, are seen in both simulations. This suggests that the greatest effect in

changing convergence occurred over the region where the SST data were improved.

The large differences in sensible heat flux are partly a result of the increased wind velocities seen in the experimental simulation; however, the regions where the wind was slightly greater were quite localized. In both simulations, the majority of the coastal region had wind velocities that differed less than 6 kts. This suggests that the large values of sensible heat flux seen in the experimental simulation were more a factor of the high resolution SST data. It was these data that revealed a more defined GSF, as well as two warm core surface filaments with SST values 5-7°C greater than that of the control's SST data. Thus, it is likely that the surface-level convection of the experimental simulation is driven by the increased value and resolution of the Gulf Stream's western boundary SSTs.

In the experimental simulation, the enhanced vertical velocity and reduction in low-level static stability along the GSF swath generate greater surface-level convergence and frontogenesis. This convergence is the major difference in the simulations, as well as a sign that the high resolution SST data did affect the track by changing the strength and location of the frontal boundaries. Stronger near-surface vorticity is seen in the experimental simulation relative to the control simulation in the vicinity of the coastal front extending northeast from the low center. This coastal front, which formed above the tight marine thermal gradient of the GSF, is not seen in the control simulation. It is the enhanced effectiveness of vortex stretching associated with the convergence along this frontal boundary that can explain the tendency for a stronger storm in the experimental simulation.

10.3 Sensitivity to Boundary Layer Baroclinicity

The slope of the ASCII forecast regression fit is matched by the similar slope of the three simulations. Although these three simulations shared, for the most part, the same upper-level forcing characteristics, it turns out that the numerical values for this case were very close to the "average" for all the cases (1991-2002) thus placing the fit in the middle of the distribution. The PSBI for simulation (a) was unrealistic in a sense that using the "skin temperature" data placed the warm-core eddy partly inside the Pamlico Sound (which is not physically possible). However, for this study, it was the objective to have unrealistically large, as well as small, PSBI values to separate the magnitudes of the surface forcing.

Limitations of the study were mainly a function of grid resolution which rounded the numerical values based on distance, as well as the inherent inability to separate the 500-mb trough from the surface low's feedback. The boundary conditions imposed by the domain size were likely limiting the differences in the development in addition to the conditions stated above.

Regardless, the change in surface deepening rate did follow the trend forecasted by ASCII. Analysis of the individual simulations revealed a much deeper low pressure for (a) resulting from the vortex stretching and convergence along the frontal boundary that formed over the GSF connecting the southern branch to the warm-core eddy (literally on Cape Hatteras). As a result, the track took a much more westerly jog until north of the region where the GSF in (a) was more in line with (b) and (c). Simulation (c) had the lowest PSBI, yet still continued to deepen to a rather large storm. Although there was still a significant thermal gradient (compared to no gradient), most of the cyclogenesis was likely in response to the upper-level trough. As seen in Figure 8.12, the three simulations aligned nicely with

the ASCII regression fit, and offer a second method of verification to the original climatology, as well as further isolating the contribution of SST gradients to extratropical cyclogenesis.

10.4 Sensitivity to Gulf Stream Position

In this experiment, the SST gradient was not changed, it was just shifted east by 1° and 2.5° of latitude for the *Exp-1* and *Exp-2* simulations, respectively. Thus, the "low-level cyclogenesis" in response to the thermal gradient was not significantly damped, but occurred further east. The shift in storm track, as seen in the various 10-m wind plots, was caused by the horizontal displacement of the coastal front. It is evident from Chapter 7 that the surface low pressure will attempt to track along the frontal boundary formed over the GSF as a result of the pre-existing vorticity. By altering the track of the surface low, the feedback link to the upper-level trough was "interrupted" thus reducing the surface-level cyclogenesis. This "interruption" occurred in a spatial reference frame by causing the surface cyclone to track further east for the *Exp-1* and *Exp-2* simulations. As a result, the maximum upper to lower-tropospheric positive feedback occurred later in those respective simulations. This is most noticeable in the plots of precipitation, and the time series of sea-level pressure. The convection delay over North Carolina is likely a factor of the advecting of warm air at the surface-level being delayed from linking with the region of divergence aloft because the source of the warm air has been shifted to the east for each consecutive experimental simulation. Cross sections of vorticity and plots of vertical motion reveal significant differences which verify the contrasting degrees of feedback between the simulations.

The lack of deepening in *Exp-2*, as compared to the *Cntl*, is likely a result of the vertical feedback link's horizontal displacement being too large. As discussed in Chapters 4 and 7, pre-existing vorticity along the coastal front, which develops in response to the thermal gradient of the GSF, plays a crucial role in the future track of the surface cyclone. However, in the experimental simulations, the displacement caused the surface low to track further east, and out in front of the ideal zone to phase with the upper-level trough. In addition to the lack of development related to upper-to-lower-level trough linkage, the warm advection takes longer to reach the regions of 500-hPa divergence. Granted, the warm air advection is generating its own upper-level divergence, via building the downstream ridge, the 500-hPa trough is still further away (horizontally) from the surface low in *Exp-1* and *Exp-2*, than in the *Cntl* simulation. Thus, the corresponding temporal delays result in the maximum QPF occurring further north.

The PSBI comparison illustrates a very important aspect of this experiment, and possibly warrants changing the protocol of horizontal thermal gradient measurements for ASCII. Obviously the second sensitivity study is simulating the opposite extreme from the first sensitivity study, and it would not be particularly realistic to place the GSF over 300 km east of Charleston, SC. However, the objective was to use an extreme event to test how ASCII handles storms at its limits. After all, it is the severe storms which are of most concern to society. In Chapter 8, it was shown that by damping the thermal magnitude of the Gulf Stream, the developing coastal low pressure was significantly weakened. This was expected, and the PSBI was in full agreement. The inherent limitation with that method was the inability to separate the reduction in SST from the position of the GSF. This experiment left the SST of the Gulf Stream the same, and just shifted its location to the east. Since the

near-coastal SSTs were extended to the shifted location of the GSF, the actual "thermal gradient" induced by the GSF was not changed, but moved. However, the PSBI measurement is made from land (Wilmington and Cape Hatteras, NC) which, for this case, must span the entire region of extended near-shore SSTs before reaching the GSF, thus making Δx very large over a region where the SST does not change. As expected, the storm rapidly developed over the GSF, albeit further east for each consecutive simulation. In all the simulations, there is little difference ($<5^{\circ}\text{C}$) between the land surface temperatures and the near-shore SSTs. The premise that rapid cyclogenesis occurs over a region where the cold air is advected over warm water with little time to modify still holds true. In this experiment, there was little modification between the coast and the GSF despite the change in distance over which the cold air was advected.

This reveals two key aspects, both of which are in line with previous findings from Chapters 5, 7, and 8: i) The magnitude of the Gulf Stream's SST exerts a more significant influence on surface cyclogenesis as opposed to the SST gradient¹. This is concluded from comparing results from Chapter 8 with those in Chapter 9. ii) The actual width of the thermal gradient over which the SSTs of the near-shore waters transition to the SSTs of the Gulf Stream, is more important than the distance of the GSF from the shoreline.

The second point leads to the conclusion that Δx (the denominator in the PSBI) may be better suited for the ASCII forecast method if it were a measurement over which only the

¹ This can only be stated for the region east of North and South Carolina, and assumes that the coastal land temperatures and near-shore water temperatures are much colder than the maximum SST values of the Gulf Stream (e.g., January, February, etc.).

SST was changing, thus reducing forecast errors for cases where the thermal gradient is tight and the Gulf Stream's SST is high, yet the position of the GSF is far from shore and the near-shore waters have a constant SST.

REFERENCES

- Bjerknes, J., and J. Holmboe, 1944: On the theory of cyclones. *J. Meteor.*, **1**, 1-22.
- Blackadar, A.K., 1976: Modeling the nocturnal boundary layer. *Preprints of Third Symposium on Atmospheric Turbulence and Air Quality*, Raleigh, NC, 19-22 October 1976, Amer. Meteor. Soc., Boston, 46-49.
- Blackadar, A.K., 1979: High resolution models of the planetary boundary layer. *Advances in Environmental Science and Engineering*, 1, No. 1. Pfaffin and Ziegler, Eds., Gordon and Breach Sci. Publ., New York, 50-85.
- Blanton, J. O., L. P. Atkinson, L. J. Pietrafesa, and T. N. Lee, 1981: The intrusion of Gulf Stream Water across the continental shelf due to topographically induced upwelling. *Deep Sea Res.*, 28A(4): 393-405.
- Brennan, M. J., and G. M. Lackmann 2004: The role of antecedent precipitation in the development of the 24-25 January 2000 U.S. east coast snowstorm, 20th Conference on WAF/16th Conference on NWP, 84 AMS Annual Meeting, 11-15 January, 2004. Amer. Meteor. Soc., CD-ROM, 8.3.
- Bosart, L.F., 1981: The Presidents' Day snowstorm of 18-19 February 1979; A synoptic scale event. *Mon. Wea. Rev.*, **109**, 1542-1566.

Bosart, L.F., C. J. Vaudo, and H. J. Helsdon, Jr., 1972: Coastal Frontogenesis. *J. Appl. Meteor.*, **11**, 1236-1258.

Bright, D. R., and S. L. Mullen, 2002: The sensitivity of the numerical simulation of the southwest monsoon boundary layer to the choice of PBL turbulence parameterization in MM5. *Wea. Forecasting*, **17**, 99-114.

Brooks, D.A., and J.M. Bane, 1978: Gulf Stream deflection by a bottom feature off of Charleston, South Carolina. *Science*, **201**, 1225-1226.

Bunker, A.F., 1976: Computations of surface energy flux and annual air-sea interaction cycles of the North Atlantic Ocean., *Mon.Wea. Rev.*, **104**, 1122-1140.

Bunker, A., and L.V. Worthington, 1976: Energy exchange charts of the North Atlantic Ocean, *Bull. Amer. Meteor. Soc.*, **57**, 450-467.

Buizza, R. and P. Chessà, 2002: Prediction of the U.S. Storm of 24-26 January 2000 with the ECMWF Ensemble Prediction System. *Mon. Wea. Rev.*, **130**, 1531-1551.

Carlson, T.N., and F.E. Boland, 1978: Analysis of urban-rural canopy using a surface heat flux / temperature model. *J. Appl. Meteor.* **17**, 998-1013.

Chen, F., and J. Dudhia, 2001: Coupling an advanced land surface hydrology model with the Penn State/NCAR MM5 modeling system. Part 1: Model description and implementation. *Mon. Wea. Rev.* **129**, 569-586.

Childs, P., S. Raman, R. Boyles, 2004: The influence of highly resolved sea surface temperatures on meteorological simulations off the Southeast US coast. 20th Conference on WAF/16th Conference on NWP, 84 AMS Annual Meeting, 11-15 January, 2004

Chou, S.H., and D. Atlas, 1982: Satellites estimates of ocean-air heat fluxes during cold-air outbreaks. *Mon. Wea. Rev.*, **110**, 1434-1450.

Chou, S.H., D. Atlas, and E.N. Yeh, 1986: Turbulence in a convective marine atmospheric boundary layer. *J. Atmos. Sci.*, **43**, 547-564.

Cione, J. J., S. Raman, and L. J. Pietrafesa, 1993: The effect of Gulf Stream-induced baroclinicity on the U.S. east coast winter cyclones. *Mon. Wea. Rev.*, **121**, 421- 430.

Cione, J. J., and S. Raman, 1995: A numerical investigation of surface-induced mesocyclogenesis near the Gulf Stream. *Tellus*, **47A**, 815-833.

Cione, J. J., S. Raman, R.A. Neuherz, L. J. Pietrafesa, K. Keeter, and Xiaofeng Li, 1998: The Use of Pre-storm Boundary Layer Baroclinicity in Determining and Implementing the Atlantic Surface Cyclone Intensification Index. *Bound.-Layer Meteor.*, **89**, 211-224.

Cohen, C., 2002: A comparsion of cumulus parameterizations in idealized sea-breeze simulations. *Mon. Wea. Rev.*, **130**, 2554-2571.

Davis, C.A., and K. Emanuel, 1991: Potential vorticity diagnostics of cyclogenesis. *Mon. Wea. Rev.*, **119**, 1929-1953.

Davis, C. A., Stoelinga, M. T., Kuo, Y.-H., 1993: The integrated effect of condensation in numerical simulations of extratropical cyclogenesis. *Mon. Weather Rev.*, **121**, 2309-2330.

Deardorff, J.W., 1972: Parameterization of the planetary boundary layer for use in general circulation models. *Mon. Wea. Rev.*, **100**, 93-106.

Delsol, F., K. Miyakoda, and R.H. Clarke, 1971: Parameterized processes in the surface boundary layer of an atmospheric circulation model. *Quart. J. Roy. Meteor. Soc.*, **97**, 181-208.

Dirks, R. A., J. P. Kuttner, and J. A. Moore, 1988: Genesis of Atlantic Lows Experiment (GALE): An Overview, *Bull. Amer. Meteorol. Soc.* **69**, 147-160.

Dudhia, J., 1993: A nonhydrostatic version of the Penn State / NCAR mesoscale model: Validation tests and simulation of an Atlantic cyclone and cold front. *Mon. Wea. Rev.*, **121**, 1493-1513.

Fantini, M., 1991: The Influence of Heat and Moisture Fluxes from the Ocean on the Development of Baroclinic Waves, *J. Atmos. Sci.* **47**, 840-855.

Forbes, G.S., R.A. Anthes, and D.W. Thomson, 1987: Synoptic and mesoscale aspects of an Appalachian ice storm associated with cold-air damming, *Mon. Wea. Rev.*, **115**, 564-591.

Fritsch, J.M. and J.S. Kain, 1993: Convective parameterization for mesoscale models: The Fritsch-Chappell scheme. The Representation of cumulus in numerical models. K. A. Emanuel and D. J. Raymond, eds, Meteorological Monographs. Amer. Meteor. Soc., 159-164.

Gorshkov, S.G., 1978: *World Ocean Atlas, Vol II, Atlantic and Indian Oceans*; Pergamon NY, 306 pp.

Grell, G., Y.-H. Kuo, and R. J. Pasch, 1991: Semi-prognostic tests of cumulus parameterization schemes in the middle latitudes. *Mon. Wea. Rev.*, **119**, 5-31.

Grell, G., 1993: Prognostic evaluation of assumptions used by cumulus parameterizations. *Mon. Wea. Rev.*, **121**, 764-787.

Grell, G.A., J. Dudhia, and D.R. Stauffer, June 1994: A Description of the Fifth-Generation Penn State/NCAR Mesoscale Model (MM5), Tech. Rep. NCAR/TN-398+STR, National Center for Atmospheric Research, Boulder, Colorado.

Grell, G.A., J. Dudhia, and D.R. Stauffer, 1995: A description of the fifth-generation Penn State NCAR Mesoscale Model (MM5). NCAR Technical Note TN-398+STR. 122 pp.

Griffith,C.G., W.L.Woodley, P.G.Grube, D.W.Martin, J.Stout, and D.N.Sikdar, 1978: Rain estimation from geosynchronous satellite imagery: Visible and infrared studies. *Mon.Wea.Rev.*, **106**, 1153-1171.

Grossman, R.L., 1988: Boundary layer warming by condensation: Air-sea interaction during an extreme cold air outbreak fro the eastern coast of the United States, *Seventh Conference on Oceanic-Atmospheric Interaction. Amer. Meteor. Soc.* 31 January- 5 February, 1988.

Hall, M.M., and N.P. Fofonoff, 1992: Downstream development of the Gulf Stream from 68° to 55°W . *Journal of Physical Oceanography*, **23**, 225-249.

Hasse, L., M. Gruenwald, J. Wucknitz, M. Dunckel, and D. Schriever, 1978: Profile derived turbulent fluxes in the surface layer under disturbed and undisturbed conditions during GALE. *Meteor.*, **13**, 24-40.

Hogg, N.G. and W.E. Johns, 1995: Western boundary currents. *U.S. National Report to International Union of Geodesy and Geophysics 1991-1994*, Supplement to *Reviews of Geophysics*, **33**, 1311-1334.

Holt, T., and S. Raman, 1990: Marine boundary-layer structure and circulation in the region of offshore re-development of a cyclone during GALE. *Mon. Wea. Rev.*, **118**, 392-410.

Holton, James, R., 1992: *Introduction to Dynamic Meteorology*. 3d ed. Academic Press Ltd., London, U.K..

Hoskins, B.J., 1991: Towards a PV - Theta view of the general circulation; *Tellus*, **43AB**, 27 - 35

Hoskins, B.J., M.E. McIntyre, and A.W. Robertson, 1985: On the use and significance of isentropic potential vorticity maps; *Quart. J. R. Meteor. Soc.*, **111**, 877 - 946

Huang, C. Y., and S. Raman, 1990: Numerical simulation of cold air advection over the Appalachian mountains and the Gulf Stream. *Mon. Wea. Rev.*, **118**, 343-361.

Huang, C. Y., and S. Raman, 1992: A three-dimensional numerical investigation of North Carolina coastal front and the Gulf Stream rainband. *J. Atmos. Sci.*, **49**, 560-584.

Huh, O.K., L.J. Rouse, and N.D. Walker, 1984: Cold air outbreaks over the northwest Florida continental shelf: Heat Flux Processes and Hydrographic Changes, *J. Geophys. Res.*, **89**, 717-726.

Huo, Z., D.L. Zhang and J. Gyakum 1999: The interaction of potential vorticity anomalies in extratropical cyclogenesis. Part I: Static piecewise inversion. *Monthly Weather Review*, **127**, 2546-2561

Jang, K.-I., Zou, X., M. S. F. V. De Pondeca, M. Shapiro, C. Davis and A. Krueger, 2003: Incorporating TOMS Ozone Measurements into the Prediction of the Washington, D.C., Winter Storm during 24–25 January 2000. *J. App. Meteor.*, **42**, 797–812.

Johns, W.E., T.J. Shay, J.M. Bane, D.R. Watts, 1995: Gulf Stream structure, transport, and recirculation near 68° W. *Journal of Geophysical Research*, **100**, 817-838.

Kalnay, E., M. Kanamitsu, R. Kistler, W. Collins, D. Deaven, L. Gandin, M. Iredell, S. Saha, G. White, J. Woollen, Y. Zhu, M. Chelliah, W. Ebisuzaki, W. Higgins, J. Janowiak, K. C. Mo, C. Ropelewski, J. Wang, A. Leetmaa, R. Reynolds, Roy Jenne, and Dennis Joseph, 1996: The NCEP/NCAR 40-Year Reanalysis Project. *Bull. Amer. Meteor. Soc.*, 1996, **77**, 437-431.

Kocin, P. J. and L. W. Uccellini, 1985a: A survey of major east coast snow storms, 1960-1983. Part 1: Summary of surface and upper level characteristics. NASA TM 86196, 214pp.

Kocin, P. J. and L. W. Uccellini, 1985b: A survey of major east coast snow storms, 1960-1983. Part 2: Case studies of eighteen storms. NASA TM 86195, 101pp.

Kocin, P. J. and L. W. Uccellini, 1990: Snowstorms along the Northeastern United States Coast, 1955 to 1985. American Meteorological Society, Meteorological Monograph No. 44, 280.

Kuo, Y.H., and R. J. Reed, 1988: Numerical Simulation of an Explosively Deepening Cyclone in the Eastern Pacific. *Mon. Wea. Rev.*, **116**, 2081-2105.

Kuo, Y.H., and S. Low-Nam, 1990: Prediction of Nine Explosive Cyclones over the Western Atlantic Ocean with a Regional Model. *Mon. Wea. Rev.*, **118**, 3-25

Kuo, Y. H., R. J. Reed, and S. Low-Nam, 1990: Effects of surface energy fluxes during the early development and rapid intensification stages of seven explosive cyclones in the Western Atlantic. *Mon. Wea. Rev.*, **119**, 457-476.

Langland, R. H., M. A. Shapiro, and R. Gelaro, 2002: Initial condition sensitivity and error growth in the forecast of the 25 January 2000 east coast snowsnow. *Mon. Wea. Rev.*, **130**, 957-974.

Lenschow, D.H., and E.M. Agee, 1976: Preliminary results from the Air-Mass Transformation Experiment (AMTEX), *Bull. Amer. Meteor. Soc.*, **57**, 1346-1355.

Lenschow, D.H., J.C. Wyngaard, and W.T. Pennel, 1980: Mean and second-moment budgets in a baroclinic convective boundary layer, *J. Atmos. Sci.*, **37**, 1313-1326.

Liu, W.T., K.B. Katsaros, and J.A. Businger, 1979: Bulk parameterization of air-sea exchanges of heat and water vapor including the molecular at the interface., *J. Atmos. Sci.*, **36**, 1722-1735.

Mariano, A.J., T.M. Chin and E.H. Ryan, R. Kovach and O.B. Brown, 2002: On Gulf Stream Path Variability. *J. Physical Ocean.*, (submitted).

Mellor, G. L., and T. Yamada, 1982: Development of a turbulence closure model for geophysical fluid problems. *Rev. Geophys. Space Phys.*, **20**, 851–875.

Mironov, D.V., Gryank V.M., Lykossov, V.N., and Zilitinkevich, S.S., 1999: Comments on "A new second-order turbulence closure scheme for the planetary boundary layer" by K. Abdella and N. McFarlane. *J. Atmos. Sci.*, **56**, 3478-3481.

Moore, J. T. and T. E. Lambert, 1993: The use of equivalent potential vorticity to diagnose regions of conditional symmetric instability. *Wea. and Forecasting*, **8** , 301-308.

Morgan, M.C., and J.W. Neilsen-Gammon, 1998: Using tropopause maps to diagnose midlatitude weather systems. . *Mon. Wea. Rev.*, **126**, 2555-2579.

Munk, W.H., 1950: On the wind-driven ocean circulation. *J. of Meteor.*, **7**, 79-93.

Nowlin, W.D., and C.A. Parker, 1974: Effects of a cold air outbreak of the shelf waters of the Gulf of Mexico. *J. Phys. Oceans*, **4**, 467-486.

Nuss, W.A., and R.A. Anthes, 1987: A numerical investigation of low-level processes in rapid cyclogenesis. *Mon. Wea. Rev.*, **115**, 2728-2743.

Pietrafesa, L.J., L.P. Atkinson, and J.O. Blanton, 1978: Evidence for the deflection of the Gulf Stream by the Charleston rise. *Gulfstream*, vol. IV, 9, 3-7.

Pietrafesa, L.J., G.S. Janowitz, and J. Whittman, 1985: Physical oceanographic processes in the Carolina capes. *Coastal and Estuarine Sci.*, **2**, 23-33.

Pleim, J. E., J. S. Chang, 1992. A non-local closure model for vertical mixing in the convective boundary layer. *Atm. Env.*, 26A, 965-981.

Price, J.D., and G. Vaughan, 1993: The potential for stratosphere - troposphere exchange in cut - off - low systems; *Quart. J. Roy. Meteor. Soc.*, **119**, 343 – 365

Raman, S., A.J. Riordan, T. Holt, M. Stunder, and J. Hinman, 1986: Observations of the marine boundary layer thermal structure over the Gulf Stream during a cold air outbreak., *J. Appl. Clim. Meteorol.*, **25**, 14-21.

Raman, S., and A.J. Riordan, 1988: The Genesis of Atlantic Lows Experiment: The Planetary Boundary Subprogram., *Bull. Amer. Meteor. Soc.*, **69**, 161-172.

Raman, S., and N.C. Reddy , 1996: Numerical simulation of a mesolow over a Gulf Stream filament. *Pure and Applied Geophysics*, **147**, 789-819.

Reddy, N. C., and S. Raman, 1994: Scales and spectra of turbulence over the Gulf Stream. *Bound.- Layer Meteor.*, **68**, 387-417.

Reddy, N. C., and S. Raman, 1996: Validity of similarity relations over the Gulf Stream. *Tellus*, **48A**, 368-382.

Reed, R.J., and M.D. Albright, 1986: A case study of explosive cyclogenesis in the Eastern Pacific. *Mon. Wea. Rev.*, **114**, 2297-2319.

Reisner, J., R. J. Rasmussen, and R. T. Bruintjes, 1998: Explicit forecasting of supercooled liquid water in winter storms using the MM5 mesoscale model. *Quart. J. Roy. Meteor. Soc.*, **124B**, 1071-1107.

Reynolds, R.W., and T.M. Smith, 1994: Improved global sea surface temperature analyses using optimum interpolation. *J. Climate*, **7**, 929-948.

Richardson, P.L., 1985: Average velocity and transport of the Gulf Stream near 55°W. *Journal of Marine Research*, **42**, 83-111.

Richtmeyer, R.D., 1957: Difference methods for Initial-Value Problems. Interscience, New York, 283 pp.

Rogers, E., and L. F. Bosart, 1986: An investigation of explosively deepening oceanic cyclones. *Mon. Wea. Rev.*, **114**, 702-718.

Rooney, D.M., G.S. Janowitz, and L.J. Pietrafesa, 1978: A simple model of the deflection of the Gulf Stream by the Charleston rise. *Gulfstream*, vol.4, 11, 2-7.

Sanders, F.J., and J.R. Gyakum, 1980: Synoptic-dynamic climatology of the “bomb”. *Mon. Wea. Rev.*, **108**, 1589-1606.

Sanders, F., 1986: Explosive cyclogenesis over the west-central North Atlantic Ocean, 1981-84, I, Composite Structure and Mean Behavior, *Mon. Wea. Rev.*, **114**, 1781-1794.

Sanders, F., 1987: Skill of NMCooperational models in predictions of explosive cyclogenesis. *Weather and Forecasting*, **2**, 322-336.

Smith, S.D., C.W. Fairall, G.L. Geernaert and L. Hasse, 1996: Air-sea fluxes: 25 years of progress. *Bound. Layer Meteorol.* **78**, 247-290.

Stein, U., and P. Alpert, 1993: Factor separation in numerical simulations, *J. Atmos. Sci.*, **50**, 2107-2115.

Stoelinga, M. T., 1996: A potential vorticity-based study of the role of diabatic heating and friction in a numerically simulated baroclinic cyclone. *Mon. Weather Rev.*, **124**, 849-874.

Sutcliffe, R. C., 1939: Cyclonic and anticyclonic development. *Quart. J. Roy. Meteor.*, **65**, 518-524.

Stommel, H.M., 1948: The westward intensification of wind-driven ocean currents. *Transactions, Amer. Geophys. U.*, **29**, 202-206.

Sutcliffe, R. C., 1947: A contribution to the problem of development. *Quart. J. Roy. Meteor.*, **73**, 370-383.

Sutcliffe, R.C. and A.G. Forsdyke, 1950: The theory and use of upper air thickness patterns in forecasting. *Quart. J. Roy. Meteor. Soc.*, **76**, 189-217.

Sverdrup, H.U., 1947: Wind-driven currents in a baroclinic ocean; with application to the equatorial currents of the eastern Pacific. *Proceedings of the National Academy of Sciences*, **33**, 318-326.

Tracton M. S., and J. Du, 2001: Application of the NCEP/EMC short-range ensemble forecast system (SREF) to predicting extreme precipitation events. *Symposium on Precipitation Extremes: Prediction, Impacts, and Responses*, Albuquerque, New Mexico, Amer. Meteor. Soc., *Preprints*, 64-65.

Uccellini, L. W., 1990: Processes Contributing to the Rapid Development of Extratropical cyclones. *Extratropical Cyclones, Palmn Memorial Volume*, C. W. Newton and E. O. Holopainen, Eds., Amer. Meteor. Soc., 81-105.

Uccellini, L. W., and P. J. Kocin, 1987: The interaction of jet streak circulations during heavy snow events along the East Coast of the United States. *Wea. Forecasting*, **1**, 289-308.

Uccellini, L. W., R. A. Peterson, K. F. Brill, P. J. Kocin, and J. J. Tuccillo, 1987: Synergistic interactions between an upper-level jet streak and diabatic processes that influence the development of a low-level jet and a secondary coastal cyclone. *Mon. Wea. Rev.*, **115**, 2227-2261.

Vukovich, F.M., J.W. Dunn, and B.W. Crissman, 1991: Aspects of the evolution of the marine boundary layer during cold air outbreaks off the southeast coast of the United States. *Mon. Wea.. Rev.*, **119**, 2252-2278.

Warner, T.T., M. N. Lakhtakia, J. D. Doyle, and R. A. Pearson 1990: Marine atmospheric boundary layer circulations forced by Gulf Stream sea surface temperature gradients. *Mon. Wea.. Rev.*, **118**, 309-323.

Wayland, R., and S. Raman, 1989: Mean and turbulent structure of a baroclinic marine boundary-layer during the 28 January 1986 cold air outbreak (GALE86). *Bound.-Layer Meteor.*, **48**, 227-254.

Wylie, D.P., 1979: An application of a geostationary satellite rain estimation technique to an extratropical area. *J. Appl. Meteor.*, **18**, 1640-1648.

Xie, L., L.J. Pietrafesa, and S. Raman, 1996: Mesoscale air-sea interactions over the continental shelf off the Carolina coast. *The Global Atmosphere and Ocean System*, **4**, 65-88.

Xie, L., L.J. Pietrafesa, and S. Raman, 1999: Coastal ocean-atmosphere coupling. *Coastal and Estuarine Studies*, **56**, 101-123.

Zhang, D.L., and R.A. Anthes, 1982: A high-resolution model of the planetary boundary Layer-sensitivity tests and comparisons with SESAME-79 data. *J. Appl. Meteor.*, **21**, 1594-1609.

Zhang, F., C. Snyder, and R. Rotunno, 2003: Effects of moist convection on mesoscale predictability. *Journal of the Atmospheric Sciences*, **60**, 1173-1185.

Zhang, F., C. Snyder, and R. Rotunno, 2002: Mesoscale Predictability of the “Surprise” Snowstorm of 24-25 January 2000, *Mon. Wea. Rev.*, **130**, 1617-1632.

Zishka, K. M., and P. J. Smith, 1980: The climatology of cyclones and anticyclones over North America and surrounding ocean environs for January and July, 1950-77. *Mon. Wea. Rev.*, **108**, 387-401.

Zupanski M., and D. Zupanski, D. F. Parrish, E. Rogers, and G. Dimego, 2002: Four-dimensional variational data assimilation for the blizzard of 2000. *Mon. Wea. Rev.*, **130**, 1967-1988.

APPENDIX A: PORTING MM5 TO OS X

A.1 Motivation

Methods discussed below will work on Apple's G3, G4, and dual processor G5s. This was an MM5 side project that began in the summer of 2002. The objective was to get MM5 (any version) up and running on a "Mac". Since the new OS X operating system is UNIX based, this did not seem like such an impossible task. The motivation for this was based on two reasons: i) the new G5 dual 2 GHz clock speeds exceed the fastest AMD chip, and ii) this has not been attempted by anyone else to date. In fact, networked G5s at Virginia Tech posted faster clock speeds than Cray's X1.¹ Before further discussion, I would like to thank Jeff Wragg (College of Charleston / Apple Computer Inc. beta testing) for providing advice on compiler structure, Robert Fovell (UCLA) for helping with the MM5 code modification, Richard Yablonsky (NCSU) for his expertise in multiple processor LINUX systems, and Mike McLaughlin (Univ. of Utah) for advice on Darwin, x11, and running the dual G5 in rootless mode for Yellow Dog LINUX.

A.2 Procedure

This procedure is based on the LINUX configuration methods, thus the basic build methods for MM5 are assumed to be understood. There are several different versions of compilers that will work; however, Absoft 8.0, which is used here, is the only tried and true for any version of OS X. At the writing of this appendix, OS X 10.3.4 (Panther), was the most recent update for Apple's system. This method will work on Jaguar also.

¹ Lyman, Jay, 30 October 2003: Technews world report, www.technewsworld.com

- (1) Use a UFS-formatted disk, partition or disk image to preserve case sensitivity. These can be created in Disk Utility. The model needs to differentiate between files ending in .F and .f.
- (2) TERRAIN requires NCAR Graphics compiled using the same compiler. Pre-compiled Absoft binaries, along with the source code, for version 4.3.1 are available. I would suggest building it from scratch though, as some of the pre-complied binaries may have links to other software not installed, or installed in another directory.
- (3) The XLF compiler will also work if using no more than 1 or 2 CPUs on a single node, the MM5/SMP version below is by far the path of least trouble. The stock version of MM5 runs with very minor alterations to a few configure and makefiles. IBM's xlf has SMP support "out of the box".
- (4) For the MPP version, the CPP preprocessor is used to convert a *.F file containing directives into a *.f file. As of gcc 3.3, the Mac's CPP inserts a line starting with "#pragma". This is ignored by Absoft, but will crash the xlf. The Makefiles usually have to be rewritten to strip off the offending line immediately after preprocessing, using a sed command. Otherwise, add -xassembler-with-cpp to the CPPFLAGS in the Makefile.

A.2.1 TERRAIN

Start in the TERRAIN directory, rename either Makefile.IBM OSX or
Makefile.ABSOFT OSX to Makefile

>make

Then rename either terrain.deck.ABSOFT or terrain.deck.IBM to terrain.deck, and modify the file to specific simulation parameters

- i) NCARGRAPHICS in chosen Makefile. IBM version is set to NONCARG by default.
- ii) src/Makefile was modified to cut "#pragma" lines generated by cpp with gcc 3.3.
Abssoft ignores these, but xlf may freeze.
- iii) terdrv.F was modified to fix problem with call to watercheck routine. Ignore the redundant sqrt error. This appears to be irrelevant.

A.2.2 REGRID

Start in the REGRID directory, rename either Makefile.IBM OSX or
Makefile.ABSOFT OSX to Makefile

>make

Altered files: top level Makefile (replaced LINUX with Darwin),
regridder/src/proc_namelist.F, added ranlib in pregrid/util/Makefile,
pregrid/grib.misc/rd_grib.F

Darwin could be an entire chapter, but the line must be drawn somewhere.

A.2.3 INTERPF

Start in the INTERPF directory, rename either Makefile.IBM OSX or
Makefile.ABSOFT OSX to Makefile

>make

MM5/SMP -- single node

The MPP below is based on the original LINUX code.

A.2.4 Preparation for MM5

Edit the configure.user file to select FC and FCFLAGS lines for SMP or non-SMP version. Then replace the Makefile in the MM5 directory with the modified version to force a call to ranlib.

```
>make
```

Then replace &END with / in the deck file. A successful run will produce mmlif in the Run directory. If running in tcsh (which should be the case when using Darwin or x11 on a G3, G4, or G5 PowerMac), make sure these setenv commands are issued:

```
>setenv OMP_NUM_THREADS 2 [for a node with 2 CPUs]
```

```
>setenv STACKSIZE 8192 [seems to work fine]
```

```
>unlimit
```

```
>limit coredumpsize 0
```

A.2.5 MM5/MPP

Copy either configure.user.Absoft OSX.MPP or configure.user.IBM OSX.MPP to configure.user. Then edit the variables LINUX_MPIHOME and LOCAL_LIBRARIES to the path of mpich-1.2.5. In the MPP/RSL directory, copy either Makefile.RSL.Absoft OSX or Makefile.RSL.IBM OSX to Makefile.RSL. In the MPP/RSL/RSL directory, copy either makefile.darwin.Absoft or makefile.darwin.IBM to makefile.darwin. Then edit IDIR, CC and FC in makefile.darwin to the path of mpich-1.2.5. Next, edit FFLAGS in makefile.darwin to reflect flags used in configure.user. Make sure the LINUX_MPIHOME and LOCAL_LIBRARIES variables in configure.user point to locations consistent with mpich

location set in makefile.darwin

```
>make mpp
```

Make sure to make mpclean for minor model changes, and make uninstall for major changes, prior to recompiling. Single CPU executables can be built from this code; rename either configure.user.IBM OSX.1cpu or configure.user.Absoft OSX.1cpu to configure.user and issue make command.

A.2.6 mpich 1.2.5 for MM5/MPP

Below is the tsch syntax using Absoft:

```
>setenv FC f90 (not referencing f77 at all avoids problems with incompatible f77-f90 flags)
```

```
>setenv FFLAGS "-YEXT_NAMES=LCS -YEXT_SFX=_"
```

```
>setenv RSHCOMMAND "/usr/bin/ssh -1"
```

```
>setenv CFLAGS -fno-common
```

Change the configuration line: ./configure --with-device=ch_p4

```
>setenv P4_SOCKETBUFSIZE 65536
```

This last command enables full utilization of both cpus if using a dual processor G5. On a side note, this makes great graphics when using Vis5D, at 5 to 6 times as fast as the 3 GHz Intrex LINUX machine in the NC State Climate Office. When changing parameters, the make clean in mpich does NOT always delete everything, so when starting again, re-untar the tar file.

A.3 GrADS and Vis5D on OS X

During the initial stages of this project, GrADS was used in its LINUX form and run in an emulation window, but as of June 2004, the good people of the Center for Ocean-Land-Atmosphere Studies (COLA) have released a version the runs native in OS X (Jaguar or Panther). This made the post processing of the January 2000 "snowstorm" discussed in Chapter 7 much easier because the file headers need not be changed since it was run on a "Mac" from the beginning. Vis5D, which still does not run native, is a bit more complicated since the makefile need to be altered. It is a simple task of removing the -byteswapio flag, and the code runs in the LINUX rootless mode problem free. This made animations much easier because there was no need run it elsewhere, and the graphics capabilities of the G5 supercede any AMD or Intel processor.